Transition Modelling for Helicopter Flows

by

Georgios Zografakis (BSc. MSc.)

A thesis submitted in partial
fulfillment of the requirements for
the degree of Doctor of Philosophy
University of Liverpool
Engineering
November 2012

Declaration

I hereby declare that this dissertation is a record of work carried out in the School of Engineering at the University of Liverpool during the period from August 2008 to November 2012. The dissertation is original in content except where otherwise indicated.

November 2012

.....

(Georgios Zografakis)

Abstract

This thesis presents the development, validation and application of a numerical method for the calculation of laminar to turbulent transition effects for flows related to helicopters.

At certain conditions, as the rotor blades and the helicopter fuselage move through the fluid, the flow changes from laminar to turbulent. In order to accurately predict the flow, a Computational Fluid Dynamics (**CFD**) code should also predict this change and define the transition onset. The objective of this research would therefore be to develop a method to incorporate these transition effects inside the CFD solver, **HMB**. This computational code is a development of the Liverpool CFD group. The main developments carried out in the present thesis are: (i) the validation of the transition methods, (ii) the implementation of intermittency based transport models in the above code, (iii) the extension of the validation for the calculation of the transition flow around a helicopter fuselage and rotors.

Several transition modelling approaches have been proposed in the literature starting from simple algebraic expressions like the Michel's method and moving to more advanced multi-equations models. To provide baseline data for comparisons, this work was first focused on the implementation of transition models based on empirical correlations. Although, these methods are simple to implement, they suffer from two main problems: (i) there is no theoretical basis for the validity of these models in unsteady flows and (ii) the models depend on integration of flow variables that must be carried out in a streamwise direction.

At a second stage, a recent transition model was also assessed. This model is based on local information and solves two extra partial differential equations similar to the ones used for two-equation turbulence models. However, it is not free of empirical correlations and longer CPU times was needed.

The lack of a universal treatment for modelling transitional flows, combined with the lack of detailed experimental data, makes the development and evaluation of transition models difficult. The accuracy of the selected models was assessed against the few existing experimental results. For the validation of the models on aerofoils, the experimental results from the LABM laboratory and ONERA were used. The data of the LABM laboratory include steady and unsteady tests cases for a NACA 0012 aerofoil. The second set of cases is from ONERA and includes experimental data for the steady compressible flows around the ONERA A aerofoil. For further comparison, the models were also assessed against the experimental data of the NLF-0416 and S809 aerofoils. For each of the aerofoil cases, the computations were also compared with the XFOIL code. Dramatic improvements in the computed surface pressure and skin friction distributions have been observed over those computed using conventional fully turbulent simulations. Corresponding changes are also observed in the computed lift and drag coefficients when the transition onset is predicted for the two-dimensional flows.

To validate further the models and improve their implementation on the HMB, another set of tests on more complex three-dimensional cases were considered. These cases included data from the ROBIN fuselage. This is a fuselage configuration where the transition boundary on the fuselage has been visualised during recent NASA experiments. Finally, rotor calculations in hover and forward-flight have been attempted and the results have been compared against existing experimental data.

Publications

Papers in Conference Proceedings

G.Zografakis and G.N. Barakos, Transition Modelling for Rotorcraft CFD, *34th European Rotorcraft Forum, Liverpool, UK, 16–18 September*, 2008.

Presentations without Proceedings

The BURN House Helicopter Weekend, Fettercairn Parish, Scotland 27-30 April, 2008.

Journal Papers in Preparation

G.Zografakis and G.N. Barakos, *Transition Correlation for Boundary Layer Flows.*

G.Zografakis and G.N. Barakos, *Transition Modelling for Rotor and Complex Flows.*

Internal Reports

G. Zografakis, *Pitching-Translational Motion of a Rotor Blade using HMB v1.5*, 2009

G. Zografakis, *Transition Modeling in HMB*, 2013

G. Zografakis, *Surface Roughness Models in HMB*, 2013

G. Zografakis, *Instructions for the use of ST2 Wind Tunnel*, Manual, 2010

G. Zografakis, *Instructions for the use of Supersonic Wind Tunnel*, Manual, 2013

Acknowledgements

First and foremost, I would like to thank my supervisor Professor George Barakos for his continuous help, patience and support. His technical knowledge and experience have played a very important role in my research and have provided invaluable contribution throughout this project. It is his everlasting enthusiasm and passion for reasearch a source of encouragement and strength for me.

I would also like to thank Dr. Mark Johnson for his supervision and willingly offer of his support and guidance during the research.

I am grateful for the financial support of AgustaWestland and the University of Liverpool. Especially, I would like to thank Dr. A. Brocklehurst for his kindly help and support of experimental data for the research.

Many thanks have to be granted to all the members of CFD lab at the University of Liverpool, both past and present. They had create an environment, within I have been very lucky to work. I have enjoyed working with this group of people because of the quality of work produced and the diversity and character of the people that make it. In particular I would like to thank Dr. Mark Woodgate for his unselfishly devoting time of his, on problems of mine. It has been a privilege to work with you all.

In addition, I am very thankful to the engineers of the university for their help and advice during the wind tunnel experiment.

Last and not least, I would like to thank my family for their encouragement and support. Their unconditional support and understanding in every aspect was a source of calm and relaxation.

Contents

List of Figures

List of Tables

Nomenclature

Symbols	Definition
A	Amplitude disturbance
a	local growth rates
C_D	Drag coefficient
C_L	Lift coefficient
C_P	Pressure coefficient
C_M	Momentum coefficient
C_μ	Closure coefficient for one-equation models
C_f	Skin-friction coefficient : $C_f = \frac{\tau_w}{(1/2)\rho U_\infty^2}$
c	Chord length
$\tilde{d}$	Distance from nearest wall
E	Total energy
e	Specific internal energy
f_x, f_y, f_z	Fluctuation frequencies in x, y, z directions
F_{length}	Transition length function
F_{onset}	Function that trigger intermittency
$F_{\theta t}$	Blending function
G_{ij}	Favre-averaged stress tensor
H	Shape factor
h_s	Sand grain roughness height
J	Jacobian determinant
k	Turbulent kinetic energy
K	Flow acceleration parameter : $K = (\frac{\nu}{U^2})\frac{dU}{ds}$
L	Length
M_∞	Freestream Mach number
M_{tip}	Rotational Mach number
N	N factor for e^N method
Pr	Prandtl number : $Pr = \frac{C_p \mu}{\kappa}$
p	Pressure
Q_i	Sub-grid heat flux tensor
q_i	Heat flux vector
R	Rotor radius
R_t	Turbulent Reynolds number for $\kappa - \varepsilon$ model
R_T	Turbulence Reynolds number : $R_T = \frac{\rho k}{\mu \omega}$
R_ω	Turbulent Reynolds number for $\kappa - \omega$ model
Re	Reynolds number based on chord and. freestream conditions : $Re = \frac{\rho U c}{\mu}$
Re_θ	Momentum thickness Reynolds number : $Re = \frac{\rho U \theta}{\mu}$
$Re_{\theta c}$	Critical momentum thickness Reynolds number
$Re_{\theta t}$	Transition momentum thickness Reynolds number : $Re = \frac{\rho U \theta_t}{\mu}$
Re_v	Vorticity (Strain rate) Reynolds number : $Re_v = \frac{\rho y^2 S}{\mu}$

$\tilde{Re_{\theta t}}$	Scalar transition momentum thickness Reynolds number
S	Absolute value of the strain rate : $S = (2S_{ij}S_{ij})^{1/2}$
S_{ij}	Mean strain-rate tensor : $S_{ij} = \frac{1}{2}(\frac{\partial u_i}{\partial x_j} + \frac{\partial u_j}{\partial x_i})$
S_R	Coefficient for the Hellsten and Laine roughness model
T	Temperature
t	Time
y^*	Non-dimensionalised wall distance for turbulent flow
y^+	Non-dimensionalised wall distance for non-turbulent flow
y_n	Distance from the nearest wall
x, y, z	Cartensian coordinates
U	Local velocity : $U = (u^2 + v^2 + w^2)^{1/2}$
U_∞	Freestream velocity
U_e	Edge velocity of the boundary layer
u, v, w	Velocity components in X,Y,Z direction
u', v', w'	Turbulent velocity fluctuations in X,Y,Z direction
u_τ	Frictional velocity
V	Volume

Greek Symbols	**Definition**
α	Incidence angle
β	Fluctuation decay parameter
β_0	Blade coning angle
β_{1c}	Longitudinal flapping angle
β_{1s}	Lateral flapping angle
γ	Intermittency
δ	Kronecker delta
δ	Cell height
δ^*	Displacement thickness
ε	Turbulent dissipation rate
η, θ, ξ	Curvilinear coordinates
θ	Momentum thickness
θ_0	Blade collective pitch
θ_{1c}	Lateral cyclic pitch
θ_{1s}	Longitudinal cyclic pitch
κ	Reduced frequency
Λ	Polhausen parameter
λ_θ	Pressure gradient parameter : $\lambda_\theta = (\frac{\rho\theta}{\mu}) \cdot (\frac{dU}{ds})$
μ	Molecular viscosity
μ	Rotor advance ratio : $\mu = \frac{M_\infty}{M_{tip}}$
μ_T	Eddy viscosity
$\tilde{\mu}$	Undamped eddy viscosity
ν	Kinematic viscosity
ν_t	Kinematic eddy viscosity
$\tilde{\nu}$	Working eddy viscosityfor the Spalart-Allmaras model
ρ	Density
τ	Turbulent time-scale
τ	Turbulence level : $\tau = 100\frac{\sqrt{\frac{1}{3}\overline{u'^2} + \overline{v'^2} + \overline{w'^2}}}{U_\infty}$
τ_{ij}	Viscous stress tensor
τ_{ij}^R	Reynolds stress : $\tau_{ij}^R = -\rho\overline{u_i' u_j'}$
τ_w	Wall shear stress
Tu	turbulence intensity
σ	Turbulent Prandtl number
Ω	Absolute value of vorticity : $\Omega = (2\Omega_{ij}\Omega_{ij})^{1/2}$

$\Omega_X, \Omega_Y, \Omega_Z$	Dimensionless streamwise, normal and spanwise frequencies : $\Omega_X = \frac{2\pi f_x \delta}{U}, \Omega_Y = \frac{2\pi f_y \delta}{V}, \Omega_Z = \frac{2\pi f_z \delta}{W}$
Ω_{ij}	Vorticity tensor : $\Omega_{ij} = \frac{1}{2}(\frac{\partial u_i}{\partial x_j} - \frac{\partial u_j}{\partial x_i})$
ω	κ-specific dissipation rate
ω	Turbulent frequency

Acronyms	Definition
AHD	(Arnal-Habiballah-Delcourt criterion)
BL	Boundary Layer
BILU	Block Incomplete Lower-Upper factorisation
BSL	BaSeLine
CFD	Computational Fluid Dynamics
CFL	Courant-Friedrichs-Lewy number
DNS	Direct Numerical Simulation
HMB	Helicopter Multi-Block
LABM	Laboratoire d'Aerodynamique et de Biomecanique du Mouvement
LES	Large Eddy Simulation
NASA	National Aeronautics and Space Administration
NACA	National Advisory Committee for Aeronautics
ONERA	Office National d'Etudes et de Recherches Aérospatiales
RANS	Reynolds Averaged Navier-Stokes
RMS	Root Mean Square
LE	Leading Edge
SA	Spalart-Almaras one equation turbulence model
SST	Shear Stress Transport
TE	Trailing Edge
URANS	Unsteady Reynolds Averaged Navier-Stokes

Subscripts	Definitions
0	Initial value
av	Cell-averaged values
e	Boundary layer edge value
E	End of the transition region
i, *j*, *k*	Index i,j,k (=1,2,3...)
l	Laminar flow
rough	Roughness
sg	Sub-grid
S	Start of the transition region
t	Turbulent flow
tr	Transition
w	Wall value
∞	Freestream condition

Superscripts	Definitions
*	Non-dimensional parameters
I	Inviscid terms
V	Viscous terms
$n, n+1$	Time step
	Mean value
'	Fluctuating value

Chapter 1

Introduction

Helicopters are important flying machines, equipped with capabilities, enabling them to fly missions impossible for any other type of flying vehicle. Their unique ability of vertical take off and landing has made helicopters important for many civil and military applications. Although and regardless of the amount of rotorcraft research that has been carried out during the last years, the ability to accurately predict the flow field around a helicopter in hover or in forward flight is still a challenge. In the helicopter flows, there are regions where different flow phenomena coexists while strong interactions between the different regions can occur. Hence, accurate predictions of power and performance for helicopters rotors even at conditions inside the flight envelope are challenging for the current Computational Fluid Dynamics (**CFD**) methods.

Regardless of the substantial work reported on improving the accuracy of the CFD tools in engineering predictions, especially in the turbulence modelling areas, numerical simulation of laminar-to-turbulent transitional flows remains an unsolved problem in fluid mechanics. An understanding of the phenomenon and what is physically happening in the transitional region, continues to be unknown despite more than a century of research work in this field. For most CFD calculations, the laminar flow is transformed immediately to turbulent and the transitional region is often ignored, even if the length of the later can occupy a large part of the domain.

The importance of the flow transition region has been recognised by many researchers and it plays a role in the performance of aerodynamic devices. Failing to accurately predict transition would result in erroneous flow variables, while transition modelling leads to correct estimations of skin friction and separation flow and results in

better predictions especially for CFD codes.

1.1 Literature Survey

The main objective of the literature review was to gain an understanding of published works related to transition flow modelling and learn from their findings about the basic flow physics of the problem and the existing models. As this research is concerned with the effects of transition on rotorcraft, the survey was expanded with a search for existing experimental transition data. The papers are divided into three categories based on the cases used for the validation. Initially, work related to the work done on aerofoils are presented and are followed by works on helicopter fuselages and rotor blades.

1.1.1 Data and Work on Aerofoils

Johansen and Sorenson [1] compared transition predictions obtained using an empirical model (Michel criterion) with those obtained using a simplified e^N method. The flow was computed using the SST $\kappa - \omega$ two equation turbulence model. The results were computed using the EllipSys2D solver which is based on a multi-block finite volume discretisation of the Reynolds averaged Navier-Stokes equations in general curvilinear coordinates. For the pressure-velocity coupling, the SIMPLE method was used and the solution of the momentum equations was obtained using a second order upwind scheme. For the calculation of the transition length, Johansen and Sorenson used the empirical method of Chen and Thyson modified by Cebeci. This model scales the eddy viscosity by an intermittency function which is given by:

$$G_{\gamma_r} = 213[log(Re_{x,tr}) - 4.732]/3 \tag{1.1}$$

For testing, two aerofoils were used, the NACA 0012 at $Re = 3 \times 10^6$ and a 19% thick FX-66-S-196 V1 Wortmann aerofoil at $Re = 1.5 \times 10^6$. The predicted transition location obtained with the e^N method was generally further downstream than with the empirical models although both methods compared favourably with measurements. The e^N model resulted in better predictions and was more stable in comparison with the Michel's criterion. The transition onset predicted by Michel's criterion showed a more fluctuating behaviour than that predicted with the e^N method.

In 2001, Brodeur [2] presented a boundary layer transition prediction methodology and applied it to a two-dimensional Reynolds averaged Navier Stokes solver. The baseline code was the incompressible INS2D using the artificial compressibility formulation. The NFL-0416 and the S809 aerofoils were used for their calculations.

For testing, Brouder considered the one-equation Baldwin-Barth and Spalart-Allmaras turbulence models. Because of some deficiencies in the velocity profiles generated by the Spalart-Allmaras model, all calculations utilised the Baldwin-Barth turbulence model. In general, the numerical results agreed well with the experimental data. It was shown that the transition model could simulate better the experimental data than the fully turbulence model. The model could even capture the developed bubble, as observed from the negative values of the obtain skin-friction. However, the model failed to capture some of the finer details of the instability growth in the laminar boundary layer.

Geissler [3] presented results for the performance of various turbulence and transition models for unsteady separated flows. His findings were compared against existing experimental data and published numerical results. The time-dependent, compressible, Reynolds averaged Navier Stokes equations were solved using an implicit finite-difference method on body fitted C-type grids that moved with the aerofoil. The NACA 0012 was solved in harmonic oscillation and the Beam and Warming factored scheme was used. The spatial derivatives were calculated via central differences and kept second order accurate. A variety of turbulence models like the Baldwin-Lomax, the Spalart-Allmaras, the Wilcox's $\kappa - \omega$ model and Menter's SST $\kappa - \omega$ model were used. None of the models managed to fully predict the dynamic stall cases. Only the Spalart-Allmaras model simulated reasonably well some of the flow physics, although it demonstrated a delay at the transition onset. A buffet case resulted in good agreement with the experiments although the configuration used was simpler than a normal supercritical aerofoil. Finally, Geissler [3] showed that even if the same numerical scheme for the Navier Stoke equations and the same turbulence model was used for other flow cases, the produced results were not satisfactory, probably due to the fact that the details of the numerical implementation have an important influence on these very sensitive type of flows.

Hill [4] explored the use of empirical models in the prediction of transition for aerofoils Reynolds averaged Navier-Stokes equations together with the $\kappa - \omega$ turbulence model of Wilcox. The empirical model of Michel[5] was used for the onset and extend of the transition flow. The model was demonstrated for two values of Re and for the NACA 0012 and Aerospatiale A (or ONERA A) aerofoils. It was also used to study the transitional flow of an hovering rotor but in a decoupled fashion. For the NACA 0012 aerofoil, the comparison of the computed and measured data was good for either $Re = 10^5$ or 2.88×10^6 which were considered as low and high Reynolds number test cases

respectively. For small incidence angles, the transition location was measured although for higher incidence angles, the computed transition location was generally aft in comparison with the experimental data but the prediction was acceptable. During calculations with the Aerospatiale A aerofoil, it was observed that the computed skin friction, pressure distribution and boundary profiles showed improvement in comparison with the fully turbulence model.

The employed experimental data were provided by Berton et al. [6] for studying the steady and unsteady boundary layer behaviour and the periodic separation process occurring on a NACA 0012 aerofoil oscillating in pitch. Their setup can be seen in the figure 1.1(a) and consists of an oscillating device located underneath the wind tunnel test section which drives the pitching motion of the aerofoil according to:

$$\alpha(t) = \alpha_0 + \Delta(\alpha \cos \omega t) \tag{1.2}$$

where α_0 is the mean incidence and ω the rotational frequency. Flow visualisation was carried out using small particles illuminated by a laser light sheet near the mid-span plane of the model wing. The optical head of the Embedded Laser Doppler Velocimeter (as seen at figure 1.1(b)) was installed on the oscillating frame giving it the ability to move together with the pitching aerofoil. At high angles of attack, the separated flows occurring on the upper surface of the aerofoil were due to the bursting of the leading edge bubble. On the other hand, at lower pitching angles with no separated flow, the bubble remained located close to the leading edge and its size was small. The height of the bubble can be observed due to the fact that few particles are entering into the bubble. Berton [7] studied qualitatively and quantitatively the steady and unsteady flow physics around the NACA0012 aerofoil in 2D and 3D flow configurations. Attention was given to the creation and growth of the laminar separation bubble and the reaction of the bubble as the angle of attack was increased or decreased. The flow features around the aerofoil were analysed using flow visualisations and velocity measurements. As the angle of attack increased, the length of the bubble decreased although its height kept increasing.

Savill [8] evaluated turbulence models for transition under the influence of free-stream turbulence. The assessed models include: correlation/mixing length and integral methods,a range of one-equation models, k-ε, k-ω, k-τ and k-ε/k-l two-equation models, various RST closures, different sub-grid models for Large Eddy Simulations and finally Direct Numerical Simulations. The objective was to test the ability of current turbulence models to predict the effect of variable intensity, isotropic, free-stream turbulence on the initial development and subsequent transition of a laminar boundary layer, in either zero or favourable-to-adverse pressure gradient representative of an aft-loaded gas turbine

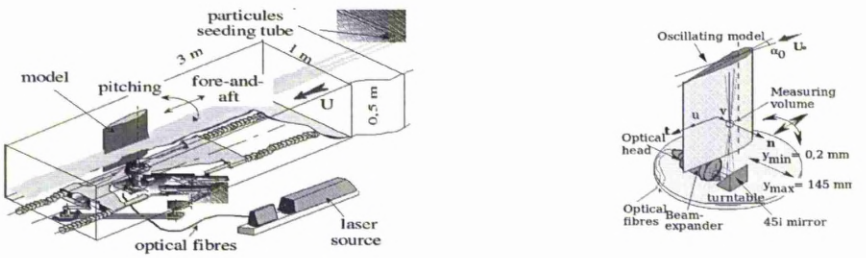

(a) LABM Wind tunnel configuration

(b) Embedded Laser Doppler Velocimeter

Figure 1.1: Wind tunnel configuration and the Embedded Laser Doppler Velocimeter of LABM [7].

blade. The test cases showed that none of the current models are sufficient for transition prediction. Improvements in the models will come from a better appreciation of the physical processes occurring at low-Re flows as distinct from low-Re near wall flows. Models that satisfy the wall-limiting conditions for u, v and ε, are better at predicting transition than those that satisfy either one or neither of these. Models that employ damping factors are more appropriate for the prediction of low-Re transitions regions than ones that introduce a dependence on wall-proximity. The former models contain functions of the wall distance and that is the reason for not predicting the transition flows correctly.

Stock [9] used the coupled Navier-Stokes equations with e^N transition prediction to validate the natural transition aerofoil experiments in wind tunnels for which the limiting factor N was not known a priori. The NFL-0416 laminar aerofoil and the NACA 64_2A015 section where chosen for the validation and were tested in the low-speed NASA Langley Low-Turbulence Pressure Tunnel LTPT and in the NASA Ames 12-Foot Pressure Tunnel, respectively. Both aerofoils were tested under different Reynolds numbers and a range of different angles of attack were used. This work illustrated some deficiencies in the predictive capability of the e^N method.

Moens et al. [10] within the EUROLIFT EU presented the measurements of the transition location and the predictions on a generic high-lift swept wing. An experimental database was built and the effect of Reynolds number on transition location was studied. The transition location was computed and not imposed a priori. The ONERA AFV model was used and it was tested at two sweep angles, $\phi = 30^o$ and $\phi = 40^o$ and for a range of Reynolds numbers. The aerofoil was equipped with a number of pressure taps and hot films. The paper demonstrated only the results for $\phi = 40^o$, a slat leading edge $\delta_{slat} = 30^o$ and a flap $\delta_{flap} = 20^o$. A structured multi-block mesh was used together with the elsA code. For $Re = 7.510^6$ and $M = 0.2$, the turbulence models of Spalart-Allmaras, Wilcox's $\kappa - \omega$ and

Smith's $\kappa - l$ were tested at three different angles of attack. It was apparent that the $\kappa - \omega$ model overestimated the pressure peak on the slat and the main wing and did not result in the correct lift coefficient. On the other hand the Spalart-Allmaras and $\kappa - l$ models were satisfactory. It was observed that as the Reynolds number increased, the upstream displacement of the transition location at low angles of attack was correctly simulated. For the calculation of the transition location, the Arnal-Habiballah-Delcourt (AHD) criterion[11,12] in combination with the Gleizes criterion for the Tollmien-Schlichting instabilities were used. For transition due to cross-flow, the C1 criterion[12,13] was used. The computation started with fully turbulent models and then the transition location was calculated up to convergence. It was reported that the elsA code agreed with the experiments when computations took transition criteria into account and even captured the separation bubble.

1.1.2 Data and Work on Helicopter Fuselage

For many years, little attention has been devoted to the research of the helicopter fuselage aerodynamics. However, the fuselage can significantly affect the overall performance of the helicopter at all flight conditions. Fuselage drag amounts to 50% of total helicopter drag in high-speed flight and its reduction is a major design target. Currently, several research programmes funded from EU and NASA involve investigation of helicopter aerodynamics. The aim of fuselage flow modelling is to better predict the drag of the overall aircraft and improve understanding of how this might be reduced.

Table (1.1.2) presents a summary of the rotorcraft simulations reported in the literature.

It was in 1979 when Freeman and Mineck [14] conducted a series of wind tunnel tests over a helicopter fuselage at Langley subsonic wind tunnel. The tests were carried out with a specially created fuselage geometry. This geometry is representative of a wide range of helicopter fuselages without being specific to any and is known as the Rotor Body InteractioN (ROBIN) geometry. A large amount of experimental data on fuselage were gathered but they were not analysed. Freeman and Mineck [14] looked at time-averaged surface pressure measurements, with and without a rotor present.

After the initial study in 1979, there were several subsequent studies to address the interaction between rotor wake and fuselage. These studies tried to impose a rotor solution onto a fuselage solution.

In an effort to closely replicate the wind tunnel environment, Mineck [18] included the 'sting' support of the

Model	Paper	Rotor	Fuselage	CFD	Exp
ROBIN	Mineck & Gorton [15]	*	*		*
	Freeman & Mineck [14]	*	*		*
	Freeman [16]		*	*	
	Chaffin & Berry [17]	*	*	*	
	Mineck [18]		*	*	*
	Chaffin & Berry [19]		*	*	
	Berry *et al.* [20]	*	*	*	
	Schweitzer [21]		*	*	
	Boyd *et al.* [22]	*	*	*	
	Sides *et al.* [23]	*	*	*	
Dauphine	Costes *et al.* [24]		*	*	
	Berry & Bettschart [25]	*	*	*	*
	Sides *et al.* [23]	*	*	*	*
BO105	Splettstoesser *et al.* [26]	*	*		*
	Khier *et al.* [27]	*	*	*	
Apache	Schweitzer [21]		*	*	

Table 1.1: Summary of the rotorcraft simulations.

tunnel model in the simulation. The results were compared against the steady pressure data from the original 1979 report [14] and correlated closely, when evaluated with the sting in place. Without, the predicted flow field in the vicinity of the sting is not in agreement with experiment, although the discrepancies do not propagate widely. Comparison between the newer unstructured code and the earlier structured thin-layer Navier Stokes solver [19] reveal larger differences.

In 1999 there was another effort, also at Langley [21], which used the code PUMA to study various difficult geometries including the ROBIN and the Apache. The steady inviscid solution method was partly adequate for the isolated fuselage, but future development to rotor-fuselage interaction required a much better solution technique for unsteady flows. The thesis by Schweitzer [21] was a feasibility study in preparation for an unstructured approach to a complete rotor-fuselage model.

Till recently, there was a lack of detailed experimental data on the area of transition modelling for rotorcraft applications. In 2005, collaborations of European universities and helicopter companies launched the Generation of Advanced Helicopter Experimental Aerodynamic Database for CFD code validation also known as GOAHEAD project. The project used a model similar to a modern transport helicopter consisting of the main rotor, the fuselage and the tail rotor and it took place at the DNW LLF wind tunnel in the Netherlands. Beside, the wide range of measurements, like global forces, steady and unsteady pressures, the GOAHEAD project produced some transition data. On the other hand, the placement of hot films on the surfaces triggered the flow and the full free development of

transition was not observed.

1.1.3 Data and Work on Rotor

Rotary wing applications have been the subject of extensive numerical research since the advent of CFD. This is due to the complexity of rotor flows which makes CFD analyses significantly harder. There are several factors contributing to this difficulty and they can be grouped into two categories. Initially, the flow physics of a rotating wing is rich in terms of fluid phenomena. Phenomena like laminar to turbulence transition, strong vortices interacting with each other and with the rotor blades and formation of wake behind the rotor are some of the issues that CFD methods have to cope with. Moreover, a second category of problems comes from the strong link between the aerodynamics and dynamics of the rotor blades. It is almost impossible to consider one without the other and the link between the two is the balance of forces acting on the rotor, Problems like the trimming problem complicate the numerical simulations of rotors in forward flight[28].

In 2000 full Navier-Stokes solutions for rotors remained too expensive in terms of CPU-time, so a hybrid schemes were proposed, Boyd and et al. [22] coupled a thin layer Navier-Stokes with a pressure jump boundary condition based on a Generalised Dynamic Wake Theory Iterative calculation of the rotor loading. The methodology is similar to that of Chaffin and Berry [17]. At that time, full Navier-Stokes solution of rotors and fuselage with Chimera grids were too expensive and only proof of concept studies could be conducted.

As the power of computers increased, NASA worked again on the results of their first attempt of 1979[14]. The main intention was to provide usable data for validation of more powerful CFD techniques. The tests were carried out at four different advance ratios and three thrust coefficients. The rotor was mounted above the fuselage and the entire rotor system could be tilted, as well as having a fully articulated hub. Rotors loads and moments were measured. The surface pressure was measured on the fuselage at a range of stations. Pressure drag and skin friction increased with advance ratio.

1.2 Objectives

The main aim of this research is to develop an improved predictive capability for helicopter flows. As transition plays an important role in aerodynamics, this project aims to develop better CFD methods with transition modelling that are

robust and effective for industrial applications.

The objectives of this research effort can be summarised as follows:

• To investigate the effects and behaviour of transitional flows around steady and unsteady aerofoils, around helicopter fuselage and around helicopter rotors.

• To develop and implement boundary layer transition models for aerofoils, helicopter fuselages and rotors.

• To validate and verify numerical methods by comparison of computed results with experimentally measured data and independent calculations.

• To explore newly developed $\kappa-\omega-\gamma-Re_\theta$ models for transition predictions.

1.3 Thesis Outline

The remaining of this thesis is organised as follows:

Chapter 2 introduces the governing equations for the compressible fluid flow along with the formulation for the moving coordinate systems. This chapter contains details for the employed solver used in this work, the Helicopter Multi-Block (HMB) solver. The different transition models implemented in the code are also explained. Firstly, the principles of the empirical correlation models of Michel and Cebeci Smith are presented. Then the main points of the $\kappa-\omega-\gamma-Re_\theta$ model are described. The implementation of the latter model in the solver is presented in Appendix A.

Chapter 3 summarises the experimental data and conditions for the two dimensional test cases. The experiments carried out by ONERA and LABM are presented in this chapter. These tests took place over a range of parameters. Data for different Reynolds number, Mach number and free-stream turbulence intensity are presented. Besides ONERA A and symmetric NACA0012 aerofoil, the flow around the NLF-0416 and S809 aerofoil are discussed. Also in this chapter, the computational results for each a aerofoil are presented. The lift and drag produced from the code with the implemented transitional models are compared again the existing experimental data and the XFOIL code. The estimated surface pressure and skin friction coefficients are presented while the location where transition starts is indicated.

Chapter 4 discuss the experimental data for more complex three dimensional cases. The ROBIN fuselage case is explained while data from a fast forward flying UH60 and a hovering rotor are presented. The results from

transitional models are compared against the fully turbulent computations and the existing experimental data. The changes of the surface pressure coefficient and the transition onset on the ROBIN fuselage are presented in this chapter. The research is also extended to a fast forward flying UH60 and a hovering rotor.

Chapter 5 concludes the thesis and offers suggestions for future work.

The appendices offer more details on the implementation of $\kappa - \omega - \gamma - Re_\theta$ model. While, the last part is devoted on the experimental work was conducted as part of this thesis.

Chapter 2

Physics and models for transitional flows

2.1 Computational Fluid Dynamics

All computations in this thesis were performed using the Liverpool Helicopter Multi-Block (HMB) solver. The flow solver has been continually revised and updated over a number of years and has been successfully applied to a variety of problems including cavity flows, rotors, wind turbine and full helicopter configurations among others. The code is a 3D multi-block structured solver for the Navier-Stokes equations. The Navier-Stokes equations are Partial Differential Equations (PDEs) that describe the three fundamental laws of conservation:

1. Conservation of Mass (Continuity Equation).
2. Conservation of Momentum (Newton's 2nd Law).
3. Conservation of Energy (1st Law of Thermodynamics).

The continuity equation simply states that the mass must remain the same. In Cartesian coordinates, the law is written as:

$$\frac{\partial \rho}{\partial t} + \frac{\partial (\rho u_i)}{\partial x_i} = 0 \tag{2.1}$$

where ρ is the density of the fluid, t is the time and u_i is the velocity vector. The Einstein's summation is used here and subscript i represents x,y, or z.

The second principle is Newton's Second Law and states that momentum is conserved. Written in Cartesian coordinates, it reads:

$$\frac{\partial (\rho u_i)}{\partial t} + \frac{\partial (\rho u_i u_j)}{\partial x_j} = \rho f_i - \frac{\partial p}{\partial x_i} + \frac{\partial \tau_{ij}}{\partial x_j} \tag{2.2}$$

where f_i represents the body forces, p the pressure and τ_{ij} the viscous stress tensor. The latter can be defined as

$$\tau_{ij} = \mu \left[\left(\frac{\partial u_i}{\partial x_j} + \frac{\partial u_j}{\partial x_i} \right) - \frac{2}{3} \delta_{ij} \frac{\partial u_k}{\partial x_k} \right] \tag{2.3}$$

μ is the molecular viscosity and δ_{ij} represents the Kronecker delta.

The third principle can be written in Cartesian coordinates as

$$\frac{\partial \rho E}{\partial t} + \frac{\partial}{\partial x_j} \left[u_i (\rho E + p) \right] - \frac{\partial}{\partial x_j} \left(u_i \tau_{ij} - q_j \right) = 0. \tag{2.4}$$

and represents the First Law of Thermodynamics. In the above equation of Energy Conservation, E is the total energy of the fluid, defined as

$$E = \left[e + \frac{1}{2} u_i u_i \right] \tag{2.5}$$

and e is the specific internal energy with $u_i u_i$ representing the kinetic energy per unit volume of fluid.

The heat flux vector, q_i, is calculated using Fourier's Law of heat conduction

$$q_i = -k \frac{\partial T}{\partial x_i} \tag{2.6}$$

where k is the coefficient of thermal conductivity which is a material property and T is the temperature of the fluid.

An ideal gas approximation is used and the adiabatic index is set to $\gamma = 1.4$. Sutherland's law is used to calculate the viscosity:

$$\mu = \mu_{ref} \left(\frac{T}{T_{ref}} \right)^{\frac{3}{2}} \frac{T_{ref} + S}{T + S} \tag{2.7}$$

where S is the Sutherland temperature (S= 110.4[K]) and μ_{ref} is the reference viscosity at the reference temperature T_{ref}. The values for the last coefficients are $1.716 \times 10^{-5} [\frac{kg}{(m \cdot s)}]$ and 273.15 [K] respectively.

2.2 Vector Form of the Conservation Laws

The three laws of conservation can be combined and written in a convenient compact vector form, which is referred to as the Navier-Stokes equations of viscous flow and is given below:

$$\frac{\partial \mathbf{W}}{\partial t}+\frac{\partial\left(\mathbf{F}^{i}+\mathbf{F}^{v}\right)}{\partial x}+\frac{\partial\left(\mathbf{G}^{i}+\mathbf{G}^{v}\right)}{\partial y}+\frac{\partial\left(\mathbf{H}^{i}+\mathbf{H}^{v}\right)}{\partial z}=0 \tag{2.8}$$

$\mathbf{W}$ is the vector of conservative variables and is defined by

$$\mathbf{W}=(\rho,\rho u,\rho v,\rho w,\rho E)^{T} \tag{2.9}$$

where the variables ρ, u, v, w, p and E have their usual meaning, density, three components of velocity, pressure and total energy, respectively. The superscripts i and v in Equation 2.8 denote the inviscid and viscid components of the flux vectors $\mathbf{F}$ (in the x-direction), $\mathbf{G}$ (in the y-direction) and $\mathbf{H}$ (in the z-direction). The inviscid flux vectors, $\mathbf{F}^{i}$, $\mathbf{G}^{i}$ and $\mathbf{H}^{i}$, are given by

$$\begin{aligned}
\mathbf{F}^{i}&=\left(\rho u,\rho u^{2}+p,\rho uv,\rho uw,u(\rho E+p)\right)^{T},\\
\mathbf{G}^{i}&=\left(\rho v,\rho uv,\rho v^{2}+p,\rho vw,v(\rho E+p)\right)^{T},\\
\mathbf{H}^{i}&=\left(\rho w,\rho uw,\rho vw,\rho w^{2}+p,w(\rho E+p)\right)^{T}.
\end{aligned} \tag{2.10}$$

while the viscous flux vectors, $\mathbf{F}^{v}$, $\mathbf{G}^{v}$ and $\mathbf{H}^{v}$, contain terms for the heat flux and viscous forces exerted on the body and can be represented by

$$\begin{aligned}
\mathbf{F}^{v}&=\left(0,\tau_{xx},\tau_{xy},\tau_{xz},u\tau_{xx}+v\tau_{xy}+w\tau_{xz}+q_{x}\right)^{T},\\
\mathbf{G}^{v}&=\left(0,\tau_{xy},\tau_{yy},\tau_{yz},u\tau_{xy}+v\tau_{yy}+w\tau_{yz}+q_{y}\right)^{T},\\
\mathbf{H}^{v}&=\left(0,\tau_{xz},\tau_{yz},\tau_{zz},u\tau_{xz}+v\tau_{yz}+w\tau_{zz}+q_{z}\right)^{T}.
\end{aligned} \tag{2.11}$$

where the term τ_{ij} represents the viscous stress tensor and q_i the heat flux vector.

2.3 Solution Method

The HMB solver uses a cell-centered finite volume approach combined with an implicit dual-time method. This means that the solution marches in pseudo-time for each real time-step to achieve fast convergence.

According to the finite volume method, the RANS equations can be discretised for each cell as:

$$\frac{d}{dt}\left(\mathbf{W}_{i,j,k}\mathcal{V}_{i,j,k}\right)+\mathbf{R}_{i,j,k}=0. \tag{2.12}$$

where $\mathcal{V}_{i,j,k}$ denotes the cell volume and $\mathbf{R}_{i,j,k}$ represents the flux residual.

The implicit dual-time method proposed by Jameson[29] is used for time-accurate calculations. The residual is redefined to obtain a steady state equation which can be solved using acceleration techniques. The following system of equations are solved in the implicit scheme during the dual-time integration process:

$$\frac{\Delta V\mathbf{W}^{m+1}_{i,j,k} - \Delta V\mathbf{W}^{m}_{i,j,k}}{\Delta V\Delta\tau} + \frac{\Delta V\mathbf{W}^{n+1}_{i,j,k} - \Delta V\mathbf{W}^{n}_{i,j,k}}{\Delta V\Delta t} = \mathbf{R}^{n+1}_{i,j,k} \tag{2.13}$$

where ΔV is the change in cell volume, $\Delta\tau$ is the pseudo time-step increment and Δt is the real time-step increment. The flux residual $\mathbf{R}^{n+1}_{i,j,k}$ is approximated by:

$$\mathbf{R}^{n+1}_{i,j,k} \approx \mathbf{R}^{n}_{i,j,k} + \frac{\partial \mathbf{R}^{n}_{i,j,k}}{\partial \mathbf{W}^{n}_{i,j,k}} \left(\mathbf{W}^{n+1}_{i,j,k} - \mathbf{W}^{n}_{i,j,k}\right) \tag{2.14}$$

By substituting eqn. (D.3) into eqn. (D.2), the resulting linear system can be written as:

$$\left(\frac{1}{\Delta t} + \left(\frac{\partial \mathbf{R}}{\partial \mathbf{W}}\right)^{n}\right)\Delta\mathbf{W} = -\mathbf{R}^{n} \tag{2.15}$$

where the subscripts i,j,k have been dropped for clarity and ΔW is used for $\left(\mathbf{W}^{n+1}_{i,j,k} - \mathbf{W}^{n}_{i,j,k}\right)$.

Osher's upwind scheme [30] is used to resolve the convective fluxes although Roe's flux-splitting scheme [31] is also available. The Monotone Upstream-centered Schemes for Conservation Laws (MUSCL) variable extrapolation method[32] is also employed to formally provide third-order accuracy. The Van-Albada limiter is also applied to remove any spurious oscillations across shock waves. The central differencing spatial discretisation method is used to solve the viscous terms. The non-linear system of equations that is generated as a result of the linearisation is then solved by integration in the pseudo-time using a first-order backward difference. A Generalised Conjugate Gradient (GCG)[33] method is then used in conjunction with a Block Incomplete Lower-Upper (BILU)[33] factorisation as a pre-conditioner to solve the linear system of equations, which is obtained from a linearisation in pseudo-time.

The HMB flow solver can be used in serial or parallel mode. To obtain an efficient parallel method based on domain decomposition, different methods are applied to the flow solver [34]. An approximate form of the flux Jacobian resulting from the linearisation in pseudo-time is used which reduces the overall size of the linear system by reducing the number of non-zero entries. Between the blocks of the grid, the BILU factorisation is also decoupled thereby reducing the communication between processors. Each processor is also allocated a vector that contains all the halo cells for all the blocks in the grid. Message Passing Interface (MPI) is used for the communication between the processors in parallel.

A number of turbulence models have been implemented into HMB. The one-equation SA turbulence model[35], two-equation Wilcox $k-\omega$ [36] and Menter's $k-\omega$ Shear-Stress Transport (SST)[37]turbulence models were implemented for this project. All these turbulence models and indeed the simulation techniques are described in greater detail in the following sections.

2.4 General Description of Turbulence and its Modelling

Turbulent flows contain structures which show rapid fluctuations in time and space. A broad range of scales are observed to exist at high Reynolds numbers where turbulence develops as an instability of the laminar flow. Starting with the laminar flow, fluid layers slide smoothly past each other and the molecular viscosity dampens any high-frequency small-scale instability. At high Reynolds number, the flow reaches a periodic state. The character of the flow also changes and becomes more diffusive and dissipative. This flow has increased mixing friction, heat transfer rate and spreading rate. Boundary layers consequently become thicker and less susceptible to separation.

The non-linearity of the Navier-Stokes equations leads to interactions between the turbulent fluctuations of different wavelengths and directions. Wavelengths extend from a maximum comparable to the width of the flow to a minimum fixed by viscous dissipation of energy. A key process that spreads the motion over wide range of wavelengths is called vortex stretching. Turbulent structures in the flow gain energy if the vortex elements are primarily orientated in a direction that allows the mean velocity gradients to stretch them. This mechanism is called production of turbulence. The kinetic energy of the turbulent structures is then convected, diffused and dissipated.

Most of the energy is carried by the large scale structures, the orientation of which is sensitive to the mean flow. The large eddies cascade energy to the smaller ones via stretching. Small eddies have less pronounced preference in their orientation and statistically appear to be isotropic. For the shortest wavelengths, energy is dissipated by viscosity. This description corresponds to what is known as isotropic turbulence. For this flow, the ratio of the largest to smaller scale increases with Reynolds number.

A turbulence model therefore needs to account for some part of the fluctuating motion in order to keep the computing cost down. The optimum model should therefore be simple to implement, general and derived out of the flow physics. It is equally important that the model is computationally stable and co-ordinate invariant. These statistical turbulence models are applied to a special form of the equations of motion called the Reynolds-Averaged

Navier-Stokes (**RANS**) equations.

2.5 Averaged Equations

In a turbulent flow, the fields of pressure, velocity, temperature and density vary randomly in time. Reynold's approach involves separating the flow quantities into mean and random parts. The quantities are presented as a sum of the mean flow value $\overline{\phi}$ and the fluctuating part ϕ':

$$\phi = \overline{\phi} + \phi' \tag{2.16}$$

This formulation is then inserted into the conservation equations and a process known as **Reynolds averaging** is performed. Three averaging methods are possible:

- Time Averaging.
- Spatial Averaging.
- Ensemble Averaging.

2.5.1 Time Averaging

Time averaging is the most common averaging method. It can only be used for statistically stationary turbulent flows, i.e. flows not varying with time on the average. For such flows, the mean flow value is defined as:

$$\overline{u_i} = \lim_{T\to\infty} \frac{1}{T} \int_{t_0}^{t_0+T} u_i(t)\,\mathrm{d}t \tag{2.17}$$

In practice, $T \to \infty$ means that the integration time T needs to be long enough relative to the maximum period of the assumed fluctuations.

2.5.2 Spatial Averaging

Spatial averaging can be applied to homogeneous turbulence. This turbulent flow is uniform in all directions, on average. In this case, a parameter is averaged over all the spatial directions by performing a volume integral. The mean flow value is defined as:

$$\overline{u_i} = \lim_{V\to\infty} \frac{1}{V} \int\int\int_V u_i(x,t)\,\mathrm{d}t \tag{2.18}$$

where V represents the volume of the domain.

2.5.3 Ensemble Averaging

The most general type of averaging is called ensemble averaging and is applicable to flows that decay in time, for instance. This method of averaging is similar to time-averaging but rather than dividing by the integration time, T, the mean flow value is obtained by taking a sum over all the measurements or samples, N, and is defined by:

$$\overline{u_i} = \lim_{N\to\infty} \frac{1}{N} \sum_{n=1}^{N} u_i(x,t) \tag{2.19}$$

2.6 Reynolds-Averaged Navier-Stokes Equations in Compressible Flow

Although the Navier-Stokes equations describe adequately turbulent flows, the large number of temporal and spatial turbulent scales associated with high Reynolds numbers make it difficult to resolve all the turbulent scales computationally. In such circumstances, the averaging of the equations for the conservation of mass, momentum and energy leads to the creation of the Reynolds-Averaged Navier-Stokes (RANS) equations. The time-averaged mass and momentum equations take the following form:

$$\begin{aligned} \frac{\partial u_i}{\partial x_j} &= 0 \\ \frac{\partial (\rho u_i)}{\partial t} + \frac{\partial (\rho u_i u_j)}{\partial x_i} &= \rho f_i - \frac{\partial p}{\partial x_i} + \frac{\partial}{\partial x_j}\left(\tau_{ij} + \tau_{ij}^R\right) \end{aligned} \tag{2.20}$$

From eqn (2.20) is obvious that the continuity equation remains the same since it is linear with respect to velocity. However, extra terms appear in the momentum equation due to the non-linearity of the convection term. The extra terms are called the Reynolds Stresses, τ_{ij}^R, and in tensor notation are $-\rho\overline{u_i' u_j'}$. A similar result is obtained for the energy equation. The main problem in turbulence modelling involves calculating the Reynolds stresses from the known mean quantities. One common approach is the Boussinesq's approximation.

2.7 Boussinesq-Based Models

The Boussinesq approximation is based on an analogy between viscous and Reynolds stresses and expresses these as a product of the eddy viscosity (μ_t) and the velocity gradient. The Boussinesq's eddy viscosity hypothesis states that:

$$-\rho\overline{u_i'u_j'} = \mu_t\left[\left(\frac{\partial u_i}{\partial x_j}+\frac{\partial u_j}{\partial x_i}\right)-\frac{2}{3}\delta_{ij}\frac{\partial u_k}{\partial x_k}\right]-\frac{2}{3}\rho\delta_{ij}k \tag{2.21}$$

where k represents the specific kinetic energy of the fluctuations and is given by

$$k \equiv \frac{u_i'u_i'}{2} \tag{2.22}$$

The key idea behind Boussinesq's hypothesis is that the Reynolds stresses can be calculated as a product of the dynamic eddy-viscosity, μ_t, and the strain-rate tensor of the mean flow.

2.8 Turbulence Closure

To compute the eddy viscosity μ_t, further modelling is required and it is at this point that turbulence models come into play. Turbulence models are classified into categories based on the number of transport equations required to calculate μ_t. According to the number of transport equations needed for the calculation of the eddy viscosity, the Boussinesq-based models are classified as:

- **Algebraic** or **zero-equation** models, such as the Cebeci-Smith [38] and Baldwin-Lomax [39] models.
- **One-equation** models, such as the Spalart-Allmaras [35] and Baldwin-Barth [40] models.
- **Two-equation** models, such as the $k-\omega$ [41], $k-\varepsilon$ [42] and SST [43] models.
- **Multi-equation** models: three-equation [44–46], four-equation [47], five-equation [48,49] and multiple time-scale [50–52] models.

An additional family of models solves equations for all components of the Reynolds stress tensor. These are also known as Reynolds Stress Models (RSM), second-order closures or second-moment closures and Algebraic Reynolds Stress Models or (ARSM).

2.8.1 Viscosity-Dependent Parameters

The non-dimensionalised wall distances for turbulent flow, (y^*), and laminar flow, (y^+), are defined as:

$$y^* \equiv \frac{y_n k^{1/2}}{\nu}, \qquad y^+ \equiv \frac{y_n u_\tau}{\nu}, \tag{2.23}$$

where y_n is the distance of a fluid point to the nearest wall, $u_\tau \equiv \sqrt{\tau_w/\rho}$ is the friction velocity and τ_w represents the dynamic wall shear stress. Turbulent Reynolds numbers for the $k-\varepsilon$ model (denoted by R_T) and for the $k-\omega$ model (denoted by R_ω) are given by the following equation:

$$R_T \equiv \frac{k^2}{\nu\varepsilon}, \qquad R_\omega \equiv \frac{k}{\nu\omega}. \tag{2.24}$$

The term ε is the dissipation rate of k per unit mass of fluid, and is usually defined by:

$$\varepsilon = \nu \overline{\frac{\partial u_i'}{\partial x_k}\frac{\partial u_i'}{\partial x_k}} \tag{2.25}$$

while the term ω is the specific dissipation rate and is defined by:

$$\omega = \frac{\varepsilon}{k\,C_\mu} \tag{2.26}$$

2.8.2 Algebraic Models

The simplest turbulence models are the algebraic or zero-equation ones, that consist of algebraic relations to define the local eddy viscosity. The models are based on Prandtl's Mixing Length hypothesis and the most representative example is the Baldwin-Lomax[39] algebraic model. It was developed in 1978 and it uses two different formulations for the inner and outer regions of the boundary layer. It can provide reasonably accurate predictions for turbulent boundary layers, as long as the pressure gradient is not too large, having the advantage that does not require evaluation of the boundary layer thickness. However, this model over predicts the drag coefficient[53] and is problematic for complex geometries and massively separated flows. The Cebeci-Smith's model is also popular and works well in subsonic equilibrium turbulent boundary layers. Between these two models, the major difference is in their treatment of the outer layer[54].

2.8.3 One-equation Models

As an alternative to the algebraic models, one-equation models have been developed to improve turbulent flow predictions by solving one partial differential equation. This type of model was designed to improve on the ability of

algebraic models to account for the convection and diffusion of turbulence by capturing some of the flow history effects on the eddy viscosity. This was accomplished by employing an additional transport equation, usually for the the kinetic energy of turbulence[54], k . In his book, Wilcox [55] provides a general form of this transport equation which has the following form:

$$\rho\frac{\partial k}{\partial t}+\rho u_j\frac{\partial k}{\partial x_j}=\tau_{ij}\frac{\partial u_i}{\partial x_j}-\rho\varepsilon+\frac{\partial}{\partial x_j}\left[\mu\frac{\partial k}{\partial x_j}-\frac{1}{2}\rho\overline{u_i'u_i'u_j'}-\overline{p'u_j'}\right] \tag{2.27}$$

The first term ($\tau_{ij}\frac{\partial u_i}{\partial x_j}$) on the right-hand side represents the production of turbulence. From the terms in the square brackets, the first ($\frac{\mu}{\rho}\frac{\partial k}{\partial x_j}$) is the molecular diffusion term, the second ($\overline{u_i'u_i'u_j'}$) is the turbulent flux of the turbulent kinetic energy and the third ($\frac{1}{\rho}\overline{p'u_j'}$) is the pressure diffusion term, which is usually neglected due to its small contribution.

The eddy viscosity for one-equation turbulence models is usually calculated by:

$$\mu_t=\rho C_\mu l\sqrt{k} \tag{2.28}$$

where C_μ is a coefficient specific to the model and l is the turbulent length scale, a quantity to describe the size of the large eddy in a turbulent flow.

The Baldwin-Barth [40] and the Spalart-Allmaras[35] are the most common one-equation models. Flow history effects on the turbulent kinetic energy are better accounted for in one-equation models due to the additional differential equation and this can be particularly important in unsteady non-equilibrium flows. Specially tuned for aerodynamic flows with adverse pressure gradients and transonic flow conditions, the one-equation models work well for flow regions where the mean velocity gradient is zero. Better prediction of near-wall effects and transition, can also be integrated into their formulation by adding extra source/sink terms. For the above reasons, one-equation models have gained popularity in aerospace applications. The disadvantage of one-equation models is that no mechanism for the computation of the length scale, l, is included making the prediction of highly turbulent flows (with a broad range of length scales) difficult. In that respect, one-equation models are still similar to algebraic models.

Spalart-Allmaras Turbulence Model

The Spalart-Allmaras[35] one-equation model is similar to the Baldwin-Barth, but was developed later. This model was assembled using empiricism and dimensional analysis. This model is based on a single transport equation for a

non-dimensional quantity $\tilde{\nu}$ which is equivalent to the eddy viscosity ν_t far from the wall. The transport equation for the model is given as:

$$\frac{D\tilde{\nu}}{Dt} = c_{b1}\tilde{S}\tilde{\nu} + \frac{1}{\sigma}[\nabla((\nu+\tilde{\nu})\nabla\tilde{\nu} + c_{b2}(\nabla\tilde{\nu})^2] - c_{w1}f_w[\frac{\tilde{\nu}}{d}]^2 \tag{2.29}$$

where the turbulent viscosity ν_t is linked to the variable $\tilde{\nu}$

$$\nu_t = f_{v1}\tilde{\nu}, \quad f_{v1} = \frac{\chi^3}{\chi^3 + c_{v1}^3}, \quad \chi = \frac{\tilde{\nu}}{\nu} \tag{2.30}$$

and ν is the molecular viscosity.

The first term on the right hand side of the eqn. (2.59) deals with the production of turbulent viscosity. The third term is a sink term and will decrease the eddy viscosity if $c_{w1}f_w > \frac{c_{b1}}{k^2}f_{t2}$.

The transport equation requires the knowledge of a number of intermediate functions and variables. The modified strain rate for the Spalart-Allmaras turbulence model and the function f_{v2} are given as:

$$\tilde{S} = S + \frac{\tilde{\nu}}{k^2d^2}f_{v2}, \quad f_{v2} = 1 - \frac{\chi}{1+\chi f_{v1}} \tag{2.31}$$

where S is the magnitude of vorticity.

The wall function f_w is given as:

$$f_w = g[\frac{1+c_{w3}^6}{g^6+c_{w3}^6}]^{1/6} \tag{2.32}$$

where the intermediate variables are calculated as:

$$g = r - c_{w2}(r^6 - r), \quad r = \frac{\tilde{\nu}}{\tilde{S}k^2d^2} \tag{2.33}$$

Values for the Spalart-Allmaras turbulence model are given in table (2.8.3):

Constant	c_{b1}	σ	c_{b2}	κ	c_{w2}	c_{w3}	c_{v1}
Value	0.1355	2/3	0.622	0.41	0.3	2	7.1

Table 2.1: Closure coefficients for the SA model[35].

The constant c_{w1} is defined as

$$c_{w1} = \frac{c_{b1}}{\kappa} + \frac{(1+c_{b2})}{\sigma} \tag{2.34}$$

2.8.4 Two-Equation Models

By far the most popular type of turbulence model used is of the two-equation type. Two-equation models are 'complete', i.e. can be used for predicting properties of a given flow with no prior knowledge of the turbulence structure or flow geometry. Two transport equations are used for the calculation of the turbulent kinetic energy, k , and turbulence length scale, l, or a function of it. The choice of the 2nd variable is arbitrary and many proposals have been presented. The most popular involves using:

- ε : dissipation rate of turbulence.
- ω : k-specific dissipation rate.
- τ : turbulent time-scale.

One of the original versions of this type of turbulence models and still widely used is the $k-\varepsilon$ model. This model was developed by Jones and Launder [42] in 1972. The turbulence scale in the $k-\varepsilon$ model is calculated using a second transport equation for the turbulent dissipation rate, ε. The eddy viscosity for the $k-\varepsilon$ model is typically derived from:

$$\mu_T = C_\mu \rho \frac{k^2}{\varepsilon} \tag{2.35}$$

where C_μ is a model coefficient. The advantage of the $k-\varepsilon$ model is that it performs well for attached flows with thin shear layers and jets but fails to predict the correct flow behaviour in many flows with adverse pressure gradients, extended separated flow regions, swirl, buoyancy, curvature secondary flows and unsteady flows.

Another widely used model is the $k-\omega$ model. In 1988, Wilcox [41] developed the famous $k-\omega$ model which was originally conceived by Kolmogorov. The $k-\omega$ model is similar to the $k-\varepsilon$ model but instead uses the k -specific dissipation rate as a second variable to compute the turbulent length scale. The eddy viscosity is obtained by:

$$\mu_T = \rho \frac{k}{\omega} \tag{2.36}$$

Although the $k-\omega$ model provides better performance in adverse pressure gradient flows, it suffers largely from the same problems as the $k-\varepsilon$ model. Hybrid versions of the $k-\omega$ and $k-\varepsilon$ models called the Baseline $k-\omega$ and SST models were later introduced by Menter [43]. These and in particular the SST version, perform better in separated flows. The idea behind the Baseline $k-\omega$ model is to exploit the robust and accurate formulation of the $k-\omega$ model

near the wall but to also take advantage of the lack of sensitivity to free-stream values of the $k-\varepsilon$ model away from the wall. Menter [43] achieved this by transforming the $k-\varepsilon$ model into the same format as the $k-\omega$ formulation. This process generated an additional cross-diffusion parameter in the ω transport equation. For the SST model [43], Menter's idea was to improve the Baseline $k-\omega$ model by including terms to account for the transport of the principal shear stress.

Model equations: $k-\omega$

The mathematical formulation of the different types of the linear $k-\omega$ two-equation turbulence models discussed in the previous sections are described here. Since the introduction of the linear $k-\omega$ model by Wilcox in 1988 [41], the other notable modification to the $k-\omega$ model came from Menter in 1994 [43] who proposed the hybridisation of the $k-\omega$ model with the $k-\varepsilon$ model, as described previously. Table 2.2 lists the four most popular versions of the $k-\omega$ models.

Researcher	Model
Wilcox (1988) [41]	linear $k-\omega$
Wilcox (1994) [56]	$k-\omega$
Menter (1994) [43]	Baseline Model
Menter (1994) [43]	SST Model

Table 2.2: Different types of linear $k-\omega$ turbulence models

The turbulence transport equations used in the formulation of the $k-\omega$ models are given by:

$$\frac{\partial}{\partial t}(\rho k)+\frac{\partial}{\partial x_j}(\rho U_j k)=\frac{\partial}{\partial x_j}\left[\left(\mu+\frac{\mu_t}{\sigma_k}\right)\frac{\partial k}{\partial x_j}\right]+\rho\left(P-\beta^*\omega k\right) \tag{2.37}$$

$$\frac{\partial}{\partial t}(\rho\omega)+\frac{\partial}{\partial x_j}(\rho U_j\omega)=\frac{\partial}{\partial x_j}\left[\left(\mu+\frac{\mu_t}{\sigma_\omega}\right)\frac{\partial\omega}{\partial x_j}\right]+\rho\left(\frac{\alpha}{\nu_t}P-\frac{\beta}{\beta^*\omega^2}\right)+\rho S_l \tag{2.38}$$

In the transport equation for k and ω above, the production of turbulence, P, and the dissipation rate specific to k , P_ω, is defined by:

$$P_k=\tau_{ij}^R\frac{\partial u_i}{\partial x_j}, \qquad P_\omega=\rho\frac{\alpha}{\nu_t}P_k. \tag{2.39}$$

The values of the closure coefficients used in all the types of linear $k-\omega$ models discussed here are given in the Tables 2.3 and 2.4.

Type of Model	α^*	β^*	α	β
Wilcox (1988) [41]	1	$\frac{9}{100}$	$\frac{5}{9}$	$\frac{3}{40}$
Wilcox (1994) [56]	$\frac{\frac{1}{40}+\frac{R\omega}{6}}{1+\frac{R\omega}{6}}$	$\frac{9}{100}\frac{\frac{5}{18}+\left(\frac{R\omega}{8}\right)^4}{1+\left(\frac{R\omega}{8}\right)^4}$	$\frac{5}{9}\frac{\frac{1}{10}+\frac{R\omega}{2.7}}{1+\frac{R\omega}{2.7}}$	$\frac{3}{40}$
Menter (1994) [43] ***(Baseline)***[1]	1	0.09	$B\begin{pmatrix}0.553\\0.440\end{pmatrix}$	$B\begin{pmatrix}0.075\\0.083\end{pmatrix}$
Menter (1994) [43] ***(SST)***[2]	$\min\left(1,\frac{0.31}{F_2}\frac{\omega}{\bar{w}}\right)$	0.09	$B\begin{pmatrix}0.553\\0.440\end{pmatrix}$	$B\begin{pmatrix}0.075\\0.083\end{pmatrix}$

Table 2.3: Values of closure coefficients used in linear $k-\omega$ models (continued)

Type of Model	σ_k	σ_ω	S_l
Wilcox (1988) [41]	2	2	0
Wilcox (1994) [56]	2	2	0
Menter (1994) [43]***(Baseline)***[1]	$\frac{1}{B\begin{pmatrix}0.5\\1.0\end{pmatrix}}$	$\frac{1}{B\begin{pmatrix}0.5\\0.856\end{pmatrix}}$	$B\begin{pmatrix}0\\\frac{1.71}{\omega}\nabla k\cdot\nabla\omega\end{pmatrix}$
Menter (1994) [43]***(SST)***[2]	$\frac{1}{B\begin{pmatrix}0.85\\1.0\end{pmatrix}}$	$\frac{1}{B\begin{pmatrix}0.5\\0.856\end{pmatrix}}$	$B\begin{pmatrix}0\\\frac{1.71}{\omega}\nabla k\cdot\nabla\omega\end{pmatrix}$

Table 2.4: Values of closure coefficients used in linear $k-\omega$ models (concluded)

Menter's models [43] are constructed as a 'blend' of the $k-\omega$ and $k-\varepsilon$ models. Here the $k-\varepsilon$ model is phrased in the same form as the $k-\omega$ model so as to exploit its independence of free-stream values. The blending of the $k-\varepsilon$ and $k-\omega$ model values for α, β, σ_k^{-1} and σ_ω^{-1} is (in this notation) given by the following equation:

$$B\begin{pmatrix}a\\b\end{pmatrix}\equiv F_1 a+(1-F_1)\,b. \tag{2.40}$$

The blending function is defined by

$$F_1=\tanh\left(\arg_1^4\right), \tag{2.41}$$

where

$$arg_1=min\left[\max\left(\frac{k^{1/2}}{\beta^*\omega y},\frac{500\nu}{y_n^2\omega}\right),\frac{2k\omega}{y_n^2\max\left(\nabla k\cdot\nabla\omega,0.0\right)}\right]. \tag{2.42}$$

The SST model places an additional vorticity-dependent limiter on the shear stress

$$F_2=\tanh\left(arg_2^2\right),\qquad arg_2=\max\left(\frac{2k^{1/2}}{\beta^*\omega y},\frac{500\nu}{y^2\omega}\right). \tag{2.43}$$

Note that this model also uses a slightly different value of σ_k.

2.9 Transitional flow physics

When a body travels inside a fluid, the flow is considered to be either laminar or turbulent. For laminar flow, the fluid moves in ordered and layered streams while for turbulent, the fluid follows a more chaotic motion. In reality, the flow over the surface of the body cannot be characterised as either fully laminar or fully turbulent. Instead, there are regions of laminar and turbulent flow joined by regions of transitional flow. The size of the transition regions may increase and become a large part of the flow. It was Osborne Reynolds who first demonstrated the transition to turbulent flow during an experiment. Generally, transition is considered as a complex physical process by which instabilities in the laminar boundary layer result in the breakdown of the ordered laminar flow structure into turbulence.

It is observed that the stability of the laminar boundary layer flow is affected by various types of disturbances which are either generated from the surface itself or exist in the free-stream. The surface roughness of the body is part of the surface disturbances, while acoustic waves, particles in the flow, and pressure fluctuations are included in the outer flow. The onset and the length of transition are influenced by a range of interrelated factors which are given below:

- Reynolds Number
- Mach Number
- Surface Roughness
- Pressure Distribution
- Free-stream Turbulence

Transition is a complicated process and a thorough description of it for all types of transitional flows is difficult. In general, transition occurs in three main modes, natural, bypassed and separated flow. In the following paragraphs these modes will be introduced.

Natural transition occurs when a stream of low level of free-stream turbulence is sheared over a solid surface. It is initiated by the growth of unstable, two-dimensional disturbances in the laminar boundary layer. The existence of these disturbances was first demonstrated in 1949 by the experiments of Schubauer and Skramstad [57] for incompressible flows over flat plates. In fact, the concept of periodic oscillations travelling in the laminar boundary layer has

been postulated many years earlier by Rayleigh (1887) and Prandtl (1921). It was, however, in 1929 when Tollmien produced a complete theory of boundary layer instability and Schlichting calculated the total amplification of the most unstable frequencies in 1933. Initially, their work received little acceptance because of the lack of experimental results. The experiments of Schubauer and Skramstad [57] , however, demonstrated the existence of the so called 'Tollmien-Schlichting waves'. As the Tollmien-Schlichting waves propagate downstream, they amplify and become associated with vorticity concentration regions along discrete lines. This leads to their distortion into vortex loops. The vortex loops continue to distort and expand until turbulent spots are found. The last stage of the natural transition involves the formation of turbulent spots which were first observed by Emmon in 1951. The mechanism of creation and growth of spots was observed with the use of visualisation techniques in a simple water channel. Once created, the spots spread along the flow in an angle of about 11 degrees, growing laterally and axially[58]. They originate at a random locations and resembles arrowheads [59]. Figure (2.2) shows the geometry of turbulent spots. As they move downstream, they continue to enlarge and their overlap increases. Finally, transition to turbulent boundary layer is complete and the turbulent spots are agglomerating forming turbulent flow stream.

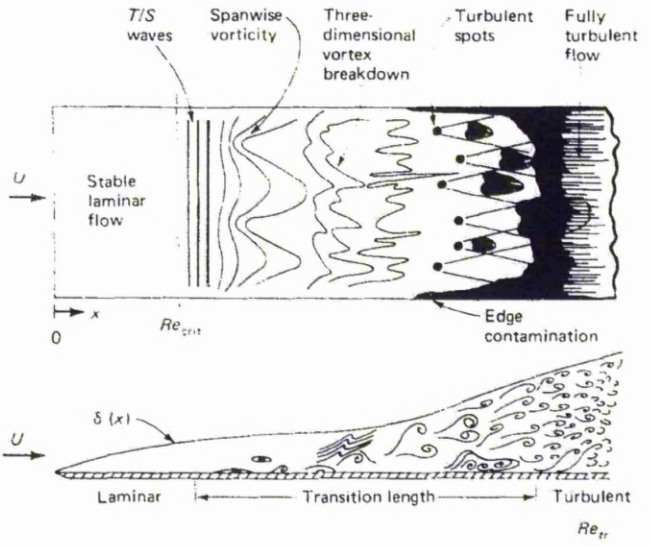

Figure 2.1: Description of the boundary layer natural transition process [59].

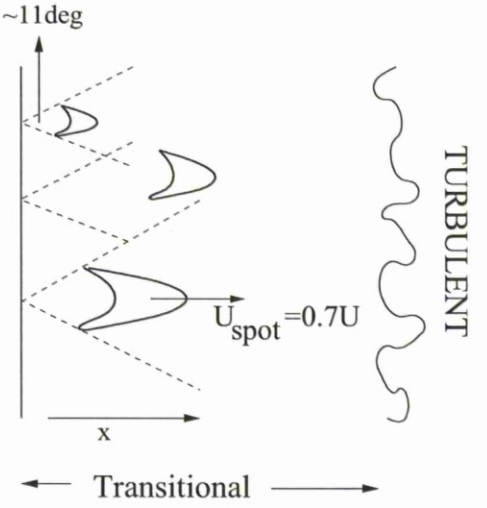

Figure 2.2: Presentation of the geometry and growth of turbulent spots [58] .

If the flow bypasses completely the initial stage of the natural transition then a complex phenomenon occurs called forced or bypassed transition. In this mode, the intensity of the disturbances is high and the boundary layer fluctuations grow rapidly. The free-stream turbulence levels are usually high and the early stages of the natural transition are bypassed and Tollmien-Schlichting waves are not present. Turbulent spots are directly produced within the boundary layers.

Separated flow transition is common on aerofoils at high angles of attack and occurs as a result of laminar boundary separation. The flow may reattach downstream of the separation and become turbulent. Separated flow transition occurs when adverse pressure gradients are present and the momentum of the fluid in the boundary layer is insufficient to maintain attached flows [54]. This reattachment creates a laminar separation bubble on the surface of the aerofoil.

The essential features of a laminar separation bubble with transition are illustrated in figure (2.3). As can be seen from the figure, separation of the flow occurs at point S. The flow reattaches at point R as fully turbulent creating a laminar separation bubble. Laminar-to-turbulent transition can occur at any position T above the bubble.

One characteristic of the separation bubbles is their length, and separation bubbles can be classified into short and long, with the distinction between the two to be the effect they have on the pressure distribution. Short bubbles reattach shortly after separation and they have a local effect on flow. They can force the flow to become turbulent and are considered as a way to control performance [58]. On the other hand, long bubbles interact extensively with the

exterior flow and significantly modify the surface pressure distribution [54]. They are the reason for large losses and deviations in exit flow angles and this behaviour make them unsuitable for aeronautical applications.

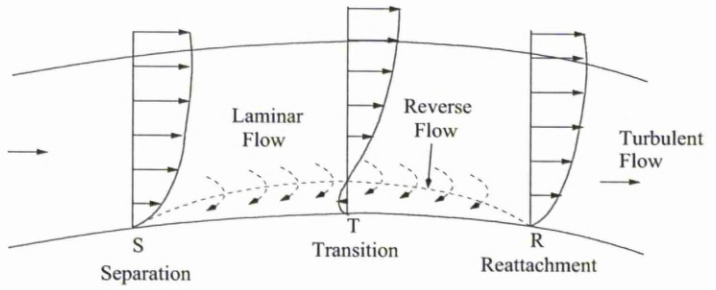

Figure 2.3: Flow around a separation bubble and corresponding velocity distribution [60].

Separation flow transition may also occur during dynamic stall. Dynamic stall is associated with unsteady separation and stall of aerodynamic bodies executing time-dependent large amplitude motions. This is also a very complex aerodynamic problem. During dynamic stall, the flow is characterised by massive unsteady separation and formation of large scale vertical structures which create extended hysteresis effects in the resulting aerodynamic loads [3].

2.10 Transition Modelling

Knowing the details of the physics of transitional flows, better models can be derived. Considering the recent advances in the computational power, one could draw the following requirements for transition models for CFD:

- The models should be of adequate accuracy for engineering calculations
- The models should be of low cost and ability to be implemented in parallel CFD codes
- The models should allow the prediction of onset and length for different transition mechanisms
- The models should have a robust integration with the existing turbulence model
- The models should be applicable to three-dimensional boundary layers

The efforts of different research groups have resulted in a range of models that can be used in different applications. A range of models were used during this project. The following section will present the various method that have be used to predict transition. A summary of all models can be seen in Table (2.10).

Approach	Method
Rough surfaces	Hellsten and Leine[61]
	Knopp *et al.*[62]
Trip function models	Spalart-Allmaras turbulence model with transitional trip function [35]
Empirical correlations	Michel [5]
	Cebeci and Smith [38]
	Abu-Ghannam and Shaw [63]
Models based on Stability Approach	e^N model
Models based on transport equations	Steelant and Dick
	Cho and Chung
	Suzen and huang
	Menter *et al.*

Table 2.5: Presentation of existing transition models.

2.10.1 Non-Dimensionalisation of Parameters and Equations

In this section, the non-dimensionalisation of the transition equations is discussed. This can be achieved by scaling length with the aerofoil length (c), velocities with the free-stream velocity (U_∞), and time by $t^* = \frac{t}{\frac{c}{U_\infty}}$.

The variables are non-dimensionalised based on:

$$\begin{gathered} x^* = \frac{x}{L}, \quad y^* = \frac{y}{L}, \quad z^* = \frac{z}{L} \\ u^* = \frac{u}{U_\infty}, \quad v^* = \frac{v}{V_\infty} \quad w^* = \frac{w}{W_\infty} \\ t^* = \frac{t}{L/U_\infty} \\ \mu^* = \frac{\mu}{\mu_\infty}, \quad \rho^* = \frac{\rho}{\rho_\infty}, \quad p^* = \frac{p}{p_\infty}, \quad T^* = \frac{T}{T_\infty} \end{gathered} \tag{2.44}$$

where the quantities with the asterisk are the dimensionless one. More information for this procedure can be found in Appendix A .

2.10.2 Roughness Transition Models

In many flows of engineering interest, there are parts of solid surfaces that are rough, like surface roughness due to manufacturing imperfections or as a long-term environmental result. These aerodynamically rough surfaces may have a strong effect on the flow field and the aerodynamic forces. In computational aerodynamics, these rough surfaces are replaced by smooth surfaces with modified boundary conditions. To estimate the flow with wall roughness two extensions of the k-ω turbulence model were considered, the Hellsten and Laine[61] and Knopp *et al.* [62] models.

Hellsten and Laine Model

Hellsten and Laine [61] proposed an improved method to predict the behaviour of turbulent flows over rough surfaces. The method is based on the $k-\omega$ SST turbulence model that is modified to incorporate the surface roughness. The model is based on the alteration of the boundary condition for ω is:

$$\omega = \frac{u_\tau^2}{\nu} S_R \tag{2.45}$$

where S_R is the non-dimensional coefficient defined as:

$$S_R = \begin{cases} (50/h_s^+)^2 & \text{for } h_s^+ < 25 \\ 100/h_s^+ & \text{for } h_s^+ > 25 \end{cases} \tag{2.46}$$

For the SST k-ω turbulence model an extra modification was developed. The SST limiter has to be active in the roughness layer deactivating the initial Menter's SST $k-\omega$ turbulence model limiter and is given as:

$$\mu_t = \frac{\alpha_1 \rho k}{max(\alpha_1 \omega, |\Omega| F_2 F_3)} \tag{2.47}$$

where $|\Omega|$ is the absolute value of vorticity and F_3 is the addition of Hellsten and Laine model given by:

$$F_3 = 1 - tanh[(\frac{150\nu}{\omega d^2})^4] \tag{2.48}$$

If the dimensionless quantities are used, eqns. (2.45) and (2.48) are written as:

$$\omega = \frac{u_\tau^{*2}}{\nu^*} S_R Re \tag{2.49}$$

$$F_3 = 1 - tanh[((\frac{150\nu^*}{\omega^* (d^*)^2}) * (\frac{1}{Re}))^4] \tag{2.50}$$

Knopp *et al.* Model

Knopp *et al.* [62] proposed another extension for accurate predictions of the effect of surface roughness. For smooth walls, the turbulent viscosity is considered zero on the wall. Instead, based on Aupoix and Spalart[64], the turbulent viscosity close to wall is equal to $\nu_{tw} = u_\tau k d_o$, where d_o is the hydrodynamic roughness length which is approximated in relation with sand-grain height h_s as $d_o \approx 0.03 h_s$.

In order to achieve good predictions for transitionally rough regimes, the boundary conditions close to the wall for k and ω are defined as:

$$k_w = \phi_{r1} k_{rough} \tag{2.51}$$

$$\omega_w = min(\frac{u_\tau}{\beta_k^{1/2} \kappa \tilde{d_o}}, \frac{60\nu}{\beta_w d^2}) \tag{2.52}$$

where k_{rough} and $\tilde{d_o}$ are given as

$$k_{rough} = \frac{u_\tau^2}{\beta_k^{1/2}} \tag{2.53}$$

$$\tilde{d_o} = 0.03 \phi_{r2} h_s \tag{2.54}$$

The ϕ_{r1} and ϕ_{r2} are blending functions designed so that the results of the model fit well with experimental data and are given by:

$$\phi_{r1} = min(1, \frac{h_s^+}{90}) \tag{2.55}$$

$$\phi_{r2} = min(1, [\frac{h_s^+}{30}]^{2/3}) min(1, [\frac{h_s^+}{45}]^{1/4}) min(1, [\frac{h_s^+}{60}]^{1/4}) \tag{2.56}$$

Non-dimensionalising the Knopp *et al.* [62] model, eqns. (2.52) and (2.53) are transformed into:

$$\omega_w^* = min(\frac{u_\tau^*}{\beta_k^{1/2} \kappa \tilde{d^*}_o}, \frac{60\nu}{\beta_w (d^*)^2 Re}) \tag{2.57}$$

$$k_{rough}^* = \frac{(u_\tau^*)^2}{\beta_k^{1/2} Re} \tag{2.58}$$

2.10.3 Spalart-Allmaras turbulence model

The Spalart-Allmaras (SA) turbulence model[35] solves only one transport equation for the quantity $\tilde{\nu}$, which is equivalent to the eddy viscosity ν_t far from the wall. The modified transport equation for the estimation of the transition flow has been constructed empirically and is given[35]:

$$\frac{D\tilde{\nu}}{Dt} = c_{b1}[1 - f_{t2}]\tilde{S}\tilde{\nu} + \frac{1}{\sigma}[\nabla((\nu + \tilde{\nu})\nabla\tilde{\nu} + c_{b2}(\nabla\tilde{\nu})^2] - [c_{w1} f_w - \frac{c_{b1}}{k^2} f_{t2}][\frac{\tilde{\nu}}{d}]^2 + f_{t1}\Delta U^2 \tag{2.59}$$

where the turbulent viscosity ν_t is linked to the variable $\tilde{\nu}$

$$\nu_t = f_{v1}\tilde{\nu}, \quad f_{v1} = \frac{\chi^3}{\chi^3 + c_{v1}^3}, \quad \chi = \frac{\tilde{\nu}}{\nu} \tag{2.60}$$

and ν is the molecular viscosity.

The first term on the right hand side of the eqn. (2.59) deals with the production of turbulent viscosity. The third term is the destruction term and it will decrease the eddy viscosity if $c_{w1}f_w > \frac{c_{b1}}{k^2}f_{t2}$.

The transport equation requires information from a number of intermediate functions and variables. The modified strain rate for the Spalart-Allmaras turbulence model is given as:

$$\tilde{S} = S + \frac{\tilde{\nu}}{k^2 d^2} f_{v2} \tag{2.61}$$

and the function f_{v2}

$$f_{v2} = 1 - \frac{\chi}{1 + \chi f_{v1}} \tag{2.62}$$

The wall function f_w is given as:

$$f_w = g\left[\frac{1 + c_{w3}^6}{g^6 + c_{w3}^6}\right]^{1/6} \tag{2.63}$$

where the intermediate variables are calculated as:

$$g = r - c_{w2}(r^6 - r), \quad r = \frac{\tilde{\nu}}{\tilde{S}k^2 d^2} \tag{2.64}$$

To initialise transition, the model requires two additional functions. As can be seen from eqn. (2.59), the production and destruction terms are multiplied by the function f_{t2} which is given by:

$$f_{t2} = c_{t3} e^{(-c_{t4}\chi^2)} \tag{2.65}$$

The reason for this function is purely numerical and is to keep the computation of models stable[35]. It is activated close to the surface and on the wake while it is equal to zero at the farfield.

To initiate transition close to specified points, an extra source term has been added on the model. This term is nonzero only in a small domain of influence around the trip points. The function f_{t1} at the forth term of eqn. (2.59) increases the eddy viscosity and is given as:

$$f_{t1} = c_{t1} g_t e^{\left(-c_{t2}\frac{\omega_t^2}{\Delta U^2}[d^2 + g_t^2 d_t^2]\right)} \tag{2.66}$$

where d_t is the distance from the field point to the trip, ω_t is the wall vorticity at the trip, and ΔU is the difference between the velocity at the field point and that at the trip.i

The function g_t is given by:

$$g_t = min(0.1, \frac{\Delta U}{\omega_t \Delta x_t}) \tag{2.67}$$

where Δx_t is the grid spacing along the wall at the trip. The reason for this factor is mainly numerical as guarantee that the trip function will be activated even for a coarse grid where the trip point can fell between two grid point[35].

For the transition version of the Spalart-Allmaras model, the additional constants are given in table (2.6).

Coefficients	c_{t1}	c_{t2}	c_{t3}	c_{t4}
Value	1	2	1.2	0.5

Table 2.6: Coefficients for the Spalart-Allmaras one-equation turbulence model with the transition modification.

For computational purposes, the eqn. (2.59) is rewritten in non-dimensional form as:

$$\frac{D\tilde{\nu}^*}{Dt^*} = c_{b1}[1-f_{t2}]\tilde{S}^*\tilde{\nu}^* + \frac{1}{Re}\frac{1}{\sigma}[\nabla((\nu^*+\tilde{\nu}^*)\nabla\tilde{\nu}^* + c_{b2}(\nabla\tilde{\nu}^*)^2] - \frac{1}{Re}[c_{w1}f_w - \frac{c_{b1}}{k^2}f_{t2}][\frac{\tilde{\nu}^*}{d^*}]^2 + Ref_{t1}\Delta U^{*2} \tag{2.68}$$

2.10.4 Empirical Correlation Based Models

One way to calculate the onset and development of the transitional flow is through the use of engineering or empirical criteria. These criteria are produced based on observed trends in experiments and provide a reasonable degree of accuracy when used to compute flows similar to which the criteria are derived for. The models usually relate the free-stream turbulence intensity (Tu) to the transition Reynolds number and the momentum thickness Reynolds number. Characteristic examples of this approach are Michel's criterion[5], the Cebeci and Smith [38] method and the Abu-Ghannam and Shaw [63] model. An estimation of the transition onset based on the previous models can be seen in figure (2.4).

2.10.5 Thwaite's Method

The empirical models usually relate the free-stream turbulence intensity (Tu) to the transition Reynolds number based on the momentum thickness Reynolds number. In order to estimate the unknown momentum thickness (θ), Thwaite's

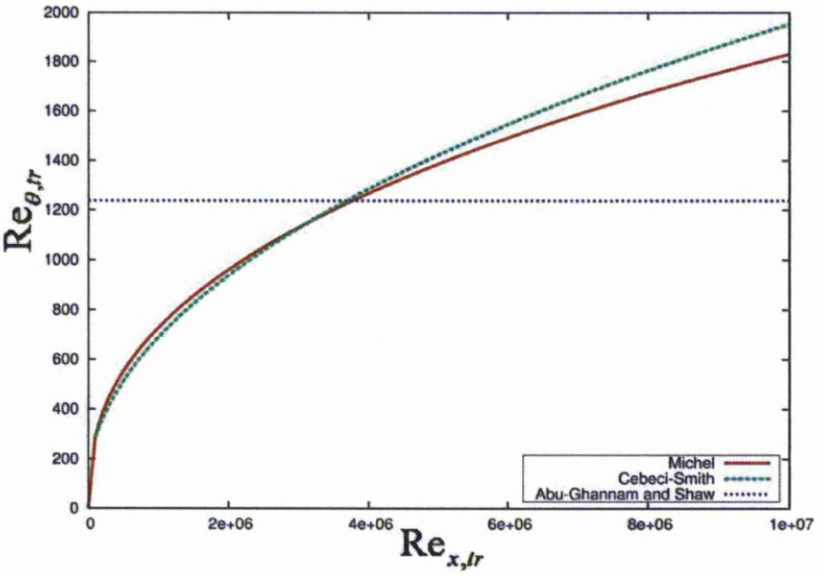

Figure 2.4: Estimation of transition onset with the use of empirical correlations. Michel's, Cebeci and Smith's criteria and Abu-Ghannam, and Shaw method are presented.

method [65] is employed. Thwaite wrote the integral momentum equation in terms of a parameter λ given by:

$$\lambda = \frac{\theta^2}{\nu}\frac{dU_e}{dx} = (\frac{\theta}{\delta})^2\Lambda \tag{2.69}$$

where $\Lambda = \delta^2\frac{\frac{dU_e}{dx}}{\nu}$ is the Polhausen parameter, ν is the kinematic viscosity, U_e is the velocity at the edge of the boundary layer, θ and δ are respectively the momentum and displacement thickness of the boundary layer.

The integral momentum equation is derived by integration of the boundary layer equations and after some algebraic manipulation it is given by:

$$\frac{C_f}{2} = \frac{d\theta}{dx} + (2+H)\frac{\theta}{U_e}\frac{dU_e}{dx} \tag{2.70}$$

where $C_f = \frac{\tau_w}{1/2\rho U_e^2}$ is the skin-friction coefficient and H is the shape factor: $H = \frac{\delta^*}{\theta}$.

Written in the following form and after some manipulation the integral momentum equation can be written in the following form:

$$U_e\frac{d}{dx}\left(\frac{\theta^2}{\nu}\right) \approx 2[S(\lambda) - \lambda(2+H)] = F(\lambda) \tag{2.71}$$

where $S(\lambda) = \frac{\tau_w\theta}{\mu U_e}$ and $H(\lambda)$ are the shear, shear-factor correlations, respectively. Based on the previous equation, Thwaite used experimental data and tried to fit them by a set of averaged single-parameter functions. He concluded that a linear correlation for the function F can adequately represent the experimental data. Thwaite's linear correlation

is given by:

$$F(\lambda) \approx 0.45 - 6.0\lambda \tag{2.72}$$

If a general linear representation for the function F is considered, for example $F(\lambda) = \alpha - \beta\lambda$, eqn. (2.71) can be written as:

$$U_e \frac{\theta^2}{\nu} = \alpha - \beta\lambda \Leftrightarrow \tag{2.73}$$

$$U_e \frac{\theta^2}{\nu} = \alpha - \beta \frac{\theta^2}{\nu} \frac{dU_e}{dx} \tag{2.74}$$

Multiplying eqn. (2.74) by $U_e^{\beta-1}$ then

$$\frac{d}{dx}\left(\frac{U_e^{\beta}\theta^2}{\nu}\right) = U_e^{\beta}\frac{\theta^2}{\nu} + \beta U_e^{\beta-1}\frac{\theta^2}{\nu}\frac{dU_e}{dx} \tag{2.75}$$

then eqn. (2.74) can be written as

$$\frac{1}{\nu}\frac{d}{dx}(\theta^2 U_e^{\beta}) = \alpha U_e^{\beta-1} \tag{2.76}$$

which upon integration, leads to the the proposed equation by Holsten and Bohlen,

$$\frac{\theta^2}{\nu} = a U_e^{-b}\left(\int_{x_0}^{x} U_e^{b-1} dx + C\right) \tag{2.77}$$

If x_0 is considered as the stagnation point, the constant C has to be zero to avoid an infinite momentum thickness. Thwaite showed that for laminar boundary layers the momentum thickness can be calculated accurately by:

$$\theta^2 \approx \frac{0.45\nu}{U_e^6}\int_{x_0}^{x} U_e^5 dx \tag{2.78}$$

The velocity at the edge of the boundary layer (U_e) is required as it can be seen from eqn. (2.78). Using Bernoulli's equation, the velocity distribution at the edge of the boundary layer around an aerofoil can be calculated and it can be given as:

$$U_e = U_\infty \sqrt{1 - C_p} \tag{2.79}$$

Equation (2.79) is valid only for incompressible flows. In order for the Thwaite's method to be used in moderate compressible flows with greater accuracy the Prandtl-Glauert compressibility correction should be used. The Prandtl-Glauert correction is given by:

$$C_P = \frac{C_P'}{\sqrt{1 - M_\infty^2}} \tag{2.80}$$

where C_P is the surface pressure coefficient for the compressible flows, C_P' is the equivalent incompressible surface pressure coefficient and M_∞ is the free-stream Mach number.

If the dimensionless quantities are considered, then the velocity distribution at the edge of the boundary layer is approximated by:

$$U_e^* = \frac{U_e}{U_\infty} \Leftrightarrow U_e^* = \frac{U_\infty\sqrt{1-C_p}}{U_\infty} \Leftrightarrow U_e^* = \sqrt{1-C_p} \tag{2.81}$$

Considering a small change at the x-direction, the integral of eqn. (2.78) can be replaced with a summation of the quantities in the same area. If the dimensionless quantities are also considered, then the equation for the calculation of the momentum thickness based on Thwaite's method is given by:

$$\theta^* = \frac{\theta}{c} \Leftrightarrow \theta^{*2} = \frac{0.45}{U_e^{*6}}\left(\sum U_e^{*5} dx^*\right)\frac{1}{Re} \tag{2.82}$$

where the summation is from the stagnation point x_0 till the current computation point

Michel's Criterion

In 1954, Michel developed a method [5] based on measurements in two-dimensional, incompressible flow. The model of Michel is based on experimental data for a flat plate with almost no pressure gradient and correlates local values of momentum thickness with the position of the transition point[1]. It states that transition takes place where:

$$Re_{\theta,tr} = 2.9 Re_{x,tr}^{0.4} \tag{2.83}$$

where $Re_{\theta,tr}$ is the Reynolds number based on momentum thickness, and $Re_{x,tr}$ is the Reynolds number, based on the distance measured from the stagnation point[1]. For incompressible flows around two dimensional aerofoils, Michel's correlation matches fairly well with the experimental data for Reynolds numbers in the region:

$$0.4 \cdot 10^6 \leq Re_c \leq 7 \cdot 10^6 \tag{2.84}$$

In order to apply Michel's criterion in CFD codes all required data like: momentum thickness, boundary layer edge velocity, and momentum thickness Reynolds number have to be calculated. For the calculation of the momentum thickness Reynolds number (Re_{mich}), the eqn. (2.83) is used:

$$Re_{mich} = 2.9(Re \cdot U_e \cdot x)^{0.4} \tag{2.85}$$

where the parameter in the power can be easily proved that is the Reynolds number based on the distance measured from the stagnation point.

$$Re \cdot U_e^* \cdot x^* = \frac{\rho U_\infty c}{\mu} \frac{U_e}{U_\infty} \frac{x}{c} = \frac{\rho U_e x}{\mu} \tag{2.86}$$

where x is the distance from the computational point to the stagnation point.

The local momentum thickness Reynolds number (Re_θ) is calculated based on:

$$Re_\theta = Re \cdot U_e^* \cdot \theta^* = \frac{\rho U_\infty c}{\mu} \frac{U_e}{U_\infty} \frac{\theta}{c} = \frac{\rho U_e \theta}{\mu} \tag{2.87}$$

Finally, the momentum thickness Reynolds number based on Michel's criterion (Re_{mich}) is compared with the local Reynolds number based on the momentum thickness (Re_θ) and the transition position is estimated as the point where:

$$Re_\theta \geq Re_{mich} \tag{2.88}$$

Cebeci and Smith Criterion

Due to its simplicity and reasonable performance, Michel's criterion has been adopted by many authors for both steady and unsteady flows. Some years later, Cebeci and Smith [38] developed an improved version of Michel's model, compatible with the e^N method and which was claimed to be more accurate. The Cebeci and Smith's correlation is given below:

$$Re_{\theta,tr} = 1.174\left(1 + \frac{22400}{Re_{x,tr}}\right) Re_{x,tr}^{0.46} \tag{2.89}$$

Equation (2.89) was derived for attached flows on aerofoils for Reynolds number greater than 2 million and is based on incompressible flow parameters [38]. In comparison with Michel's method, the Cebeci and Smith model is applicable for a wider range of local length Reynolds number:

$$0.1 \times 10^6 \leq Re_x \leq 40 \times 10^6 \tag{2.90}$$

Similar to Michel's criterion, the Cebeci and Smith method can be applied to CFD codes as soon as the momentum thickness and boundary edge are calculated. The momentum thickness Reynolds number based on the method and the local Reynolds number based on the momentum thickness (Re_θ) can be calculated from eqns. (2.89) and (2.87) respectively. Transition occurs when the momentum thickness Reynolds number based on the Cebeci and Smith method (Re_{ceb}) becomes bigger or equal to the local Reynolds number based on the momentum thickness (Re_θ).

Abu-Ghannam and Shaw Criterion

As the amount of experimental data for the onset of transition increased, Abu-Ghannam and Shaw [63] tried to fit the experimental results for the zero pressure gradient experiments on flat plates with a curve. They proposed a modification to the Hall and Gibbings relationship [63] and the momentum thickness Reynolds number at the start of transition was related with the pressure gradient parameter and the turbulence levels. Abu-Ghannam and Shaw's correlation was written in the following form:

$$Re_{\theta,S} = 163 + e^{\{F(\lambda_\theta) - \frac{F(\lambda_\theta)}{6.91}\tau\}} \tag{2.91}$$

where the value of 163 in the eqn. (2.91) was chosen as it agrees with the Tollmien-Schlichting limit of stability [63] and $F(\lambda_\theta)$ is a function based on the pressure gradient parameter and was calculated in order to satisfy the experimental data,

$$F(\lambda_\theta) = \begin{cases} 6.91 + 12.75\lambda_\theta + 63.64\lambda_\theta^2 & \text{for } \lambda_\theta < 0 \\ 6.91 + 2.78\lambda_\theta - 12.27\lambda_\theta^2 & \text{for } \lambda_\theta > 0 \end{cases} \tag{2.92}$$

The Abu-Ghannam and Shaw correlation shows good agreement with the experimental data for zero and adverse pressure gradient flows, although for favourable pressure gradients the model is not very sensitive.

Figures (2.5(a)) and (2.5(b)) present the momentum thickness Reynolds number Re_θ) and $F(\lambda_\theta)$ by Abu-Ghannam and Shaw's method for a range of pressure gradient (λ_θ).

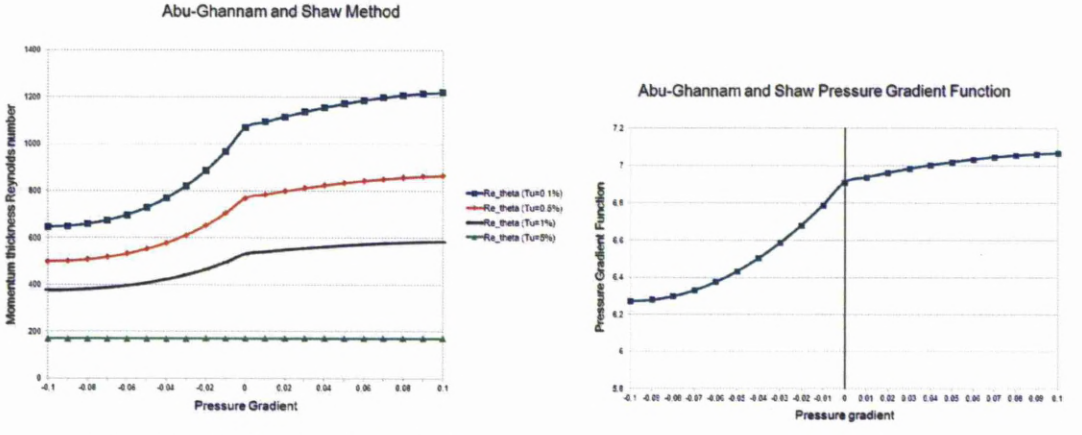

(a) momentum thickness Reynolds number Re_θ

(b) $F(\lambda_\theta)$

Figure 2.5: Momentum thickness Reynolds number (Re_θ) and function ($F(\lambda_\theta)$) of the Abu-Ghannam and Shaw method as a function of the pressure gradient (λ_θ).

2.10.6 Transition Length

Besides the onset of the transition, another important parameter for the phenomenon is the length of the region where transition occurs. Transition should not be considered as an instantaneous process but as a phenomenon which requires a length in order to be fully deployed. The distance between the point where the flow is fully laminar to the point where the flow is considered fully turbulent can be much larger than the length over which the flow is laminar.

Three different ways were selected in order to estimate the extension of the transition region. Firstly, the CFD user can define the transition length based on either existing experimental data or intuition. This can lead to very sudden increase of the skin friction coefficient. The second way to estimate the end of the transitional flow is by using the empirical correlation similar to that of Abu-Ghannam and Shaw[63]. This correlation takes into account the effects of turbulence level and pressure gradient by estimating the local Reynolds number using the information provided at the transition point. The empirical correlation of Abu-Ghannam and Shaw[63] for the end of transition is given by:

$$Re_{xE} = Re_{xS} + 16.8(Re_{xS})^{0.8} \tag{2.93}$$

A more sophisticated way for estimating the transition region is by using the empirical model suggested by Chen and Thyson[66], that scale the eddy viscosity by an intermittency function. The latter one increases from zero for laminar boundary layers to one for fully turbulent flows. The intermittency function is given by:

$$\gamma_{tr} = 1 - exp\left[\left(-\frac{u_e^3}{\nu^2 G_\gamma}\right) Re_{x_{tr}}^{-1.34}(x - x_{tr}) \int_{x_{tr}}^{x} \frac{ds}{u_e}\right] \tag{2.94}$$

or in dimensionless form

$$\gamma_{tr}^* = 1 - exp\left[\left(-\frac{u_e^{*3}}{\nu^{*2} G_\gamma}\right) Re_{x_{tr}}^{-1.34}(x^* - x_{tr}^*) \int_{x_{tr}}^{x} \frac{ds^*}{u_e^*} \cdot Re^2\right] \tag{2.95}$$

The parameter G_γ was initially suggested to have a value of 1200 for high Reynolds numbers. In order to take into account the separation at low Reynolds number flows, a different expression was suggested:

$$G_\gamma = \frac{213}{3} \cdot [log(Re_{x_{tr}}) - 4.732] \tag{2.96}$$

2.10.7 CFD Implementation of the Empirical Correlation-based Models

In order to model the influence of the transition phenomena, the transition criteria are coupled with the CFD solver and are used within each solution iteration. This provides the framework for transition modelling to be applied to

unsteady cases without any further modifications. Firstly, a compressible pressure distribution is obtained from the solver. The Prandlt-Glauert compressibility rule is applied in order to compute the equivalent incompressible solution and Bernoulli's equation provides the distribution of the velocity at the edge of the boundary layer as seen at eqn. (2.81).

In order to utilise Thwaite's method, it is important to determine the location of the stagnation point in the vicinity of the leading edge. The stagnation point is defined by calculating the surface pressure distribution for the complete aerofoil and locating the highest surface value. As soon as the stagnation point is defined, the chord-wise integration of the integral boundary layer quantities can be carried out starting from the stagnation point and proceeding downstream on both aerofoil surfaces. Thwaite's method (eqn. (2.78)) is then applied to obtain the boundary layer momentum thickness over the surfaces of the body. The empirical transition criteria are then applied to determine the onset of transition. Knowing the onset of the transition, the length of the transition region is then estimated. Finally, a sigmoidal function increases smoothly the value of intermittency from zero in the area upstream the transition onset to one downstream of the transition end point.

Figure (3.2) provides a schematic of the transition model implementation with the CFD solver.

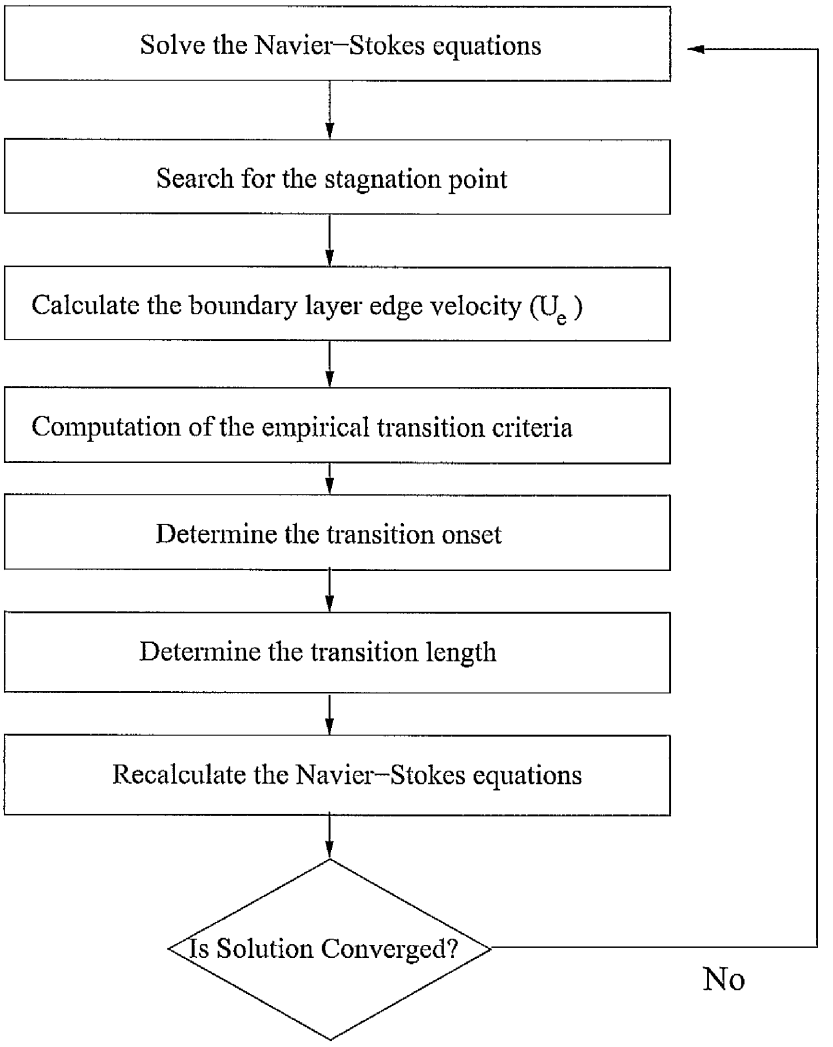

Figure 2.6: Road map for the implementation of the empirical correlation-based models.

2.10.8 Models Based on Stability Theory

Although the empirical relations are able to produce reasonably accurate transition estimates, they rely on a small number of experiments at small scale and their applicability in other cases is limited. For example Michel's method is strictly for two-dimensional incompressible flows on boundary layers [59]. At low free-stream turbulence levels, transition occurs due to the amplification of small disturbances in the laminar boundary layer which leads to the formation of turbulent spots and finally to the breakdown into turbulence. A number of methods have been developed that explore the development and the amplification of laminar instabilities. Stability theory is one of them and has been widely used [67]. The theory suggests that a small sinusoidal disturbance is imposed on a steady laminar flow and attempts to determine whether the instabilities will amplify or decay in time. The theory indicates which of the flow parameters may delay or accelerate transition[68].

As a disturbance can be considered to be a travelling wave whose amplitude varies with respect to y direction. The sinusoidal travelling wave can be given from the following equation

$$\psi(x,y,t) = \phi(y)e^{i(\alpha x-\omega t)} \tag{2.97}$$

where $i = \sqrt{(-1)}$ and the variable ψ can be the fluctuating pressure, velocity or density. The parameter α represents the dimensionless wave number and ω is the frequency of the disturbance. Both parameters can be considered as complex numbers.

In the framework of the stability theory, ω is considered real and α as complex ($\alpha = \alpha_r + i \cdot \alpha_i$). Then the fluctuating quantities are given by the following equation:

$$\psi = \phi(y)e^{-\alpha_i x}e^{i(\alpha_r x-\omega t)} \tag{2.98}$$

From equation (2.98) it is obvious that the amplitude of the disturbances depends on the value of $\alpha_r x$. If $\alpha_r x < 0$ the disturbances are damped and if $\alpha_r x > 0$ the disturbances are amplified. If $\alpha_r x = 0$ the disturbances stay neutral. If the disturbance amplitude grows, then the flow is considered unstable and transition to turbulent flow is expected.

Applying the previous equations (2.97) to the continuity and momentum equations for two-dimensional, incompressible, unsteady flow and neglecting the quadratic terms in the disturbance velocity components, the Orr-Sommerfeld equation for ω and α is derived:

$$\phi^{iv} - 2\alpha^2\phi'' + \alpha^4\phi = iR[(\alpha u - \omega)(\phi'' - \alpha^2\phi) - iR\alpha u''\phi] \tag{2.99}$$

where ϕ is the amplitude of the perturbation, the prime denotes differentiation with respect to y and R is the Reynolds number of the mean flow. Equation (2.99) is a 4^{th} order ordinary differential equation for the amplitude ϕ. The stability problem is therefore reduced to an eigenvalue problem. The solution of the Orr-Sommerfeld equation describes small disturbances which are called Tollmien-Schlichting waves.

The e^N Method

The most widely used method based on stability theory is the e^N derived from the "e^9" method of Smith and Gamberoni[69] and van Ingen[70]. This method was based on the observation of Michel, that the transition points corresponded to a total amplification of Tollmien-Schlichting waves equal to $A/A_0 \approx 10^4$. This observation led many other researchers to evaluate the eigenvalues of various boundary layer profiles and then to compute the total growth of waves of a given frequency. Smith and Gamberoni[69] and Van Ingen[70] proposed that the onset of transition occurs when the total amplification of Tollmien-Schlichting waves is equal to:

$$\frac{A}{A_0} = e^{\left[\int_{t_i}^{t_{tr}} (\omega_i) dt\right]} \approx e^9 \tag{2.100}$$

with A_0 to be initial amplitude disturbance at the first neutral stability point.

This method was later referred as "e^N" method and predicts the transition point when the amplitude of the most unstable frequency exceeds the value of the initial unstable frequency multiplied by a factor of e^N. The method is based on the growth of the Tollmien-Schlichting instabilities in the laminar boundary layer which become neutrally stable at some critical point. Downstream the critical point, the disturbances begin to grow. Transition is usually assumed to occur for N=9 [2]. This N factor is empirically determined from several experimental data and can vary from one situation to another.

As mentioned before, the Orr-Sommerfeld equation gives the locus of the neutral points forming a boundary between stability and instability. When a downstream propagating wave of frequency f_1 crosses the boundary, its amplitude begins to increase. The wave inside the stable region will be amplified to a maximum and then it will be damped again downstream. The wave amplitude at any station inside the stable region can be related to its initial amplitude at the neutral point and the envelope of the curves for the ratio (A/A_0) is called the 'N-factor'.

The e^N method involves the calculation of accurate laminar boundary layer velocity profiles at various stream-wise stations beginning at the stagnation point. These velocity profiles are used to evaluate the stability properties of

the flow from the Orr-Sommerfeld equation. The 'N-factor' is obtained by integrating the local growth rates and is defined as

$$N = \int_{x_0}^{x} (-\alpha_i) dx \tag{2.101}$$

The calculated N factor is compared with a pre-determined value that has been deemed to signify the onset of the transition. This process continues until the local amplification factor attains a value greater or equal to the transition amplification factor.

This means that the method is not free of empiricism as the 'N-factor' depends on the employed wind tunnel setup and the free-stream environment. The stability analysis is based on velocity profiles obtained from highly resolved boundary layer codes that must be coupled to the pressure distribution of a RANS code. The output of the boundary layer is then transferred to a stability method which provides information back to the turbulence model in the RANS solver[71]. When a 3D flow is considered, the process becomes more complex. This was one of the reason that lead to the development of the $\kappa - \omega - \gamma - Re_\theta$ model. There was a need for a model that would be more CFD compatible and would be easier to incorporate in the existing codes.

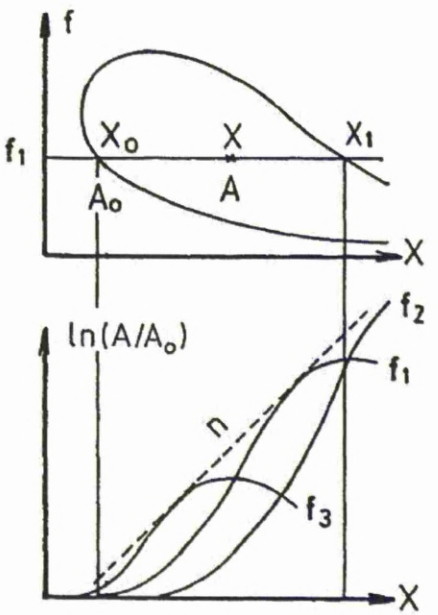

Figure 2.7: Principle of the e^N method [59].

2.10.9 Intermittency Transport Model

In 1951, Emmon, during experiments in shallow water flows, characterised transition as an eruption of turbulent spots. He considered a turbulent spot production function $g(x,y,z,t)$ which was related to the probability of the flow being turbulent at some point, the intermittency factor γ, given by the equation:

$$\gamma = 1 - e^{(-\int g(x,y,z,t)dV)} \tag{2.102}$$

Above a certain Reynolds number the flow becomes intermittent, which means that it alternates in time between laminar and turbulent states. The intermittency factor γ is defined as the fraction of time during which a point in the flow is occupied by the turbulent spots or in other words the time that the flow is turbulent during the transition phase. As γ increases from 0 to 1 through the transition zone, all averaged flow properties adjust smoothly from laminar to turbulent values.

Based on Emmon's idea, Dhawan and Narasihma [72] developed an algebraic equation to describe the connection between the spot generation and the stream-wise evolution of the intermittency factor. Their correlation is given by the following equation:

$$\gamma = \begin{cases} 1 - e^{\left[-(x-x_t)^2 \frac{n\sigma}{U}\right]} & \text{if } x \geq x_t \\ 0 & \text{if } x \leq x_t \end{cases} \tag{2.103}$$

where U is considered to be the free-stream velocity, x_t is the point of transition onset, n is the turbulent spot formation rate and σ is the spot propagation parameter.

For these models, the intermittency is implemented in a computer code by multiplying the eddy viscosity of a turbulence model by the value of intermittency. Upstream of the transition onset the intermittency is considered as zero. Once the onset of transition occurs, the intermittency is multiplied with the eddy viscosity and as the intermittency increases from zero to one, a fully turbulent boundary is achieved.

Many researchers, mainly in the field of turbomachinery, worked on intermittency models. The main shortcoming of these models is that they require the solution of a set of turbulent and a set of non-turbulent equation of mass, momentum and energy. This is computational expensive as the number of equations doubles. Moreover, these models are based on non-local formulations and typically require information on the boundary layer and the state of flow outside of it [71].

Steelant and Dick Model

Steelant and Dick [73] developed in 1996 an intermittency transport model for flows in gas turbines. The model follows the Dhawan and Narasimha [72] correlation for the intermittency factor in the transitional zone. The transport equation that Steelant and Dick [73] derived is given in eqn 2.104

$$\frac{\partial \rho \gamma}{\partial t} + \frac{\partial \rho u_i \gamma}{\partial x_j} = P \tag{2.104}$$

The production term P is

$$P = (1-\gamma)\rho\sqrt{u^2+v^2}\beta(s), \tag{2.105}$$

where

$$\beta(s) = 2f(s)f'(s) \tag{2.106}$$

The distribution breakdown f(s) is

$$f(s) = \frac{as'^4 + bs'^3 + cs'^2 + ds' + e}{gs'^3 + h} \tag{2.107}$$

and $f'(s)$ is the first derivative with respect to parameter s

$$f(s) = \frac{4as'^3 + 3bs'^2 + 2cs' + d}{3gs'^2} \tag{2.108}$$

The parameter s is the streamline coordinate which for two dimensions is given by

$$s = \int \frac{udx + vdy}{\sqrt{u^2+v^2}} \tag{2.109}$$

and $s' = s + s_t$ where s_t is the transition location.

The coefficients for the functions are

a	b	c	d	e	h	g
$\sqrt{n\sigma/U}$	-0.4906	$0.204(\frac{n\sigma}{U})^{-0.5}$	0.0	$0.04444(\frac{n\sigma}{U})^{-1.5}$	10e	1.0

Table 2.7: Coefficients for the intermittency transport model of Steelant and Dick.

The parameter $n\sigma$ in table (2.7) has been correlated by Mayle [58] based on intermittency measurements for zero pressure gradient flows as:

$$n\sigma = 1.25 \cdot 10^{-11} Tu^{7/4} \tag{2.110}$$

$$Re_{tr} = 420 Tu^{-0.69} \tag{2.111}$$

Steelant and Dick [73] tested their model for zero, adverse and favourable pressure gradient flows. They coupled their model with two sets of Navier-Stokes equations, one for the laminar and one for the turbulent phase of the flow. Moreover, they modelled the turbulence by using the $\kappa-\varepsilon$ model. In order to derive their conditioned averaged Navier-Stokes equations, they decomposed all the quantities into mean and fluctuating components. For example:

$$\phi = \begin{cases} \bar{\phi}_l + \phi_l' & \text{for } \gamma = 0 \\ \bar{\phi}_t + \phi_t' & \text{for } \gamma = 1 \\ \bar{\phi} + \phi' & \text{otherwise} \end{cases} \tag{2.112}$$

where $\bar{\phi}$ is the mean component of the quantity ϕ and ϕ' is the fluctuating one. The subscripts l and t stand for laminar and turbulent respectively.

Although, the model from Steelant and Dick [73] shows good agreement for the stream-wise variation of γ, it fails to predict the variation of γ at the cross-stream direction. Furthermore, the use of the conditionally averaged values for the Navier-Stokes equations and for the turbulence model is a basic deficiency for Computational Fluid Dynamics codes as extra difficulty and time would be needed in comparison with the solution of the averaged Navier-Stokes equations.

Cho and Chung Model

Cho and Chung [74] in 1992 proposed a $\kappa-\varepsilon-\gamma$ model for free-shear flows. Their model expresses the eddy viscosity in terms of κ, ε and γ and has been used for plane and round jets, planar far wakes and planar mixing layers.

Their intermittency equations are:

$$u_j \frac{\partial \gamma}{\partial x_j} = D_\gamma + S_\gamma \tag{2.113}$$

where the diffusion term D_γ and the source term S_γ are:

$$D_\gamma = \frac{\partial}{\partial x_j}\left[(1-\gamma)\frac{\nu_t}{\sigma_g}\frac{\partial \gamma}{\partial x_j}\right] \tag{2.114}$$

$$S_\gamma = C_{g1}\gamma(1-\gamma)\frac{P_{k,s}+P_{k,n}}{k} + C_{g2}\frac{k^2}{\varepsilon}\left(\frac{\partial \gamma}{\partial x_j}\right)^2 - C_{g3}\gamma(1-\gamma)\frac{\varepsilon}{k}\Gamma \tag{2.115}$$

and the closure coefficients take the values

$$\sigma_g = 1.0, \quad C_{g1} = 1.6, \quad C_{g2} = 0.15, \quad C_{g3} = 0.16 \tag{2.116}$$

The terms $P_{k,s}$ and $P_{k,n}$ represent the production of turbulent kinetic energy by shear and normal strains respectively.

$$P_{k,s} = -\overline{u_i u_j}\frac{\partial u_i}{\partial x_j}, \ (i \neq j) \tag{2.117}$$

and,

$$P_{k,n} = -\overline{u_i u_j}\frac{\partial u_i}{\partial x_j}, \ (i = j) \tag{2.118}$$

The first term in the S_γ equation expresses the generation of intermittency owing to the production of the turbulent kinetic energy. While, the second term represents the increase of γ by the spatial inhomogeneity. Finally, the last term represents the amount of the intermittency entrained by the interaction between the mean velocity gradient and the intermittency field [74].

Suzen and Huang Model

In 2000 Suzen and Huang [75] developed a transition model based on the combination of two transition models. They blended the transport equation model of Steelant and Dick [73] with the transition model of Cho and Chung [74]. The idea was to combine the desired properties of each model into one transport equation. The Steelant and Dick [73] model was chosen for its ability to produce the stream-wise variation of the Dhawan and Narasimha [72] intermittency and the Cho and Chung[74] model for its ability to provide a realistic variation of the intermittency in the cross-stream direction.

The transport equation of the model blends the source terms of the two previous models. The equation for the intermittency has the following form,

$$\frac{\partial \rho\gamma}{\partial t} + \frac{\partial \rho u_j \gamma}{\partial x_j} = D_\gamma + H_\gamma \tag{2.119}$$

where the diffusion term D_γ and source term H_γ are represented by:

$$D_\gamma = \frac{\partial}{\partial x_j}\left[(1-\gamma)\gamma\sigma_{\gamma l}\mu_l + (1-\gamma)\sigma_{\gamma t}\mu_t\right]\frac{\partial \gamma}{\partial x_j} \tag{2.120}$$

and

$$H_\gamma = (1-\gamma)\left[(1-F)T_0 + F(T_1 - T_2)\right] + T_3 \tag{2.121}$$

where

$$\sigma_{\gamma l} = \sigma_{\gamma t} = 1.0 \tag{2.122}$$

The term T_0 is the production term from the Steelant and Dick [73] model and is given by

$$T_0 = 2C_0\rho\sqrt{u_k u_k}f(s)f'(s), \tag{2.123}$$

$$C_0 = 1.0 \tag{2.124}$$

where ρ is the fluid density, u_k is the velocity component and the $f(s)$ is the distributed breakdown function which has the form

$$f(s) = \frac{as'^4 + bs'^3 + cs'^2 + ds' + e}{gs'^3 + h} \tag{2.125}$$

$s' = s - s_t$ with s the distance along the stream-wise coordinate and s_t is the transition location.

The model's coefficients are given in table (2.8).

a	b	c	d	e	h	g
$50\sqrt{n\sigma/U}$	-0.4906	$0.204(\frac{n\sigma}{U})^{-0.5}$	0.0	$0.04444(\frac{n\sigma}{U})^{-1.5}$	10e	50.0

Table 2.8: Coefficients for the intermittency transport model of Suzen and Huang.

As can be seen, the coefficients for the Suzen and Huang model are the same as of the Steelant and Dick [73] model except from coefficients a and g that are multiplied by a value of 50.

T_1 and T_2 are the production terms of the Cho and Chung [74] model. T_1 represents the production of turbulence kinetic energy P_k and is given by

$$T_1 = C_1\gamma\frac{P_k}{k} = \frac{C_1\gamma}{k}\tau_{ij}\frac{\partial u_i}{\partial x_j}, \tag{2.126}$$

$$C_1 = 1.6 \tag{2.127}$$

where the shear stresses are defined based on Boussinesq's hypothesis as

$$\tau_{ij} = \mu_t\left[\frac{\partial u_i}{\partial x_j} + \frac{\partial u_j}{\partial x_i} - \frac{2}{3}\frac{\partial u_k}{\partial x_k}\delta_{ij}\right] - \frac{2}{3}\rho k\delta_{ij} \tag{2.128}$$

T_2 represents the production resulting from the interaction between the mean velocity and the intermittency field and is given as:

$$T_2 = C_2\gamma\rho\frac{k^{3/2}}{\varepsilon}\frac{u_i}{\sqrt{u_k u_k}}\frac{\partial u_i}{\partial x_j}\frac{\partial \gamma}{\partial x_j}, \tag{2.129}$$

$$C_2 = 0.16 \tag{2.130}$$

The source terms of the two models are coupled together with of a blending function F which facilitates the gradual switch from T_0 to $(T_1 - T_2)$ inside the transition region. In regions where $F = 0$ the Suzen and Huang model

reduces to the Steelant and Dick [73] model whereas in regions where $F = 1$ the Cho and Chung[74] term $(T_1 - T_2)$ is activated. The blending function F is given by:

$$F = \tanh^4 \left[\frac{k/W\nu}{200(1-\gamma^{0.1})^{0.3}} \right] \tag{2.131}$$

where W is the magnitude of the strain rate.

T_3 is a diffusion related production term which is given by

$$T_3 = C_3 \rho \frac{k^2}{\varepsilon} \left[\frac{\partial \gamma}{\partial x_j} \right]^2, \tag{2.132}$$

$$C_3 = 0.15. \tag{2.133}$$

2.10.10 Intermittency and Vorticity Reynolds number Model

Based on the positive results that the intermittency-based models have, in 2006, Menter and Langtry [76] developed their approach to use only local flow information in order to activate or damp the production term in the intermittency equation. Instead of using the momentum thickness Reynolds number to trigger the onset of transition, the vorticity Reynolds number was selected as the link between the correlation and the intermittency equation,

$$Re_v = \frac{\rho y^2}{\mu} \frac{\partial u}{\partial y} = \frac{\rho y^2}{\mu} S \tag{2.134}$$

where y is the distance from the nearest wall and S is the strain rate magnitude ($S = (2S_{ij}S_{ij})^{1/2}$). Since the vorticity Reynolds number is based on the density, viscosity, wall distance and vorticity, it is considered a local property and can be calculated at every grid point independently of any other.

This transition model do not attempt to model the physics of the transition process but form a framework for the implementation of transition correlations into the CFD codes.

Intermittency Transport Equation

The proposed model is based on two transport equations. The first one is a transport equation for intermittency γ and is used to trigger the transition process locally. The intermittency function is coupled with the SST $k-\omega$ based turbulence model and it is used to turn on the turbulent kinetic energy downstream of transition points. The transport equation for the intermittency γ is given by:

$$\frac{\partial(\rho\gamma)}{\partial t} + \frac{\partial \rho u_j \gamma}{\partial x_j} = P_{\gamma 1} - E_{\gamma 1} + P_{\gamma 2} - E_{\gamma 2} + \frac{\partial}{\partial x_j} \left[\left(\mu + \frac{\mu_t}{\sigma_f} \right) \frac{\partial \gamma}{\partial x_j} \right] \tag{2.135}$$

where the parameters P and E are the production and destruction terms of the equation.

The source term for this equation are defined as follows:

$$P_{\gamma 1} = c_{\alpha 1} F_{length} \rho S (\gamma F_{onset})^{c_\alpha} \tag{2.136}$$

and

$$P_{\gamma 2} = c_{\alpha 2} \rho \Omega \gamma F_{turb} \tag{2.137}$$

where Ω is the vorticity magnitude ($\Omega_{ij} = \frac{1}{2}(\frac{\partial u_i}{\partial x_j} - \frac{\partial u_j}{\partial x_i})$). The role of these terms is to ensure that the intermittency remains zero in the laminar boundary layer and it is active in any other point of the flow. The magnitude of the $P_{\gamma 1}$ term is controlled by the transition length function (F_{length}).

The function F_{onset} is an empirical correlation used to trigger the intermittency production. It controls the length of the transition region and is a function of the vorticity Reynolds number. It is designed to change rapidly from a value of zero in a laminar boundary layer to a value of one in every location where transition occurs. The function F_{onset} is given by:

$$F_{onset1} = \frac{Re_v}{2.193 \cdot Re_{\theta c}} \tag{2.138}$$

$$F_{onset2} = \min\left[\max\left(F_{onset1}, F_{onset1}^4\right), 2.0\right] \tag{2.139}$$

$$F_{onset3} = \max\left[1 - \left(\frac{Re_T}{2.5}\right)^3, 0\right] \tag{2.140}$$

$$F_{onset} = \max\left(F_{onset2} - F_{onset3}, 0\right) \tag{2.141}$$

where the turbulence Reynolds number is given by

$$R_T = \frac{\mu_t}{\mu} = \frac{\rho k}{\mu \omega} \tag{2.142}$$

and $Re_{\theta c}$ is the critical Reynolds number where the intermittency begins to increase in the boundary layer. This occurs upstream of the transition Reynolds number ($Re_{\theta t}$) as there should be an increase of the turbulence before any change in the laminar profile occurs. The empirical correlation for the parameter $Re_{\theta c}$ was proprietary in the initial paper[76] and was referred as a function of $\tilde{R}e_{\theta t}$.

The function F_{length} in eqn. (2.136) is an empirical correlation that controls the length of the transition region and the magnitude of the two production terms. This function was also proprietary in the initial paper.

The destruction/relaminarisation sources are defined as follows:

$$E_{\gamma 1} = c_{e1} P_{\gamma 1} \gamma \quad and \quad E_{\gamma 2} = c_{e2} P_{\gamma 2} \gamma \tag{2.143}$$

These terms ensure that the intermittency remains close to zero in the laminar boundary layer. The constants c_{e1} and c_{e2} control the strength of the destruction terms and ensure that these are smaller than the production terms.

The function F_{turb} is used to disable the destruction/relaminarisation sources outside of a laminar boundary layer or in the viscous sub-layer and is defined as:

$$F_{turb} = e^{-(Re_T/4)^4} \tag{2.144}$$

The coefficients used in the intermittency equation are:

c_a	c_{e1}	c_{a1}	c_{e2}	c_{a2}	σ_f
0.5	1.0	2.0	50	0.06	1.0

Table 2.9: Coefficients for the intermittency transport equation.

The boundary conditions for the intermittency γ is zero normal flux at the wall and 1 at an inlet. The latter value of intermittency at the inlet is in order to form a framework for the implementation of the correlation-based into the general-purpose CFD. One of the requirements of the model is the grid has a y^+ less of 1. This is necessary in order to capture correctly the laminar and transitional boundary layers [77]. If the y^+ is more than 5 then the transition onset location is expected to move upstream.

Momentum Thickness Reynolds Number Transport Equation

In addition to the transport equation for the intermittency, another transport equation is solved. This equation is for the transition momentum Reynolds number and is the link between the local information and the intermittency. With this way, the model manages to capture the non-local influence of the turbulence intensity which changes due to the decay of the turbulence kinetic energy in the free-stream and due to changes in the free-stream velocity outside the boundary layer. Moreover, it ties the empirical correlation to the onset of criteria in the intermittency equation [76]. The transport equation for the scalar transition momentum thickness Reynolds number $\tilde{Re}_{\theta t}$ is given by:

$$\frac{\partial(\rho \tilde{Re}_{\theta t})}{\partial t} + \frac{\partial(\rho u_j \tilde{Re}_{\theta t})}{\partial x_j} = P_{\theta t} + \frac{\partial}{\partial x_j}\left[\sigma_{\theta t}(\mu + \mu_t)\frac{\partial \tilde{Re}_{\theta t}}{\partial x_j}\right] \tag{2.145}$$

The source term $P_{\theta t}$ is designed to force the transported scalar $\tilde{Re}_{\theta t}$ to match the value of $Re_{\theta t}$ which is calculated from an empirical correlation using information from outside the boundary layer. The source term is defined as follows

$$P_{\theta t} = c_{\theta t}\frac{\rho}{t}\left(Re_{\theta t} - \tilde{Re}_{\theta t}\right)(1.0 - F_{\theta t}) \tag{2.146}$$

where t is a time scale which is present for dimensional reasons and is given by

$$t = \frac{500\mu}{\rho U^2} \tag{2.147}$$

$F_{\theta t}$ is a blending function that turns off the source term in the boundary layer and allows the transported scalar $\tilde{Re}_{\theta t}$ to diffuse in the free-stream. It is zero in the free-stream and one in the boundary layer. The definition for the function $F_{\theta t}$ is given by

$$F_{\theta t} = \min\left\{\max\left[F_{wake}e^{(-(y/\delta))^4}, 1.0 - \left(\frac{\gamma - 1/c_{e2}}{1.0 - 1/c_{e2}}\right)^2\right], 1.0\right\} \tag{2.148}$$

where

$$\theta_{BL} = \frac{\tilde{Re}_{\theta t}\mu}{\rho U}, \quad \delta_{BL} = \frac{15}{2}\theta_{BL}, \quad \delta = \frac{50\Omega y}{U}\delta_{BL}, \tag{2.149}$$

$$Re_{\omega} = \frac{\rho\omega y^2}{\mu}, \quad F_{wake} = e^{(-(Re_{\omega}/10^5))^2} \tag{2.150}$$

The function F_{wake} ensures that the blending function is not active in the wake downstream of the aerofoil.

The coefficients for the momentum thickness Reynolds number transport equation are:

$c_{\theta t}$	$\sigma_{\theta t}$
0.03	2.0

Table 2.10: Coefficients for the momentum thickness Reynolds transport equation.

The boundary conditions for the scalar quantity $Re_{\theta t}$ is zero flux at the wall, while for the inlet its value is calculated from an empirical correlation based on the inlet turbulence intensity.

Implementation for Separated Flow

For separated flow, it was observed by Menter *et al.* [76] that the model predicts the turbulent reattachment location far downstream. It was considered that the reason for this behaviour was the fact that the turbulent kinetic energy k failed

to reach a value that could lead to the reattachment of the laminar separation boundary layer. The solution was given by letting the local intermittency to exceed the value of one wherever the laminar boundary layer separates. This will lead k to obtain values which will cause earlier reattachment. Hence, to overcome this discrepancy, a modification to the transition model for the case where separation of the laminar boundary layer occurs was introduced and a new intermittency was calculated:

$$\gamma_{sep} = \min\left\{s_1 \max\left[\left(\frac{Re_v}{2.193 \cdot Re_{\theta c}}\right) - 1.0\right] F_{reattach}, 2\right\} F_{\theta t}, \tag{2.151}$$

where the constant s_1 is given by

$$s_1 = 8.0 \tag{2.152}$$

The value of this constant controls the size of the separation bubble.

For aeronautical applications, Menter and his coworkers ([78]) modified eqn. (2.151) into

$$\gamma_{sep} = \min\left\{s_1 \max\left[\left(\frac{Re_v}{3.235 \cdot Re_{\theta c}}\right) - 1.0\right] F_{reattach}, 2\right\} F_{\theta t}, \tag{2.153}$$

considering the constant $s_1 = 2$.

$F_{reattach}$ disables the modification once the viscosity ratio is large enough to cause re-attachment and is given by

$$F_{reattach} = e^{-(Re_T/20)^4}. \tag{2.154}$$

$F_{\theta t}$ is a blending function defined in eqn. (2.146) and is used to confined the modification inside the boundary layer.

After the calculation of this extra value, the final intermittency factor is given by

$$\gamma_{eff} = \max(\gamma, \gamma_{sep}) \tag{2.155}$$

Coupling the Transition Model with the Turbulence Model

The transition model is coupled with the Shear Stress Transport (SST) k-ω turbulence model. It turns on the production term of the turbulent kinetic energy downstream of the transition point [79]. The equations for the SST k-ω turbulence model are:

$$\frac{\partial}{\partial t}(\rho k) + \frac{\partial}{\partial x_j}(\rho u_j k) = \tilde{P}_k - \tilde{D}_k + \frac{\partial}{\partial x_j}[(\mu + \sigma_k \mu_t)\frac{\partial k}{\partial x_j}] \tag{2.156}$$

$$\frac{\partial}{\partial t}(\rho\omega)+\frac{\partial}{\partial x_j}(\rho u_j\omega)=\alpha\frac{P_k}{\nu_t}-D_\omega+Cd_\omega+\frac{\partial}{\partial x_j}[(\mu+\sigma_k\mu_t)\frac{\partial\omega}{\partial x_j}] \tag{2.157}$$

where the new production and destruction terms for the turbulent kinetic energy are given as:

$$\tilde{P}_k=\gamma_{eff}P_k \tag{2.158}$$

$$\tilde{D}_k=\min[\max(\gamma_{eff},0.1),1.0]D_k \tag{2.159}$$

where γ_{eff} is the effective intermittency obtained from eqn. (2.155). From the previous equations, it is obvious that the production term for the turbulence dissipation ratio is not modified.

In order the coupling to be complete, a last modification have to be applied in the blending function of the turbulence model. The modified blending function is given as:

$$R_y=\frac{\rho y\sqrt{k}}{\mu},\quad F_3=e^{-(R_y/120)^8},\quad F_1=\max(F_{1orig},F_3) \tag{2.160}$$

Empirical Correlation in the $\kappa-\omega-\gamma-Re_{\theta t}$ Transition Model

There is an experimental correlation that relates the momentum thickness Reynolds number at the transition point, $Re_{\theta t}$, with the turbulence intensity and other quantities in the free-stream. A number of improvements have been proposed and in this project the empirical correlation modified by Langtry [78] was selected. Two different regions for the local turbulence intensity were taken and the correlation for the transition momentum thickness Reynolds number is given by:

$$Re_{\theta t}=\begin{cases}(1173.51-589.428Tu+\frac{0.2196}{Tu^2})F(\lambda_\theta) & \text{if } Tu\leq 1.3\\ 331.50(Tu-0.5658)^{-0.671}F(\lambda_\theta) & \text{if } Tu>1.3\end{cases} \tag{2.161}$$

The blending function F has also been modified in order to improve the predictions for natural transition. The modified function F is given by:

$$F(\lambda_\theta)=\begin{cases}1-(-12.986\lambda_\theta-123.66\lambda_\theta^2-405.689\lambda_\theta^3)e^{-[Tu/1.5]^{1.5}} & \text{if } \lambda_\theta\leq 0\\ 1+0.275(1-e^{-35\lambda_\theta})e^{-Tu/0.5} & \text{if } \lambda_\theta>0\end{cases} \tag{2.162}$$

λ_θ is the pressure gradient parameter and is given by:

$$\lambda_\theta=(\frac{\rho\theta^2}{\mu})\frac{dU}{ds} \tag{2.163}$$

where dU/ds is the acceleration along in the stream-wise direction and is calculated by taking the derivative of the velocity in the x,y and z direction and summing the contribution of these derivatives along the stream-wise flow direction:

$$U = (u^2 + v^2 + w^2)^{1/2} \tag{2.164}$$

$$\frac{dU}{dx} = \frac{1}{2}(u^2 + v^2 + w^2)^{-1/2}[2u\frac{du}{dx} + 2v\frac{dv}{dx} + 2w\frac{dw}{dx}] \tag{2.165}$$

$$\frac{dU}{dy} = \frac{1}{2}(u^2 + v^2 + w^2)^{-1/2}[2u\frac{du}{dy} + 2v\frac{dv}{dy} + 2w\frac{dw}{dy}] \tag{2.166}$$

$$\frac{dU}{dz} = \frac{1}{2}(u^2 + v^2 + w^2)^{-1/2}[2u\frac{du}{dz} + 2v\frac{dv}{dz} + 2w\frac{dw}{dz}] \tag{2.167}$$

$$\frac{dU}{ds} = \frac{u}{U}\frac{dU}{dx} + \frac{v}{U}\frac{dU}{dy} + \frac{w}{U}\frac{dU}{dz} \tag{2.168}$$

For numerical robustness, the pressure gradient and the acceleration parameter and the empirical correlation are limited as

$$-0.1 \leq \lambda_\theta \leq 0.1\,, \quad Tu > 0.027, \quad Re_{\theta t} \geq 20 \tag{2.169}$$

The empirical correlation is used only in the source term of the momentum thickness Reynolds number transport equation (2.146). The equations for the empirical correlation have to be solved iteratively as they require the calculation of the momentum thickness (θ) inside the pressure gradient parameter (λ_θ). For an initial guess of the local θ, eqns (2.161) and (2.162) are solved considering zero pressure gradient and local values for U, ρ and μ.

The correlation for the critical momentum thickness Reynolds number is defined as follows:

$$Re_{\theta c} = \begin{cases} \tilde{Re}_{\theta t} - 396.035 \cdot 10^{-2} + (-120.656 \cdot 10^{-4})\tilde{Re}_{\theta t} + (868.23 \cdot 10^{-6})\tilde{Re}_{\theta t} + (-696.506 \cdot 10^{-9})\tilde{Re}_{\theta t} & \text{if } \tilde{Re}_{\theta t} \leq 1870 \\ \tilde{Re}_{\theta t} - (593.11 + 0.482 \cdot (\tilde{Re}_{\theta t} - 1870)) & \text{if } \tilde{Re}_{\theta t} \geq 1870 \end{cases} \tag{2.170}$$

The last correlation that describes the length of the transition model based on the T3B, T3A and T3A- experiments. The empirical correlation for the F_{length} is based on $Re_{\theta t}$ and is given by

$$F_{length} = \begin{cases} 39.8189 - (119.27 \cdot 10^{-4})\tilde{Re}_{\theta t} - (132.567 \cdot 10^{-6})\tilde{Re}_{\theta t}^2 & \text{if } \tilde{Re}_{\theta t} < 400 \\ 263.404 - (123.939 \cdot 10^{-2})\tilde{Re}_{\theta t} + (194.548 \cdot 10^{-5})\tilde{Re}_{\theta t}^2 - (101.695 \cdot 10^{-8})\tilde{Re}_{\theta t}^3 & \text{if } 400 \geq \tilde{Re}_{\theta t} < 596 \\ 0.5 - 3.0 \cdot 10^{-4} \cdot (\tilde{Re}_{\theta t} - 596.0) & \text{if } 596 \geq \tilde{Re}_{\theta t} < 1200 \\ 0.3188 & \text{if } 1200 \geq \tilde{Re}_{\theta t} \end{cases} \tag{2.171}$$

Figures (2.8(a)) and (2.8(b)) present the equations for the critical momentum thickness Reynolds number ($Re_{\theta c}$) and the function for the length of transition flow (F_{length}) based on Langtry and Menter work. It can be seen that the functions are smooth and continuous.

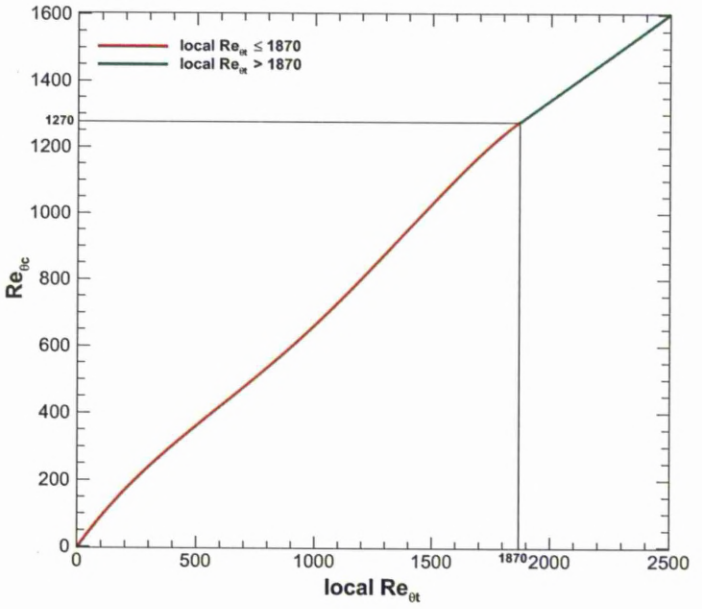

(a) $Re_{\theta c}$

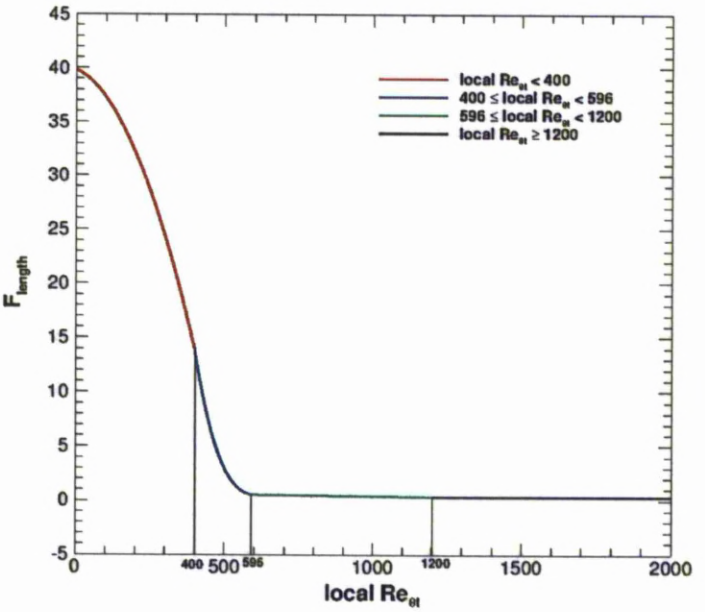

(b) F_{length}

Figure 2.8: The critical momentum thickness Reynolds number ($Re_{\theta c}$) and function for the length of transition flow (F_{length}) based on Langtry and Menter work[77].

Table (2.11) summarises the functions and parameters for this model.

Function	Equation
Source term for γ	$(1-c_{e1}\gamma)\cdot c_{a1}F_{length}\rho S(\gamma F_{onset})^{c\alpha}$
Second source term for γ	$(1-c_{e2}\gamma)\cdot_{\alpha 2}\rho\Omega\gamma F_{turb}$
Source term for $\tilde{Re}_\theta$	$P_{\theta t}=c_{\theta t}\frac{\rho}{T}\left(Re_{\theta t}-\tilde{Re}_{\theta t}\right)(1.0-F_{\theta t})$
Blending function	$F_{\theta t}=\min\max[F_{wake}e^{(-(y/\delta))^4},1.0-\left(\frac{\gamma-1/c_{e2}}{1.0-1/c_{e2}}\right)^2],1.0$
Blending function for the wake	$F_{wake}=e^{(-(Re\omega/10^5))^2}$
Intermittency for separated flow	$\gamma_{sep}=\min\left\{s_1\max\left[\left(\frac{Re_v}{3.235\cdot Re_{\theta c}}\right)-1.0\right]F_{reattach},2\right\}F_{\theta t}$
Re-attachment function	$F_{reattach}=e^{-(Re_T/20)^4}$
Local momentum thickness Reynolds number	$Re_{\theta t}=(1173.51-589.4287Tu+\frac{0.2196}{Tu^2})\cdot F(\lambda_\theta)$, if $Tu\leq 1.3$ $Re_{\theta t}=331.50(Tu-0.5658)^{-0.671}F(\lambda_\theta)$, if $Tu\geq 1.3$
Critical momentum thickness Reynolds number	$Re_{\theta c}=\tilde{Re}_{\theta t}-(593.11+0.482(\tilde{Re}_{\theta t}-1870))$, if $\tilde{Re}_{\theta t}\geq 1870$ $Re_{\theta c}=\tilde{Re}_{\theta t}-396.035\cdot 10^{-2}-(120.656\cdot 10^{-4})\cdot\tilde{Re}_{\theta t}+(868.23\cdot 10^{-6})\cdot\tilde{Re}_{\theta t}-(696.506\cdot 10^{-9})\cdot\tilde{Re}_{\theta t}$, otherwise
Transition length function	$F_{length}=39.8189-(119.27\cdot 10^{-4})\tilde{Re}_{\theta t}-(132.567\cdot 10^{-6})\tilde{Re}_{\theta t}^2$, if $\tilde{Re}_{\theta t}<400$ $F_{length}=263.404-(123.939\cdot 10^{-2})\tilde{Re}_{\theta t}+(194.548\cdot 10^{-5})\tilde{Re}_{\theta t}^2-(101.695\cdot 10^{-8})\tilde{Re}_{\theta t}^3$, if $[400\geq\tilde{Re}_{\theta t}<596]$ $F_{length}=0.5-0.0003\cdot(\tilde{Re}_{\theta t}-596.0)$, if $[596\geq\tilde{Re}_{\theta t}<1200]$ $F_{length}=0.3188$, otherwise
Momentum thickness	$\theta_{BL}=\frac{\tilde{Re}_{\theta t}\mu}{\rho U}$
Boundary layer thickness	$\delta_{BL}=\frac{15}{2}\theta_{BL}$
Displacement	$\delta=\frac{50\Omega y}{U}\delta_{BL}$
Pressure gradient	$\lambda_\theta=(\frac{\rho\theta^2}{\mu})\frac{dU}{ds}$
Flow acceleration	$K=(\frac{\nu}{U^2})\frac{dU}{ds}$

Table 2.11: Functions and parameters of the $\kappa-\omega-\gamma-Re_\theta$ model and their equations.

Implementation of the $\kappa-\omega-\gamma-Re_{\theta t}$ Transition Model

Based on the theory, the computation steps can be concentrated on the following four steps: (a) solve the momentum and the continuity equations, (b) solve the turbulence model with the modified blending function f_1; the k-equation with the modified production term $\tilde{P}_k$ and destruction $\tilde{D}_k$ terms, and the ω-equation, and then calculate the eddy viscosity, (c) compute the empirical correlation of transition momentum thickness Reynolds number $Re_{\theta t}$ and finally (d) solve the transition equations for $\gamma-$ and $\tilde{Re}_{\theta t}$[80].

A flow chart for the implementation of the model for the prediction of transition onset can be seen in figure (2.9).

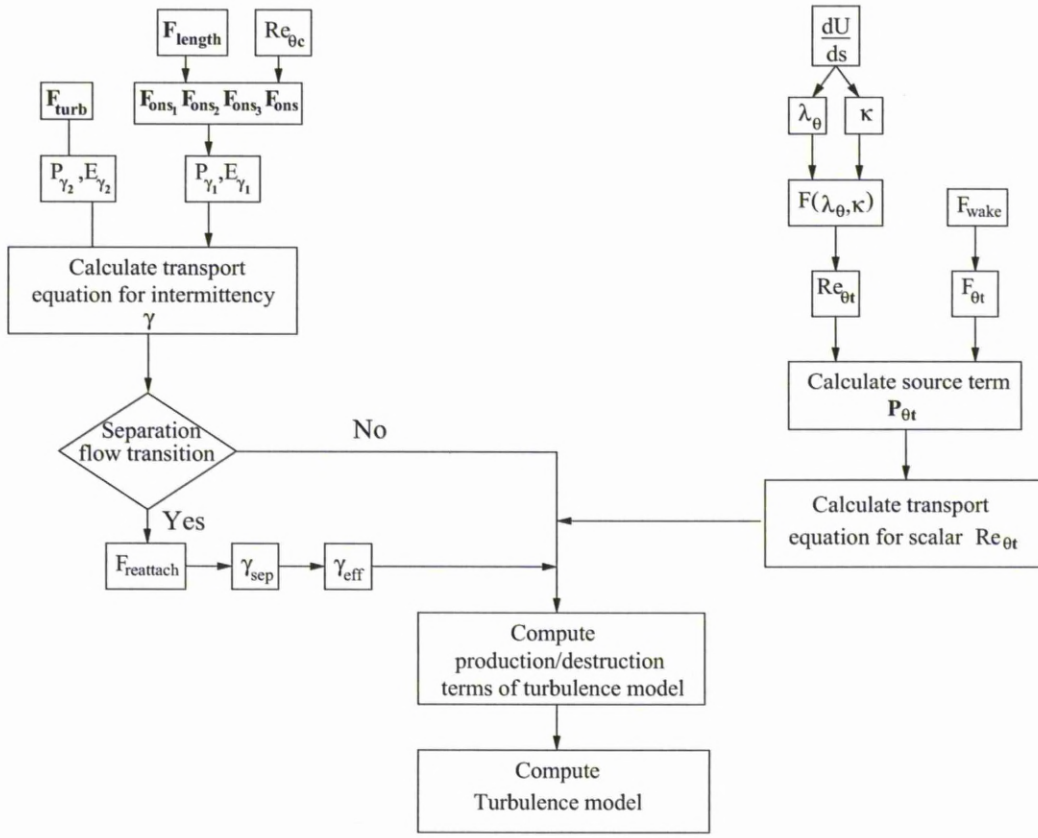

Figure 2.9: Road map for the implementation of Menter's model.

2.11 Summary

In this chapter, the physics and the models related to the complex phenomenon of transition are presented. The discussion in the chapter, starts with the presentation of the two-dimensional form of the Navier-Stokes equations and how they are reformed in a formula more suitable to calculate the flow around bodies.

Then the approach to turbulent modelling has been discussed and more details have been provided for the $\kappa - \omega$ and $\kappa - \omega$ SST models, These models are presented as more suitable in the current study.

The key physical processes of the complex phenomenon of transition are presented. Then a hierarchy of transition prediction and modelling techniques have been presented. These methods vary in complexity from simple engineering criteria to complex transport equation models.

The criteria of Michel, Cebeci and Smith, and Abu-Ghannam and Shaw were selected for the prediction of the onset of natural transition. These correlation based models require the knowledge of non-local information in order to predict the transition onset. Thwaite integral boundary layer method has been adopted in to provide a source of the required laminar boundary layer data for the criteria. The transition models have been integrated with the turbulence model to provide the onset of transition.

Finally the new transition model of $\kappa - \omega - \gamma - Re_{\theta t}$ is introduced. The model is developed based on local information and has eliminate the need of any non-local operation as required from the empirical correlation models. As a result, the transition model is more compatible with the existing CFD codes. It requires the solution of two extra transport equations, one for the intermittency and one for a transition onset criterion in terms of momentum thickness Reynolds number. The model has been calibrated in order to be used with $\kappa - \omega$ SST turbulence model.

Chapter 3

Modelling of 2D cases

The transition models described in the previous chapter have to be validated. This chapter describes the available experimental data and the grid generation for the 2D validation test cases used in this work. The test cases include the Aerospatiale A (ONERA A), the NACA 0012, the NLF-0416 and the S809 aerofoils. For all these aerofoils, the available experimental data were compared with the XFOIL results. XFOIL uses the e^N method for transition prediction and is a popular tool for aerofoil aerodynamics. If specified, the free-stream turbulence levels were matched during calculations. If the free-steam turbulence intensity is not known from the experiments then an estimate was made.

For the calculation of the flow around an aerofoil, the most suitable mesh-generation methods were used. A C-topology was used for the majority of the aerofoil grids. At least 200 nodes were placed on each side of the aerofoil and spline curves were used to interpolate these. On the surface of the aerofoil a cosine law is used and the nodes are clustered at the leading and trailing edges where the cell spacing is considered at 10^{-5}. The far-field, has to be big enough to avoid setting the boundary conditions at regions near the aerofoil. A distance of 10 chords is chosen and a minimum number of 100 nodes on the edges normal to the surface is considered. The exponential law is used for the edges that are perpendicular to the aerofoil and as a result, the spacing of the first cells at these edges is set at 10^{-5}. For the far-field, the idea is to keep as smooth as possible.

3.1 ONERA Aerofoil

The Aerospatiale A or ONERA A aerofoil was designed at Aerospatiale in 1986 and it was used for the European CFD validation study (**ECARP**). The main objective of this project was to investigate the performance of a variety of state-of-art turbulence models of the period[81]. The experiments were carried out for a range of Reynolds numbers and incidences. The ONERA A aerofoil can be seen in figure (3.1).

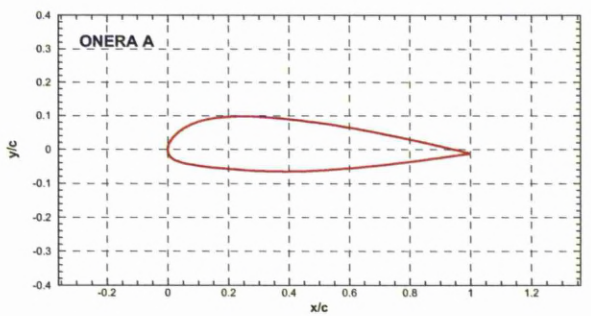

Figure 3.1: The ONERA A aerofoil.

The ONERA A aerofoil provides a substantial challenge to computational methods since its stall process is complex. It was observed that the aerofoil produced a laminar separation bubble on the upper surface in the leading edge region even at moderate incidence angles. Moreover, stall on the aerofoil was initiated by the advance of trailing edge separation due to strong adverse pressure gradient on the aft part of the suction side of the aerofoil.

Two sets of experiments were carried out for this aerofoil. The first was conducted at the ONERA Fauga-Mauzac F1 wind tunnel, at Mach numbers of $M = 0.15$, 0.22 and 0.3 and a range of Reynolds numbers from $Re = 2 \times 10^6$ to 7.5×10^6. For each Reynolds number, a large range of incidence angles was considered. The F1 test cases provide measurements for the lift, drag, skin friction and surface pressure distributions. Table (3.1) provides the parameters for the F1 test case.

A second experiment was also performed for the ONERA A aerofoil in the CFM/F2 wind tunnel. This wind tunnel is of closed-circuit type, working at ambient pressure. It has free-stream turbulent level less than 0.06%. Measurements were conducted at Mach and Reynolds numbers of 0.15 and 2×10^6 respectively. Table (3.2) presents the conditions of the test. The F2 wind tunnel not only provided measurements for the same parameters as in the F1 test case but also boundary layer quantities like displacement thickness (δ), momentum thickness (θ) and detailed experimental profiles of the velocity and turbulent stresses at incidence angles of 7.2, 12.3, and 13.3 degrees.

F1 Wind Tunnel		
Measurements	Mach number	Reynolds number (10^6)
Drag Coefficient (C_D)	0.15	2.08, 3.13, 5.25, 7.57
	0.22	5.22
	0.3	5.25
Skin Friction Coefficient (C_F)	0.15	2.05, 3.13, 5.24, 7.54
	0.22	5.22
	0.3	5.25
Lift Coefficient (C_L)	0.15	2.07 , 3.13 , 5.25 , 7.54
	0.22	5.22
	0.3	5.25
Pressure Coefficient (C_p)	0.15	2.07 , 3.13 , 5.25 , 7.54
	0.22	5.22
	0.3	5.25
Lift-to-Drag ratio (L/D)	0.15	2.07 , 3.13 , 5.25 , 7.54
	0.22	5.22
	0.3	5.25

Table 3.1: Summary of the parameters of the F1 tests of the ONERA A section.

F2 Wind Tunnel			
Measurements	Mach number	Reynolds number	Incidence Angle (degree)
Drag Coefficient (C_D)	0.15	2×10^6	3.1°- 16.3°
Friction Coefficient (C_F)	0.15	2×10^6	3.1°- 14.3°
Lift Coefficient (C_L)	0.15	2×10^6	3.1°- 18.2°
Pressure Coefficient (C_p)	0.15	2×10^6	0.1°- 18.2°
Lift-to-Drag ratio (L/D)	0.15	2×10^6	
Displacement thickness (δ^*)	0.15	2×10^6	7.2°, 12.3°, 13.3°
Momentum thickness (θ)	0.15	2×10^6	7.2°, 12.3°, 13.3°

Table 3.2: Summary of the parameters of the F2 tests of the ONERA A section.

3.1.1 ONERA F1 Experimental Data

The surface pressure coefficients for the ONERA F1 experiments are presented in figure (3.2). The results are for a range of incidence angles while a Mach number of $M = 0.15$ and a Reynolds number of $Re = 2.07 \times 10^6$ were considered. The suction peak increased as the angle of attack increased and the aerofoil stalled at 17 degrees. For the 20 degrees incidence, the surface pressure coefficient presents a plateau which is characteristic of a stalled aerofoil. The shape of the curve near the trailing edge suggests the presence of vortex shredding.

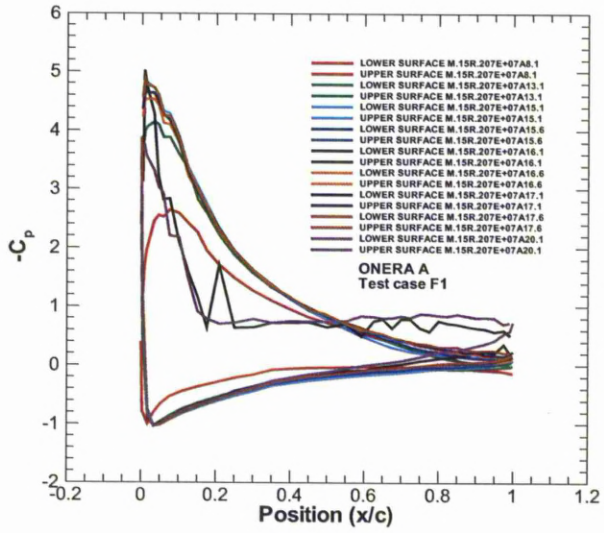

Figure 3.2: Surface pressure coefficients for various incidence angles for the ONERA A aerofoil (F1 experiments, $M = 0.15$ and $Re = 2.07 \times 10^6$).

Figures (3.3(a)) and (3.3(b)) present the results for the lift coefficient as a function of the Mach and Reynolds numbers, respectively. Considering a constant Reynolds number of $Re = 5.22 \times 10^6$, figure (3.3(a)) presents the lift for three Mach numbers, of M=0.15, 0.22 and 0.30. The lift decreases as the Mach number increases. It is obvious from the figure (3.3(a)) that the case with Mach number at M=0.3 produces the smallest peak C_l. On the other hand, the case at lower Mach number presents the higher lift peak. In figure (3.3(b)), the Mach number is kept constant at $M = 0.15$ and the Reynolds varied from $Re = 2.07 \times 10^6$ to 7.54×10^6. For incidences angles lower than 10 degrees the aerofoil produced similar amounts of lift. As the angle of attack increased and at Reynolds number of $Re = 5.25 \times 10^6$, the section produced the highest amount of lift and highest lift peak. The case for Reynolds number at $Re = 2.07 \times 10^6$ presents some discrepancies close to stall.

Similar to the previous comparisons, figures (3.3(c)) and (3.3(d)) illustrate the total drag coefficient initially as a function of Mach number and then as a function of Reynolds number. For the first case, two Reynolds numbers with close values are considered while the Mach number is varied between $M = 0.15$ and 0.22. As can be seen from figure (3.3(c)), the case with the higher Mach number produces the lowest drag coefficient. On the other hand, when the Mach number is kept constant at $M = 0.15$ and the Reynolds number increases from $Re = 2.07 \times 10^6$ to $Re = 7.57 \times 10^6$, the drag reduces for incidence angles higher than 10 degrees. For angles of attack lower than 10 degrees, the case with the lower Reynolds number produces the most drag. It is characteristic that the cases with higher Reynolds number produces similar amounts of drag.

Figures (3.4(a)) - (3.4(d)) show the skin friction distribution for a range of Reynolds numbers. Considering a constant Mach number of $M = 0.15$ the skin friction coefficient around the ONERA A aerofoil is presented for a variety of incidence angles. There is a small reduction of C_f as the angle of attack increased. Similar results are observed in figures (3.5(a)) - (3.5(b)) where the skin friction distribution is presented for a variety of angles while the Mach and Reynolds numbers are considered constant at $M = 0.22$ and $Re = 5.22 \times 10^6$, respectively.

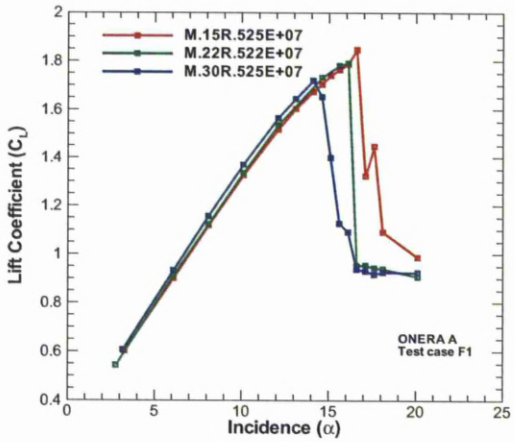

(a) Lift coefficient for a range of Mach numbers

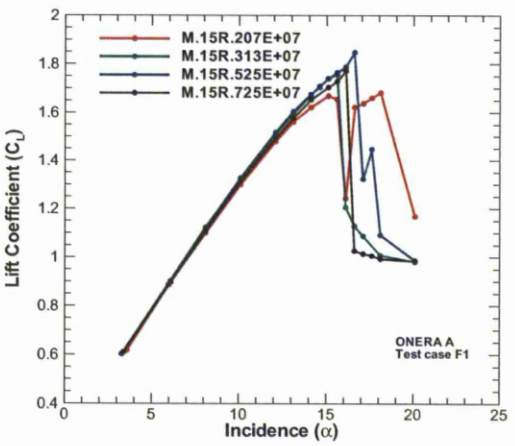

(b) Lift coefficient for a range of Reynolds numbers

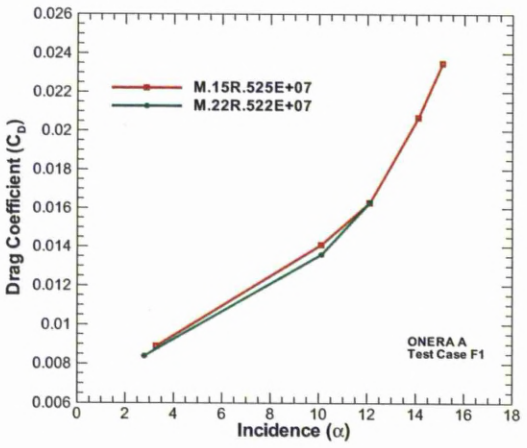

(c) Drag coefficient for a range of Mach number

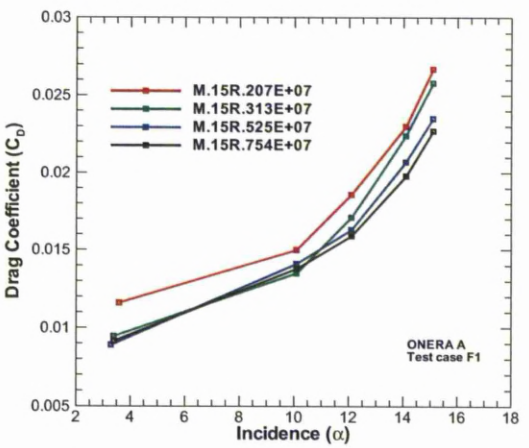

(d) Drag coefficient for a range of Reynolds number

Figure 3.3: Lift and drag coefficients as function of incidence for the ONERA A section. The experiments correspond to the F1 test case.

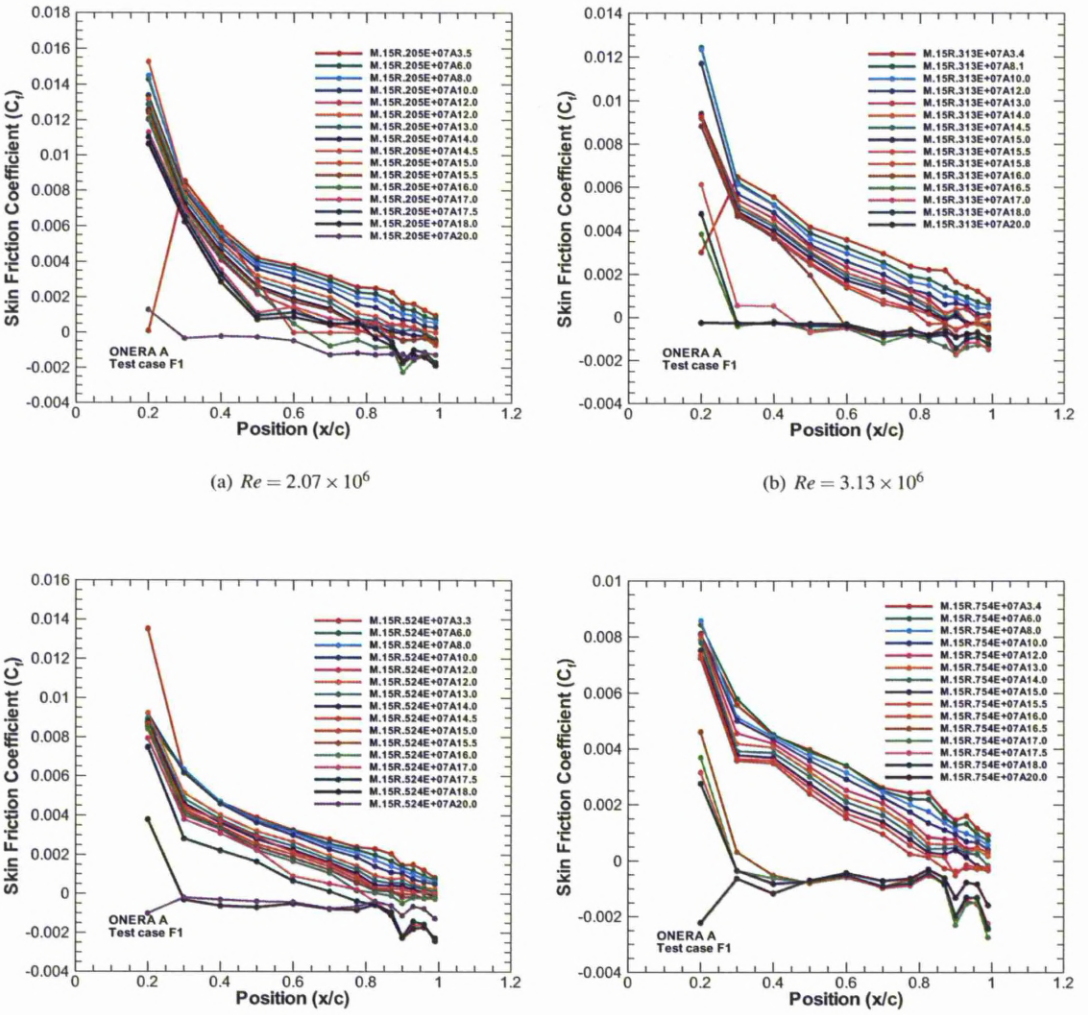

(a) $Re = 2.07 \times 10^6$

(b) $Re = 3.13 \times 10^6$

(c) $Re = 5.24 \times 10^6$

(d) $Re = 7.54 \times 10^6$

Figure 3.4: Skin friction measurements as function of incidence angle for the ONERA A aerofoil (F1 experiments, $M = 0.15$).

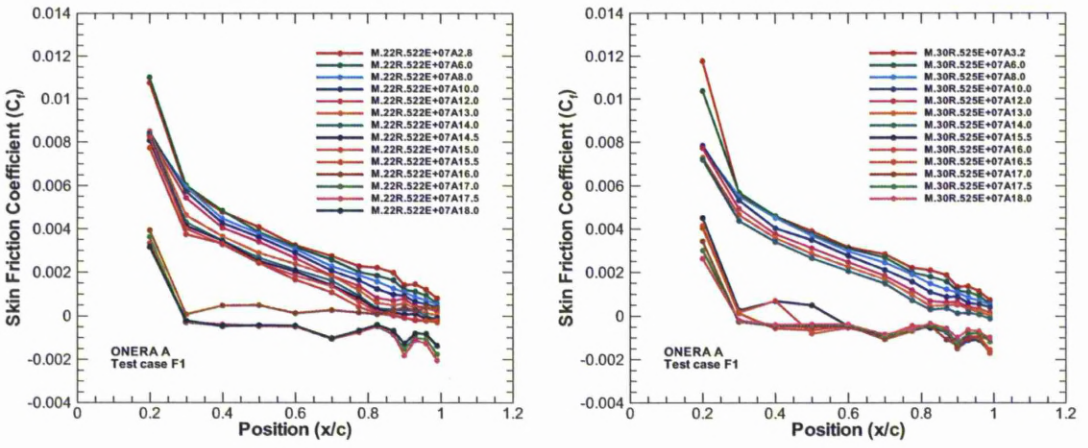

(a) $Re = 5.22 \times 10^6$ (b) $Re = 5.25 \times 10^6$

Figure 3.5: Skin friction measurements as function of incidence angle for the ONERA A aerofoil (F1 experiments, $M = 0.15$).

3.1.2 ONERA F2 Experimental Data

The ONERA A aerofoil was also tested at a different wind tunnel where new data were collected. Figure (3.6(a)) shows the surface pressure coefficient for a range of incidences from 5.2 degrees to 17.7 degrees. It is obvious that the results do not show the discrepancies that are present at similar conditions for the F1 experiment. Figure (3.6(b)) presents the skin friction coefficient on the upper surface for a range of angles of attack. As the incidence increases, a reduction at the skin friction is observed while intense discrepancies occur close to the trailing edge of the aerofoil for 14 degrees of angle of attack.

Figures (3.7(a)) and (3.7(b)) show the lift and drag coefficients for the ONERA A aerofoil. At an incidence of 13.8 degrees, the aerofoil produces the maximum lift, although, post this incidence the drag distribution shows an abrupt increase.

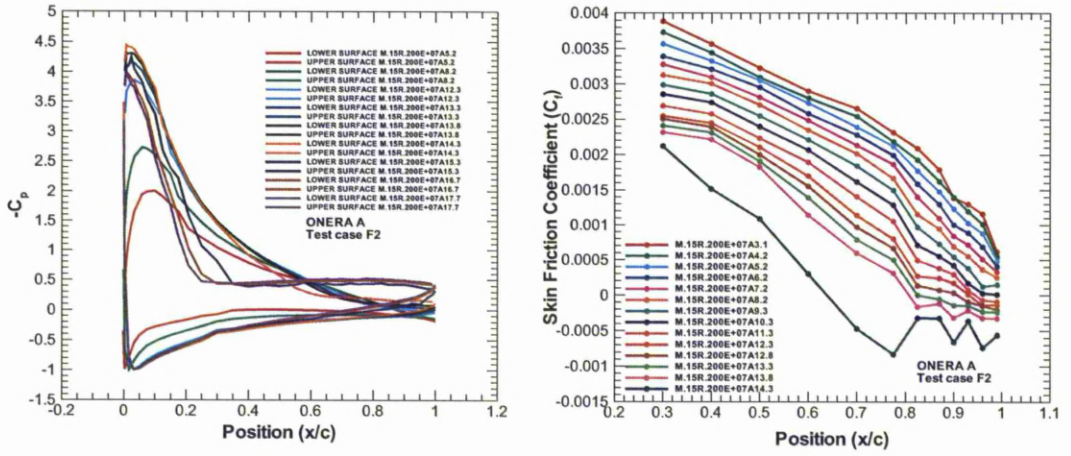

(a) Surface pressure coefficient

(b) Skin friction coefficient

Figure 3.6: Surface pressure coefficients and skin friction coefficients as functions of incidence for the ONERA A aerofoil (F2 experiments, $M = 0.15$ and $Re = 2 \times 10^6$).

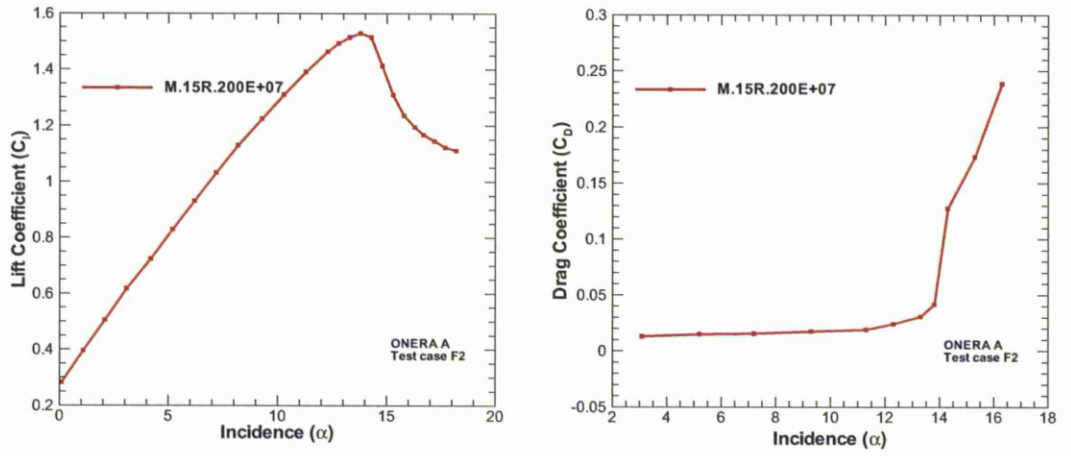

(a) C_L

(b) C_D

Figure 3.7: Lift and drag as a function of incidence angle for the ONERA A aerofoil (F2 experiments, $M = 0.15$ and $Re = 2 \times 10^6$).

The ONERA F2 test cases also include boundary layer information. Figures (3.8(a)) and (3.8(b)) show the displacement and momentum thickness at three different incidence angles. Both displacement and momentum thickness increase as the angle of attack increases at constant Mach and Reynolds numbers.

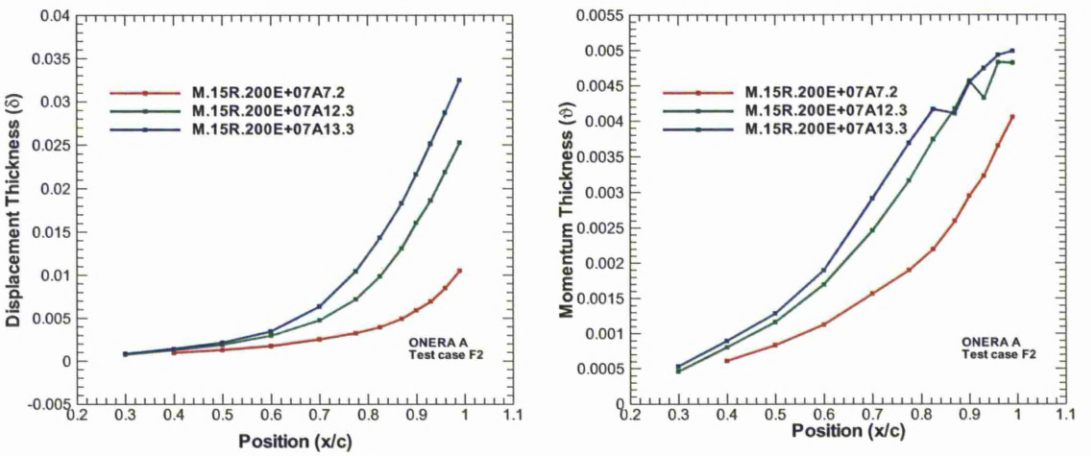

(a) Displacement Thickness

(b) Momentum Thickness

Figure 3.8: Displacement and momentum thickness as a function of incidence angle for the ONERA A aerofoil (F2 experiments, $M = 0.15$ and $Re = 2 \times 10^6$).

The ONERA F2 measurements include profiles of the velocity and turbulent stresses inside the boundary layer. The measurements for these quantities were divided into two cases. The first case includes the results normal to the surface of the aerofoil and the second one the results measured normal to the free-stream. The profiles normal to the surface are included in the first case which is called T1. The second case includes the results normal to free-stream. Schematics of the two cases are shown in figures (3.9(a)) and (3.9(b)).

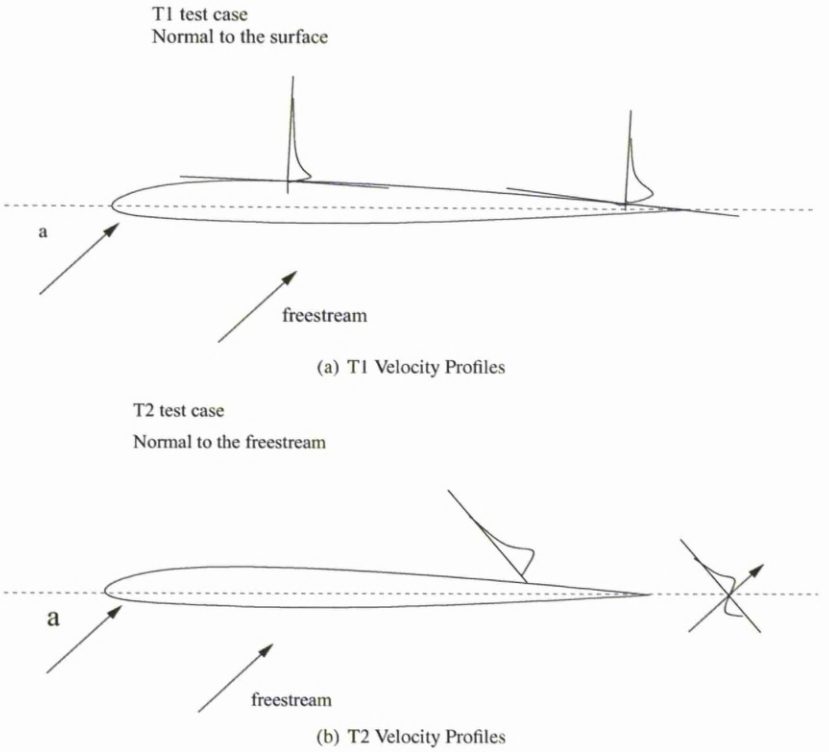

Figure 3.9: Schematics for the T1 and T2 velocity profiles for the F2 ONERA A experiments.

Figure 3.10 presents the comparison for the lift coefficient for the two test cases. As shown that the results for the F1 test case present some anomalies near stall.

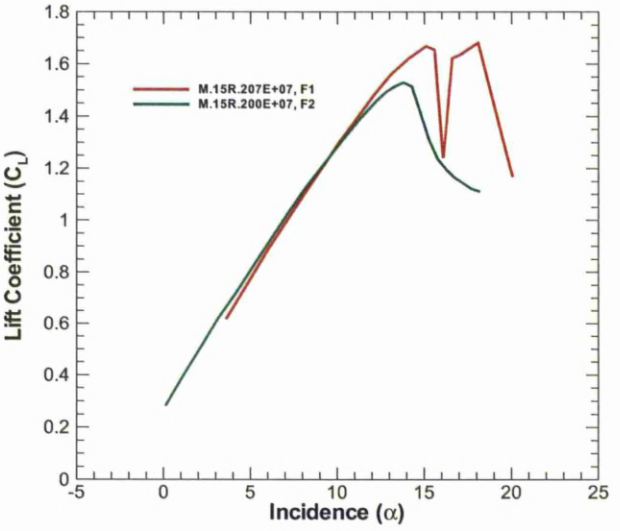

Figure 3.10: Comparison of the lift coefficient for the F1 and F2 tests cases. The F1 test case was measured at Mach number $M = 0.15$ and Reynolds number $Re = 2.07 \times 10^6$. The F2 test case was measured at Mach number $M = 0.15$ and Reynolds number $Re = 2 \times 10^6$.

Since the measurements in the F1 tunnel at Mach number 0.15 and Reynolds number 2.07×10^6 presented anomalies, this test case was replaced by the F2 data set at similar conditions. The deficiencies of the specific condition for the F1 test case can be observed in the figure (3.10) where the lift coefficients of the two cases are compared. Based on this figure, the F2 data set was used for Mach number $M = 0.15$ and Reynolds number $Re = 2 \times 10^6$ as well as for the comparison of boundary layer quantities. For lift and drag calculations at higher Reynolds numbers, the rest of the F1 data sets were appropriate.

3.1.3 CFD Mesh - ONERA A aerofoil

Care has been taken for the construction of the grid for the ONERA A aerofoil based on experiments. The domain extends 10 chord length upstream of the leading edge and downstream of the trailing edge. In the cross-stream direction, 10 chord lengths above and below the aerofoil were used. The grid is comprised of 201 points around

the aerofoil distributed using a hyperbolic law, while normal to wall, 61 points under exponential law were distributed keeping the first cell distance at 10^5. The grid used during the computation is shown in figures (3.11(a)) and is (3.11(b)) and it consists of approximately 40000 nodes.

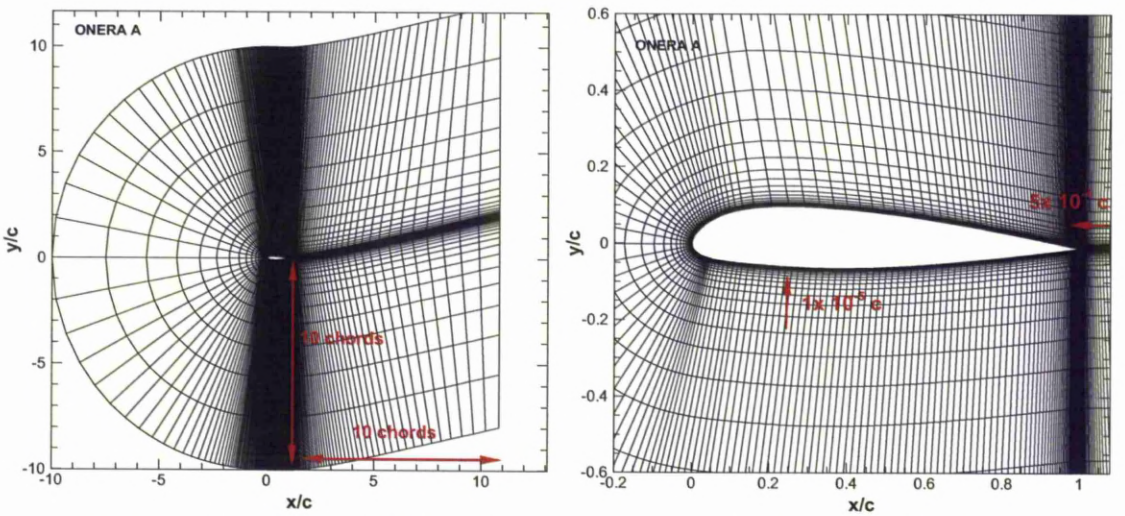

(a) Full view of the 2D mesh around ONERA A aerofoil

(b) Detailed view of the mesh around ONERA A aerofoil

Figure 3.11: 2D mesh around ONERA A aerofoil.

In order to define the correct size of the grid, another two mesh were created, one with 33900 points and one with 129320 points. Figure (3.12) show the comparison of the lift coefficient for the different grids. The mesh with the extra points estimates higher lift from the other two cases. The grid with approximate 40000 nodes develeps the same lift as the more sparce grid. As it was demonstrated by Depommier[82], the addition of more points along the chord moves the transition towards the leading edge.

3.2 Transitional Flow over the ONERA A Aerofoil

The two-dimensional flow around the ONERA A arofoil was performed at conditions similar to the experiments performed by ONERA[81]. Initially, the effect of roughness on the aerodynamic characteristics of the aerofoil was studied. This was followed by calculations using the empirical correlations.

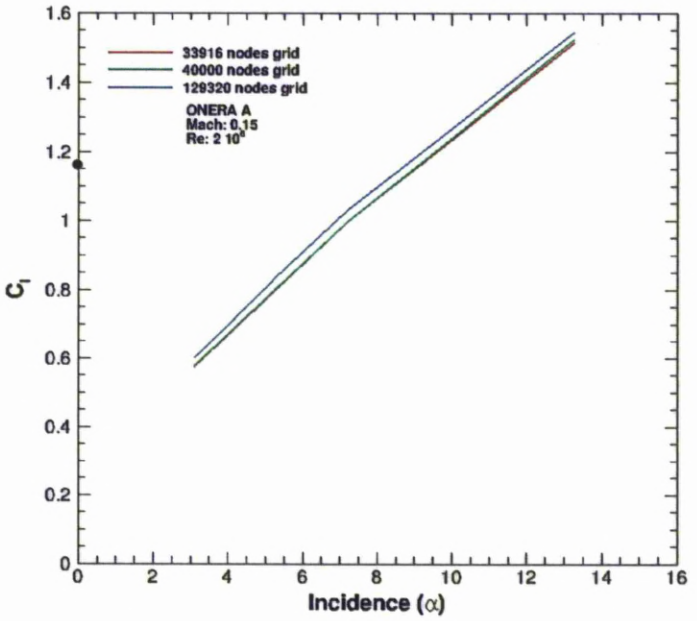

Figure 3.12: Comparison of the lift coefficient for the different meshes. The calculations were performed at Mach number $M = 0.15$ and Reynolds number $Re = 2 \times 10^6$.

3.2.1 Modelling Roughness effects over the ONERA A aerofoil

To analyse the distributed roughness on the aerofoil, the rough wall boundary conditions were considered on a limited section of the aerofoil surface while smooth wall boundary conditions were applied everywhere else. For the specific calculations, the roughness was limited on the 10% of the aerofoil chord starting from the leading edge. The Reynolds number and Mach numbers were considered at $Re = 2 \times 10^6$ and $M = 0.15$ respectively. The calculations were carried out for a range of incidence angles from 3.1 degrees to 16.3 degrees while the values of equivalent sand-grain roughness used are $h_S/c = 1 \times 10^{-4}$ and 2×10^{-4} as suggested by the test cases of Knopp et al [62]. These values correspond to real roughness of h=0.055mm and h=0.0689mm respectively[83].

Lift and Drag Calculations

The lift coefficient around the ONERA A aerofoil using the SST $k-\omega$ and the baseline $k-\omega$ models can be seen in figures (3.13(a)) and (3.13(b)). Each of the figures presents the comparison between the Hellsten and Knopp roughness models with the existed experimental data from F1 and F2. In all cases the roughness models show a similar trend to the fully turbulent calculations which try to follow the results from the F2 experiment. As the sand-grain roughness increases and higher incidence angles are used, less lift is developed. Moreover, the models show a sensitivity on

the turbulence model that is used. For the baseline $k-\omega$, less lift is produced in comparison to the calculation with the SST $k-\omega$ turbulence model. As the experiments did not consider roughness, the comparisons were used as indications that the roughness models models can follow the trend observed at the lift and drag calculations.

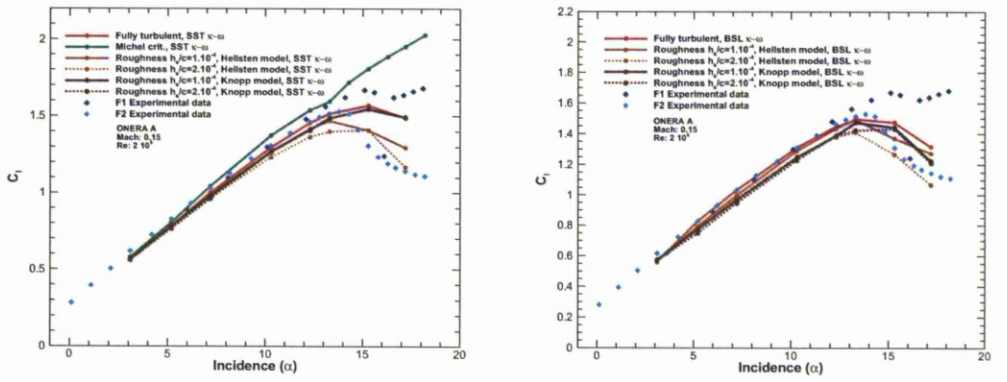

(a) SST $k-\omega$ model (b) BSL $k-\omega$ model

Figure 3.13: Lift coefficient over a ONERA A aerofoil. Comparison between the Hellsten and Laine and Knopp roughness models and the experimental data from F1 and F2. Computations have been conducted with SST and BSL $k-\omega$ turbulence models.($M=0.15$, $Re=2\times10^6$)

The drag coefficients presented in figures (3.14(a)) and (3.14(b)) corresponds to a total drag, is the sum of viscous and pressure drag. The roughness models show a tendency to follow the experimental data from the F2 test case even if they produce lower values of drag. For high angles of attack, the Hellsten and Laine model shows an increased value of drag.

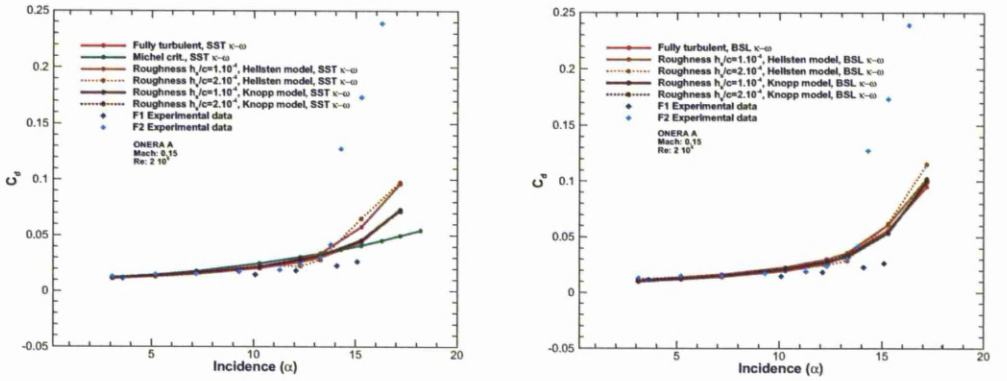

(a) SST $k-\omega$ model (b) BSL $k-\omega$ model

Figure 3.14: Drag coefficient over a ONERA A aerofoil. Comparison between the Hellsten and Laine and Knopp roughness models and the experimental data from F1 and F2. Computations have been conducted with SST and BSL $k-\omega$ turbulence models.($M=0.15$, $Re=2\times10^6$)

Surface Pressure and Skin Friction Distributions

Figures (3.15(a))-(3.16(b)) show the surface pressure coefficient for incidence angles of 7.2 degrees and 12.3 degrees. For the cases where the roughness models are compiled with the SST $k-\omega$ turbulence model, both roughness models appear to have a lower pressure peak than the experimental data or the fully turbulent results. For the cases where the baseline $k-\omega$ is used the Hellsten and Laine roughness model shows a higher pressure peak than the fully turbulent calculations but again it is lower than what the experimental data.

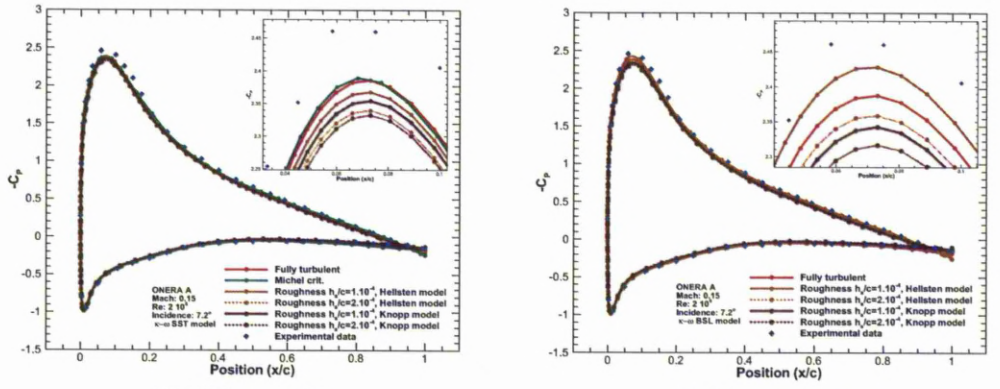

(a) SST $k-\omega$ model

(b) BSL $k-\omega$ model

Figure 3.15: Surface pressure coefficient for the ONERA A aerofoil at 7.2 degrees. Comparison between the Hellsten and Knopp roughness models with the experimental data. ($M = 0.15$, $Re = 2 \times 10^6$).

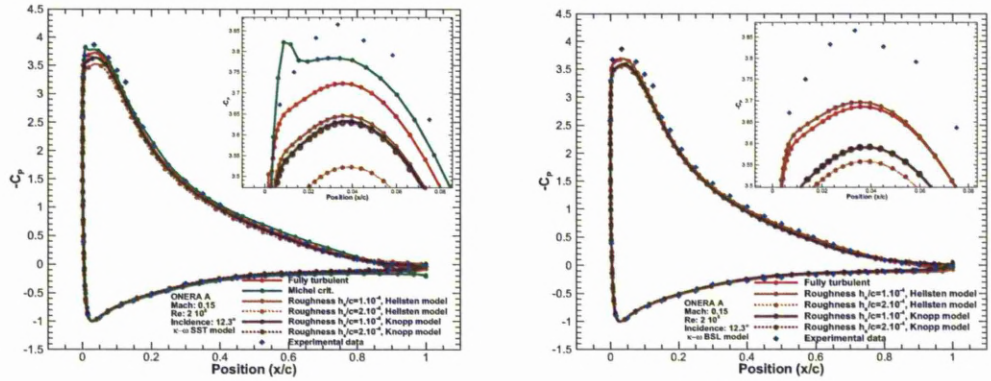

(a) SST $k-\omega$ model (b) BSL $k-\omega$ model

Figure 3.16: Surface pressure coefficient for the ONERA A aerofoil at 12.3 degrees. Comparison between the Hellsten and Knopp roughness models with the experimental data. ($M = 0.15$, $Re = 2 \times 10^6$).

When the skin friction coefficient was calculated, figures (3.17(a)) and (3.18(b)), all models showed a tendency to follow the fully turbulent calculations with the Knopp model and low sand-grain roughness to be closer to them. As was observed in the surface pressure coefficient comparisons, increased sand-grain roughness does not mean an overall increase of the skin friction.

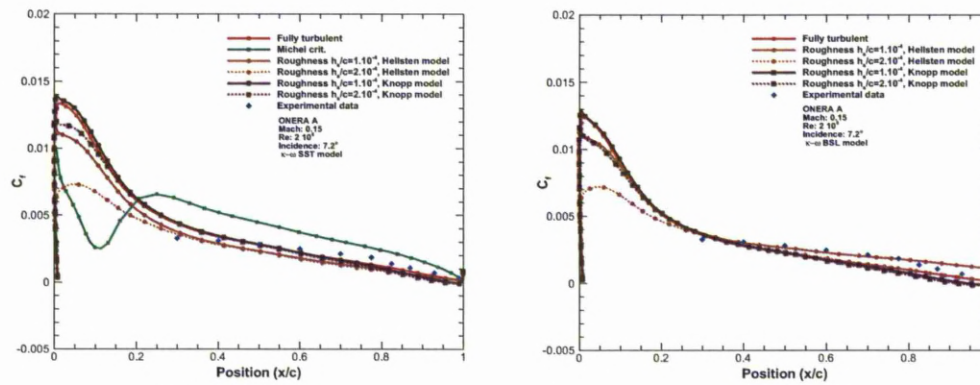

(a) SST $k-\omega$ model (b) BSL $k-\omega$ model

Figure 3.17: Skin friction coefficient over the ONERA A aerofoil for 7.2 degrees angle of attack. Comparison between the computations with Hellsten and Knopp roughness models and experimental data. ($M = 0.15$, $Re = 2 \times 10^6$)

3.2.2 Empirical Transition Models over the ONERA A Aerofoil

Besides using the ONERA A aerofoil to model the roughness effect, the aerofoil was used to validate the empirical correlation transition models. Three calculations were performed at conditions similar to the experiments performed by ONERA [81]. For the first set of calculations, the Reynolds number and Mach numbers were considered at $Re = 2 \times 10^6$ and $M = 0.15$ respectively. Furthermore, the aerofoil was also tested at Reynolds numbers of $Re = 3.13 \times 10^6$ and

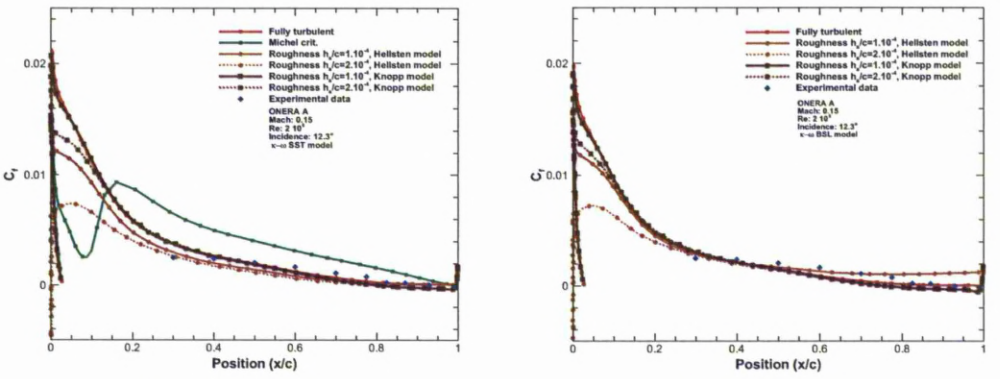

(a) SST $k-\omega$ model (b) BSL $k-\omega$ model

Figure 3.18: Skin friction coefficient over the ONERA A aerofoil 12.3 degrees angle of attack. Comparison between the computations with Hellsten and Knopp roughness models and experimental data. ($M = 0.15$, $Re = 2 \times 10^6$)

$Re = 5.25 \times 10^6$. For both Reynolds numbers, the Mach number was $M = 0.15$ and the flow was computed at incidence angles of 8, 13 and 17 degrees. The first angle of attack is far from stall, the second one is near stall and the last one is post stall. Table (3.3) summarises the parameters of computations.

Case	Mach Number	Reynolds Number	Angle (degrees)
1	0.15	2×10^6	3.1 , 5.2 , 7.2
			12.3 , 13.3 , 14.3
			15.3 , 16.3
2	0.15	3.13×10^6	8 - 13 - 17
3	0.15	5.22×10^6	8 - 13 -17

Table 3.3: Summary of the parameters for the computed ONERA A aerofoil test cases.

Lift and drag calculations

Lift and drag coefficients as function of the incidence angle are presented in figures (3.19) and (3.20). The figures show the comparison between the results of the HMB code using the empirical correlations transition models with estimates from the XFOIL code, and the experimental measurements from the F1 and F2 sets. The calculations for the XFOIL code were obtained considering both fully turbulent and laminar conditions with $N_{crit} = 2.6$ and $N_{crit} = 9$ respectively.

As can be seen from figure (3.19(a)), the results for the empirical correlations are in good agreement with the experimental data for incidence angles below 13 degrees. For angles of attack higher than 13 degrees both criteria result in overprediction of the produced lift. The latter is due to the presence of the transition points close to the leading

edge on the upper surface and therefore the flow is stalled like for the fully turbulent case. The lift coefficient calculated by the HMB code for both sets of empirical criteria show a tendency to follow the F1 experimental data. The results of the code for the fully turbulent conditions underpredicts both experimental data for low angles of attack. Moreover, for incidence angles greater than 12 degrees HMB approximates better the F1 experimental data showing similar lift peak. The XFOIL code for the fully turbulent conditions ($N_{crit} = 2.6$) follows the F1 experimental measurements showing of similar peak for the lift. On the other hand, for $N_{crit} = 9$, the XFOIL code agrees better with the experimental data. For the case where $Re = 3.13 \times 10^6$, the lift coefficient can be seen in figures 3.19(b)). The results show a similarity with the case of $Re = 2 \times 10^6$ where the empirical correlations of the Michel and Cebeci Smith overpredict the experimental data. Both models continue to overestimate the lift even for angles of attack higher than 15 degrees where the experiments show a reduction of lift. This reduction of the lift is captured from the fully turbulent conditions but it is not observed in the transition calculations. The XFOIL code, on the other hand, underestimates the produced lift. Even for the case where $Re = 5.25 \times 10^6$, transition calculations overpredicted the estimated lift as it can be seen in figure (3.19(c)).

Figure (3.20(a)) shows the comparison of the drag coefficients calculated by the HMB and XFOIL codes with the experimental data for the case of $Re = 2 \times 10^6$. Both codes fail to predict correctly the drag, although they follow a similar trend with the F1 experimental data. The HMB code overpredicts the drag coefficient for all the incidence angles using either fully turbulent conditions or one of the empirical correlations. Michel's criterion predicts similar values of drag coefficient with the Cebeci and Smith correlation, a behaviour that was also observed during the calculation of the lift coefficient. On the contrary, XFOIL underpredicts the experimental F1 data when fully turbulent conditions are considered. For higher turbulence intensity, the XFOIL code shows a somehow better agreement with the F1 experimental data but not with F2. Cases with $Re = 3.13 \times 10^6$ and $Re = 5.25 \times 10^6$ can be seen in figures (3.20(b)) and (3.20(c)) respectively. The predictions for the drag coefficients based on the transition models fail to agree with the experimental data for both Reynolds numbers. The HMB code overpredicts the drag for fully turbulent and transitional calculations. The XFOIL code for $N_{crit} = 9$ underpredicts the produced drag.

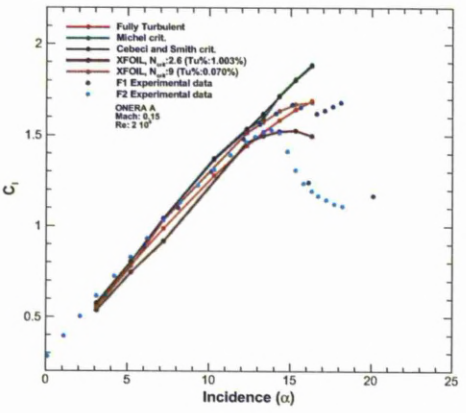

(a) ($M = 0.15, Re = 2 \times 10^6$)

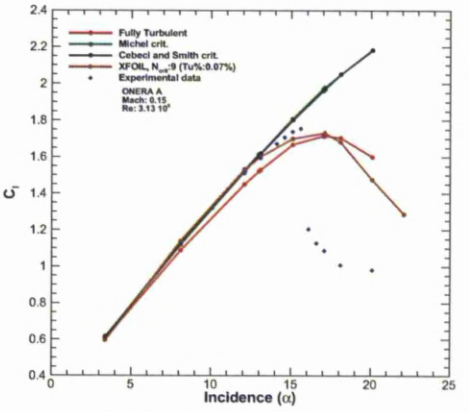

(b) ($M = 0.15, Re = 3.13 \times 10^6$)

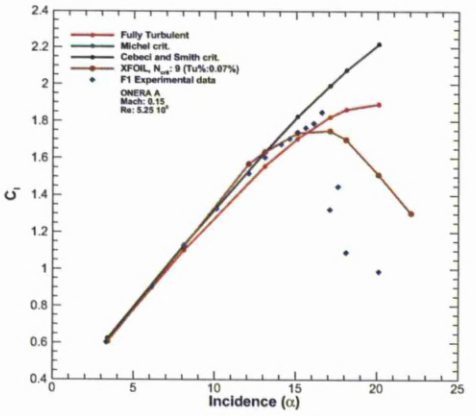

(c) ($M = 0.15, Re = 5.25 \times 10^6$)

Figure 3.19: Lift coefficient of the ONERA A aerofoil. Comparison between fully turbulent and empirical criteria (Michel and Cebeci-Smith) for the HMB code with XFOIL calculations and experimental data from the F1 and the F2 sets. The XFOIL calculations are for $N_{crit} = 2.6$ and $N_{crit} = 9$.

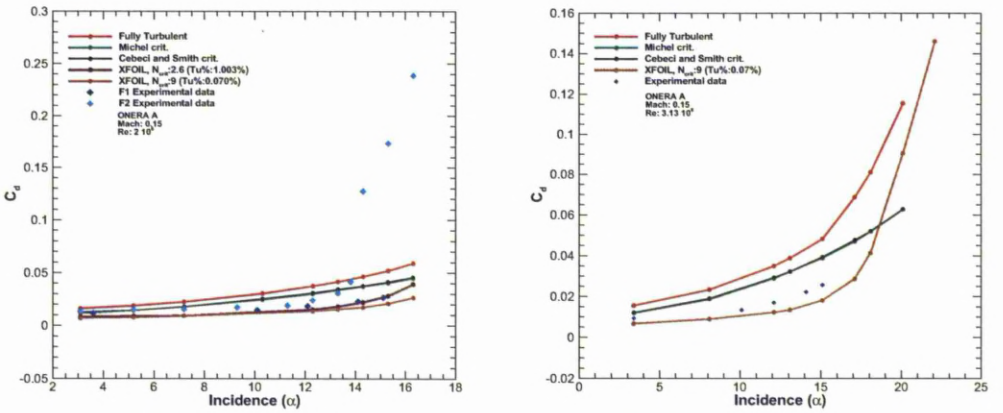

(a) ($M = 0.15, Re = 2 \times 10^6$) (b) ($M = 0.15, Re = 3.13 \times 10^6$)

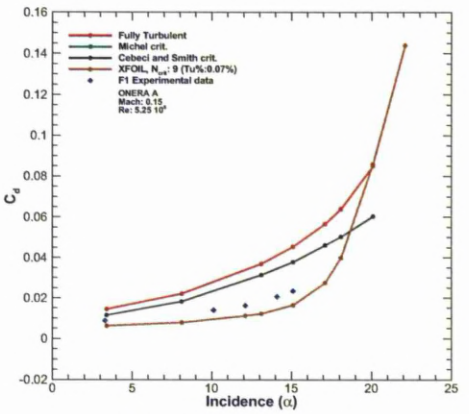

(c) ($M = 0.15, Re = 5.25 \times 10^6$)

Figure 3.20: Drag coefficient of the ONERA A aerofoil. Comparison between fully turbulent and empirical criteria (Michel and Cebeci-Smith) for the HMB code with XFOIL calculations and experimental data from the F1 and the F2 sets. The XFOIL calculations are for $N_{crit} = 2.6$ and $N_{crit} = 9$.

Transitional Flow Analysis

In order to estimate the onset of the transition from either the Michel's or the Cebeci and Smith's criteria, the point of the intersection between the momentum thickness Reynolds number and the Reynolds number calculated from the criteria must be computed. Figures (3.21(a)) - (3.21(d)) present the results for both empirical correlations and at the incidence angles of 7.2 and 13.3 degrees. As the angle of attack increases, the onset of the transitional flow moves towards the leading edge for the upper surface of the aerofoil. For the pressure side of the aerofoil, on the contrary, the onset of transition moves downwards to the trailing edge for increasing incidence angle. This means that the flow remains laminar for the majority of the pressure side.

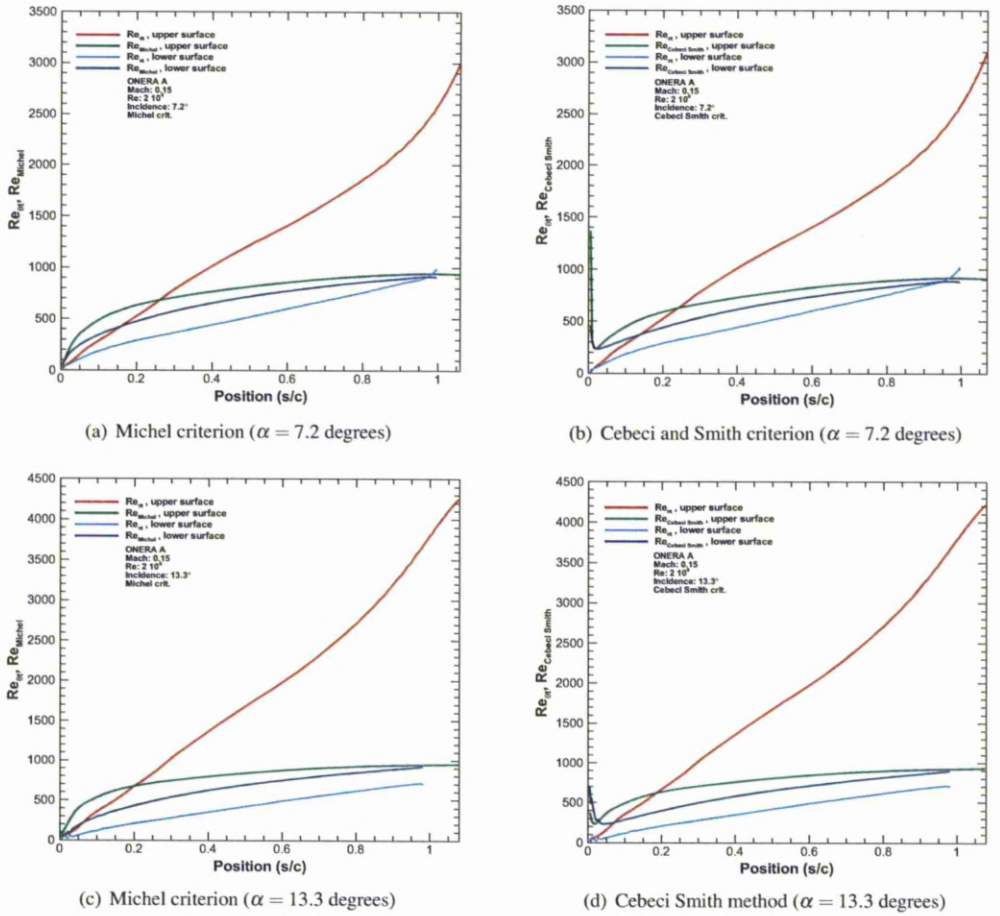

(a) Michel criterion ($\alpha = 7.2$ degrees)

(b) Cebeci and Smith criterion ($\alpha = 7.2$ degrees)

(c) Michel criterion ($\alpha = 13.3$ degrees)

(d) Cebeci Smith method ($\alpha = 13.3$ degrees)

Figure 3.21: Momentum thickness Reynolds number produced from Michel's criterion (Re_{Mich}), the Cebeci and Smith method ($Re_{Cebeci-Smith}$) and momentum thickness Reynolds number (Re_θ) around the curvilinear location downstream of the stagnation point on the upper and lower surfaces of the Onera A aerofoil. ($M = 0.15, Re = 2 \times 10^6$)

The information from the previous figures can be concentrated in figure (3.22) which presents the transition

location as a function of incidence. The computational results from the HMB code are compared with the results of XFOIL. The latter was run for two different values of the parameter N_{crit} ($N_{crit} = 2.6$, and $N_{crit} = 9$) that correspond to two different levels of turbulence intensity, from fully turbulent (1%) to laminar conditions (0.07%), respectively. The results show the typical trend observed in the previous figures with the momentum thickness Reynolds number from the different models. It is interesting that above 10 degrees the flow remains laminar for the majority of the lower surface. Also, if the two correlations are compared, the Cebeci and Smith criterion predicts the onset of transition closer to the leading edge for the upper surface than Michel's criterion. On the contrary, on the pressure side of the aerofoil, the transition point estimated with Michel's criterion is closer to the trailing edge. The XFOIL code at fully turbulent conditions predicts the onset of the transition for the whole range of incidence earlier than the other methods. Considering lower numbers of turbulence intensity, the results of the XFOIL code agree better with the outcome of the Cebeci and Smith method for the upper surface. For the lower surface and for angles of attack lower than 10 degrees, XFOIL estimates the onset of transition closer to trailing edge, and later transition than the calculations from the empirical correlations.

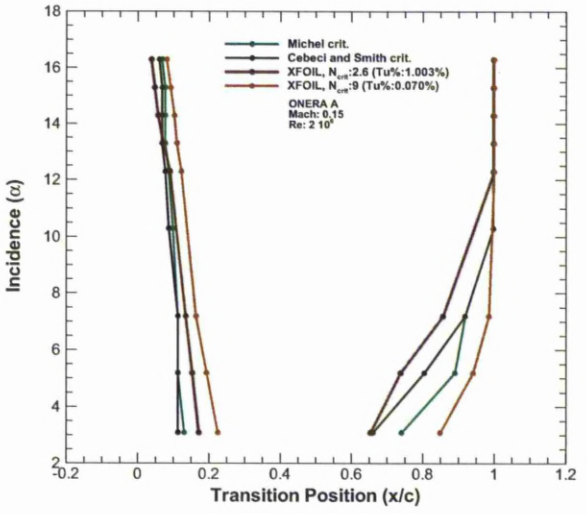

Figure 3.22: Transition point as a function of the angle of attack for the ONERA A aerofoil. Comparison between the HMB and XFOIL codes. The HMB results are computed using Michel's criterion and the Cebeci and Smith method. XFOIL calculations are for $N_{crit} = 2.6$ and $N_{crit} = 9$ ($M = 0.15$, $Re = 2 \times 10^6$).

Similar results can be observed in figures (3.23(a)) and (3.23(b)) where $Re = 3.13 \times 10^6$ and $Re = 5.25 \times 10^6$ are considered. At both conditions, the Cebeci and Smith criterion predicts slightly earlier transition in relation to Michel's correlation for the suction side of the aerofoil. For the lower surface, the start of transition based on the

Cebeci and Smith criterion occurs nearer to the trailing edge in comparison with Michel's criterion. The XFOIL, at all conditions predicted the onset of the transition on the upper surface earlier than the empirical correlations and closer to the trailing edge for the lower surface.

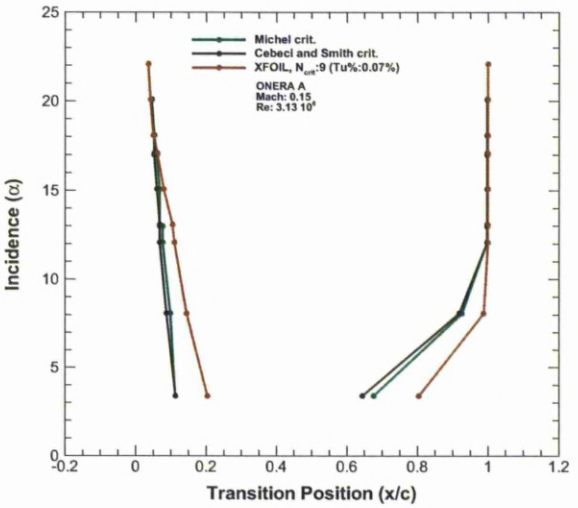

(a) ($M = 0.15, Re = 3.13 \times 10^6$)

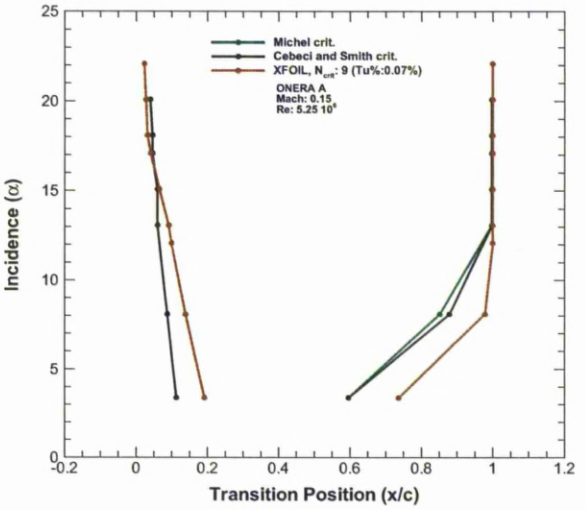

(b) ($M = 0.15, Re = 5.25 \times 10^6$)

Figure 3.23: Transition point as a function of incidence for the ONERA A aerofoil. XFOIL calculations are for $N_{crit} = 9$.

Surface Pressure and Skin Friction Distributions

The surface pressure coefficient on both sides of the aerofoil and a detailed view of the leading edge region are shown in figures (3.24(a)) to (3.24(b)). The results are for $M = 0.15$, and $Re = 2 \times 10^6$. For incidence angles lower than

7.2 degrees, the computed surface pressure distributions show good agreement with the experimental data, although, the suction peak in all calculation is slightly lower than the experimental value. Moreover, close to the trailing edge, the HMB code predicts better the surface pressure distribution in comparison to the XFOIL code which indicates flow separation. For incidence angles higher than 7.2 degrees more substantial differences are seen between the experimental and the computational results. For incidence angles higher than 13.3 degrees, the empirical correlations start to overpredict the surface pressure on the suction side of the aerofoil and fail to predict correctly the pressure close to the trailing edge due to flow separation. Post stall, HMB and XFOIL fail to predict the measured pressure distribution.

For Reynolds number at 3.13×10^6, the surface pressure distribution is shown in figures (3.25(a)) - (3.25(b)). The results are for incidence angles of 8.1 and 17.1 degrees. For angles of attack lower than the stall angle, all computations show good agreement with the experimental data. The calculations based on empirical criteria manage to compute the suction peak while the fully turbulent calculations underpredict it. The surface pressure distribution estimated with the empirical correlations is in better agreement with the experimental data. There is also an obvious surface pressure coefficient peak close to the leading edge which was also observed at lower Reynolds numbers. At 17.1 degrees, both empirical criteria failed to predict the measured surface pressure coefficient overshooting the experimental data.

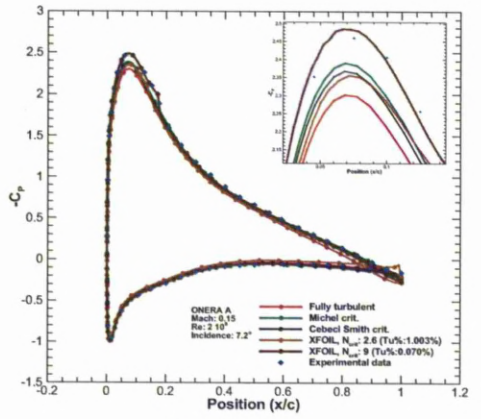

(a) α=7.2 degrees

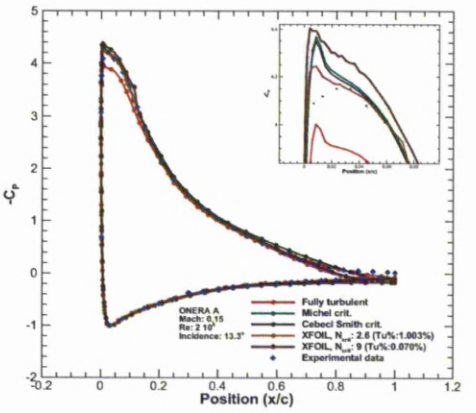

(b) α=13.3 degrees

Figure 3.24: Surface pressure coefficient for the ONERA A aerofoil. Comparison between the HMB and XFOIL codes with experimental data. The HMB results are derived considering fully turbulent conditions, Michel's criterion and Cebeci Smith method. For XFOIL, $N_{crit} = 2.6$ and 9 were considered. ($M = 0.15$, $Re = 2 \times 10^6$).

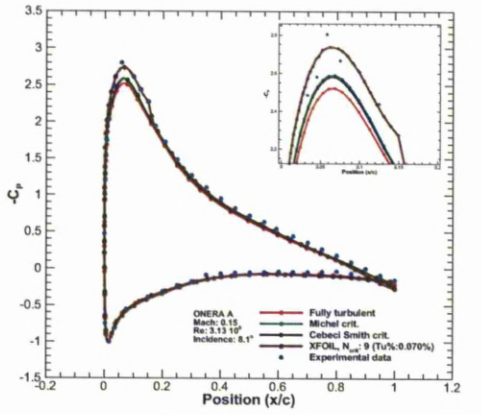

(a) α =8.1 degrees

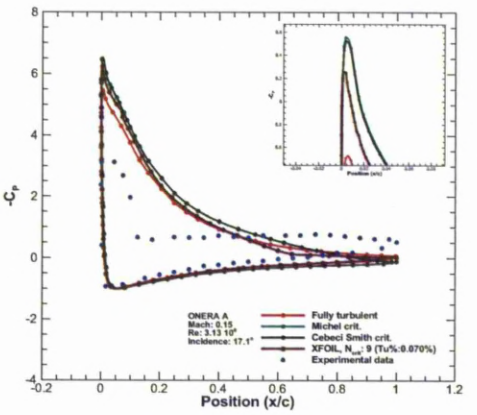

(b) α =17.1 degrees

Figure 3.25: Surface pressure coefficient for the ONERA A aerofoil. Comparison between the HMB and XFOIL codes with the experimental data. The HMB results are derived considering fully turbulent conditions, Michel's criterion and Cebeci and Smith method. For XFOIL, $N_{crit} = 9$ were used. ($M = 0.15$, $Re = 3.13 \times 10^6$).

Similar results are also presented for the case where a Reynolds number of $Re = 5.25 \times 10^6$ is considered and these can be seen on figures (3.26(a)) - (3.26(b)).

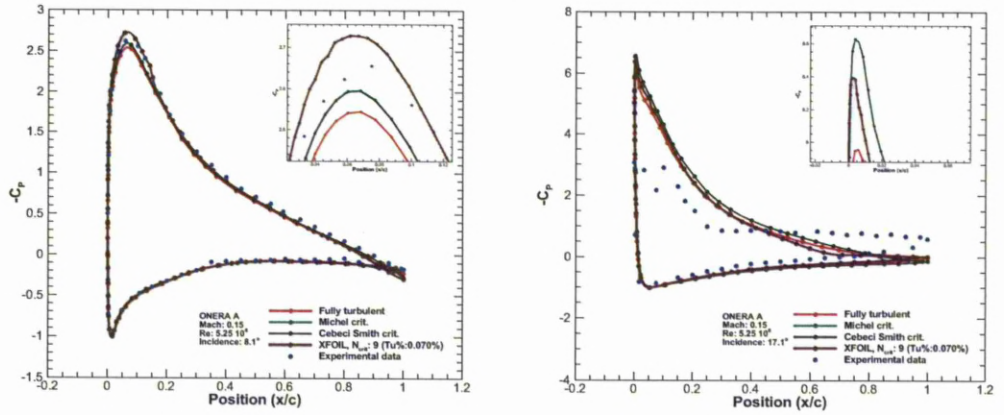

(a) α =8.1 degrees

(b) α =17.1 degrees

Figure 3.26: Surface pressure coefficient for the ONERA A aerofoil. Comparison between the HMB and XFOIL codes with the experimental data. The HMB results are derived considering fully turbulent conditions, Michel's criterion and Cebeci Smith method. For XFOIL, $N_{crit} = 9$ were used. ($M = 0.15$, $Re = 5.25 \times 10^6$).

The skin friction distribution on the suction side of the ONERA A aerofoil is shown in figures (3.27(a)) to (3.27(b)). For the case of Reynolds number at $Re = 2 \times 10^6$, three different incidence angles were considered: 7.2 and 13.3 degrees, respectively. The figures present the calculations for the fully turbulent conditions and the empirical correlations of Michel and Cebeci and Smith . The results from HMB are compared with the experimental data of the F2 test as well as with results from XFOIL. For the latter, two levels of turbulence intensity were used, $Tu\% = 0.07\%$ ($N_{crit} = 9$) and $Tu\% = 1.003\%$ ($N_{crit} = 2.6$). The skin friction distributions calculated with the empirical criteria show good agreement with the experimental data close to the trailing edge. There are no experimental data close to the leading edge of the aerofoil where the onset of transition occurs. The Cebeci and Smith method has the tendency to predict earlier the lower value of skin friction in comparison to Michel's criterion. This can explain the earlier prediction of onset that is observed with the Cebeci and Smith model. The e^N method shows similar results with the empirical correlations overpredicting the experimental data. Negatives C_f values indicate a laminar separation bubble for the case where $N_{crit} = 9$. This is not observed with the HMB code.

The skin friction distribution calculated for Reynolds number $Re = 3.13 \times 10^6$ is presented in figures (3.28(a)) -(3.28(b)). As can be seen, the fully turbulent calculation underestimates the skin friction on the suction side. Michel's criterion and the Cebeci and Smith method, which have similar values, are in good agreement with the experimental data. The results from XFOIL show improvement in comparison to the results for $Re = 2 \times 10^6$. XFOIL captures well the experimental point at 20% of the chord while the results from the empirical correlations show a milder change of the skin friction. At 17 degrees of incidence angle, none of the codes manage to accurately predict the skin friction

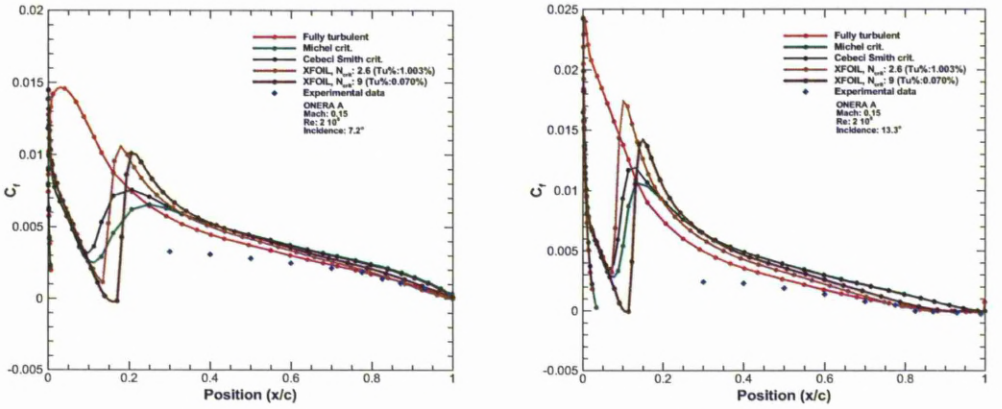

(a) α=7.2 degrees (b) α=13.3 degrees

Figure 3.27: Skin friction distribution over the ONERA A aerofoil. Comparison between the HMB and XFOIL codes and experimental data. The HMB results are derived considering fully turbulent conditions, Michel's criterion and the Cebeci and Smith method. For XFOIL, $N_{crit} = 2.6$ and 9 were considered. ($M = 0.15$, $Re = 2 \times 10^6$)

distribution.

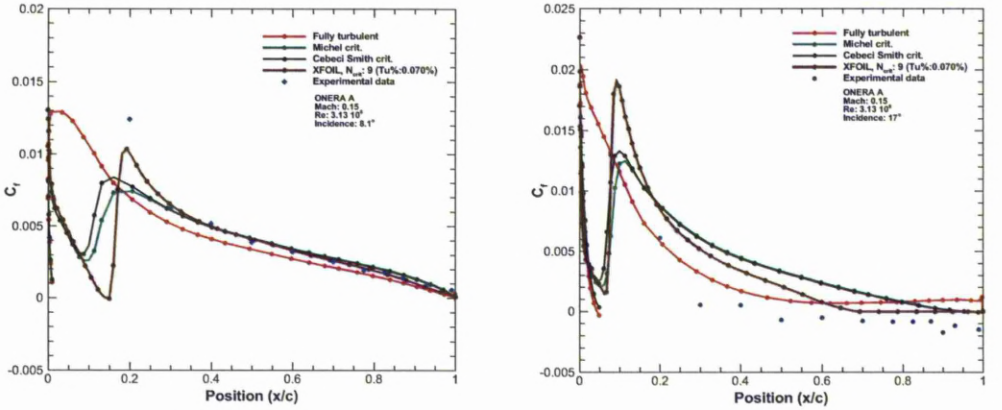

(a) α =8.1 degrees (b) α =17.1 degrees

Figure 3.28: Skin friction coefficient over the ONERA A aerofoil.Comparison between the HMB and XFOIL codes and experimental data. The HMB results are derived considering fully turbulent conditions, Michel's criterion and Cebeci Smith method. For XFOIL, a $N_{crit} = 9$ were considered. ($M = 0.15$, $Re = 3.13 \times 10^6$)

For the case of $Re = 5.25 \times 10^6$, the empirical models agree with the experimental data for almost 50% of the aerofoil chord as can seen in figures (3.29(a)) - (3.29(b)). For the case of 17 degrees, both models overpredict the skin friction coefficient. For the case where fully turbulent flow is considered, HMB underpredicts the experimental data for all angles of attack. On the other hand, XFOIL has better agreement with the experiments for all the cases. One exception is the region close to the trailing edge for 17 degrees where XFOIL fails to predict accurately the skin friction.

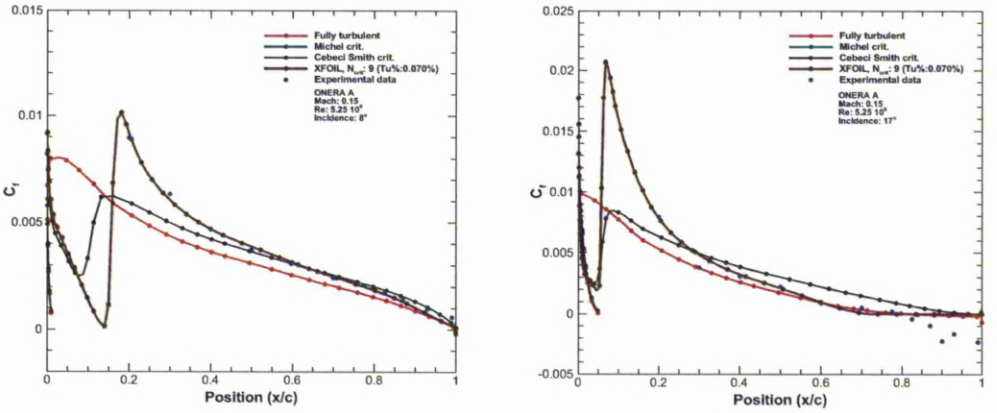

(a) α =8.1 degrees (b) α =17.1 degrees

Figure 3.29: Skin friction coefficient over the ONERA A aerofoil. Comparison between the HMB and XFOIL code and experimental data. The HMB results are derived considering fully turbulent conditions, Michel's criterion and Cebeci Smith method. For XFOIL, a $N_{crit} = 9$ were considered. ($M = 0.15$, $Re = 5.25 \times 10^6$)

3.2.3 $\kappa - \omega - \gamma - Re_{\theta t}$ Model over the ONERA A Aerofoil

The computations with the $\kappa - \omega - \gamma - Re_{\theta t}$ model over the ONERA A-aerofoil were performed for Reynolds number and Mach numbers at $Re = 2 \times 10^6$ and $M = 0.15$ respectively. The calculations with the $\kappa - \omega - \gamma - Re_{\theta t}$ model required almost double the cpu time to reach 10^{-5} at the convergence history in comparison to the fully turbulent solution.

Lift and Drag Calculations

Lift and drag coefficients as function of the incidence angle are presented in figures (3.30(a)) and (3.30(b)). The figures show the comparison between the results of the HMB code using the empirical correlations and the $\kappa - \omega - \gamma - Re_{\theta t}$ model with estimates from the XFOIL code, and the experimental measurements from the F1 and F2 sets. The calculations with XFOIL were obtained considering both fully turbulent and laminar conditions with $N_{crit} = 2.6$ and $N_{crit} = 9$ respectively. As can be seen, the results with the $\kappa - \omega - \gamma - Re_{\theta t}$ model follow the same trend with the lift and drag coefficient calculated by the HMB code with the use of the empirical correlations. The LCTM model predicts higher values of lift from the fully turbulent for incidence angle higher than 10degrees. On the other hand, the $\kappa - \omega - \gamma - Re_{\theta t}$ model produce the same amount of drag with the empirical correlation models which is lower than the fully turbulent calculations. For both, lift and drag, all models fails to follow the experimental data.

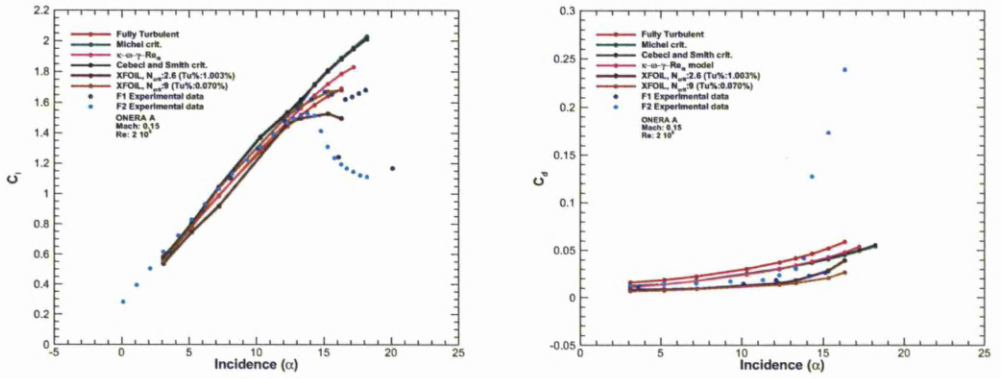

(a) C_l (b) C_d

Figure 3.30: Lift and drag coefficients as function of incidence of the ONERA A aerofoil. Comparison between fully turbulent, empirical criteria (Michel and Cebeci-Smith), $\kappa-\omega-\gamma-Re_{\theta t}$ transition model for the HMB code with XFOIL calculations and experimental data from the F1 and the F2 sets. The XFOIL calculations are for $N_{crit}=2.6$ and $N_{crit}=9.$ ($M=0.15, Re=2\times10^6$)

Transitional Flow Analysis

The onset of transition for a range of incidence angles is presented at figure (3.31). Three different methods were used, with Michel's criterion, Cebeci Smith method and $\kappa-\omega-\gamma-Re_{\theta t}$ transition model. The calculations with XFOIL code were conducted with two different levels of turbulent intensity, one at fully turbulent ($Tu(\%)=1, N_{crit}=2.6$) and one at laminar ($Tu(\%)=0.07, N_{crit}=9$). The $\kappa-\omega-\gamma-Re_{\theta t}$ transitional model follows the trend observed during the calculations with the empirical correlation models. The results for the suction side obtained by XFOIL include all transition model predictions in their envelope.

Surface Pressure and Skin Friction Distributions

The surface pressure coefficient on both sides of the aerofoil and a detailed view of the leading edge region are shown in figures (3.32(a)) to (3.32(c)). The results are for $M=0.15$, and $Re=2\times10^6$. For all incidence angles, the computed surface pressure distributions calculated with the $\kappa-\omega-\gamma-Re_{\theta t}$ transition model show good agreement with the experimental data following the same trend observed with the calculation of the empirical correlations. Although, the suction peak in all calculation for the $\kappa-\omega-\gamma-Re_{\theta t}$ transition model is lower than the experimental value, closer to the values calculated during a fully turbulent flow. As can be seen from the embedded picture, the results of XFOIL failed to estimate the experimental data, with transitional results ($N_{crit}=9$) to be close to the experiments for incidence

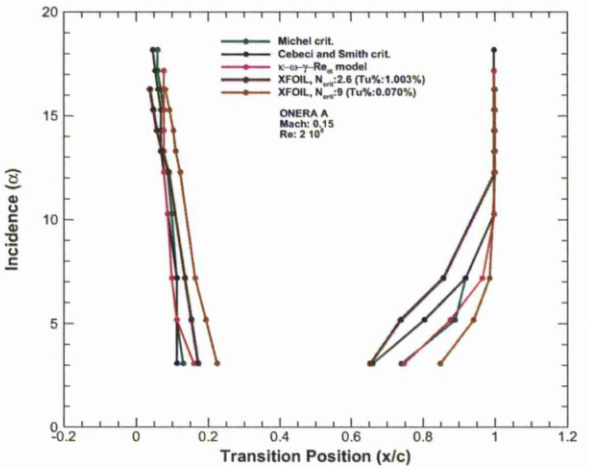

Figure 3.31: Transition point as a function of incidence for the ONERA A aerofoil. Comparison between the HMB and XFOIL codes. The HMB results are computed using Michel's criterion, Cebeci Smith method and $\kappa-\omega-\gamma-Re_{\theta t}$ model. XFOIL calculations are for $N_{crit} = 2.6$ and $N_{crit} = 9$ ($M = 0.15$, $Re = 2 \times 10^6$).

angle of 7.2 degree but when the angle of attack was increased the fully turbulent results ($N_{crit} = 2.6$) to be closer.

The skin friction distribution on the suction side of the ONERA A aerofoil is shown in figures (3.33(a)) to (3.33(c)). Three different incidence angles were considered, at 7.2, 12.3 and 13.3 degrees, respectively. As experimental data exists only close to the trailing edge of the aerofoil, the $\kappa-\omega-\gamma-Re_{\theta t}$ model agrees better with the them than with the results with the empirical correlation models or the XFOIL code which predict higher values. Explaining the results at figure (8.2), the $\kappa-\omega-\gamma-Re_{\theta t}$ transition model predicts the onset of transition earlier than the empirical correlations and XFOIL code. Also for the skin friction coefficient is easy to see that the length of transition is shorter that the one predicted with the empirical correlation models. The XFOIL results are further away from the experiments in this case.

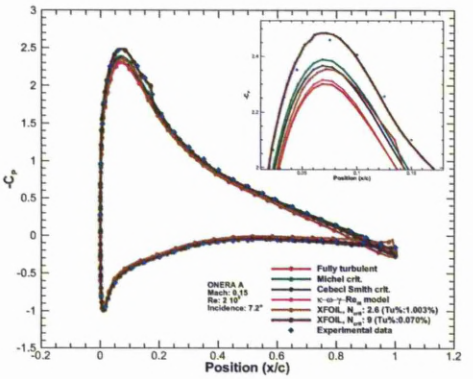

(a) α=7.2 degree

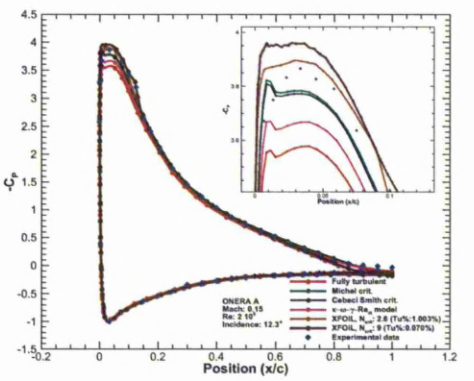

(b) α=12.3 degrees

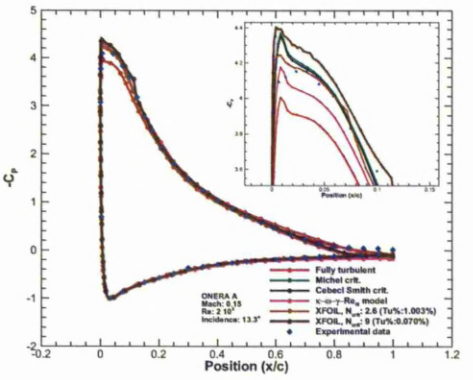

(c) α=13.3 degrees

Figure 3.32: Surface pressure distribution for the ONERA A aerofoil. Comparison between the HMB and XFOIL codes with the experimental data. The HMB results are derived considering fully turbulent conditions, Michel's criterion, Cebeci Smith method and $\kappa-\omega-\gamma-Re_{\theta t}$ transition model. For XFOIL, $N_{crit}=2.6$ and 9 were considered. $(M=0.15, Re=2\times10^6)$

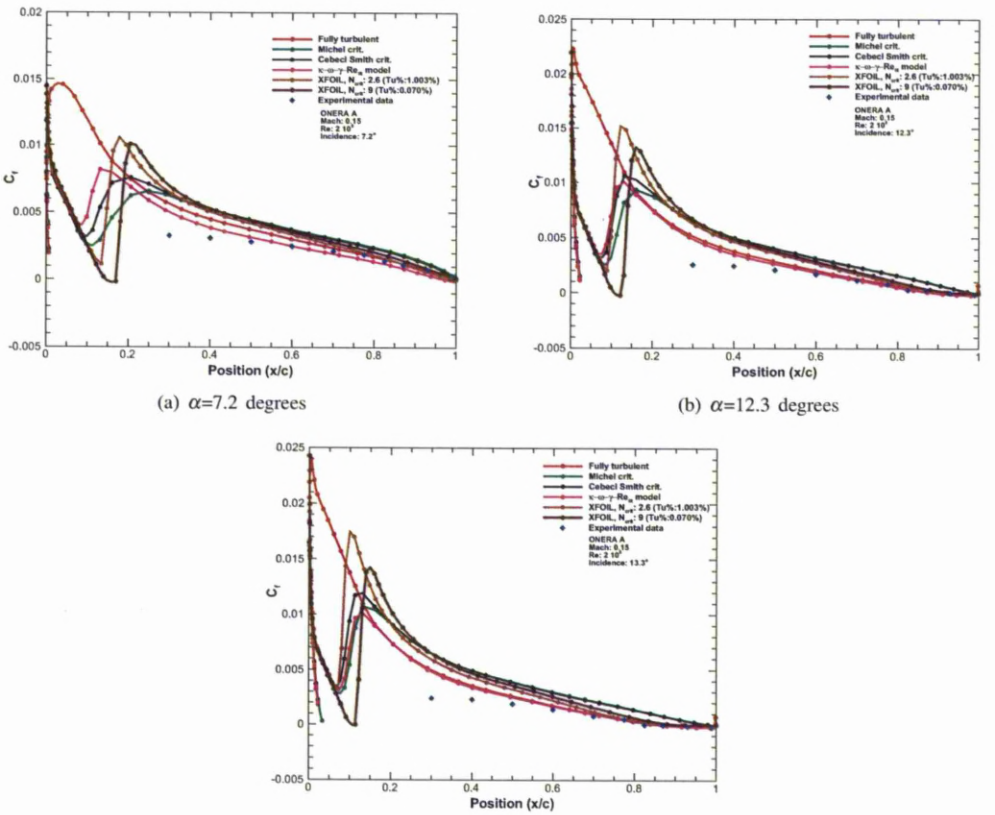

(a) α=7.2 degrees

(b) α=12.3 degrees

(c) α=13.3 degrees

Figure 3.33: Skin friction distribution for the ONERA A aerofoil. Comparison between the HMB and XFOIL codes with the experimental data. The HMB results are derived considering fully turbulent conditions, Michel's criterion, Cebeci Smith method and $\kappa-\omega-\gamma-Re_{\theta t}$ transition model. For XFOIL, $N_{crit} = 2.6$ and 9 were considered. ($M = 0.15, Re = 2\times10^6$)

3.3 NLF-0416 Aerofoil

The NLF-0416 belongs to the natural-laminar-flow aerofoil family. These aerofoils were designed and constructed from NASA for general aviation applications. The initial emphasis of this type aerofoil was to achieve higher lift coefficients and lower drag coefficient from existing aerofoils[84]. The aerofoil was tested in the Langley Low-Turbulence Pressure tunnel for a range of angles of attack, from -4 degrees to 20 degrees. The wind tunnel model of the NLF-0416 had a cord of 609mm and a span of 914.4mm. A view of the aerofoil can be seen in figure (3.34) while the points for the construction of the aerofoil are presented in table (3.4).

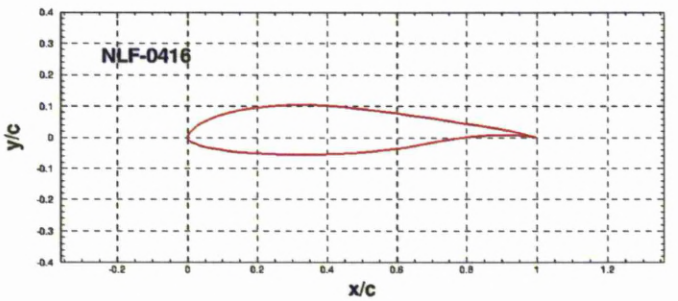

Figure 3.34: NLF-0416 aerofoil.

Upper Surface				Upper Surface			
x/c	y/c	x/c	y/c	x/c	y/c	x/c	y/c
0.00049	0.00403	0.49172	0.09166	0.00073	-0.00439	0.57122	-0.04063
0.00509	0.01446	0.54204	0.08515	0.00709	-0.01154	0.62019	-0.03250
0.01393	0.02573	0.59256	0.07801	0.01956	-0.01883	0.67014	-0.02231
0.02687	0.03729	0.64262	0.07047	0.03708	-0.02594	0.72107	-0.01221
0.04383	0.04870	0.69155	0.06272	0.05933	-0.03254	0.77156	-0.00364
0.06471	0.05964	0.73872	0.05493	0.08609	-0.03847	0.82012	0.00278
0.08936	0.06984	0.78350	0.04724	0.11708	-0.04361	0.86536	0.00667
0.11761	0.07904	0.82530	0.03977	0.15200	-0.04787	0.90576	0.00792
0.14975	0.08707	0.86357	0.03265	0.19050	-0.05121	0.93978	0.00696
0.18404	0.09374	0.80779	0.02594	0.23218	-0.05357	0.96638	0.00478
0.22169	0.09892	0.92749	0.01974	0.27659	-0.05494	0.98520	0.00242
0.26187	0.10247	0.95224	0.01400	0.32326	-0.05529	0.99633	0.00065
0.30422	0.10425	0.97197	0.00862	0.37167	-0.05462	1.00000	0.00000
0.34839	0.10405	0.98686	0.00398	0.42127	-0.05291		
0.39438	0.10162	0.99656	0.00098	0.47150	-0.05009		
0.44227	0.09729	1.00000	0.00000	0.52175	-0.04614		

Table 3.4: Somers' NLF-0416 aerofoil coordinates[84].

3.3.1 CFD Mesh - NLF-0416 aerofoil

For the calculations around the NLF-0416 aerofoil a mesh of C-topology was used. For the grid, 108 nodes were distributed on the upper surface of the aerofoil with an equal number of nodes on the lower. The wake was covered with 70 nodes while 40 nodes are distributed in the normal direction. The edges normal to the aerofoil were meshed with exponential node distributions, with first cell distance of 10^{-5} chords. The edges leaving the aerofoil's trailing edge had an exponential node distributions with the first node distance of 10^{-4} chords. In total, the grid has 46,320 nodes and is shown in figures (3.35(a)) and (3.35(b)).

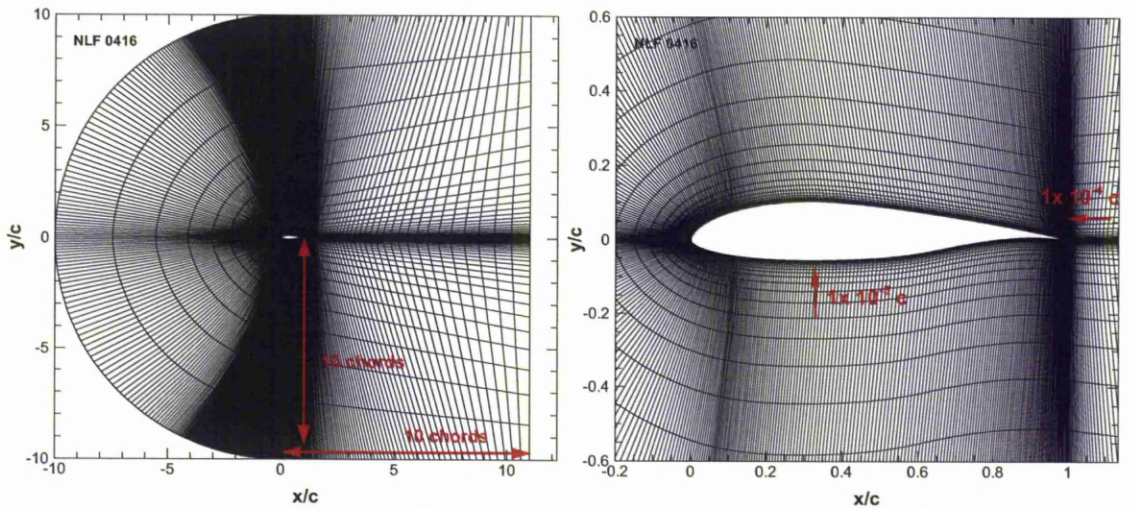

(a) Full view of the 2D mesh around NLF 0416 aerofoil

(b) Detailed view of the mesh around NLF 0416 aerofoil

Figure 3.35: 2D mesh around NLF 0416 aerofoil.

3.4 Transitional Flow over the NLF-0416 Aerofoil

For this test case, the Reynolds and the free-stream Mach numbers were $Re = 4 \times 10^6$ and $M = 0.1$. To simulate the experimental data the free-stream turbulence intensity was also set to $Tu(\%) = 0.1$. For the XFOIL code, a value of $N_{crit} = 8.15$ was considered. The calculations were carried out for a range of incidence angles.

3.4.1 Empirical Transition Models over the NLF-0416 Aerofoil

For this case, beside the criteria of Michel and Cebeci Smith, an alteration of the Michel criterion is used during the computations. As it was presented in the paper of Heister [13], the empirical correlation equation is given as:

$$Re_{Michel\,v2} = 1.174 * Re_x^{0.46} \tag{3.1}$$

As can be seen from figure (3.36), this variant of Michel criterion produces lower values of momentum thickness Reynolds number for the same displacement thickness Reynolds number.

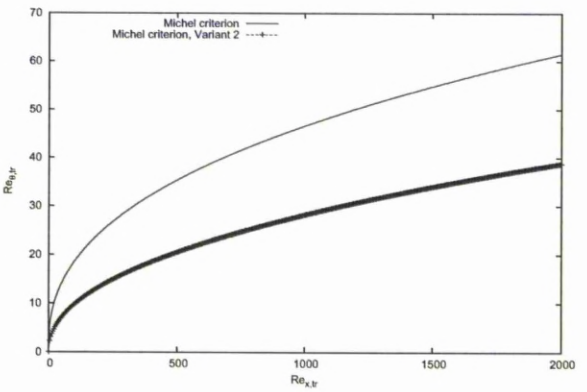

Figure 3.36: Comparison of momentum and displacement thickness Reynolds number for Michel criterion and Michel criterion variant 2.

Lift and drag calculations

Lift and drag coefficients as a function of incidence angle are presented in figures (3.37(a)) and (3.37(b)). In both cases, similar behaviour to the ONERA A and NACA 0012 aerofoils is observed. The transition models predict higher levels of lift than the fully turbulent calculations and significant lower values of drag. There is no difference between the two variants of the Michel criterion. Though, the slope of the drag coefficient calculated with XFOIL code is smaller than the fully turbulent or transitional calculations, when the reduction of total drag at 10 degrees angle of attack is approximately 10% from the other models.

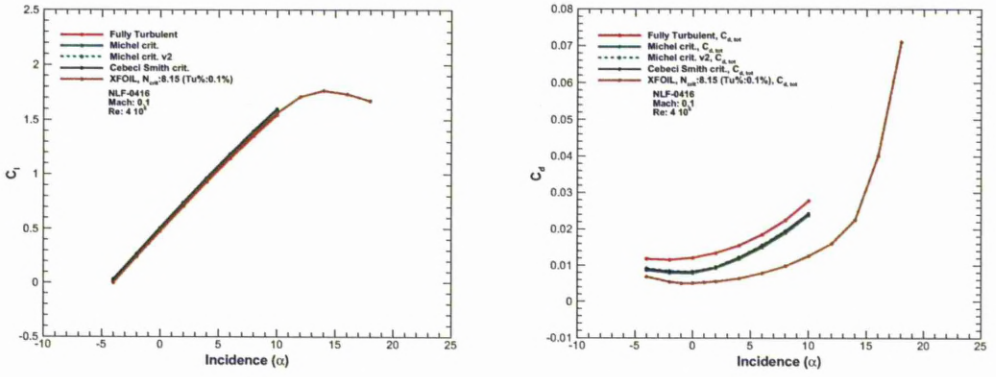

(a) C_l (b) C_d

Figure 3.37: Lift and drag coefficients as function of incidence. Results from HMB for the flow around the NLF-0416 aerofoil. The calculations are with Michel and Cebeci and Smith criteria. (M=0.1, Re=4 $\times$ 10^6, $Tu = 0.1\%$).

Transitional Flow Analysis

The following figures present the momentum thickness Reynolds number using Michel's criterion and the Cebeci Smith method for the incidence angles of 4 degrees. The cross points between the Reynolds number of each model with the momentum thickness Reynolds number defines the transition location. By increasing the angle of attack, the cross point and by definition the onset of transition in moves towards the leading edge of the aerofoil.

The onset of the transitional flow can be seen in figure (3.39). For all calculations, 25 transitional iterations with 4000 implicit and explicit steps were selected. Michel's criterion agrees well the experimental data for both surfaces of the aerofoil. The Cebeci and Smith criterion shows to underpredict the transition point for the upper surface of the aerofoil. The variant of the Michel's criterion, as it was seen from figure (3.36), estimates less momentum thickness Reynolds for the same values of displacement thickness Reynolds number which has as a result to predict an early onset of transition. On the other hand, e^N method, with the use of $N_{crit} = 8.15$ overpredicts the experimental data. It is interesting that for the lower surface at 0 degrees, XFOIL code estimates the onset of transition 15% downstream of the experimental value.

Surface pressure and Skin Friction Distribution

In this section, pressure (figures (3.40(a))- (3.40(b))) and skin friction (figures (3.41(a)) - (3.41(b))) distributions from fully turbulent and transitional calculations are presented and compared with the data from XFOIL. Results from calculations employing both Michel and Cebeci and Shaw criteria are provided. Both transition models calculated

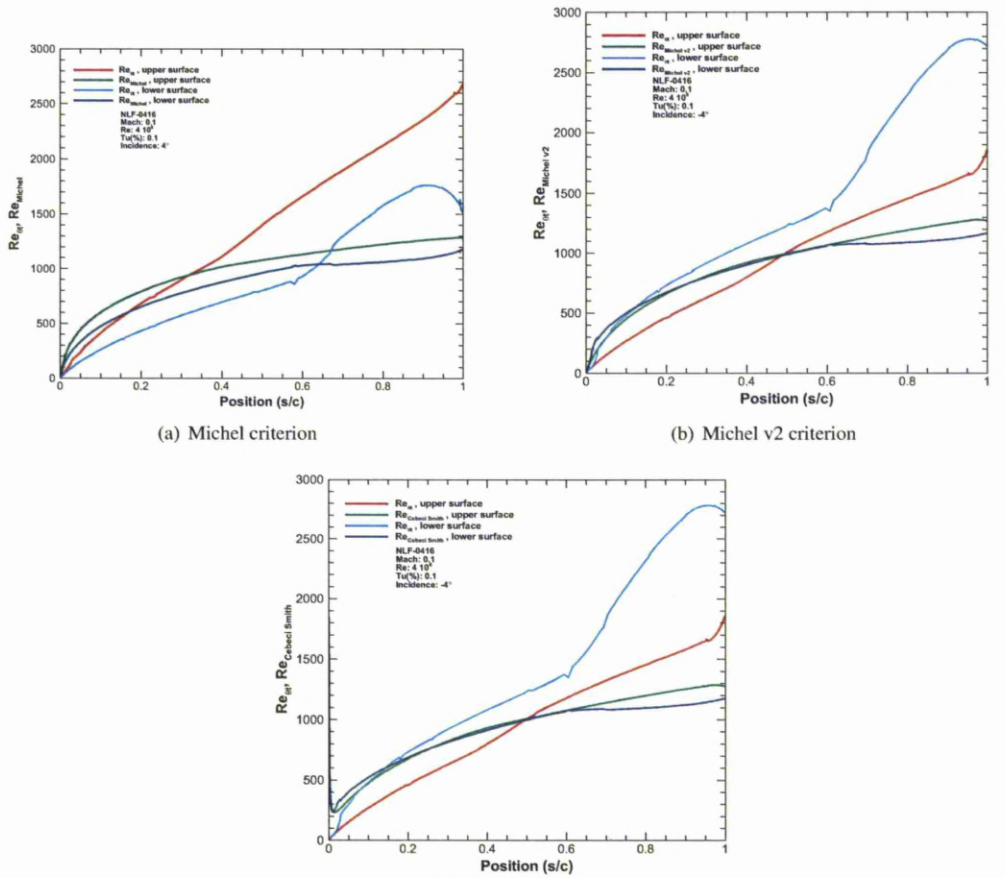

(a) Michel criterion

(b) Michel v2 criterion

(c) Cebeci Smith criterion

Figure 3.38: Momentum thickness Reynolds number produced with Michel's criterion (Re_{Mich}), the Cebeci and Smith method ($Re_{Cebeci-Smith}$) and momentum thickness Reynolds number (Re_θ) in comparison with the curvilinear location on the upper and lower surfaces of the NLF-0416 aerofoil at 4 degrees. ($M = 0.1$, $Re = 4 \times 10^6$)

increased values of C_P and higher pressure peak than the fully turbulent calculations.

When the skin friction coefficient was compared, the transition models estimated a slight increased transitional region in comparison with the XFOIL code. This was also indicated by the steep slope of C_f curve for XFOIL code. The onset of transition was calculated more downstream from the location where the Cebeci and Smith had estimated. As it was expected, see figure (3.36), the variant of Michel criterion estimated an early onset in comparison with the initial version of the model. The result from the skin friction distribution can explain figure (3.42) which show the turbulent Reynolds number distribution over the NLF-0416 aerofoil for incidence angle of 10 degrees. As it can be seen, the fully turbulent calculations considered that the flow becomes turbulent almost from the leading edge for the upper surface. The estimation of the location where $R_T = 1$ from the transition models agrees well the results for

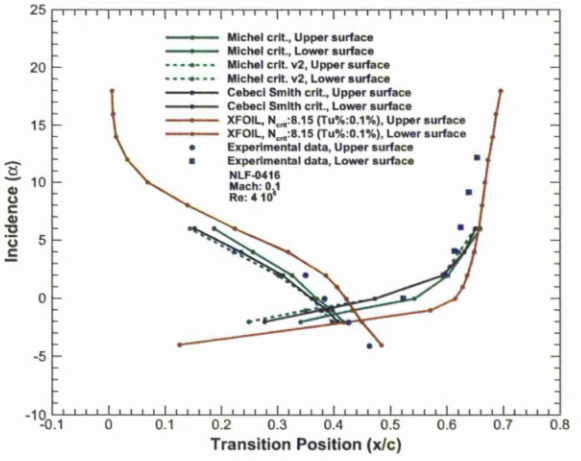

Figure 3.39: Transition point as a function of incidence for the NLF-0416 aerofoil. Experimental data in comparison to the calculations with Michel, Cebeci Smith criteria and XFOIL code. ($M = 0.1$, $Re = 4 \times 10^6$)

the calculation of skin friction distribution, with Michel's criterion variant to estimated it earlier from all the other transition models.

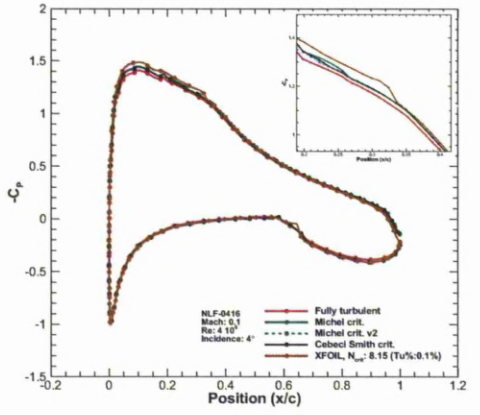

(a) α=4 degrees

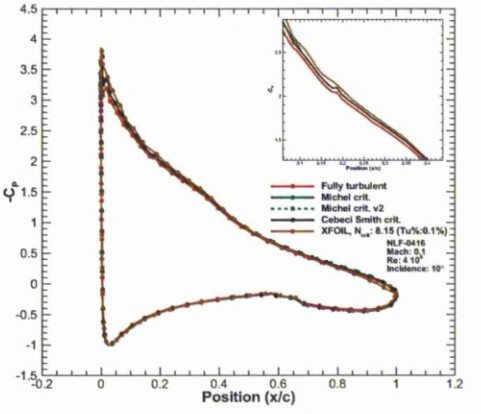

(b) α=10 degrees

Figure 3.40: Comparison of the surface pressure distribution of NLF-0416 aerofoil for HMB (fully turbulent, Michel's correlation, new Michel's criterion and Cebeci and Smith model) and XFOIL.($M = 0.1$, $Re = 4 \times 10^6$)

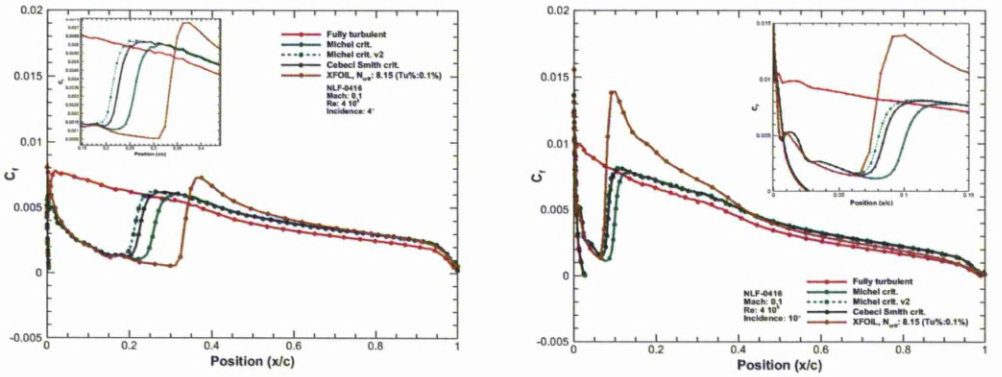

(a) α=4 degrees (b) α=10 degrees

Figure 3.41: Skin friction distribution of the NLF-0416 aerofoil. Comparison between the HMB and XFOIL codes. The HMB results for fully turbulent, the Michel's equation, the new Michel's criterion and the Cebeci and Smith model($M = 0.1, Re = 4 \times 10^6$).

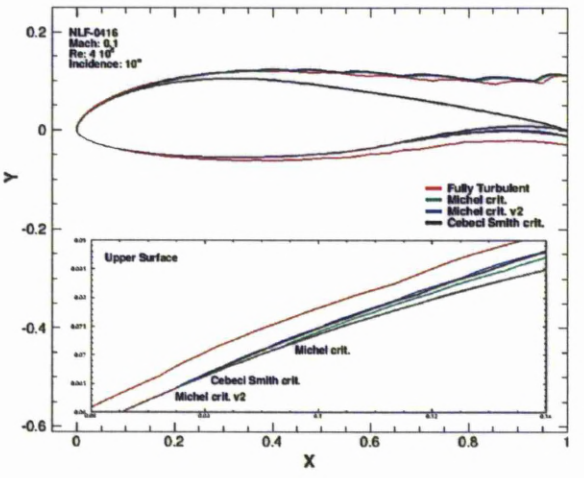

Figure 3.42: Turbulent Reynolds number distribution over the NLF-0416 aerofoil.($M = 0.1, Re = 4 \times 10^6, \alpha = 10^o$)

3.5 S809 Aerofoil

The S809 aerofoil belongs to the NREL thick-aerofoil family. It is 21% chord thick and was designed by Somers[85] in 1986 using the Eppler code. It was initially tested at the low-turbulence wind tunnel of the Delft University of Technology. The model that was constructed had a chord of 600mm and a span of 1248mm[85]. The S809 coordinates given in from Somers' report are listed in table 3.5. The S809 section is frequently used for validation of CFD methods and has been discussed in various papers[78][86].

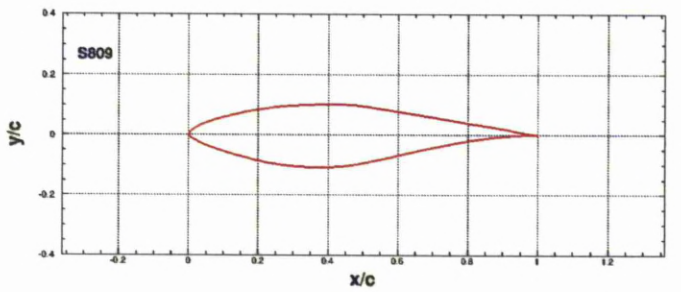

Figure 3.43: S809 aerofoil.

Upper Surface				Upper Surface			
x/c	y/c	x/c	y/c	x/c	y/c	x/c	y/c
1.000000	0.000000	0.428461	0.101760	0.000000	-0.000020	0.353370	-0.108181
0.996203	0.000487	0.382612	0.101840	0.000213	-0.001794	0.395329	-0.108011
0.985190	0.002373	0.337260	0.100070	0.001045	-0.003477	0.438273	-0.104552
0.967844	0.005960	0.292970	0.096703	0.001208	-0.003724	0.527928	-0.086571
0.945073	0.011024	0.250247	0.091908	0.002398	-0.005266	0.576211	-0.073979
0.917488	0.017033	0.209576	0.085851	0.009313	-0.011499	0.626092	-0.060644
0.885293	0.023458	0.171409	0.078687	0.023230	-0.020399	0.676744	-0.047441
0.848455	0.030280	0.136174	0.070580	0.042320	-0.030269	0.727211	-0.035100
0.807470	0.037766	0.104263	0.061697	0.065877	-0.040821	0.776432	-0.024204
0.763042	0.045974	0.076035	0.052224	0.093426	-0.051923	0.776432	-0.024204
0.715952	0.054872	0.051823	0.042352	0.124111	-0.063082	0.823285	-0.015163
0.667064	0.064353	0.031910	0.032299	0.157653	-0.073730	0.866630	-0.008204
0.617331	0.074214	0.016590	0.022290	0.193738	-0.083567	0.905365	-0.003363
0.567830	0.084095	0.006026	0.012615	0.231914	-0.092442	0.938474	-0.000487
0.519832	0.093268	0.000658	0.003723	0.271438	-0.099905	0.965086	0.000743
0.474243	0.099392	0.000204	0.001942	0.311968	-0.105281	0.996141	0.000290

Table 3.5: Somers' S809 aerofoil coordinates[85].

3.5.1 CFD Mesh - S809 aerofoil

The grid used for this aerofoil followed the same technique as the one for the previous aerofoils, with 272 nodes were equally distributed between the upper and lower surface of the aerofoil. This is close to the maximum value XFOIL can handle. 120 nodes are distributed in the normal direction and another 71 nodes in the wake. The edges normal to the aerofoil approached with an exponential distribution and first cell distance of 10^{-5} chords and the edges leaving the aerofoil trailing edge had a exponential distribution with the first node distance of 5×10^{-4} of a chord. In total, the grid has 99,360 nodes and is shown in figures (3.44(a)) and (3.44(b)).

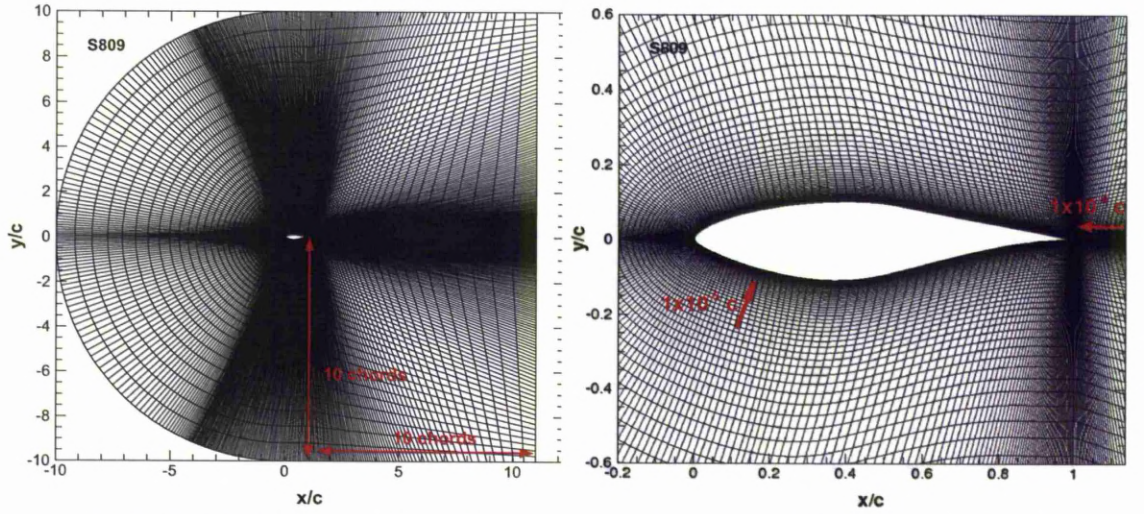

(a) Full view of the 2D mesh around S809 aerofoil

(b) Detailed view of the mesh around S809 aerofoil

Figure 3.44: 2D mesh around S809 aerofoil.

3.6 Transitional Flow over the S809 Aerofoil

For the S809 aerofoil, the Mach and Reynolds numbers were $M = 0.1$ and $Re = 2 \times 10^6$. These conditions are similar to the conditions used by Somers [85]. The calculations were carried for a range of incidence angle. Initially, the effect of roughness on the aerofoil was studied and then the calculations using the empirical correlations were followed. This aerofoil was used also for the validation of the $\kappa - \omega - \gamma - Re_{\theta t}$ model.

3.6.1 Modelling Roughness effects over the S809 aerofoil

In order to analyse the effects of roughness on the S809 aerofoil, the rough wall boundary conditions were considered on the 10% of the aerofoil chord from the leading edge while smooth wall boundary conditions were applied everywhere else. The values of equivalent sand-grain roughness used are $h_S/c = 1 \times 10^{-4}$ and 2×10^{-4} as suggested by the test cases of Knopp et al [62].

Lift and drag calculations

The lift coefficient around the aerofoil using SST $k-\omega$ and baseline $k-\omega$ can be seen in figures (3.45(a))) and (3.45(b)). Each figure presents the comparison between Hellsten and Knopp roughness models with the existed experimental data and the predictions of XFOIL code. Both roughness models failed to follow the experimental data. They showed a linear behaviour of low values of lift for incidence angles until 8 degrees. For an angle of attack higher than 8 degrees, the roughness models present an increased lift production in comparison to the experimental data. Only the Hellsten and Laine model implemented with the baseline $k-\omega$ turbulence model had a tendency to follow the latter one. The comparison with the experimental data can also be seen for the production of drag in figures (3.46(a)) and (3.46(b))). The roughness models do not agree well with the experimental data and the reason for this behaviour is hidden in the increased values that are observed in the pressure drag as can seen in figures (3.47(a)) and (3.47(b)).

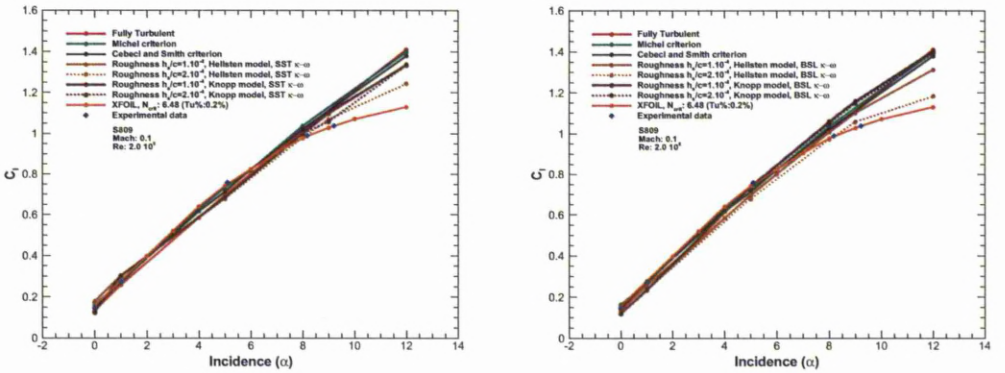

(a) SST $k-\omega$ model (b) BSL $k-\omega$ model

Figure 3.45: Lift coefficient of the S809 aerofoil. Comparison between Hellsten and Knopp roughness models and the experimental data. Computations have been conducted with SST and BSL $k-\omega$ turbulence model.(M=0.1, Re=2×10^6, $Tu(\%) = 0.2$)

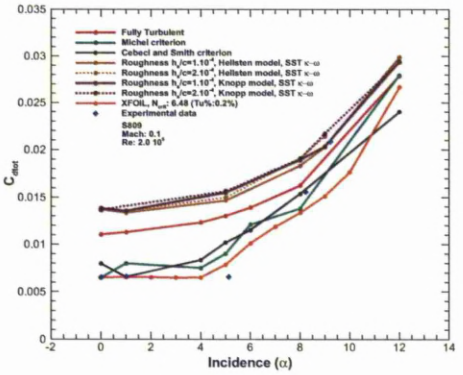

(a) SST $k-\omega$ model

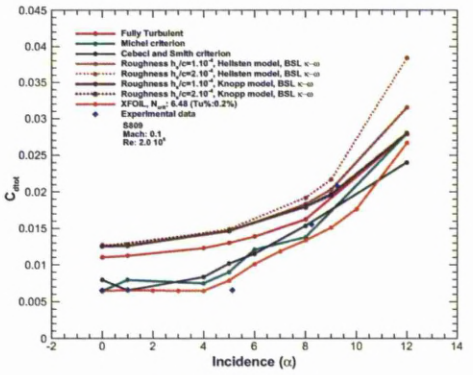

(b) BSL $k-\omega$ model

Figure 3.46: Drag coefficient of the S809 aerofoil. Comparison between Hellsten and Knopp roughness models and the experimental data. Computations have been conducted with SST and BSL $k-\omega$ turbulence model.(M=0.1, Re=2×10^6, $Tu(\%)=0.2$)

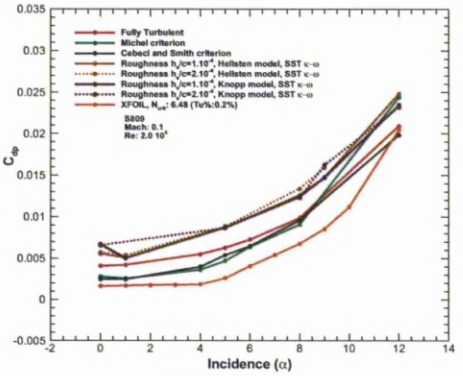

(a) SST $k-\omega$ model

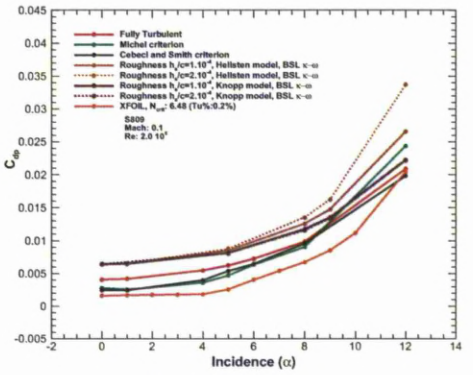

(b) BSL $k-\omega$ model

Figure 3.47: Pressure drag coefficient of the S809 aerofoil. Comparison between Hellsten and Knopp roughness models and the experimental data. Computations have been conducted with SST and BSL $k-\omega$ turbulence model.(M=0.1, Re=2×10^6, $Tu(\%)=0.2$)

Surface Pressure and Skin Friction Distributions

The computations showed in all cases increased surface pressure coefficient and high pressure peak, especially for high angle of attacks. The surface pressure coefficient for the S809 aerofoil for a range of incidence angles can be seen in figures (3.48(a)) to (3.50(b)). The rapid fluctuations on C_P distributions that are observed at the zoomed plots are due to applied roughness at 10% of the surfaces of the aerofoil.

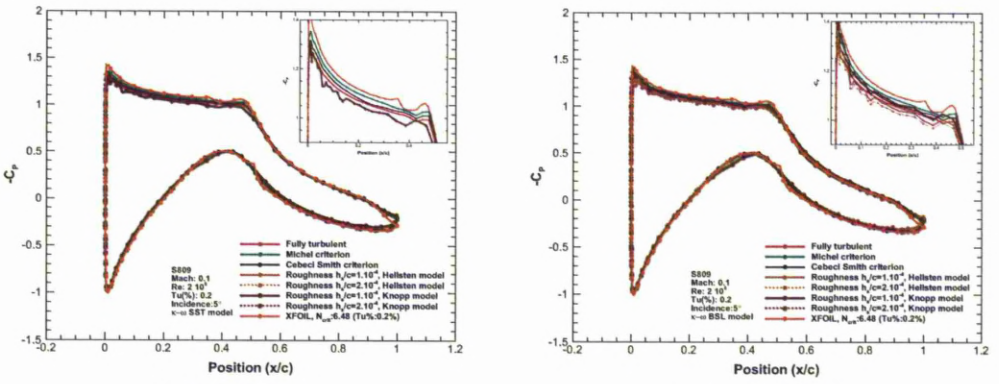

(a) SST $k-\omega$ model (b) BSL $k-\omega$ model

Figure 3.48: Surface pressure coefficient for the S809 aerofoil at 5 degrees. Comparison between the Hellsten and Knopp roughness models with the experimental data and the empirical correlation models. Two sand-grain roughness are used at $h_S/c = 1\times10^{-4}$ and 2×10^{-4}. (M=0.1, Re=2×10^6, $Tu(\%) = 0.2$).

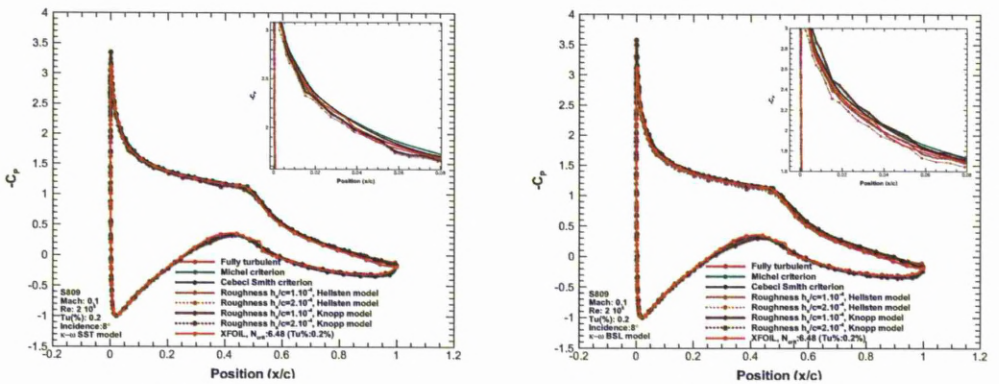

(a) SST $k-\omega$ model (b) BSL $k-\omega$ model

Figure 3.49: Surface pressure coefficient for the S809 aerofoil at 8 degrees. Comparison between the Hellsten and Knopp roughness models with the experimental data and the empirical correlation models. Two sand-grain roughness are used at $h_S/c = 1\times10^{-4}$ and 2×10^{-4}. (M=0.1, Re=2×10^6, $Tu(\%) = 0.2$).

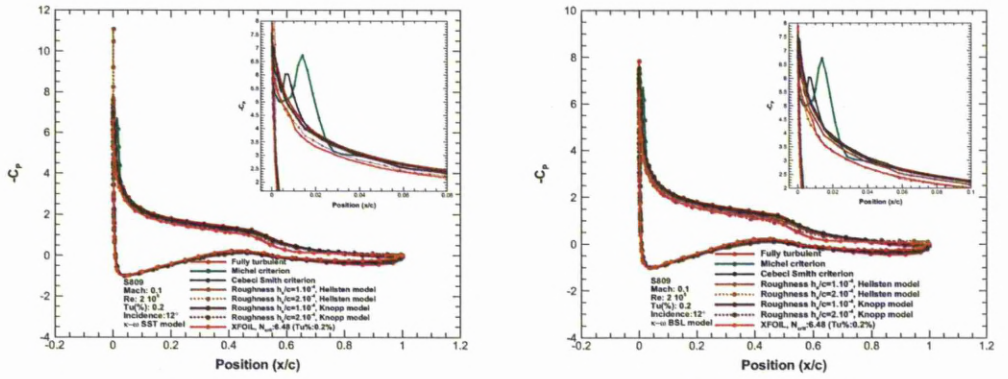

(a) SST $k-\omega$ model (b) BSL $k-\omega$ model

Figure 3.50: Surface pressure coefficient for the S809 aerofoil at 12 degrees. Comparison between the Hellsten and Knopp roughness models with the experimental data and the empirical correlation models. Two sand-grain roughness are used at $h_S/c = 1\times10^{-4}$ and 2×10^{-4}.(M=0.1, Re=2×10^6, $Tu(\%) = 0.2$).

The skin friction distribution around the S809 aerofoil can be seen in figures (3.51(a)) to (3.53(b)) for a range of incidence angles. The sudden change in shear (x/c $\approx$ 0.1) corresponds to the end of the rough region towards the smooth portion of the aerofoil. The roughness models fail to predict the laminar separation bubble that the empirical models predicts for incidence angles higher of 10 degrees.

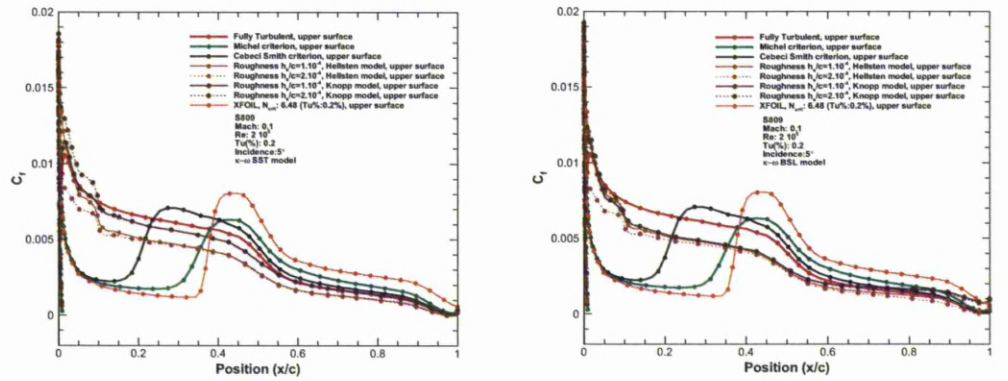

(a) SST $k-\omega$ model (b) BSL $k-\omega$ model

Figure 3.51: Skin friction coefficient for the S809 aerofoil at 5 degrees. Comparison between the Hellsten and Knopp roughness models with the experimental data and the empirical correlation models. Two sand-grain roughness are used at $h_S/c = 1\times10^{-4}$ and 2×10^{-4}.(M=0.1, Re=2×10^6, $Tu(\%) = 0.2$).

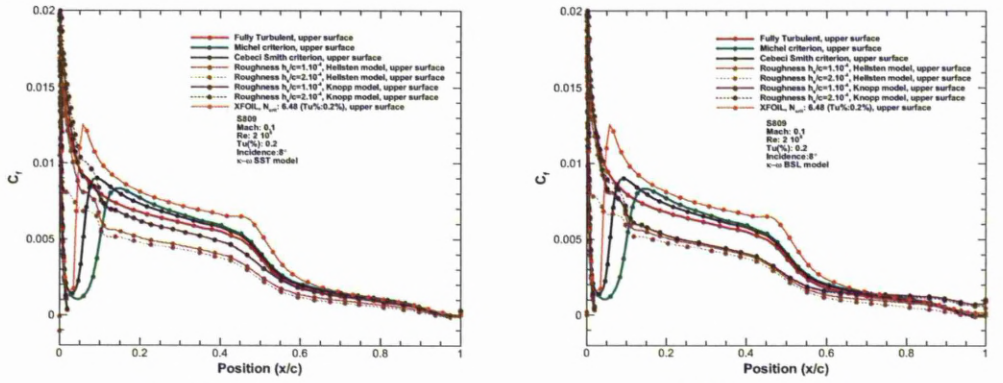

(a) SST $k-\omega$ model (b) BSL $k-\omega$ model

Figure 3.52: Skin friction coefficient for the S809 aerofoil at 8 degrees. Comparison between the Hellsten and Knopp roughness models with the experimental data and the empirical correlation models. Two sand-grain roughness are used at $h_S/c = 1\times10^{-4}$ and 2×10^{-4}.(M=0.1, Re=2×10^6, $Tu(\%) = 0.2$).

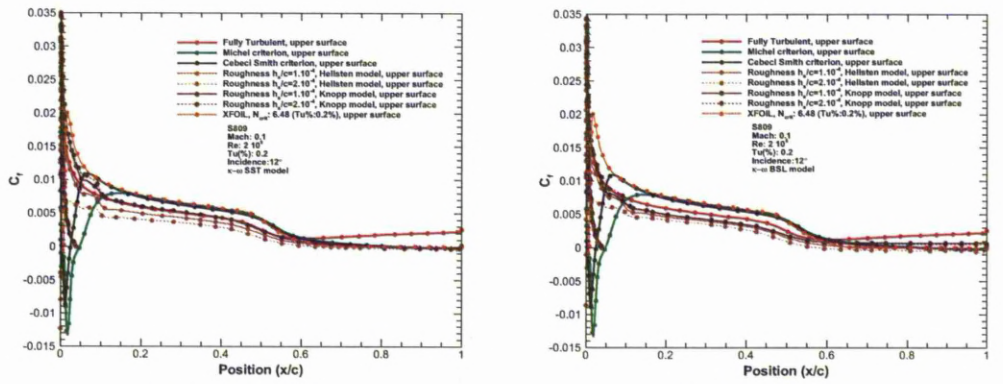

(a) SST $k-\omega$ model (b) BSL $k-\omega$ model

Figure 3.53: Skin friction coefficient for the S809 aerofoil at 12 degrees. Comparison between the Hellsten and Knopp roughness models with the experimental data and the empirical correlation models. Two sand-grain roughness are used at $h_S/c = 1\times10^{-4}$ and 2×10^{-4}.(M=0.1, Re=2×10^6, $Tu(\%) = 0.2$).

3.6.2 Empirical Transition Models for the S809 Aerofoil

In the following section the S809 aerofoil is used to validate the empirical correlation transition against the existed experimental data and the results from the XFOIL code. The aerofoil was tested at the same conditions as used by Somers [85]. The free-stream turbulence intensity was set to $Tu(\%) = 0.2$ and the calculations were carried out for a range of incidence angle from 0 to 14 degrees.

Lift and Drag Calculations

Following the trend observed on the previous aerofoils, transition models agree with the experimental data for incidence angles below 8 degrees. As the angle of attack increases the models tend to overpredict the produced lift, as fully turbulent calculations fail to predict the lift coefficient. Below 8 degrees, the fully turbulent calculations underpredict the values while for angles of attack higher than the 10 degrees produce more lift than the other methods. The XFOIL agrees well with the experimental data for the whole range of incidence angles. This information can be derived from figure (3.54(a)). On the contrary, when the estimation of drag is concerned, the majority of methods fail to agree with the experimental data. The observed discrepancy at the angle of attack of 14 degrees is due to the development of a laminar separation bubble.

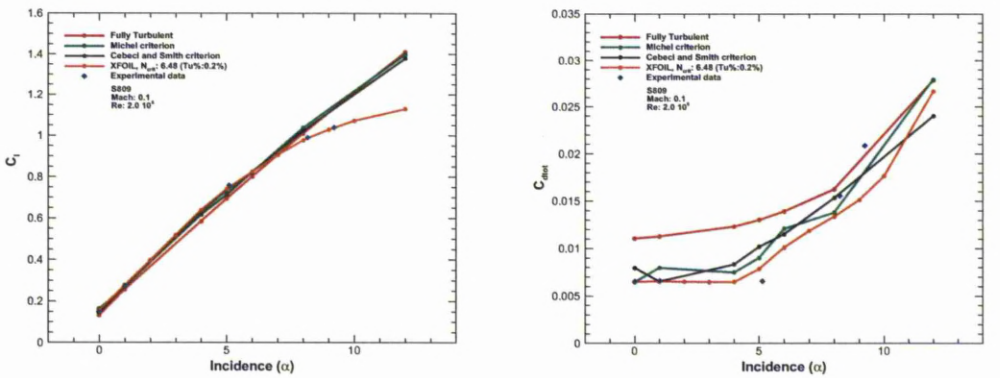

(a) C_l (b) C_d

Figure 3.54: Lift and drag coefficients as function of incidence. Experimental data and results from HMB for the flow around the S809 aerofoil. The calculations are with Michel and Cebeci and Smith criteria (M=0.1, Re=2×10^6, $Tu(\%) = 0.2$).

Transitional Flow Analysis

The transition location can be defined from the location where the momentum thickness Reynolds number of each model crosses the momentum thickness Reynolds number. These can be seen in figures (3.55(a)) to (3.55(d)) for a range of angles of attack.

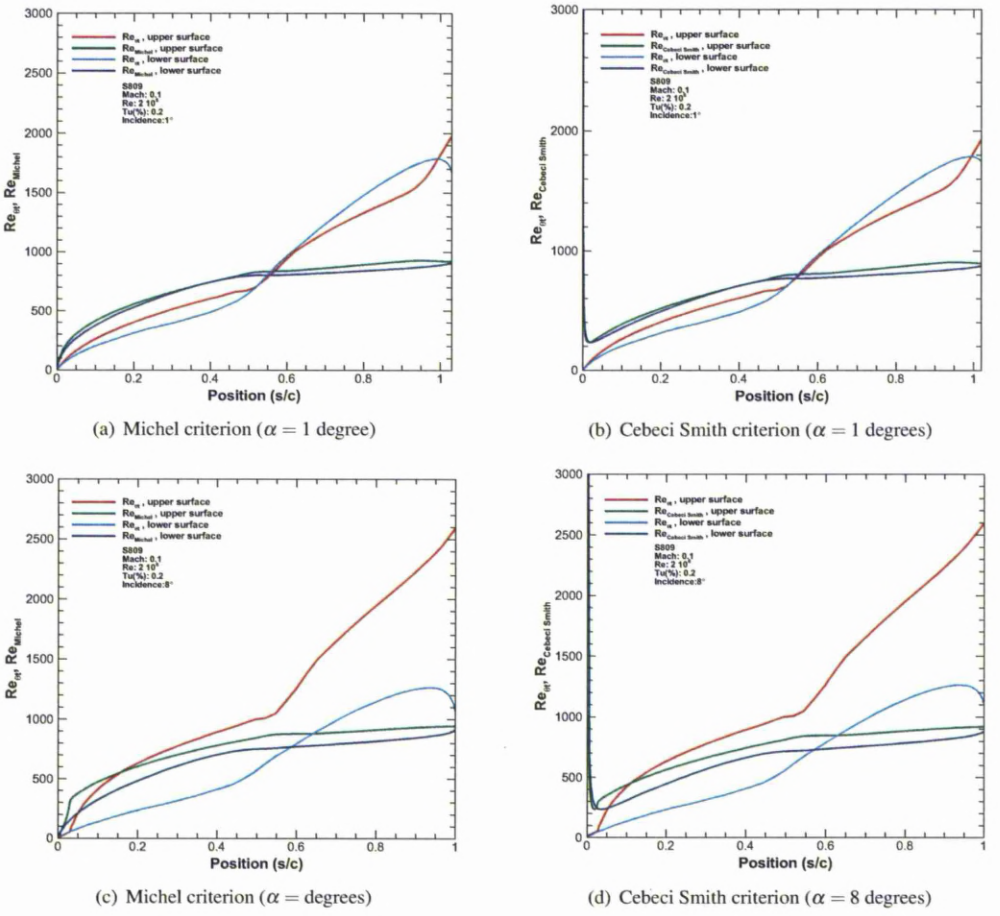

(a) Michel criterion ($\alpha = 1$ degree)

(b) Cebeci Smith criterion ($\alpha = 1$ degrees)

(c) Michel criterion ($\alpha =$ degrees)

(d) Cebeci Smith criterion ($\alpha = 8$ degrees)

Figure 3.55: Momentum thickness Reynolds number produced from Michel's criterion (Re_{Mich}), the Cebeci and Smith criterion ($Re_{Cebeci-Smith}$) and momentum thickness Reynolds number (Re_θ) in comparison with the curvilinear location of the upper and lower surfaces of the S809 aerofoil (M=0.1, Re=2×10^6, $Tu(\%) = 0.2$).

The onset of transition flow can be seen in figure (3.55) The transition models fail to predict correctly the transition location for low incidence angles. As the angle of attack increases, Michel's criterion predicts fairly well the experimental data. This occurs on incidence higher of α =5 degrees. The Cebeci and Smith model overpredicts the onset of transition for the full range of incidence angles for the upper surface of the aerofoil. On the other hand, for the pressure side both models predicts later the transition location and closer to the trailing edge. For free-stream turbulence intensity of $Tu(\%) = 0.2$, XFOIL predicts well the experimental data on both surfaces. These predictions, though, show the sensitivity of the e^N method on the aerofoil geometry where, when NFL-0416 aerofoil was used, see figure (3.39), the onset of transition from XFOIL code was predicted further downstream from the experiments.

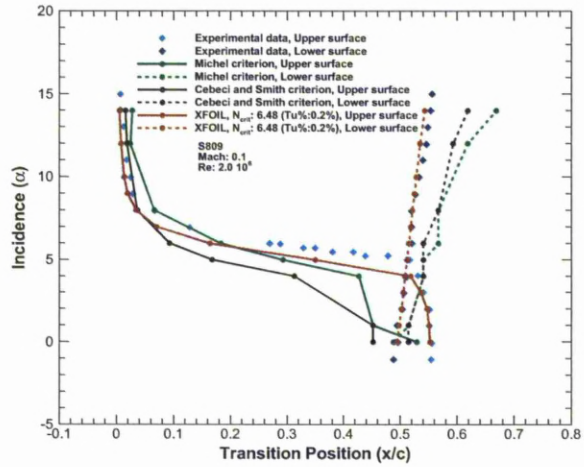

Figure 3.56: Transition point as a function of incidence for the S809 aerofoil. Experimental data in comparison to the calculations with Michel, Cebeci and Smith criteria and XFOIL code. (M=0.1, Re=2×10^6, $Tu(\%) = 0.2$)

Surface Pressure and Skin Friction Distributions

The surface pressure distribution over the S809 aerofoil for a range of incidence angle can be seen in figures (3.57(a)) to 3.57(b)). Transition models present higher pressure peak than the fully turbulent calculations or the XFOIL results. This trend changes for incidence angle of 14degrees where the fully turbulent calculations show higher pressure peak. Characteristic is the change of the pressure coefficient for the empirical correlation models at the onset of transition.

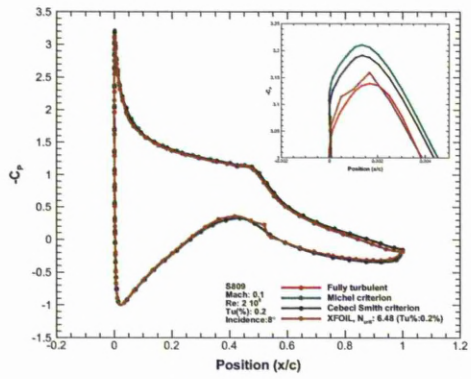

(a) α=8 degrees

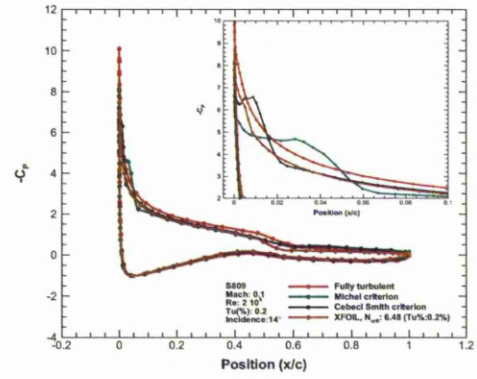

(b) α=14 degrees

Figure 3.57: Surface pressure distribution for the S809 aerofoil. Comparison between the HMB and XFOIL codes. The HMB results are derived considering fully turbulent conditions, the Michel's criterion and the Cebeci and Smith's method. For XFOIL code, $N_{crit} = 6.48$ was considered (M=0.1, Re=2×10^6, $Tu(\%) = 0.2$).

The skin friction distribution around the S809 aerofoil can be seen in figures (3.58(a)) to (3.58(d)) for a range of incidences. As can be seen, XFOIL code predicts separation at 50% of the upper surface of the aerofoil. At 1

degrees, the estimated bubble with the XFOIL code is at 5% of the surface and as the angle of attack increases the length of the bubble decreases. At 4 degrees, the separation has half the length that it had at 1 degree. For higher incidences the separation disappears. On the other hand, the transitional models fail to predict the a separation at low incidence. At incidence angles higher than 10 degrees, a laminar separation bubble is created near the leading edge. At 14 degrees, both Michel and Cebeci and Smith models predict a laminar separation bubble as it can be seen in figure (3.58(a)). This bubble is close to the leading edge of the aerofoil and has a length of 6% based on Michel and 3% based on Cebeci and Smith criterion. A general view of the bubble can be seen in figures (3.59(a)) and (3.59(b)). At such high angle of attack the flow has also separated creating recirculation of the flow. The fully turbulent calculations do not account for the formation of the laminar separation bubble at any of the angle of attack.

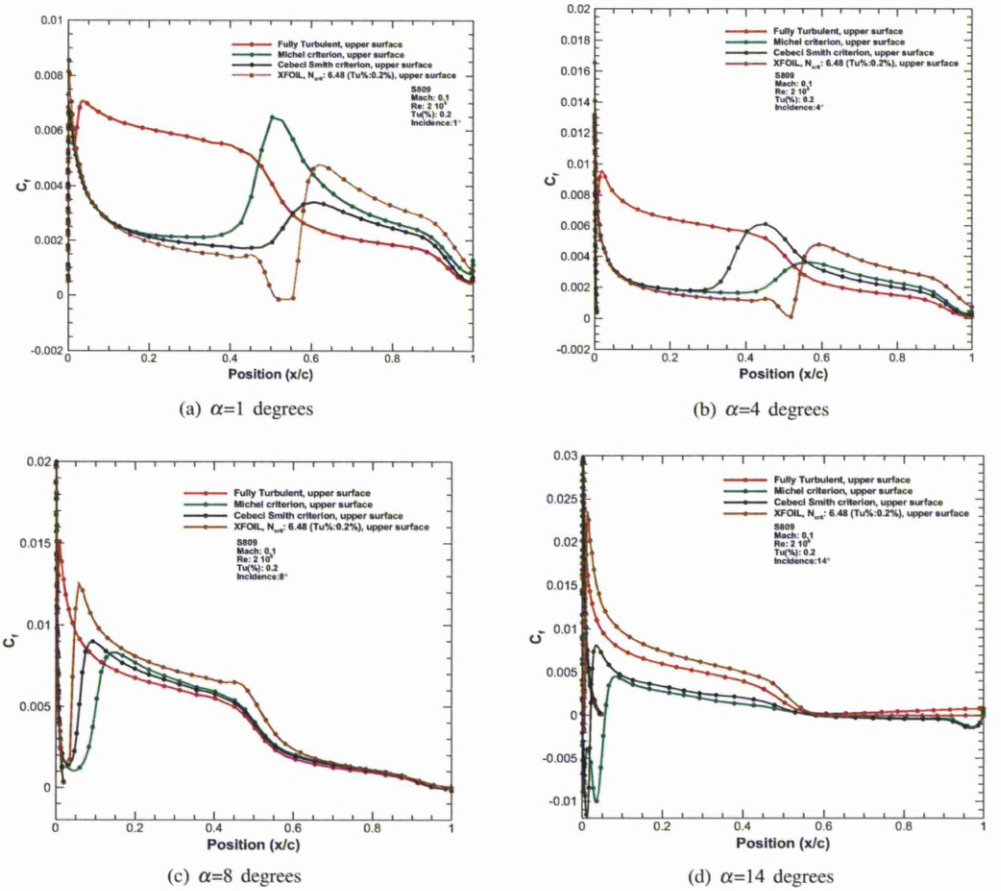

(a) α=1 degrees

(b) α=4 degrees

(c) α=8 degrees

(d) α=14 degrees

Figure 3.58: Skin friction distribution for the S809 aerofoil. Comparison between the HMB and XFOIL codes. The HMB results are derived considering fully turbulent conditions, the Michel's criterion and the Cebeci and Smith method. For XFOIL code, $N_{crit} = 6.48$ was considered degrees. (M=0.1, Re=2×10^6, $Tu(\%) = 0.2$).

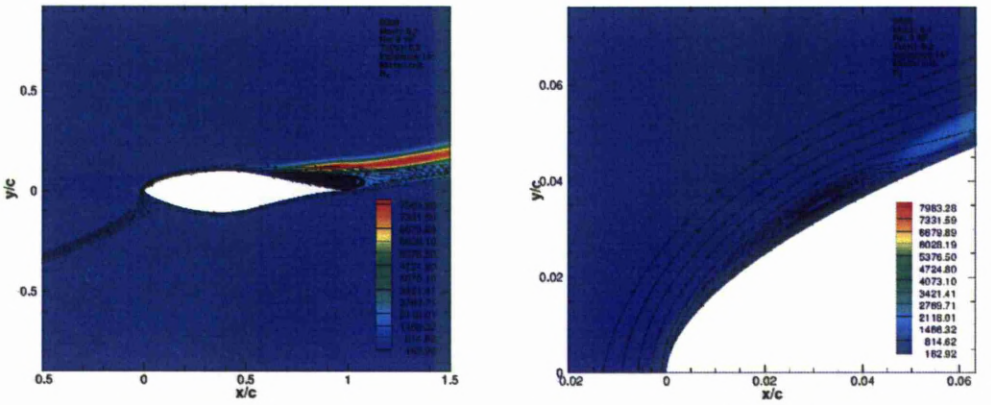

(a) General (b) Detailed

Figure 3.59: General and detail view of the flow for the S809 aerofoil. The laminar separation bubble and the separation of the flow can be seen. The Michel's criterion has been used for the calculations(M=0.1, Re=2×10^6, $Tu(\%) = 0.2$, $\alpha = 14$ degrees).

3.6.3 $\kappa - \omega - \gamma - Re_{\theta t}$ model over the S809 Aerofoil

The S809 aerofoil was also used to validate the $\kappa - \omega - \gamma - Re_{\theta t}$ model. The local correlation transition model was compared against the results of the empirical correlation transition model, XFOIL code and the experimental data.

Lift and Drag Calculations

The following figures (3.60(a)) and (3.60(b)) present the lift and drag coefficients over S809 aerofoil. The $\kappa - \omega - \gamma - Re_{\theta t}$ model estimates higher values of lift in comparison to the experimental data. When the drag is calculated, the $\kappa - \omega - \gamma - Re_{\theta t}$ model shows results close to Cebeci and Smith model.

Transitional Flow Analysis

The onset of transition for the upper and lower surface of the S809 aerofoil is presented in figure (3.60). The results are calculated with the $\kappa - \omega - \gamma - Re_{\theta t}$ model and compared against the experimental data, the results from the empirical correlation models and the XFOIL code. The LCTM model predicts the onset of transition at 45% of the upper surface when the experiments show that more than half of the upper surface of the aerofoil is laminar. The $\kappa - \omega - \gamma - Re_{\theta t}$ model underestimates the onset of transition till 6degrees of angle of attack. For higher angles, the model predicts better the experimental data than the XFOIL code or the empirical correlation transition models. For the lower surface, the model show the similar trend that was observed on the previous aerofoil test cases. The

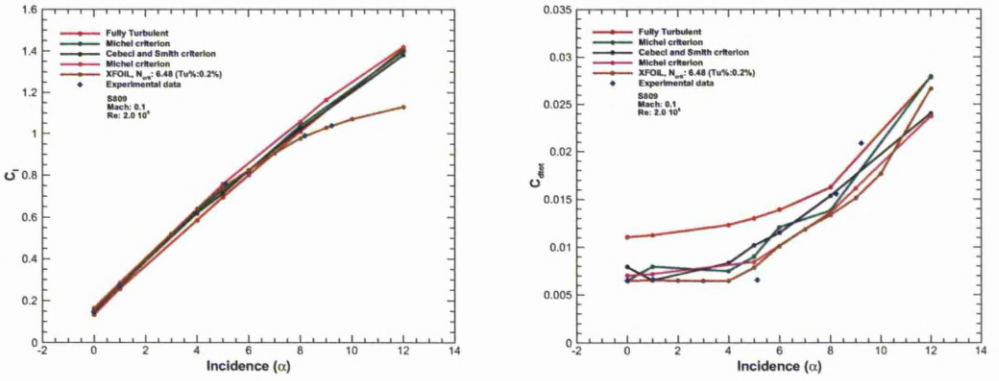

(a) C_l (b) C_d

Figure 3.60: Lift and drag coefficients as function of incidence. Experimental data and results from HMB for the flow around the S809 aerofoil. The calculations are with Michel and Cebeci and Smith criteria (M=0.1, Re=2×10^6, $Tu(\%) = 0.2$).

$\kappa - \omega - \gamma - Re_{\theta t}$ model estimates continuesly 10% earlier the start of transition in comparison with the experimental data.

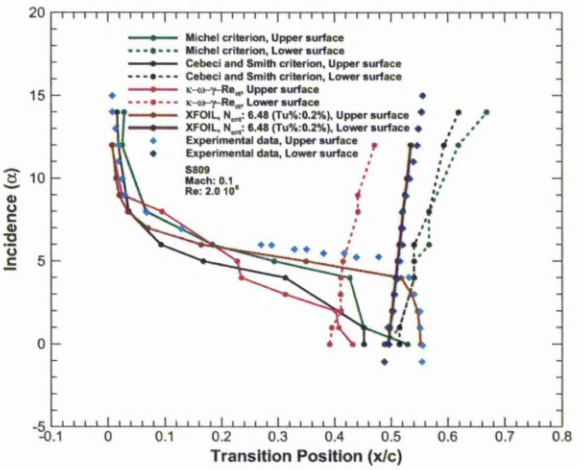

Figure 3.61: Transition point as a function of incidence for the S809 aerofoil. Experimental data in comparison to the calculations with Michel, Cebeci and Smith criteria and XFOIL code. (M=0.1, Re=2×10^6, $Tu(\%) = 0.2$)

Surface Pressure and Skin Friction Distributions

The surface pressure coefficient for incidence angles of 5 degrees and 8 degrees can be seen in figures (3.62(a)) and (3.62(b)). The $\kappa - \omega - \gamma - Re_{\theta t}$ model shows the higher pressure peak in comparison with the other models. The

results from LCTM model have similar values with results from XFOIL code for incidence angle of 5 degrees while when the angle of attack increases, the $\kappa-\omega-\gamma-Re_{\theta t}$ model show higher pressure from all the models.

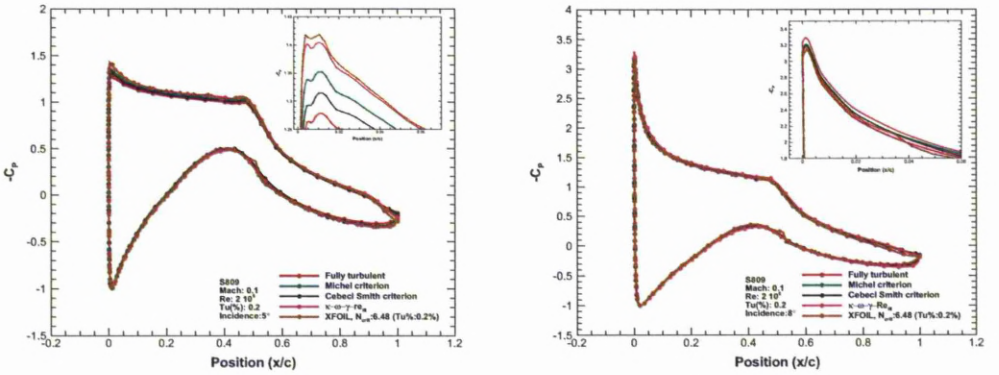

(a) α=5 degree (b) α=8 degrees

Figure 3.62: Surface pressure distribution for the S809 aerofoil. Comparison between the HMB and XFOIL codes. The HMB results are derived considering fully turbulent conditions, the Michel's criterion and the Cebeci and Smith's method. For XFOIL code, $N_{crit} = 6.48$ was considered (M=0.1, Re=2×10^6, $Tu(\%) = 0.2$).

The awkward behaviour of the $\kappa-\omega-\gamma-Re_{\theta t}$ model at figure (3.6.3) can be explained at the following figures where the skin friction distribution is presented. Skin friction calculated with the $\kappa-\omega-\gamma-Re_{\theta t}$ model at 8 degrees of incidence angle shows to agree with the empirical models while for 5 degrees the sudden increase of skin friction occurs downstream the aerofoil. This can be due to higher level of calculated pressure with the $\kappa-\omega-\gamma-Re_{\theta t}$ model than with the empirical correlation models.

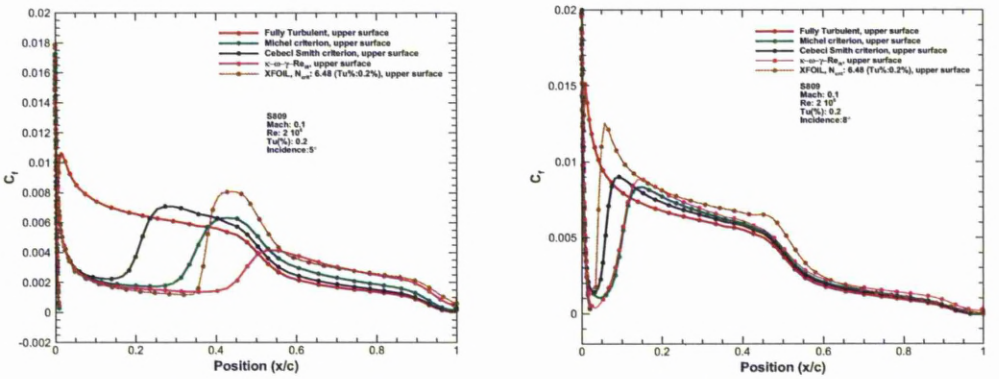

(a) α=5 degrees (b) α=8 degrees

Figure 3.63: Skin friction distribution for the S809 aerofoil. Comparison between the HMB and XFOIL codes. The HMB results are derived considering fully turbulent conditions, the Michel's criterion and the Cebeci and Smith method. For XFOIL code, $N_{crit} = 6.48$ was considered (M=0.1, Re=2×10^6, $Tu(\%) = 0.2$).

The following figures (3.64) and (3.65) show the distribution of turbulent intermittency (γ) and scalar transition

momentum thickness Reynolds number ($Re_{\theta t}$) for incidence angles of 5 and 8 degrees. Intermittency starts to have values higher than 0.1 (limit after which the flow considered as transitional) at 22% percent of the upper surface of S809 aerofoil for 5 degrees of angle of attack while for 8 degree of incidence angle, intermittency increases at 10% of the upper surface. Scalar transition momentum thickness Reynolds number ($Re_{\theta t}$) has values around the whole aerofoil, starting from 0 on the surface and reaching the value on the boundary layer edge.

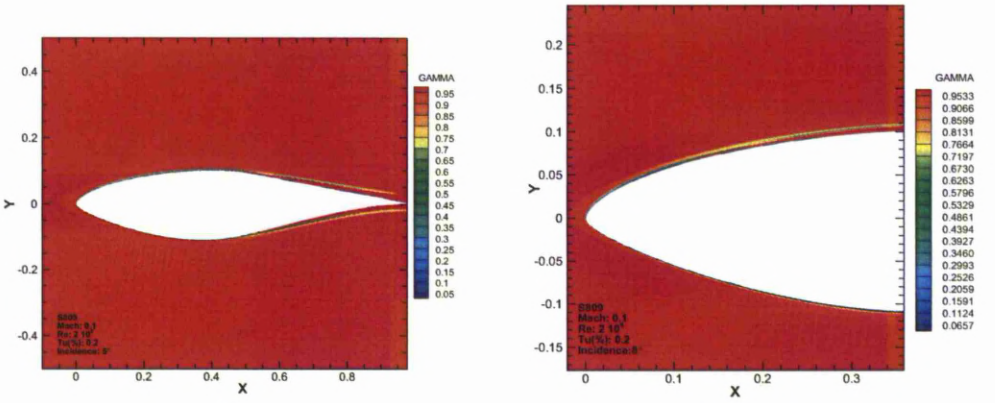

(a) α=5 degrees (b) α=8 degrees

Figure 3.64: Turbulent intermittency (γ) distribution for the S809 aerofoil. (M=0.1, Re=2×10^6, $Tu(\%) = 0.2$)

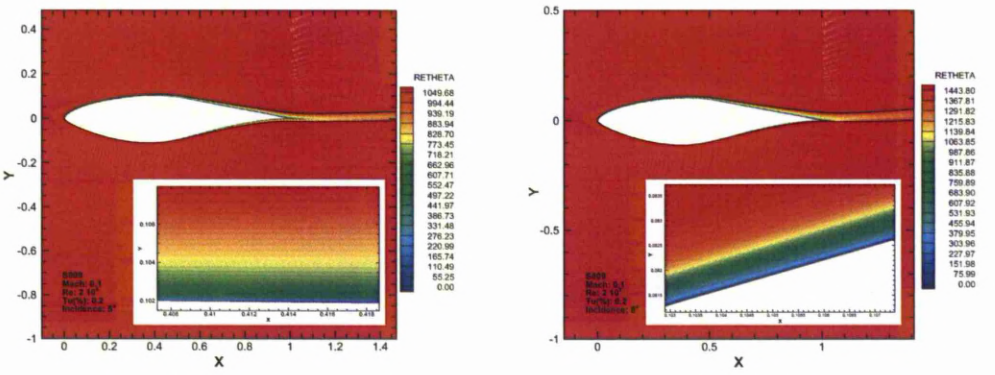

(a) α=5 degrees (b) α=8 degrees

Figure 3.65: Scalar transition momentum thickness Reynolds number ($Re_{\theta t}$) distribution for the S809 aerofoil. (M=0.1, Re=2×10^6, $Tu(\%) = 0.2$)

3.7 NACA 0012 Aerofoil

Another 2D case used in this work is the NACA 0012 aerofoil. This aerofoil belongs to the family of four digits aerofoils produced by NACA. The first two digits indicate that the aerofoil has zero camber and the latter two digits inform about the thickness of the aerofoil which is 12% of the chord. Figure (3.66) presents the aerofoil.

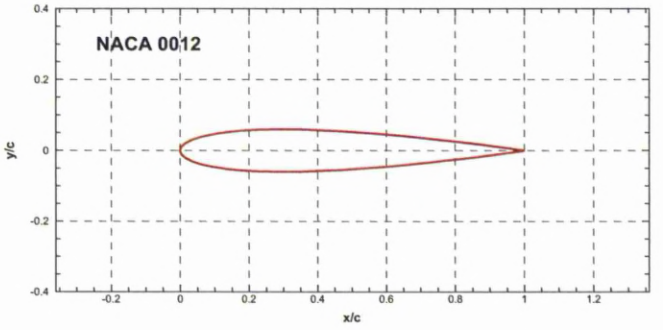

Figure 3.66: The NACA 0012 aerofoil.

This section has found widespread use in aerodynamics since it provides an acceptable compromise between high speed and low speed performance while maintaining consistently low pitching moments at most operating conditions [87]. The NACA 0012 stall process is governed by a complex combination of the competing mechanisms of trailing edge separation and leading edge separation.

The Laboratoire d'Aerodynamique et de Biomecanique du Mouvement (**LABM**) in Marseille has a track record in wind tunnel investigation of dynamic flows for the specific aerofoil. LABM conducted its experiments in their S2-Luminy subsonic wind tunnel, employing an Embedded Laser Doppler Velocimetry (ELDV) technique to obtain detailed velocity measurements inside the boundary layer for steady and oscillating NACA 0012 cases. The investigated model is supported in a vertical position and attached to the oscillating frame by means of a supporting shaft located at the quarter-chord axis.

For this work, steady and unsteady measurements are available from LABM and these are detailed in the next paragraphs.

3.7.1 NACA 0012 Aerofoil Steady Calculations

The LABM laboratory researched quantitatively and qualitatively the steady flow features around a NACA 0012 aerofoil. The aerofoil was tested at conditions shown in table (3.6), and for a range of incidence angles.

Test Cases	Case 1	Case 2
Reynolds Number	2.88×10^6	10^5
Mach Number	0.4	0.2
Range of Incidence	0-12°	0-10°

Table 3.6: Summary of the parameters for the NACA 0012 aerofoil test cases.

Table (3.7) illustrates the experimental results for the transition location of test case 1. As expected, the transition point on the upper surface moves towards the leading edge while the pressure side laminarises as the incidence approaches 10 degrees.

Incidence	Upper Surface	Lower Surface
0°	0.45	0.45
3°	0.2	0.66
5°	0.085	0.79
8°	0.024	0.92
10°	0.013	1
12°	0	1

Table 3.7: Measured transition location as a function of the angle of attack. The experimental results correspond to the LABM case 1.

3.7.2 CFD mesh - NACA 0012 aerofoil

Figure (3.67(a)) shows a view of the grid around the NACA 0012 aerofoil. It is of C-topology grid with a total number of 112,224 points. There are 488 points wrapped around the aerofoil which are equally distributed on the upper and lower surfaces. 109 nodes are distributed in the normal direction following a geometric law while an initial mesh spacing of 10^{-5}c is considered. The wake is covered with 90 nodes on geometric law and the far-field is 10 chord lengths away from the aerofoil in all directions. Figures (3.67(a)) and (3.67(b)) provide a general idea of the grid around the NACA 0012 aerofoil.

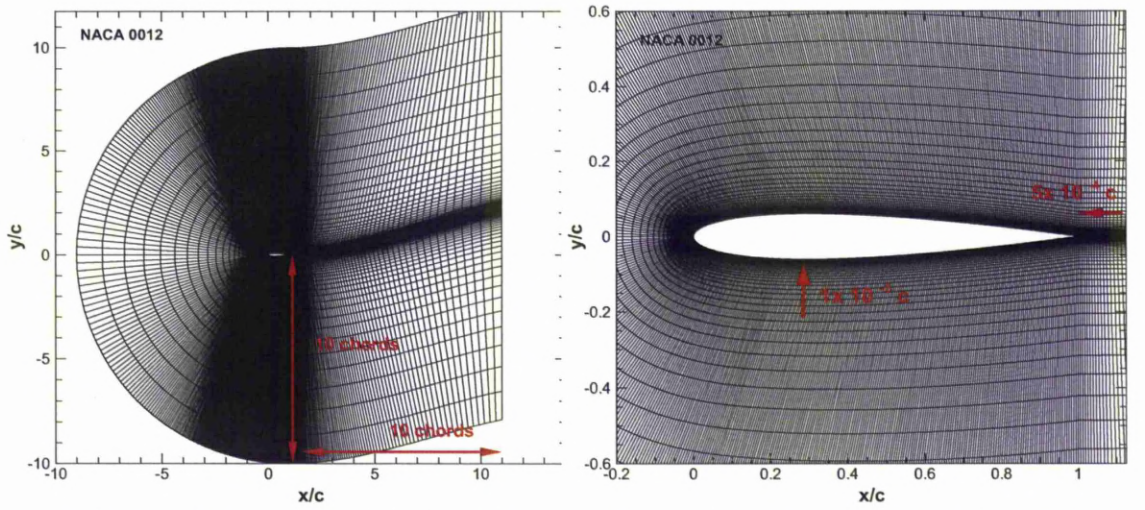

(a) Full view of the 2D mesh around NACA 0012 aerofoil

(b) Detailed view of the mesh around NACA 0012 aerofoil

Figure 3.67: 2D mesh around NACA 0012 aerofoil.

3.8 Transitional Flow over the NACA 0012 Aerofoil

The last two-dimensional test case which was used to validate the transition models was the NACA 0012 aerofoil. Initially, the aerofoil was used for the validation of the transitional version of the Spalart-Allmaras turbulence model and then was tested with the empirical correlation transition models. Finally, calculations using the $\kappa-\omega-\gamma-Re_{\theta t}$ model were performed for the specific aerofoil. In all calculations, the conditions were kept similar to the experiments performed by LABM[7].

3.8.1 Modelling the Spalart-Allmaras Turbulence Model for the NACA 0012 Aerofoil

The Spalart-Allmaras turbulence model with the transition alteration was used to calculate the flow around a NACA 012 aerofoil. For this model, the trip points on both surfaces of the aerofoil have to be pre-defined. For this reason, the transition onset estimated during the calculations of with the empirical correlation transition models were used for each angle of attack.

Lift and Drag Calculations

Figures (3.68(a)) and (3.68(b)) show the lift and drag coefficients for the NACA 0012 aerofoil at $Re = 2.88 \times 10^6$ and $M = 0.4$. The fully turbulent and transitional calculations with the use of Spalart-Allmaras turbulence model were

compared against the fully turbulent and transitional results of the empirical correlations. Due to lack of experimental data, the computations were compared against the results from XFOIL code for both fully turbulent and laminar conditions. In all cases the Spalart-Allmaras showed a similar trend with the SST $k-\omega$ fully turbulent model. In the case of incidence angle of attack $\alpha = 12$degrees, the model with the transition alternation follows the fully turbulent calculations and the results from the empirical correlations which indicate higher values of lift or drag.

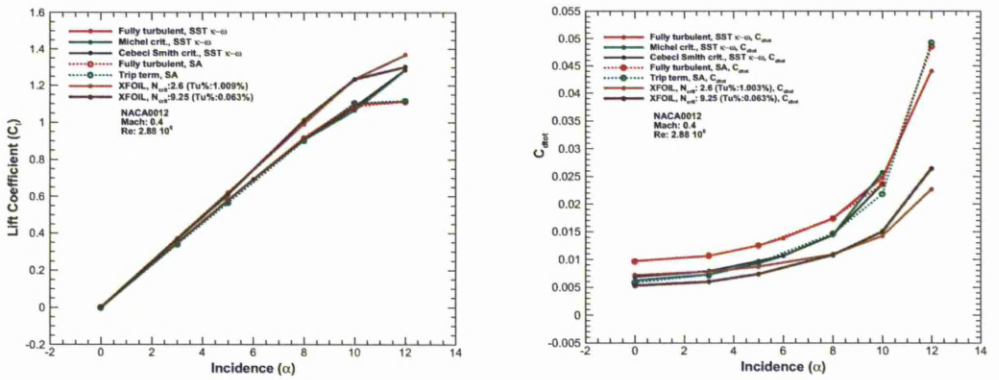

(a) C_l (b) C_d

Figure 3.68: Lift and drag coefficients for the NACA 0012 aerofoil. The calculations for Spalart-Allmaras model are compared between fully turbulent and empirical criteria (Michel and Cebeci-Smith) for the HMB code and XFOIL. The calculations for the latter one were for $N_{crit} = 2.6$ and $N_{crit} = 9.25$.($M = 0.4$, $Re = 2.88 \times 10^6$)

Surface Pressure and Skin Friction Distributions

The surface pressure coefficient for a range of incidence angles of attack can be seen in figures (3.69(a)) - (3.69(b)). The transitional version of Spalart-Allmaras turbulence model presents similar results with the fully turbulent and empirical correlation SST $\kappa-\omega$ turbulent models. Due to location of the transition onset and the longer laminar region, the results from Spalart-Allmaras showed a higher pressure peak.

Figures (3.70(a)) - (3.70(b)) show the skin friction coefficient for a NACA 0012 aerofoil. In all cases, the Spalart-Allmaras model shows similar results to the fully turbulent SST $k-\omega$ model. When the trip version of the Spalart-Allmaras turbulent model was used, it estimated a short length of the transition region. It is, however, encouraging that the Spalart-Allmaras model with transition modification captures the correct shape of skin friction curves in contrast to the fully turbulent version.

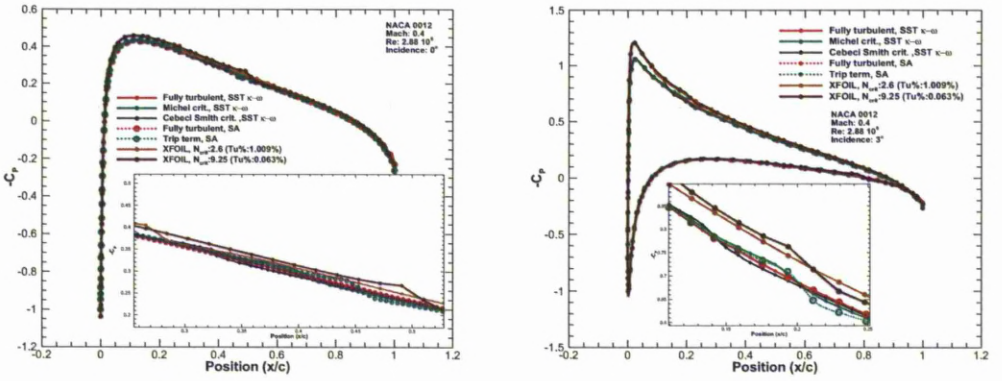

(a) $\alpha = 0$ degrees (b) $\alpha = 3$ degrees

Figure 3.69: Comparison of the surface pressure coefficient over a NACA 0012 aerofoil for HMB (fully turbulent SST k$-\omega$ Michel criterion SST k$-\omega$ fully turbulent and trip Spalart-Allmaras) and XFOIL. The calculations for the latter one are for $N_{crit} = 2.6$ and $N_{crit} = 9.25$. ($M = 0.4$, $Re = 2.88 \times 10^6$).

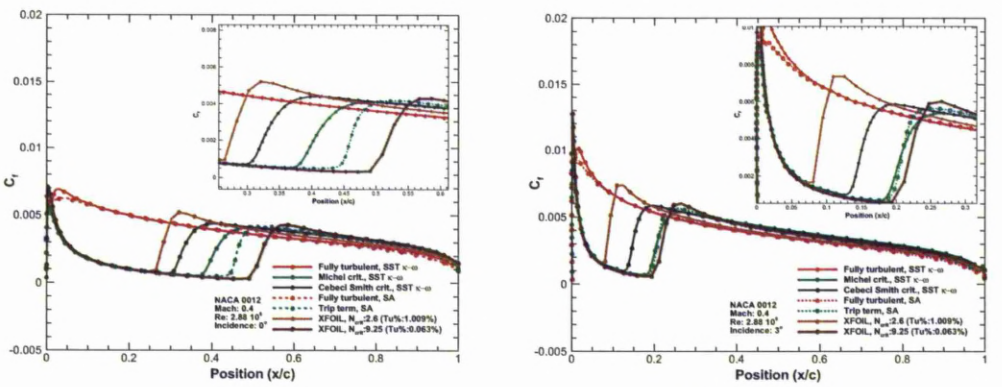

(a) $\alpha = 0$ degrees (b) $\alpha = 3$ degrees

Figure 3.70: Comparison of the skin friction coefficient for a NACA 0012 aerofoil for HMB (fully turbulent SST k$-\omega$ Michel criterion SST k$-\omega$ fully turbulent and trip Spalart-Allmaras) and XFOIL. The calculations for the latter are for $N_{crit} = 2.6$ and $N_{crit} = 9.25$. ($M = 0.4$, $Re = 2.88 \times 10^6$).

3.8.2 Empirical Transition Models over the NACA 0012 Aerofoil

The transitional flow around the NACA 0012 aerofoil was computed using empirical correlations and the conditions were similar to the experiments performed by LABM[7]. The predictions of the HMB code are compared against available experimental data and the e^N method which is used in the XFOIL [88] code.

Lift and drag calculations

The first step for the investigation of the transitional flow around a NACA 0012 aerofoil includes the results for the case of $M = 0.4$ and $Re = 2.88 \times 10^6$. Figures (3.71(a)) and (3.71(b)) present the integrated loads for the aerofoil.

The results are for the empirical criteria of Michel and Cebeci and Smith and these are compared with XFOIL code. For the XFOIL calculations, two values of the parameter N_{crit} are considered, at 9.25 (Tu(%)=0.063) and at 2.6 (Tu(%)=1.003) . The lift produced from the criteria is lower in comparison with the lift calculated with the e^N method. When drag is calculated, the results obtained from XFOIL underpredict the empirical correlations. There is also an overshoot of the drag coefficient at an incidence of 12 degrees. This overshoot is due to the formation of a laminar separation bubble, as will be described below. This is a phenomenon that neither the fully turbulent calculations nor the e^N model managed to reproduce. The drag coefficient can be analysed into two components, the friction and pressure drag coefficient as seen in figures (3.72(a)) and (3.72(b)). From the last two figures becomes obvious that the component that is mainly responsible for the drag is the pressure drag coefficient.

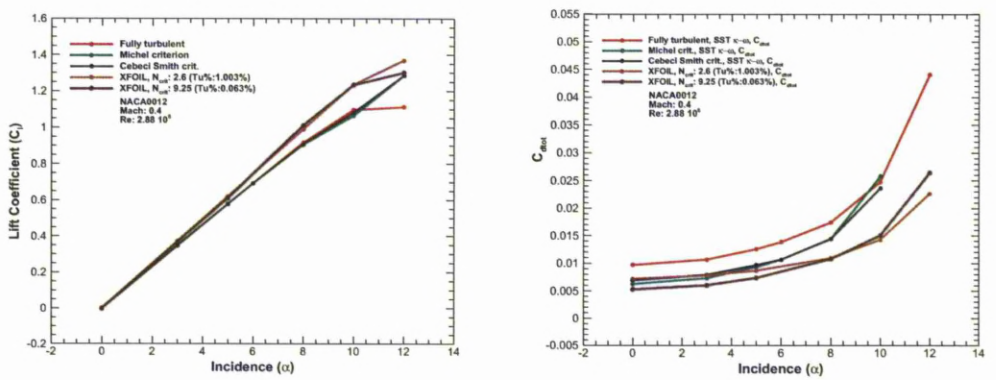

(a) C_l (b) C_d

Figure 3.71: Lift and drag coefficients for the NACA 0012 aerofoil. Comparison between fully turbulent and empirical criteria (Michel and Cebeci-Smith) for the HMB code and XFOIL. The calculations for the latter one were for $N_{crit} = 2.6$.($M = 0.4, Re = 2.88 \times 10^6$)

Figures (3.73(a)) and (3.73(b)) present the integrated loads for the case where the Reynolds number is reduced to $Re = 10^6$. The results are similar to the case for $Re = 2.88 \times 10^6$. The empirical transition models predicts lower lift and drag than the fully turbulent calculations and XFOIL. There is an increase of drag coefficient at for an incidence of 10 degrees. This increase is due to the creation of a laminar separation bubble close to the leading edge similar to the case at higher Reynolds number.

Transitional Flow Analysis

Figures (3.74(a))-(3.75(b)) present the Reynolds number produced from Michel's criterion (Re_{Mich}), the Cebeci and Smith method ($Re_{Cebeci-Smith}$) and momentum thickness Reynolds number (Re_θ) as a function of the curvilinear loca-

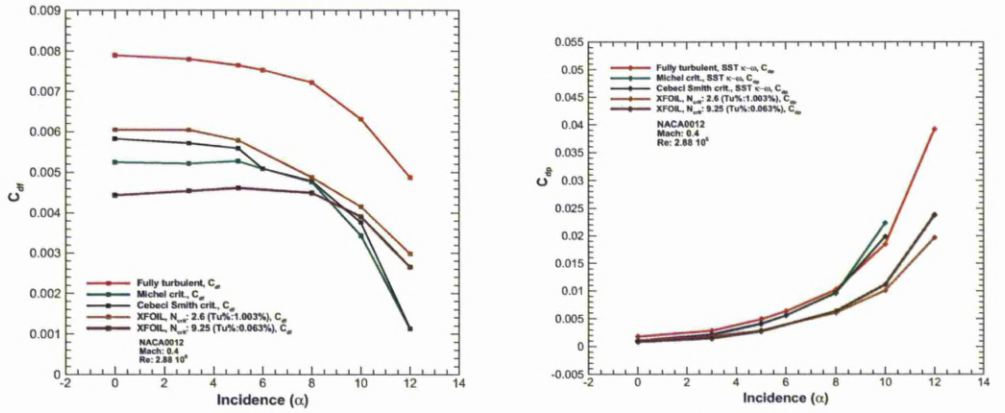

(a) Friction C_d (b) Pressure C_d

Figure 3.72: Friction and pressure drag coefficients for the NACA 0012 aerofoil. Comparison between fully turbulent and empirical criteria (Michel and Cebeci Smith) for the HMB code and XFOIL. The calculations for the latter one were for $N_{crit} = 2.6$.($M = 0.4$, $Re = 2.88 \times 10^6$)

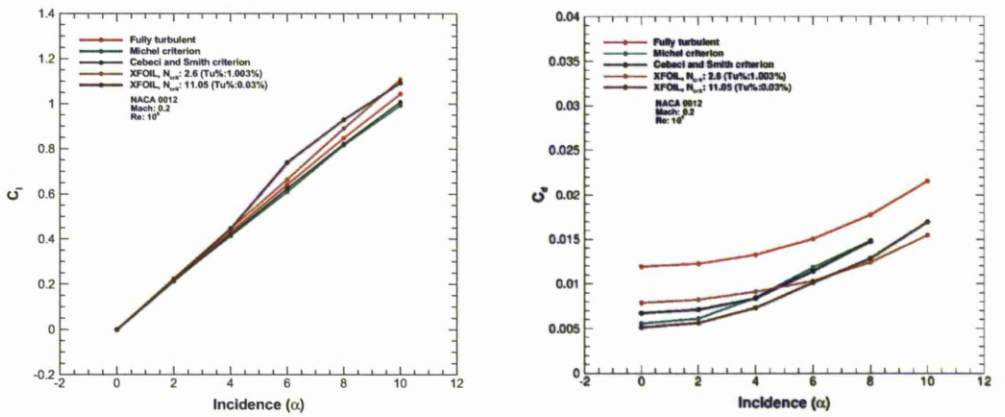

(a) C_l (b) C_d

Figure 3.73: Lift and drag coefficients for the NACA 0012 aerofoil. Comparison between fully turbulent and empirical criteria (Michel and Cebeci-Smith) for the HMB code and XFOIL. The calculations for the latter one were for $N_{crit} = 2.6$ and 11.05.($M = 0.2$, $Re = 10^6$)

tion on the upper and lower face of a NACA 0012 aerofoil for incidence angles at 0 and 8 degrees. The location where the Reynolds number of each model crosses the momentum thickness Reynolds number is considered as the onset of transition. Since the aerofoil is symmetric, for the case of 0 incidence angle, the results of the empirical transition models on the upper and lower surfaces are the same, indicating the same onset for both surfaces. As the angle of attack increases, the onset of the transitional flow moves forward closer to the leading edge for the suction side of the aerofoil. On the pressure side, the transition moves towards the trailing edge and the flow is mainly laminar.

Based on the previous results, the transition location as a function of the angle of attack for the NACA 0012

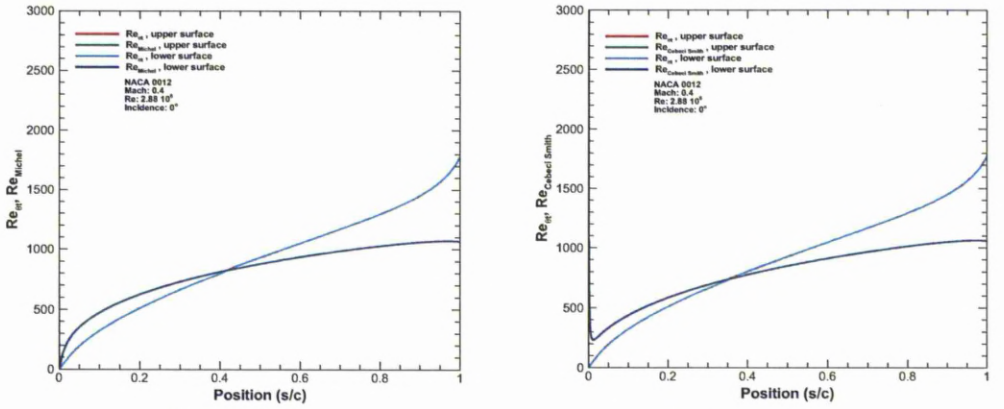

(a) Michel criterion (b) Cebeci Smith criterion

Figure 3.74: Momentum thickness Reynolds number produced from Michel's criterion (Re_{Mich}), the Cebeci and Smith's method ($Re_{Cebeci-Smith}$) and momentum thickness Reynolds number (Re_θ) in comparison with the curvilinear location on the upper and lower surface of the NACA 0012 aerofoil. ($\alpha = 0$ degrees, $M = 0.4$ and $Re = 2.88 \times 10^6$)

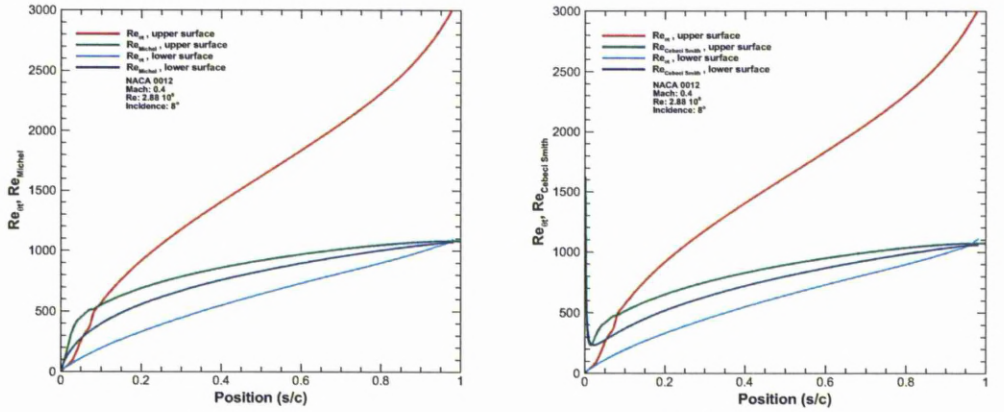

(a) Michel criterion (b) Cebeci Smith criterion

Figure 3.75: Momentum thickness Reynolds number produced from Michel's criterion (Re_{Mich}), the Cebeci and Smith's method ($Re_{Cebeci-Smith}$) and momentum thickness Reynolds number (Re_θ) in comparison with the curvilinear location of the upper and lower surfaces of the NACA 0012 aerofoil. ($\alpha = 8$ degrees, $M = 0.4$ and $Re = 2.88 \times 10^6$)

aerofoil is shown at figure (3.76). For the upper surface, HMB with Michel's criterion agree better with the experimental results for incidence angles lower than $\alpha = 3$ degrees. The Cebeci and Smith method overpredicted the onset of transition at this region. For incidence angles higher than $\alpha = 5$ degrees, the Cebeci and Smith methods predicted the transition points closer to the experimental data. For the lower surface of the aerofoil, both criteria show similar results and predict the onset of transition earlier than the experimental data. As the angle of attack increases, the models show better agreement with the experimental data (angle of attack near 8 degrees). At higher than 10 degrees the lower surface is laminar as the onset of transition is at the trailing edge. The results for 0 degrees incidence show

the Cebeci and Smith criterion to estimate the onset of transition 20% earlier from where Michel's criterion does. For these calculations, two values for the parameter of N_{crit} were considered in order to simulate the results, one turbulent $N_{crit} = 2.6$ and one laminar $N_{crit} = 9.25$. In both cases, XFOIL overpredicted the onset of transition. For the lower surface and for $N_{crit} = 9.25$, XFOIL estimated the start of transition flow closer to trailing edge even for an incidence of 6 degrees.

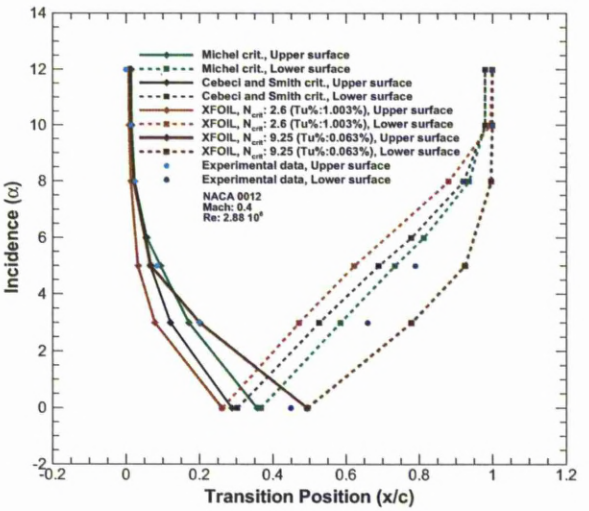

Figure 3.76: Transition location as function of the angle of attack for the NACA0012 aerofoil. Comparison between the HMB and XFOIL code with the experimental data. HMB results are derived considering Michel criterion and Cebeci Smith method. For XFOIL code, $N_{crit} = 2.6$ and 9.25 was considered. ($M = 0.4$, $Re = 2.88 \times 10^6$)

Similar results are observed for the case where the Reynolds number is $Re = 10^6$. Due to the lower Reynolds number, the criteria of Michel and Cebeci and Smith estimate a lower Reynolds number. Because of the lower Re, the cross with the local momentum thickness Reynolds number occurs later on the aerofoil. Figures (3.77(a)) and (3.77(b)) show the results for the local momentum thickness Reynolds number and Reynolds number based on Michel and Cebeci Smith correlations for incidence angles 0 degrees. When the incidence angle increases to 8 degrees, the cross occurs earlier indicating an even earlier onset of transition. Figures (3.78(a)) and (3.78(b)) show the results for the case at 8 degrees incidence angle.

Concluding from the previous results, the transition location as a function of the angle of attack for the NACA 0012 aerofoil for the lower Reynolds number can be seen in figure (3.79). The empirical correlations show results between the two extremes produced by XFOIL for $N_{crit} = 2.6$ and $N_{crit} = 11.06$. The high N_{crit} was selected to test the sensitivity of the method higher turbulence level.

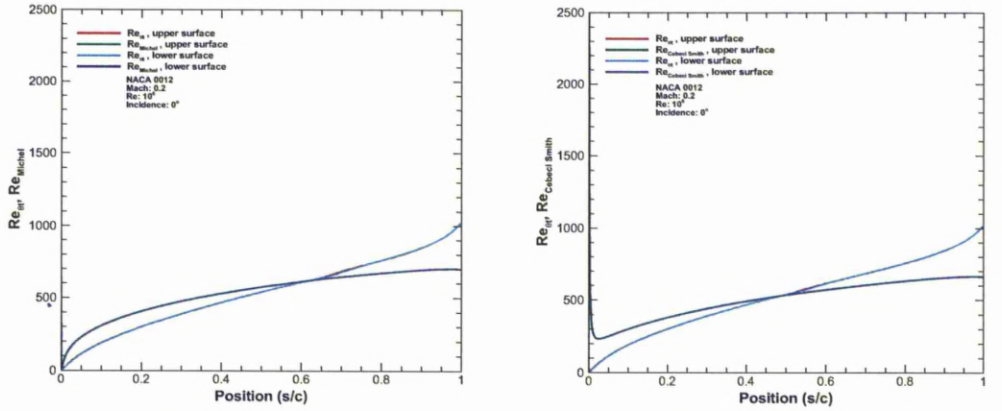

(a) Michel criterion (b) Cebeci Smith criterion

Figure 3.77: Reynolds number produced from Michel's criterion (Re_{Mich}), Reynolds number produced from Cebeci Smith's method ($Re_{Cebeci-Smith}$) and the momentum thickness Reynolds number (Re_θ) in comparison with the transition location for the upper and lower face of a NACA 0012 aerofoil. ($\alpha = 0$ degrees, $M = 0.2$ and $Re = 10^6$).

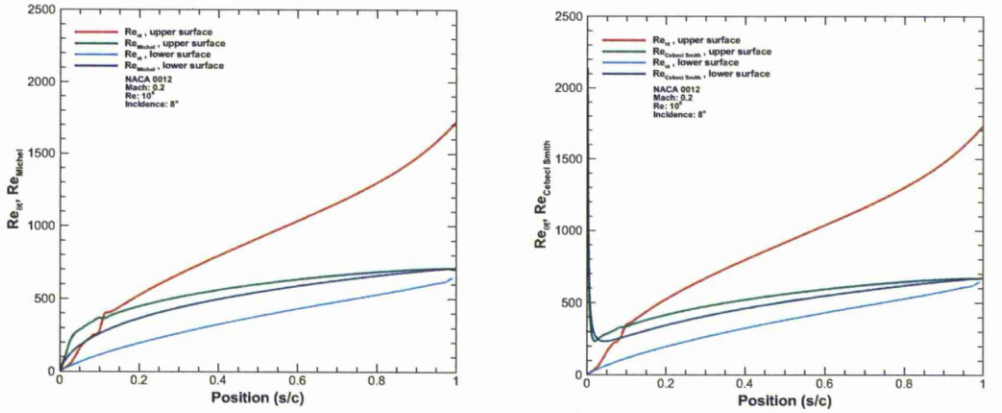

(a) Michel criterion (b) Cebeci Smith criterion

Figure 3.78: Momentum thickness Reynolds number produced from Michel's criterion (Re_{Mich}), the Cebeci and Smith's method ($Re_{Cebeci-Smith}$) and momentum thickness Reynolds number (Re_θ) in comparison with the curvilinear location of the upper and lower surfaces of the NACA 0012 aerofoil. ($\alpha = 8$ degrees, $M = 0.2$ and $Re = 10^6$).

Surface Pressure and Skin Friction Distributions

The surface pressure distribution around the NACA 0012 aerofoil for the case of $Re = 2.88 \times 10^6$ is shown in figures (3.80(a)) to (3.80(b)). Figure (3.80(a)) presents the surface pressure coefficient at $\alpha = 0$ degrees. At this angle, the results of all codes and models are similar. The difference between the criteria can be found at the point where the onset of the transition region occurs. In figure (3.80(b)), a similar plot is shown but for an incidence angle of $\alpha = 3$ degrees.

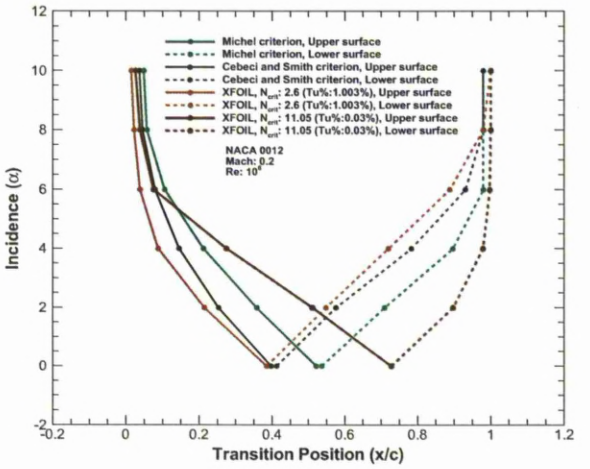

Figure 3.79: Transition location as function of the angle of attack for the NACA 0012 aerofoil. Comparison between the HMB with XFOIL code. HMB results are derived considering Michel criterion and Cebeci Smith method. For XFOIL code, $N_{crit} = 2.6$ and 11.05. ($M = 0.2$, $Re = 10^6$)

Again, the results are very similar, although XFOIL estimates higher suction peaks than HMB for all the cases. The figures show that the Cebeci Smith criterion estimates the transition onset earlier than Michel's.

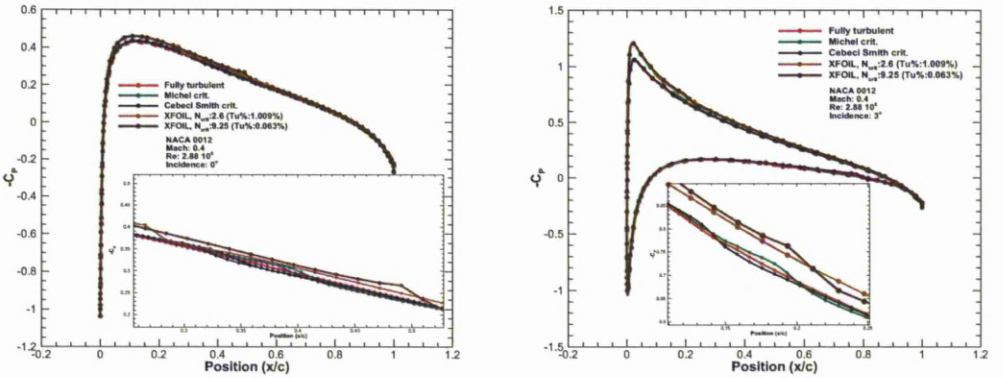

(a) $\alpha = 0$ degrees (b) $\alpha = 3$ degrees

Figure 3.80: Comparison of the surface pressure coefficient over a NACA 0012 aerofoil for HMB (fully turbulent and empirical criteria) and XFOIL. The calculations for the latter one are for $N_{crit} = 2.6$ and $N_{crit} = 9.25$. ($M = 0.4$, $Re = 2.88 \times 10^6$).

When the case with the lower Mach and Reynolds number is considered ($M = 0.2$ and $Re = 10^6$), figures (3.81(a)) - (3.81(b)) show the surface pressure distribution for a range of incidence angles. The Michel and Cebeci and Smith criteria present similar behaviour with differences only at the transition point where the models show a sudden change. As in the transition plot (3.79), the Cebeci Smith model predicts the onset of transition earlier than the Michel criterion. There is an obvious discrepancy at an angle of attack of 10 degrees which is referred to the formation of a

laminar separation bubble.

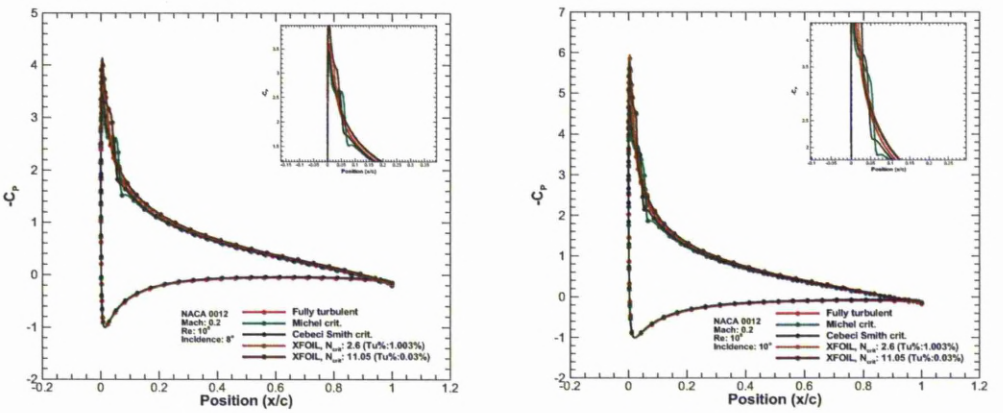

(a) $\alpha = 8$ degrees (b) $\alpha = 10$ degrees

Figure 3.81: Comparison of the surface pressure coefficient for a NACA 0012 aerofoil for HMB (fully turbulent and empirical criteria) and XFOIL. The calculations for the latter are for $N_{crit} = 2.6$ and $N_{crit} = 11.05$. ($M = 0.2$, $Re = 10^6$).

Figures (3.82(a)) and (3.82(b)) show the surface pressure coefficient for $\alpha = 8$ and 10 degrees. Both figures show that the Cebeci Smith criterion and the Michel criterion estimate the transition onset at the same location, close to the leading edge of the aerofoil. The negative values of the skin friction indicate the existence of a laminar separation bubble close to the leading edge of the aerofoil. The leading edge separation bubble can be seen in figure (3.83), which due to its existence, the turbulent Reynolds number starts to show values higher than 1.

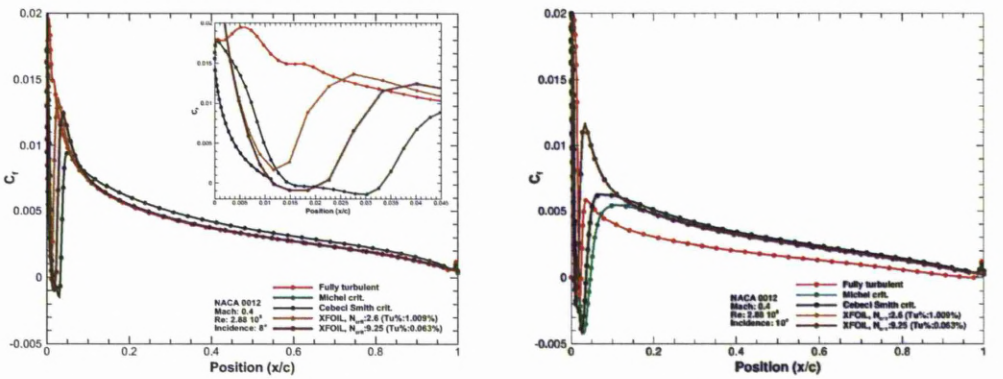

(a) $\alpha = 8$ degrees (b) $\alpha = 10$ degrees

Figure 3.82: Comparison of the skin friction coefficient for the NACA 0012 aerofoil for HMB (fully turbulent and empirical criteria) and XFOIL. The calculations for the latter are for $N_{crit} = 2.6$ and $N_{crit} = 9.25$. ($M = 0.4$, $Re = 2.88 \times 10^6$).

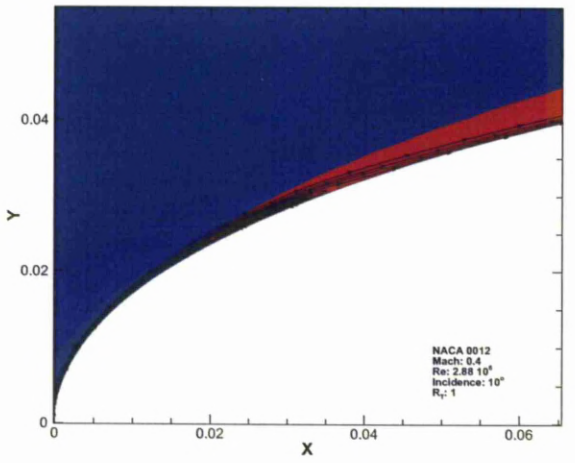

Figure 3.83: Detailed view of the flow for the NACA 0012 aerofoil. The laminar separation bubble can be seen. The turbulent Reynolds number is considered at 1. The Michel's criterion has been used for the calculations. ($M = 0.4$, $Re = 2.88 \times 10^6$, $\alpha = 10$ degrees)

The turbulent Reynolds number (R_T) over the NACA 0012 aerofoil for incidence angles of 3 and 10 degrees can be seen in figures (3.84(a)) and (3.84(b)), respectively. Turbulent Reynolds number higher than 1 means that the flow becomes turbulent. The transitional calculations show a late increase of values for R_T in comparison with the fully turbulent results. Michel criterion, at 3 degrees angle of attack, calculate the start of R_T at 18% of the upper surface while the fully turbulent has calculated close to the leading edge, at 0.0074 x/c. The Cebeci and Smith method calculates the point upstream in comparison with Michel criterion. Similar results are observed for higher incidence angles where the points are calculated further downstream. The estimated positions agree with the calculated transition onset from the empirical correlation models, seen in figure (3.79)

When the Mach number and the Reynolds number were reduced at M=0.2 and $Re = 1 \times 10^6$, respectively, the plots for the skin friction coefficient showed an delay in the onset of transition flow. As the angle of attack increases, the sudden increase of skin friction coefficient moves towards the leading edge of the aerofoil. For incidence angles higher than 8 degrees, negative values of the skin friction, similar the case with high Reynolds number, are observed indicating again the existence of a laminar separation bubble.

3.8.3 $\kappa - \omega - \gamma - Re_{\theta t}$ Model over the NACA 0012 Aerofoil

The NACA 0012 aerofoil was used to validate also the $\kappa - \omega - \gamma - Re_{\theta t}$ model. Only one test case was selected with the Reynolds number and Mach numbers to be considered at $Re = 2.88 \times 10^6$ and $M = 0.4$ respectively. The

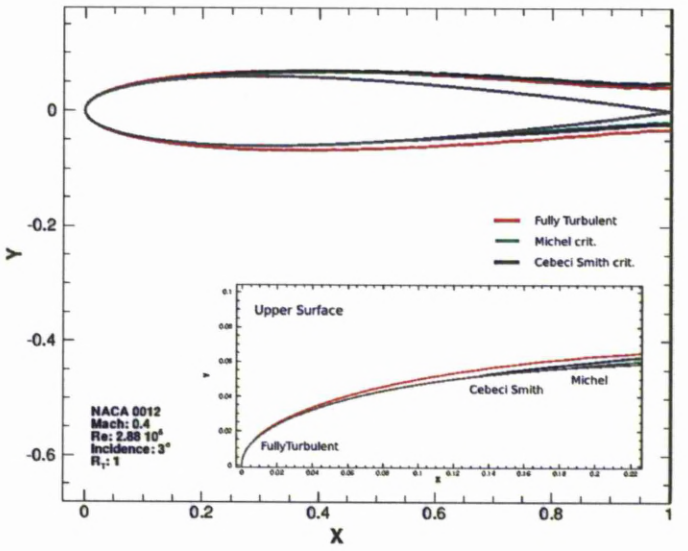

(a) $\alpha = 3$ degrees

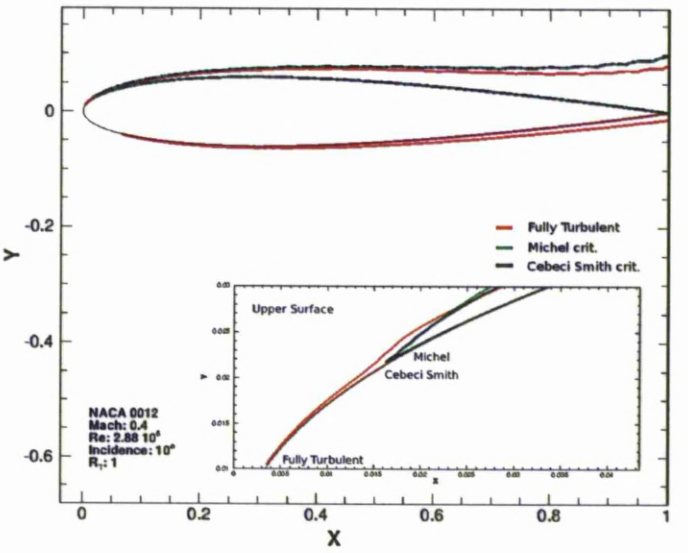

(b) $\alpha = 10$ degrees

Figure 3.84: Turbulent Reynolds number distribution over the NACA 0012 aerofoil.($M = 0.4$, $Re = 2.88 \times 10^6$).

calculations were performed for a range of incidence angle from 0 to 12 degrees.

Lift and Drag Calculations

The following figures (3.86(a)) and (3.86(b)) present the lift and drag coefficients over NACA 0012 aerofoil. The $\kappa - \omega - \gamma - Re_{\theta t}$ model follows the same trend with the empirical correlation transition models. Although, for higher

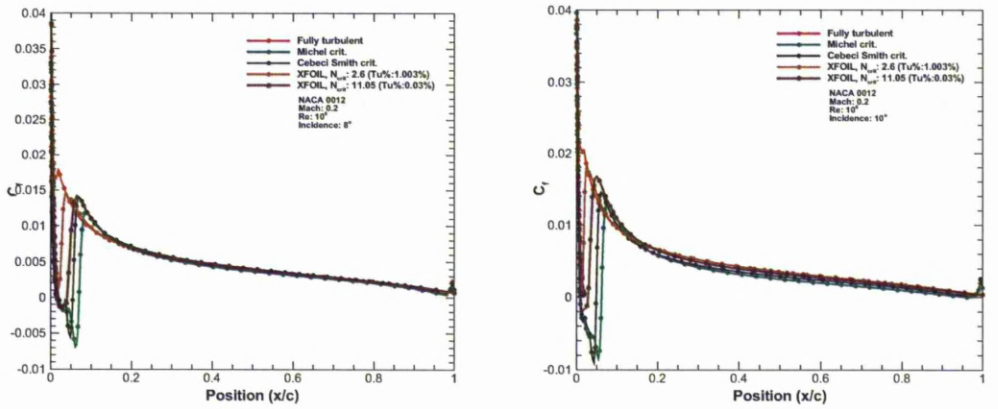

(a) $\alpha = 8$ degrees (b) $\alpha = 10$ degrees

Figure 3.85: Comparison of the skin friction coefficient over a NACA 0012 aerofoil for HMB (fully turbulent and empirical criteria) and XFOIL codes. The calculations for the latter one are for $N_{crit} = 2.6$ and $N_{crit} = 11.05$. ($M = 0.2, Re = 10^6$).

incidence angle, the $\kappa - \omega - \gamma - Re_{\theta t}$ predicts lower values of lift and drag.

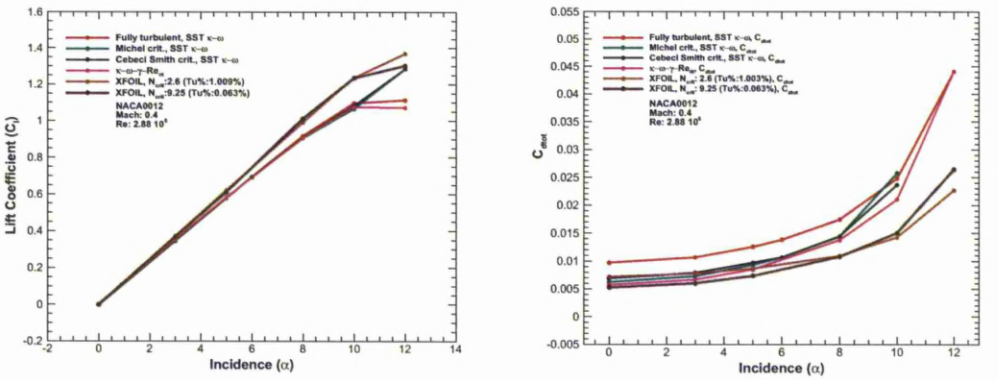

(a) C_l (b) C_d

Figure 3.86: Lift and drag coefficients as function of incidence. Comparison between fully turbulent, empirical correlation criteria (Michel and Cebeci-Smith) and $\kappa - \omega - \gamma - Re_{\theta t}$ model for the HMB code and XFOIL. The calculations for the latter one were for $N_{crit} = 2.6$ and 9.25. ($M = 0.4, Re = 2.88 \times 10^6$)

Transitional Flow Analysis

The onset of transition for the NACA 0012 aerofoil can be seen in figure (3.87). The $\kappa - \omega - \gamma - Re_{\theta t}$ model is compared against the experimental data, the calculations with the empirical correlation models and the results from XFOIL code. The model showed a good agreement with the experimental data expecially for the upper surface. For the lower surface the model predicts at longer turbulent area as underpredicts the experimental onset of transition.

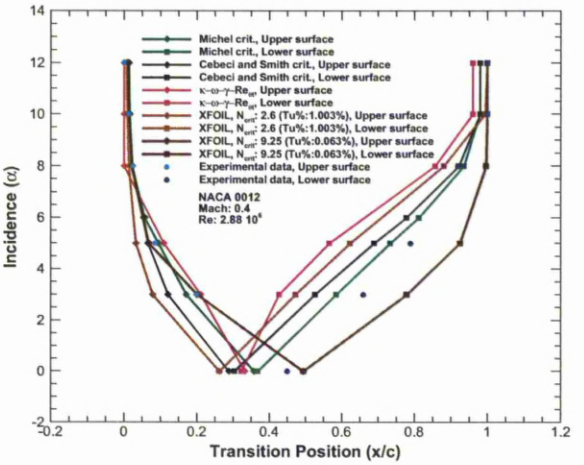

Figure 3.87: Transition location as function of the angle of attack for the NACA 0012 aerofoil. Comparison between the HMB and XFOIL code with the experimental data. HMB results are derived considering Michel's criterion, Cebeci Smith method and $\kappa-\omega-\gamma-Re_{\theta t}$ model. For XFOIL code, $N_{crit} = 2.6$ and 9.25 was considered. ($M = 0.4, Re = 2.88 \times 10^6$)

Surface Pressure and Skin Friction Distributions

A comparison between the CFD-computed results and the results from XFOIL code for the surface pressure distribution over the NACA 0012 aerofoil can be seen in figures (3.88(a)) and (3.88(b)). The CFD results include calculations using fully turbulent flow, empirical correlations and the $\kappa-\omega-\gamma-Re_{\theta t}$ transition model. The results are for 3 and 8 degrees of angle of attack. Surface pressure estimated with the $\kappa-\omega-\gamma-Re_{\theta t}$ transition model show similar trend with the empirical correlation models although the sudden change of pressure for the LCTM model indicates a later start of transition.

As seen in figure (3.87), the onset of transition based on the $\kappa-\omega-\gamma-Re_{\theta t}$ model was estimated downstream in comparison with the empirical correlation transition models. This can be seen also in figures (3.89(a)) and (3.89(b)) where the skin friction on upper surface of the aerofoil for 3 and 8 degrees. The length of the transition region based on the LCTM model is shorter than what can be calculated with the other models. The length of the transition model can be estimated as the difference between the minimum and the maximum values of the thunder-shape of the skin friction coefficient.

The intermittency (γ) distribution over the NACA 0012 aerofoil for incidence angles of 3 and 8 degrees can

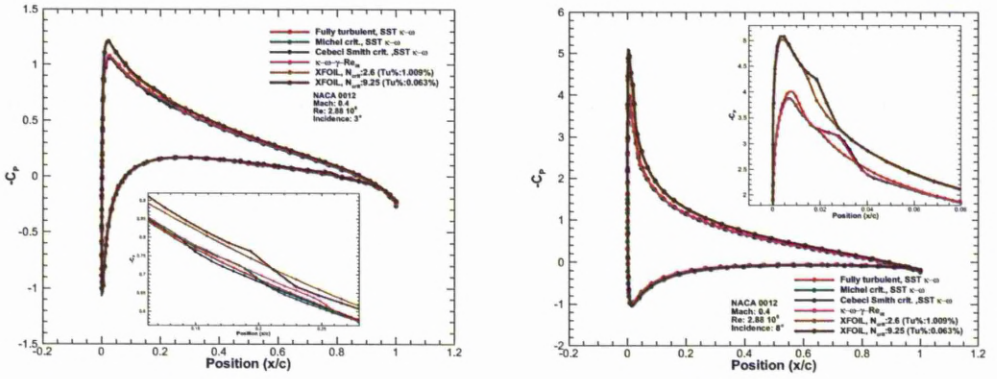

(a) α=3 degree (b) α=8 degrees

Figure 3.88: Surface pressure distribution for the NACA 0012 aerofoil. Comparison between the HMB and XFOIL codes. The HMB results are derived considering fully turbulent conditions, Michel's criterion, Cebeci and Smith method and the $\kappa-\omega-\gamma-Re_{\theta t}$ transition model. For XFOIL, $N_{crit} = 2.6$ and $N_{crit} = 9.25$ were considered. ($M = 0.4, Re = 2.88 \times 10^6$)

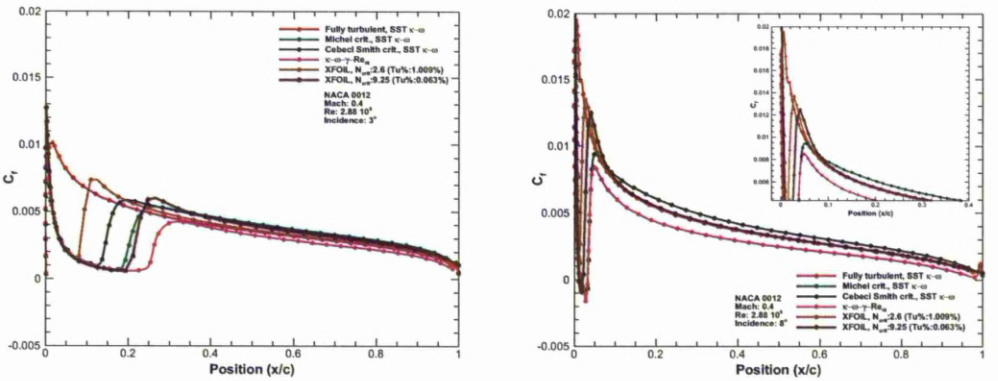

(a) α=3 degrees (b) α=8 degrees

Figure 3.89: Skin friction distribution for the NACA 0012 aerofoil. Comparison between the HMB and XFOIL codes. The HMB results are derived considering fully turbulent conditions, Michel's criterion, Cebeci Smith method and $\kappa-\omega-\gamma-Re_{\theta t}$ transition model. For XFOIL, $N_{crit} = 2.6$ and $N_{crit} = 9.25$ were considered. ($M = 0.4, Re = 2.88 \times 10^6$)

seen in figures (3.90(a)) and (3.90(b)). The intermittency starts from values close to zero on the aerofoil surface and reaches the value of 1 at the free-stream. Inside the boundary layer, the onset of transition is indicated as the point where the value of intermittency changes to higher values in the streamwise direction.

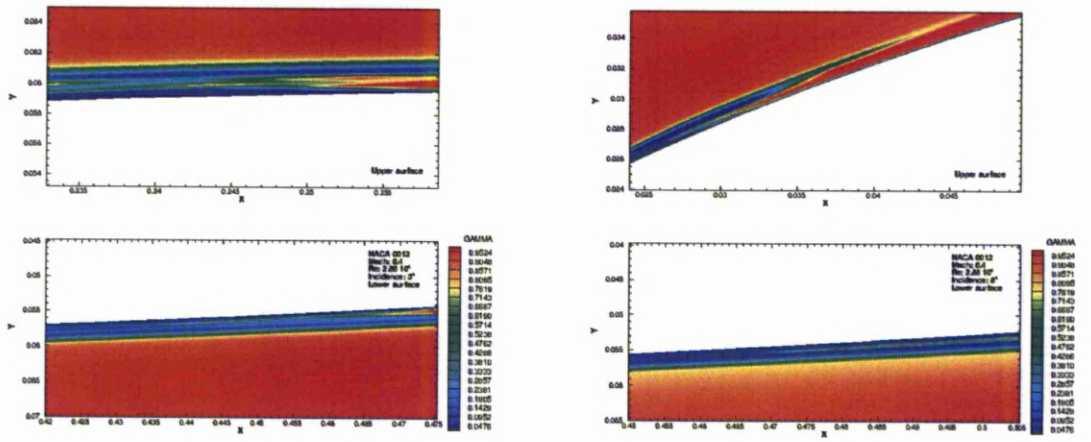

(a) α=3 degrees

(b) α=8 degrees

Figure 3.90: Turbulent intermittency (γ) distribution for the NACA 0012 aerofoil. (M=0.4, Re=2.88×10^6)

3.9 Transitional Flow over the NACA 0012 Aerofoil - Oscillating experiments

LABM also carried also experiments using an oscillating NACA 0012 aerofoil. The main goal for these tests was to study the physics of unsteady separated flows.

The time variation of the incidence for the pitching motion was considered harmonic and is given as

$$\alpha = \alpha_0 + \alpha_1 \sin(\kappa t) \tag{3.2}$$

where the angle α_0 is the mean angle and α_1 is the half amplitude of the motion. The reduced frequency was based on the chord and the free-stream velocity and given by:

$$\kappa = \frac{|\omega c|}{|2U_\infty|} \tag{3.3}$$

The aerofoil model had a chord of 0.3m and was mounted vertically in the tunnel. The free-stream was running at 5 m/s and had a turbulence intensity lower than 0.5%. Based on equation (3.2) and given that the oscillation frequency was 1 HZ, a reduced frequency of 0.188 is calculated. A mean incidence of 6.0 degrees and a half- amplitude of 6.0 degrees were used. Table (3.8) summarises the parameters for the pitching NACA 0012 test case.

Test Conditions	Pitching NACA 0012
Mach Reynolds (M)	0.2
Reynolds Number (Re_c)	10^5 and 2×10^5
Mean Incidence (α_0)	6° and 12°
Half-amplitude ($\delta\alpha$)	±6°
Reduced Frequency (κ)	0.188

Table 3.8: Conditions for the oscillating NACA 0012 test case.

These conditions were selected to provide some comparison with the steady state results for the NACA 0012 aerofoil.

Lift and Drag Calculations

Figures (3.91(a)) and (3.91(b)) show the lift and drag coefficients as function of the incidence angle. Both empirical models present similar results for the pitching oscillations. For incidence angles lower than 6 degrees, for downstroke and upstroke, the transition models predict higher lift than fully turbulent computations. For angles higher than 10 degrees this behaviour changes and the fully turbulent calculations show an increased lift coefficient. The drag coefficient is showed in figure (3.91(b)). The transition models predict higher drag during the upstroke move of the aerofoil. Similar, during downstroke the fully turbulent calculations produce higher drag than the transition models.

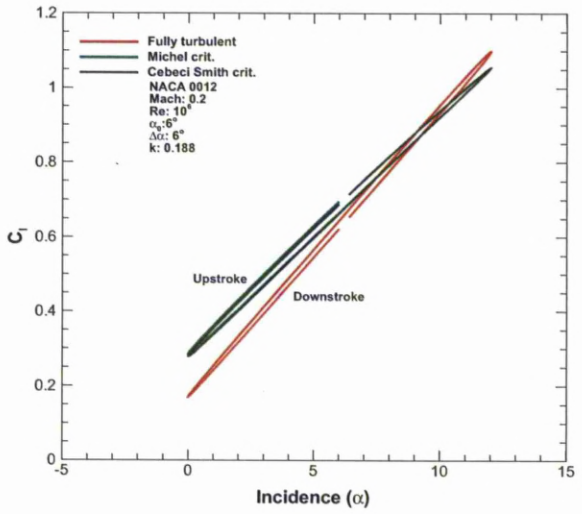

(a) C_l

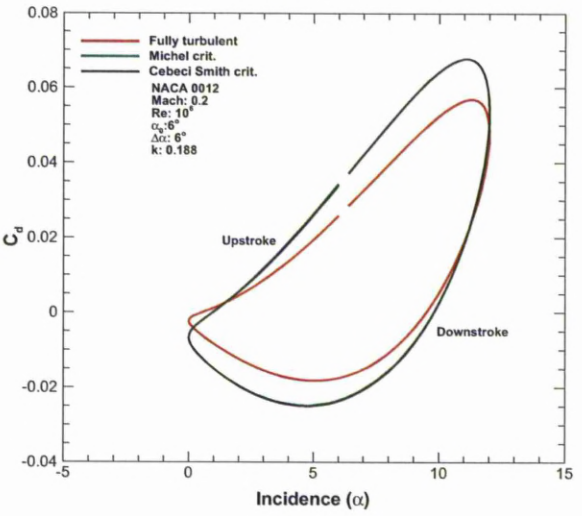

(b) C_d

Figure 3.91: Lift and total drag coefficients as function of incidence for an oscillating NACA 0012 aerofoil. The calculations are with Michel and Cebeci and Smith criteria. (M=0.2, Re=10^6)

Transitional Flow Analysis

For the case of the pitching aerofoil, the onset of transition is estimated closer to the leading edge of the aerofoil even for incidence angles close to 0 degrees. The difference of transition onset for the upper surface between the downstroke and the upstroke movement of the aerofoil is estimated to 5%. This difference is increased to 18.5% for the lower surface. Comparing the results from the unsteady calculations with the transition points derived from steady calculations for the same conditions and angle of attack, the onset of transition occurs earlier and closer to the leading edge for the case of the unsteady calculations. Larger hysteresis is experienced on the pressure side in comparison to the suction side. This is due to the presence of a laminar separation bubble on the suction side that tends to fix the transition point.

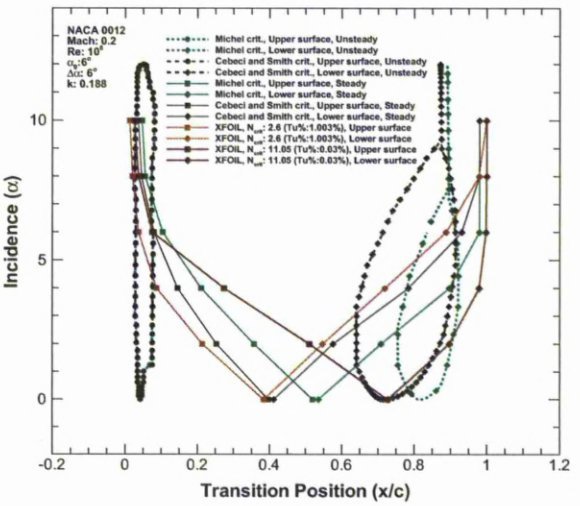

Figure 3.92: Transition point as a function of incidence for the oscillating NACA 0012 aerofoil. Comparison of the calculations between Michel, Cebeci and Smith criteria for steady and unsteady flow and XFOIL code. (M=0.2, Re=10^6, $\kappa = 0.188$)

Skin Friction Distribution

The reason for the behaviour of the transition onset between the two transitional models can be found in the skin friction coefficient plots. As can be seen in figures (3.93(a)) to (3.93(d)), a laminar separation bubble occurs at the 5% of the aerofoil chord and triggers the onset of transition. The detailed view of the flow for fully turbulent, Michel's and Cebeci and Smith criteria in figures (3.94(a)) to (3.94(c)) show the existence of the laminar separation bubble. Both transition models managed to estimate the existence of a laminar separation bubble at 8 degrees upstroke while fully

turbulent calculations clearly missed to estimate the bubble.

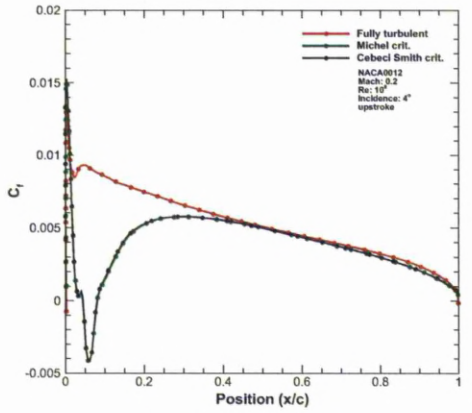

(a) α=4 degrees upstroke

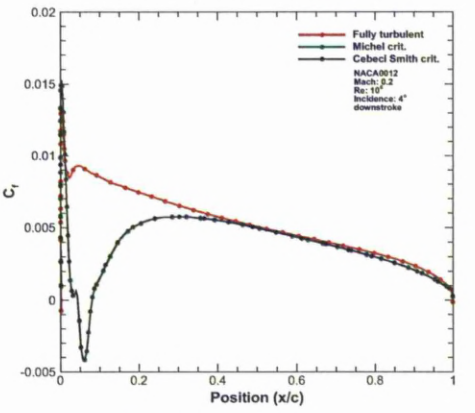

(b) α=4 degrees downstroke

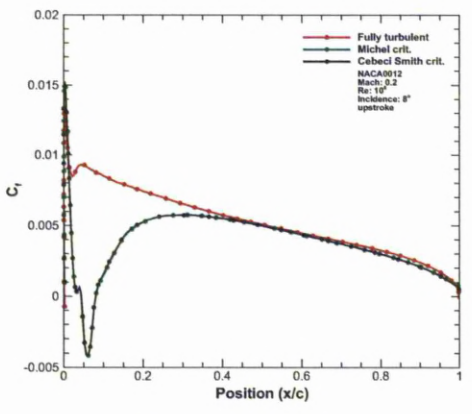

(c) α=8 degrees upstroke

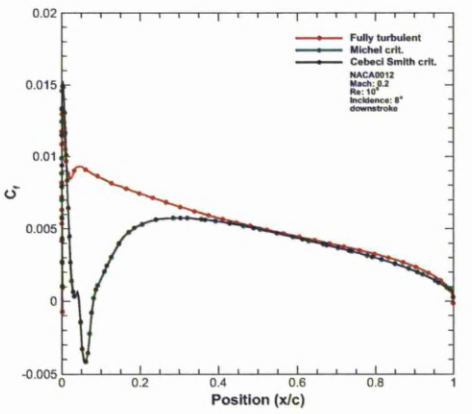

(d) α=8 degrees downstroke

Figure 3.93: Comparison of the skin friction coefficient over a pitching NACA 0012 aerofoil. (Fully turbulent vs empirical criteria, M=0.2, Re=10^6, $\kappa = 0.188$)

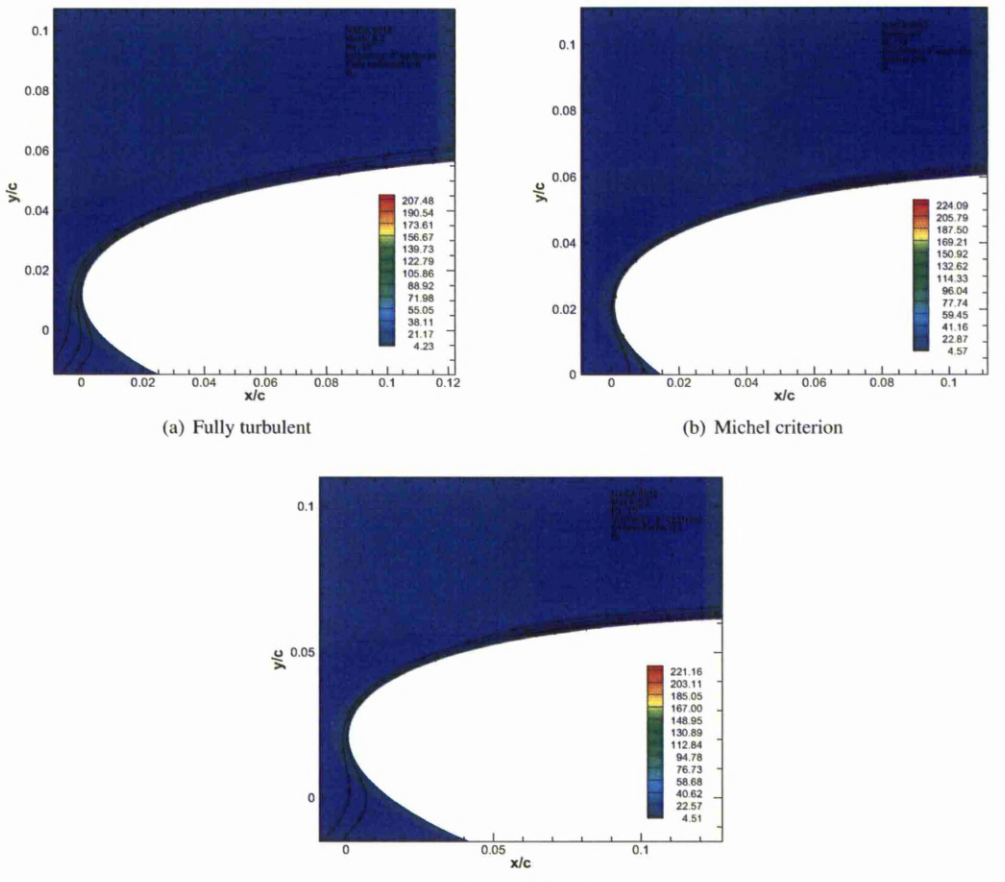

(a) Fully turbulent

(b) Michel criterion

(c) Cebeci Smith criterion

Figure 3.94: Detail view of the flow around the NACA 0012 aerofoil. Comparison between fully turbulent, Michel criterion and Cebeci and Smith method. The results are for 8 degrees of upstroke. (M=0.2, Re=10^6, $\kappa = 0.188$)

3.10 Summary

In this chapter, two roughness models, the three empirical correlation models and the $\kappa-\omega-\gamma-Re_{\theta t}$ model were validated with the use of two-dimensional flows. In general the roughness models showed the known effects of roughness on aerofoils[62], where the lift slope and the maximum lift are lower. Due to the existence of roughness, the production of drag was increased. The skin friction coefficient on the suction side of the aerofoil decline faster than the fully turbulent calculations.

When the Spalart-Allmaras turbulent models were used with the transition modification, the model required the knowledge of a predefined point to trip the flow. Predictions of lift and drag coefficients agreed better with the fully turbulent calculations. The models predicted the sudden change of the skin friction indicating transition between the laminar and turbulent solutions,as did the XFOIL code.

The empirical correlation transition models showed a fair agreement with the experimental data especially for cases at high Reynolds number. The slope of the lift curve and the maximum lift coefficient are higher compared with the experimental data while higher stall angle is estimated with the transition models. The two models, Michel and Cebeci and Smith, showed similar results with the latter predicting slightly earlier transition. The Abu-Ghannam and Shaw model estimated an early start of transition on all cases. Moreover, the model showed a sensitivity to its parameters, with the end of transition region to vary based on them.

The $\kappa-\omega-\gamma-Re_{\theta t}$ model showed satisfactory results. Even if the onset of transition was estimated slightly earlier than the empirical correlation models, the slope of the lift curve and the maximum lift coefficient was closer to the experimental data. The CPU cost of the $\kappa-\omega-\gamma-Re_{\theta t}$ model was due to the addition of extra terms in the HMB code.

Chapter 4

3D Cases: Rotor and Fuselage

As this work is concentrated on transition modelling for helicopter applications, this chapter details the few available experimental data for three dimensional test cases. The 3D cases include the ROBIN helicopter fuselage, the UH-60A rotor in fast-forward flight, the Caradonna-Tung rotor and a model tail rotor, both, in hover.

A summary of the flow conditions for the test cases can be seen in table (4).

Cases	Re_x	Mach	M_{tip}	μ	θ_{shaft}	θ_0	θ_{1s}	θ_{1c}	β_{1c}	β_0	β_{1c}
ROBIN Helicopter Fuselage	4.47×10^6	0.064									
UH-60A	4×10^6		0.368	0.67	7.3	14.6	8.63	-2.39	3.43	-1.04	-0.7
Caradonna-Tung Rotor	2×10^6		0.439								
Model Tail Rotor	1.1668×10^6		0.6								

Table 4.1: Flow conditions for the 3D test cases.

4.1 ROBIN Fuselage

For many years, little attention has been devoted to helicopter fuselage aerodynamics. However, the fuselage can significantly affect the overall performance of the helicopter in all flight conditions. This is the reason why several attempts to simulate the flow around helicopters was undertaken both in american and european research community[14]. One of the oldest geometries developed by NASA in the late 70's was the ROtor Body Interaction (ROBIN).

Freeman and Mineck [14] described a general fuselage with a set of 'super ellipse' equations. The following

equations show the generic form used for producing the family of these elliptic shapes.

$$\left[\frac{x-a}{r_{maj}}\right]^2+\left[\frac{y-b}{r_{min}}\right]^2 = 1 \tag{4.1}$$

The coordinates for the fuselage are defined in 'rings' whose size, shape and vertical position vary with location along the length of the fuselage (x-direction). Four parameters govern the characteristics of each ring: height (H), width (W), vertical position of centre (Z_0), and degree of corner sharpness (N). These are evaluated as a function of the x coordinate using the following:

$$\begin{bmatrix} H \\ W \\ Z_0 \\ N \end{bmatrix} = C_6+C_7\left[C_1+C_2\left(\frac{\frac{x}{l}+C_3}{C_4}\right)^{C_5}\right]^{\frac{1}{C_8}} \tag{4.2}$$

Having obtained the controlling parameters ($C_1 \ldots C_8$), a super-elliptical equation expressed in polar form is used for calculating the radial magnitude as a function of angular location:

$$r = \left[\frac{\left(\frac{HW}{4}\right)^N}{\left(\frac{H}{2}sin\phi\right)^N+\left(\frac{W}{2}\cos\phi\right)^N}\right]^{\frac{1}{N}} \tag{4.3}$$

Transforming back to Cartesian coordinates, each geometry point is given by:

$$\begin{bmatrix} \frac{x}{l} \\ \frac{y}{l} \\ \frac{z}{l} \end{bmatrix} = \begin{bmatrix} \frac{x}{l} \\ rsin\phi \\ rcos\phi+Z_0 \end{bmatrix} \tag{4.4}$$

where l is the length of the fuselage.

The correct set of coefficients for the ROBIN body is presented in table (4.2), and the fuselage can be seen in figure (4.1). On the other hand, there are two major drawbacks of the equations. Initially, the nose of the fuselage and the nose of the hub shroud cannot be computed directly from the equations. A further problem with the definition of the equations and the coordinates is the possibility of raising negative numbers to real powers. Due to this and for the purposes of the geometry definition, each the super-ellipses was constructed and then mirrored to form the complete shape.

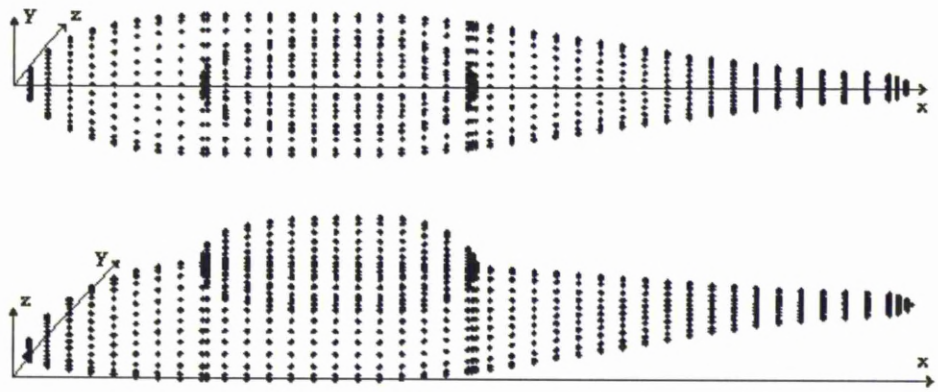

Figure 4.1: Plan and elevation of the geometry points produced by the 'super ellipse' equations for the ROBIN fuselage.

Function	$\frac{x}{l}$	C_1	C_2	C_3	C_4	C_5	C_6	C_7	C_8
H	$0 < \frac{x}{l} < 0.4$	1	-1	-0.4	0.4	1.8	0	0.25	1.8
W	$0 < \frac{x}{l} < 0.4$	1	-1	-0.4	0.4	2	0	0.25	2
Z_0	$0 < \frac{x}{l} < 0.4$	1	-1	-0.4	0.4	1.8	-0.08	0.08	1.8
N	$0 < \frac{x}{l} < 0.4$	2	3	0	0.4	1	0	1	1
H	$0.4 < \frac{x}{l} < 0.8$	0.25	0	0	0	0	0	1	1
W	$0.4 < \frac{x}{l} < 0.8$	0.25	0	0	0	0	0	1	1
Z_0	$0.4 < \frac{x}{l} < 0.8$	0	0	0	0	0	0	1	1
N	$0.4 < \frac{x}{l} < 0.8$	5	0	0	0	0	0	1	1
H	$0.8 < \frac{x}{l} < 1.9$	1	-1	-0.8	1.1	1.5	0.05	0.2	0.6
W	$0.8 < \frac{x}{l} < 1.9$	1	-1	-0.8	1.1	1.5	0.05	0.2	0.6
Z_0	$0.8 < \frac{x}{l} < 1.9$	1	-1	-0.8	1.1	1.5	0.04	-0.04	0.6
N	$0.8 < \frac{x}{l} < 1.9$	5	-3	-0.8	1.1	1	0	1	1
H	$1.9 < \frac{x}{l} < 2$	1	-1	-1.9	0.1	2	0	0.05	2
W	$1.9 < \frac{x}{l} < 2$	1	-1	-1.9	0.1	2	0	0.05	2
Z_0	$1.9 < \frac{x}{l} < 2$	0.04	0	0	0	0	0	1	1
N	$1.9 < \frac{x}{l} < 2$	2	0	0	0	0	0	1	1
H	$0.4 < \frac{x}{l} < 0.8$	1	-1	0.8	0.4	3	0	0.2	3
W	$0.4 < \frac{x}{l} < 0.8$	1	-1	-0.8	0.4	3	0	0.172	3
Z_0	$0.4 < \frac{x}{l} < 0.8$	0.122	0	0	0	0	0	1	1
N	$0.4 < \frac{x}{l} < 0.8$	5	0	0	0	0	0	1	1
H	$0.8 < \frac{x}{l} < 1.018$	1	-1	-0.8	0.218	2	0	0.2	2
W	$0.8 < \frac{x}{l} < 1.018$	1	-1	-0.8	0.218	2	0	0.172	2
Z_0	$0.8 < \frac{x}{l} < 1.018$	1	-1	-0.8	1.1	1.5	0.065	0.06	0.6
N	$0.8 < \frac{x}{l} < 1.018$	0.122	0	0	0	0	0	1	1

Table 4.2: Summary of the parameters of the ROBIN fuselage.

Table (4.2) shows a summary of all values for the coefficients used in the super-ellipse equations to compute the geometry of the ROBIN fuselage. The values are divided into sections: front of the fuselage, start of the hub shroud, end of the shroud, tail. The first part of the table presents the parameters for the analytical definition of the main body, while the last part, the parameters for the analytical definition of the pylon.

4.1.1 Steady Calculations

In 1979, Freeman and Mineck[14] produced an experimental database for ROBIN. The flow around this generic fuselage body was calculated at a range of incidence angles, from -5 degrees to 5 degrees. For the calculations, a Mach number of 0.064 and a Reynolds number of 4.47×10^6 were considered. All model dimensions were non-dimensionalised by a reference length equal to one half of the model length[18]. This distance was selected to be consistent with the results of Freeman and Mineck[14] which used the rotor radius as the reference length.

Freeman and Mineck [14] conducted their experiments at the NASA Langley subsonic wind tunnel. The model was mounted on sting at the mid-section of the body. The pressure data was gathered from taps located along the ROBIN fuselage. Figures (4.2(a)) and (4.2(b)) show the layout of the taps. The hub shroud of the helicopter was not equipped with any taps.

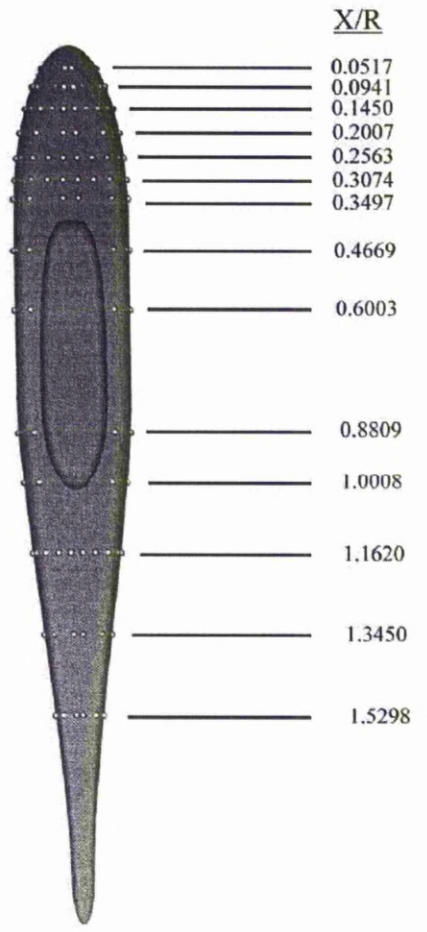

(a) Top view

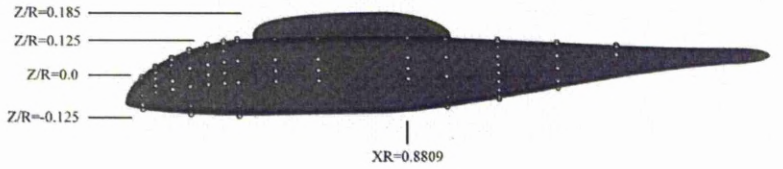

(b) Side view

Figure 4.2: Locations of the pressure taps on the ROBIN fuselage[14].

Figures (4.3(a)) - (4.3(c)) show three stations along the stream-wise axis of the ROBIN geometry. At each station, a cross section of the model with the pressure is shown compared with the computational approximation of the geometry. The measured surface pressure coefficient at each specific station is shown on the right plots.

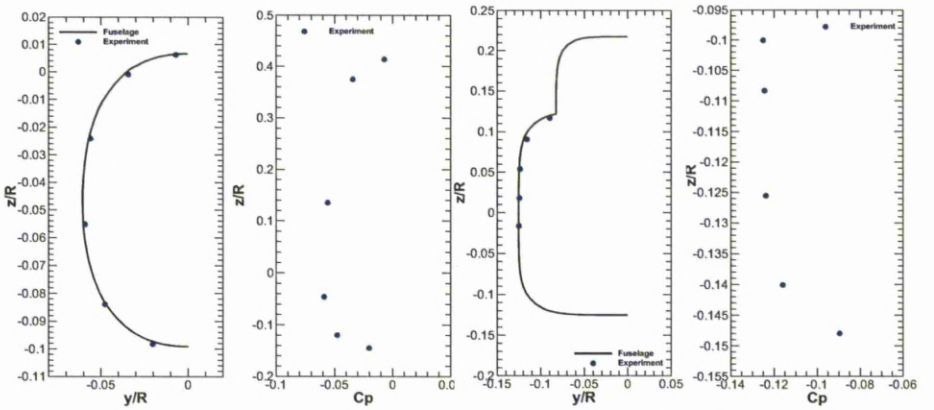

(a) Plane A

(b) Plane I

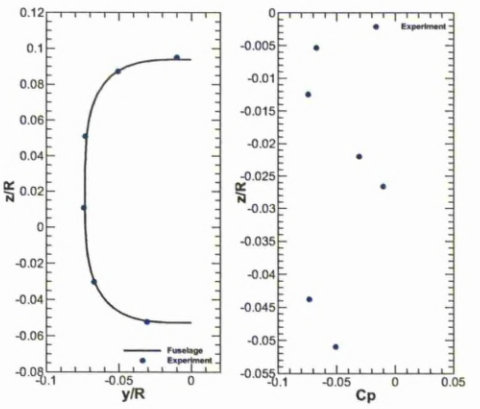

(c) Plane M

Figure 4.3: Location of the pressure taps and surface pressure distribution for different azimuth stations on ROBIN fuselage body, a=0°.

4.1.2 Grid development - ROBIN fuselage

Equations (4.1) - (4.4) produced the points of the elliptic shape and these were connected with spline curves producing the generic form of the helicopter fuselage. The fuselage is considered to be at the centre of a domain and the inflow and outflow surfaces are set to be 1.5 fuselage lengths away from the body.

Much consideration was given on the construction of the multi-block topology and an O-type grid was used. The topology was complicated by the presence of the hub shroud. The fuselage as a whole is encapsulated in a sleeve travelling between extreme ends of the fluid domain. It leaves the fuselage surface very close to the nose and the tail. In order to optimise CPU-time by concentrating points close to the surface, near- and far-field domains were created, as can be seen in figure (4.4(a)). In total, there are eight far-field, eight near-field and four sleeve blocks in each section. Figure (4.4(b)) shows a three-dimensional view of the topology for the ROBIN fuselage that includes 200 blocks.

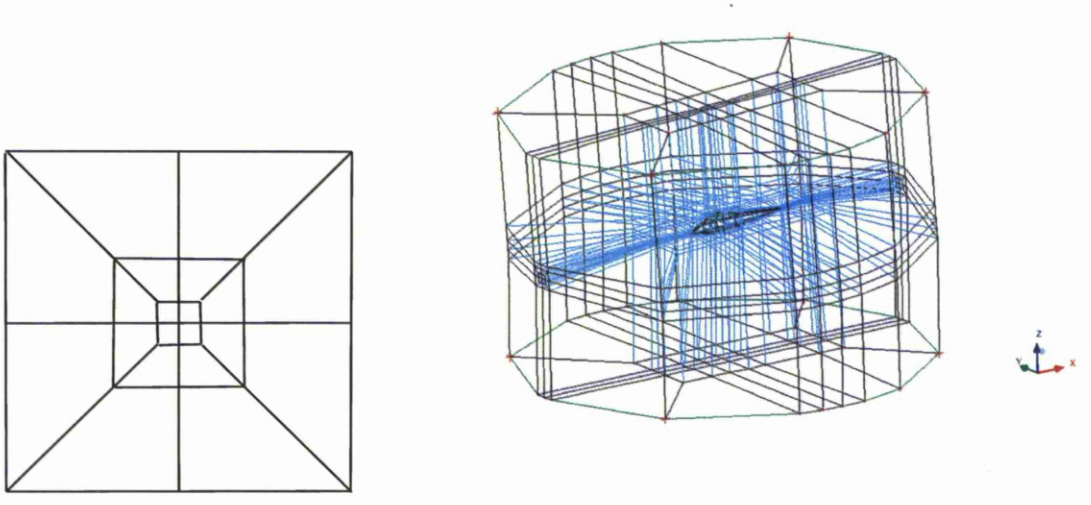

(a) Detailed (b) General

Figure 4.4: Basic idea and overview view for the ROBIN fuselage multi-block topology.

Figures (4.5(a)) and (4.5(b)) demonstrate three-dimensional views of the grid for the ROBIN fuselage. In total, the grid has 4,892,750 nodes, the majority of which were concentrated close to the surface of the body. The edges normal to the fuselage body surfaces were meshed with an exponential distribution and with a first cell distance of 1×10^{-5} fuselage lengths. A detailed view of the grid around the helicopter fuselage can be seen in figure (4.5(b)).

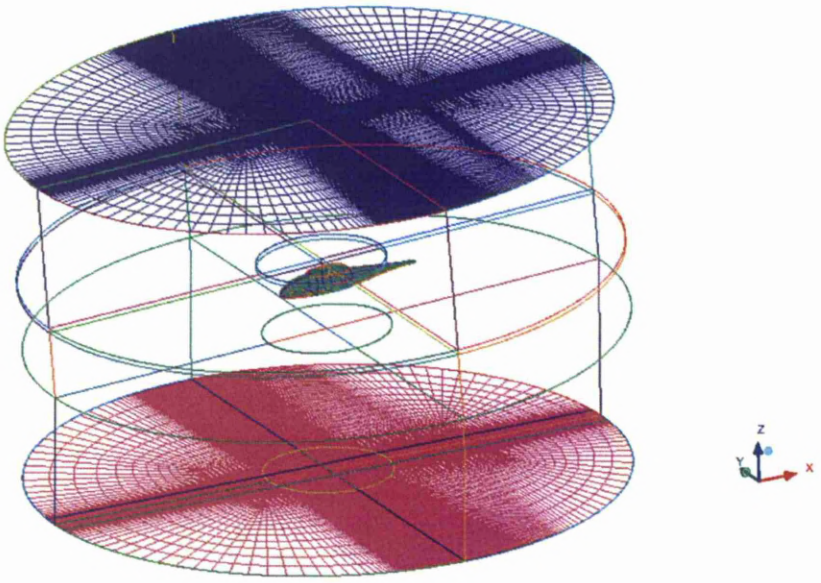

(a) General

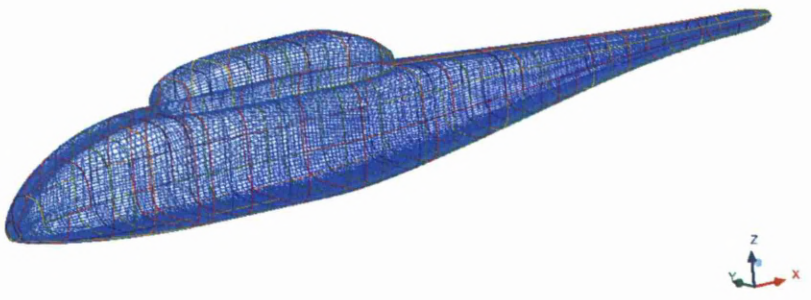

(b) Detailed

Figure 4.5: General and detailed view of the surface grid of the ROBIN fuselage.

4.1.3 Transitional Flow around the ROBIN Fuselage

For the calculations with the empirical correlation models, the flow around the ROBIN body was calculated at -5 degrees, and 5 degrees pitch angles, considering, a Mach number of 0.064 and a Reynolds number of 4.47×10^6.

The computed surface pressure coefficient distribution around the whole ROBIN body for the specific incidence angles can be seen in figures (4.6(a)) and (4.6(b)), respectively. Both figures show the existence of two stagnation points on the fuselage, one at the very front of the body and one at the hubshroud. It is obvious that for the case of -5 degrees nose down case, the fuselage presents a larger area of increased surface pressure distribution than for the case of 5 degrees.

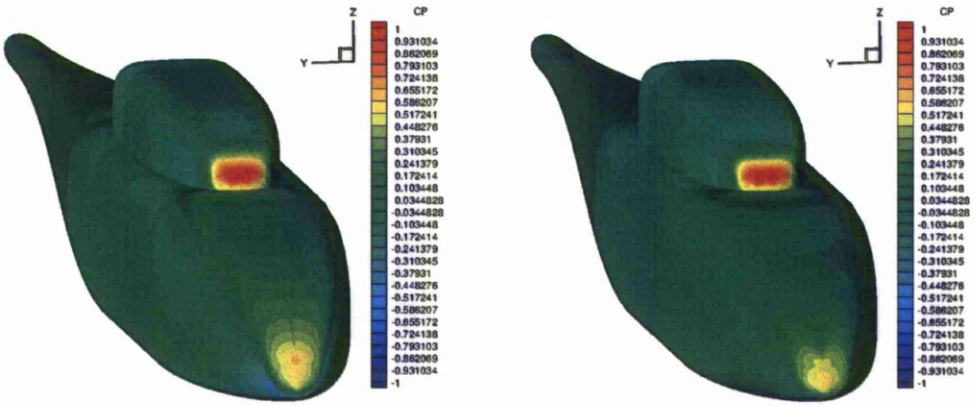

(a) α =-5 degrees (b) α =5 degrees

Figure 4.6: Surface pressure distribution around whole ROBIN fuselage ($M = 0.064, Re = 4.46 \times 10^6$).

Comparisons of the predicted surface pressure coefficients with the experimental data are presented in figures (4.7(b)) to (4.16(b)). Five stations along the streamwise coordinate of the ROBIN geometry were selected. At each longitudinal station, a cross section of the model with the pressure taps shown is compared with the computational approximation of the geometry. For each section, the surface pressure coefficient is also shown.

Figures (4.7(b)) to (4.11(b)) show the results for -5 degrees of angle of attack and the computed surface pressure distribution is in general in good agreement with the experimental data except of the first station where the computed distribution for both sides is much higher than the experimental data. This may be due to the extended increased surface pressure distribution observed previously in figure (4.6(a)) or uncertainties in the shape so near the nose. Another distinctive point is the results for the tap at station $x = 0.6003$ (figure (4.10(b))) where the sharp peak of pressure for both sides is mainly due to the intersection of the main body of the ROBIN with the doghouse and the

presence of a second stagnation point. At $x = 0.8809$ the results are in good agreement with the experimental data except for the lower portion of the body where the experimental data show to be more negative than the predictions. This discrepancy may be due to separated flow or due to the presence of the model support system of the experiment.

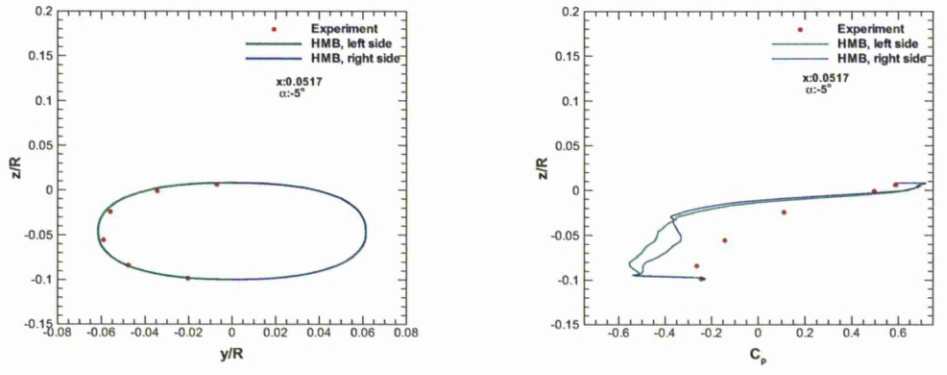

(a) Geometry (b) C_P

Figure 4.7: Comparison of experimental and computational surface pressure distributions at x=0.0517 on the ROBIN fuselage, a =-5 degrees.

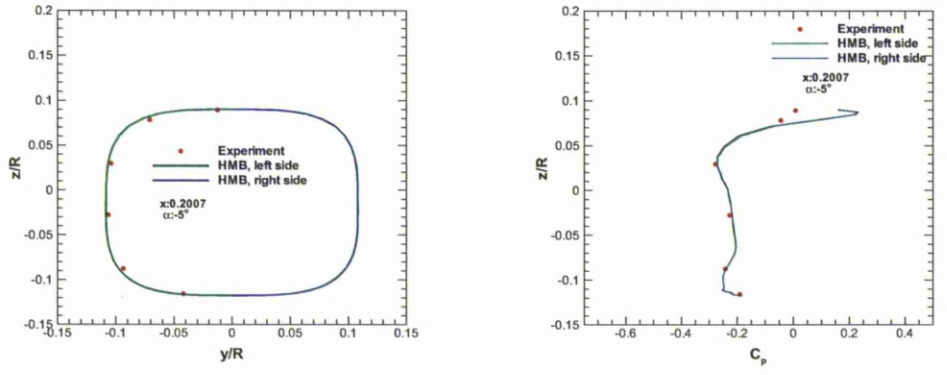

(a) Geometry (b) C_P

Figure 4.8: Comparison of experimental and computational surface pressure distributions at x=0.2007 on the ROBIN fuselage, a =-5 degrees

The surface pressure coefficient at different sections for the case of 5 degrees are presented in figures (4.12(b)) to (4.16(b)). The results for this case show similarities with those found at an angle of attack of -5 degrees. In general, the predicted pressure is in good agreement with the experiments except at the front of the fuselage for similar reasons to the -5 degrees case. At station x=0.0517, the results show similar trend with the experimental data, although the predicted surface pressure at the bottom of the body is more negative. For station x/R=0.2007, the experimental data

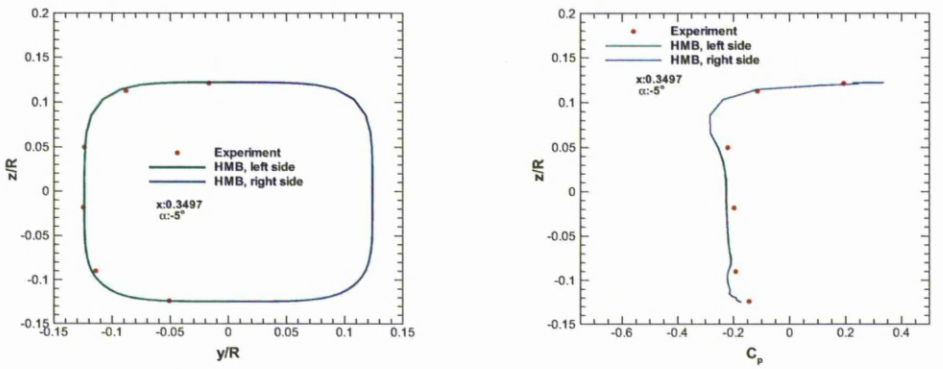

(a) Geometry (b) C_P

Figure 4.9: Comparison of experimental and computational surface pressure distributions at x=0.3497 on the ROBIN fuselage, a =-5 degrees.

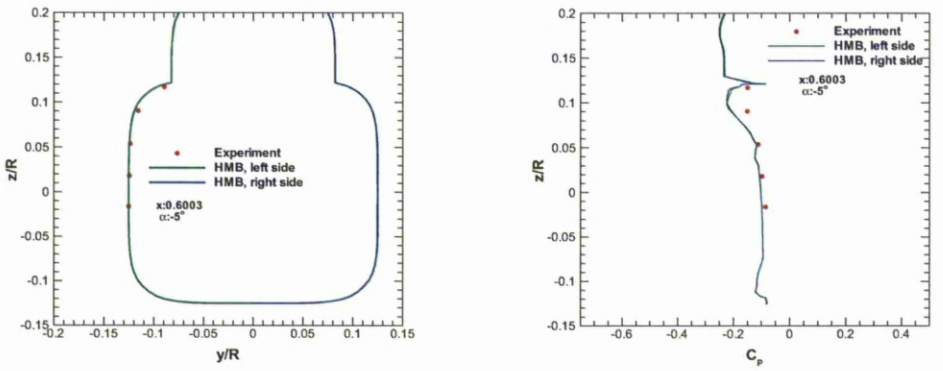

(a) Geometry (b) C_P

Figure 4.10: Comparison of experimental and computational surface pressure distributions at x=0.6003 on the ROBIN fuselage, a =-5 degrees.

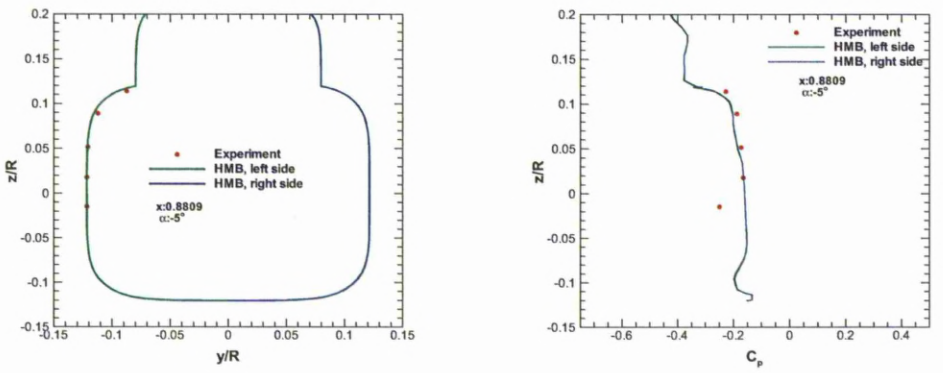

(a) Geometry (b) C_P

Figure 4.11: Comparison of experimental and computational surface pressure distributions at x=0.8809 on the ROBIN fuselage, a =-5 degrees.

show more negative surface pressure coefficient in comparison with the calculations. For the station x=0.6003, the peak pressure coefficient was observed on the upper pressure tap.

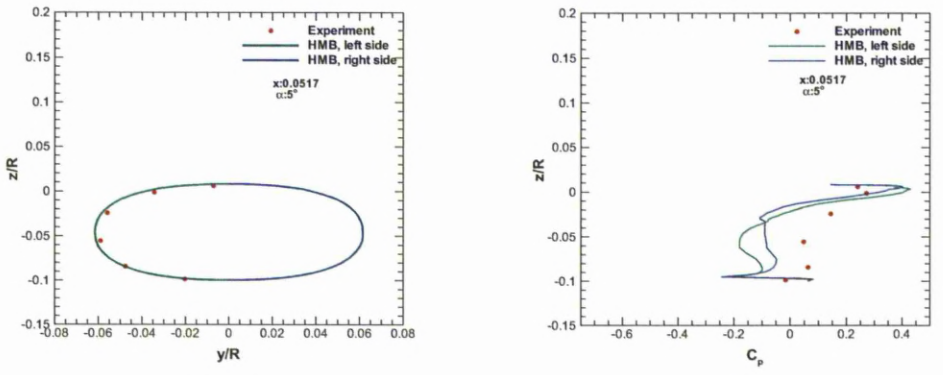

(a) Geometry (b) C_P

Figure 4.12: Comparison of experimental and computational surface pressure distribution at x=0.0517 on the ROBIN fuselage, a =5 degrees.

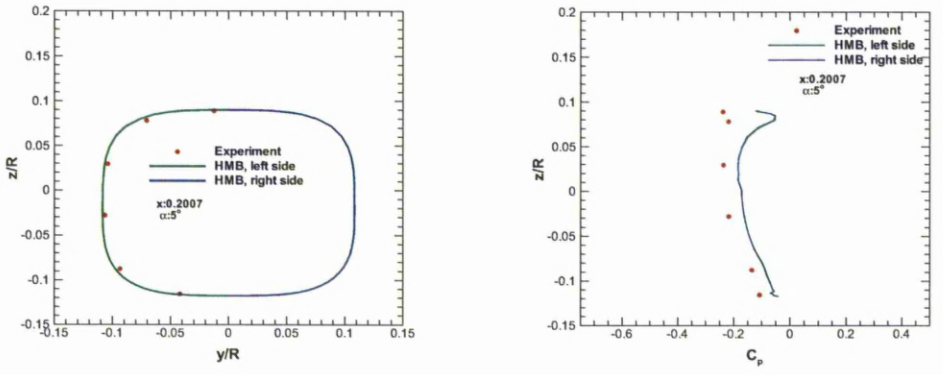

(a) Geometry (b) C_P

Figure 4.13: Comparison of experimental and computational surface pressure distribution at x=0.2007 on the ROBIN fuselage, a =5 degrees.

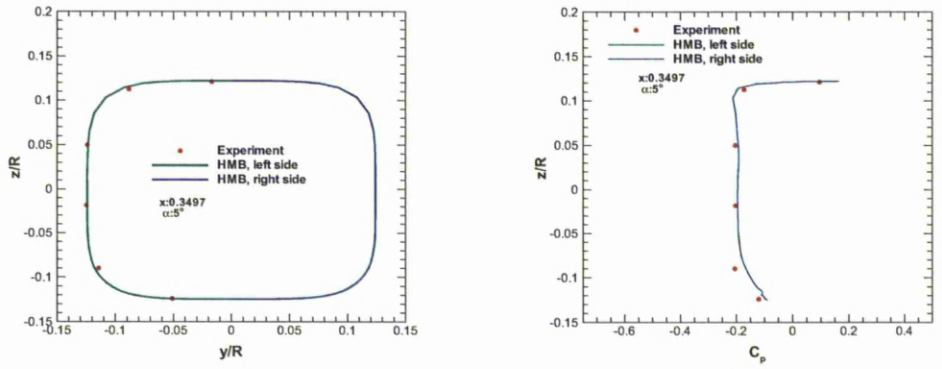

(a) Geometry (b) C_P

Figure 4.14: Comparison of experimental and computational surface pressure distribution at x=0.3497 on the ROBIN fuselage, a =5 degrees.

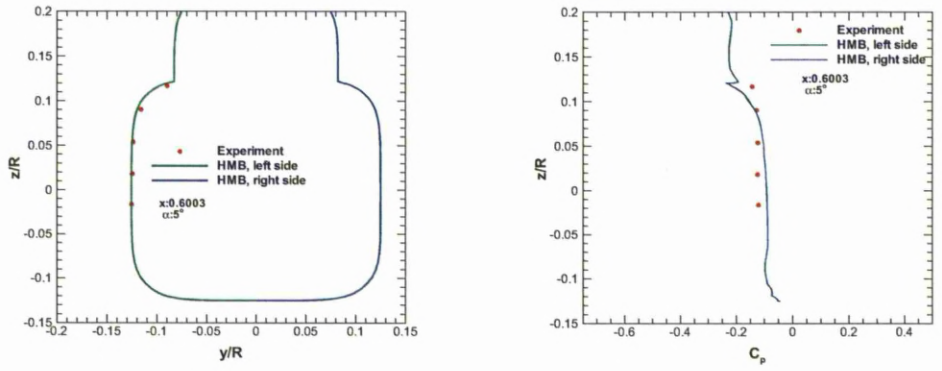

(a) Geometry (b) C_P

Figure 4.15: Comparison of experimental and computational surface pressure distribution at x=0.6003 on the ROBIN fuselage, a =5 degrees.

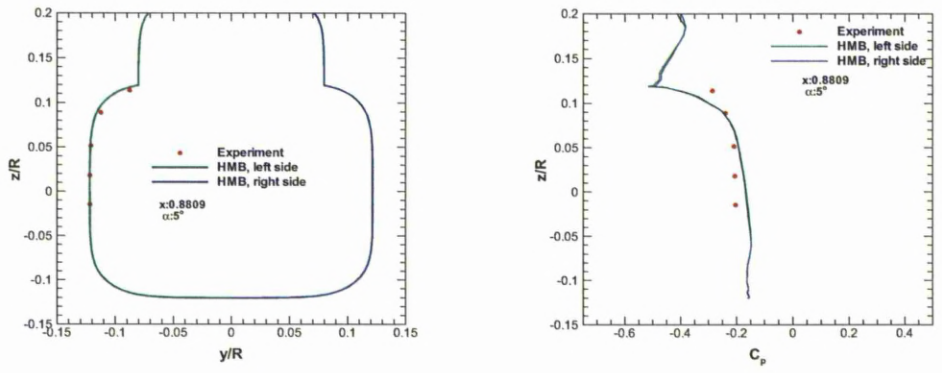

(a) Geometry (b) C_P

Figure 4.16: Comparison of experimental and computational surface pressure distribution at x=0.8809 on the ROBIN fuselage, a =5 degrees.

Empirical Transition Models over ROBIN fuselage

Based on the previous results for the surface distribution at different stations alongside the fuselage body, the transition location was calculated with the use of the empirical methods and is presented in the following figures. As the empirical correlation transition models requires the flow to be mainly two-dimensional, five different longitudinal slices were selected, three on the fuselage and two on the hubshroud. The z coordinates of each slice are presented in table (4.3) and seen in figure (7.12). With this method the three dimensional shape of the fuselage body can be manipulated as a two-dimensional shape. For each slice, the location of transition onset was estimated using the models of Michel, Cebeci and Smith and Abu-Ghannam and Shaw.

Slice	z
1	-0.004426
2	0.002182
3	0.0795
4	0.1415
5	0.1724

Table 4.3: Slices of ROBIN fuselage.

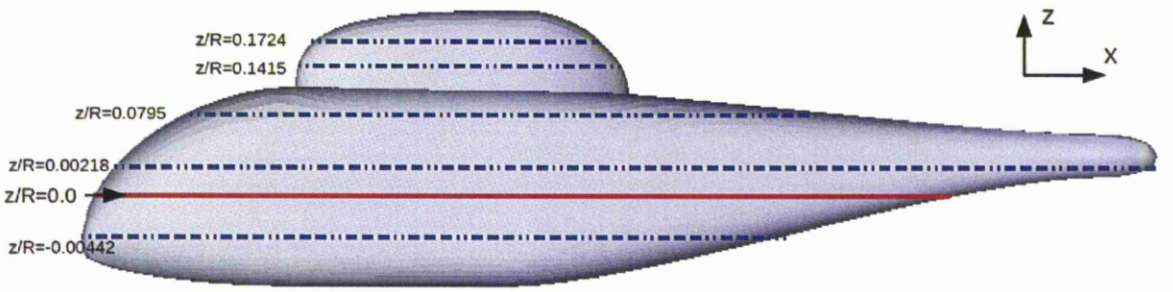

Figure 4.17: Slices of ROBIN fuselage.

As can be seen from figures (4.18(a)) and (4.19(a)), the onset of transition occurred at about 20% along the main part of fuselage body. Similar results are also observed also for the case of 5 degrees nose down, figures (4.18(b)) and (4.19(b)) respectively. When the Abu-Ghannam and Shaw model was used, the onset of transition occurred slightly earlier. The results for the end of transition based on Abu-Ghannam and Shaw model where based

on different parameters of the correlation, the method predicts the end of transitional flow after the 60% of the body. The results based on the Abu-Ghannam and Shaw model can be seen in figures (4.20(a)) and (4.21(a)) for -5 degrees and (4.20(b)) and (4.21(b)) for 5 degrees. These figures present also the sensitivity of the Abu-Ghannam and Show model to its parameters. Considering that the end of transition is given by the equation $Re_{xE} = a \cdot Re_{xS} + b \cdot (Re_{xS})^c$ and providing different values for the parameter c, the length of the transition region can be increased with transition to occurs in half of the fuselage body.

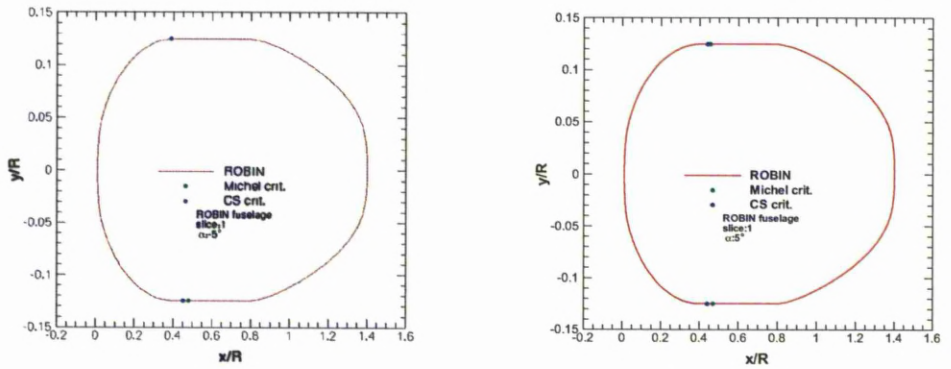

(a) $1^{st} Slice, angle: -5$ degrees (b) $1^{st} Slice, angle: 5$ degrees

Figure 4.18: Transition location for the first slice of the ROBIN fuselage. Calculations are for Michel criterion and Cebeci and Smith method. (z = -0.004426)

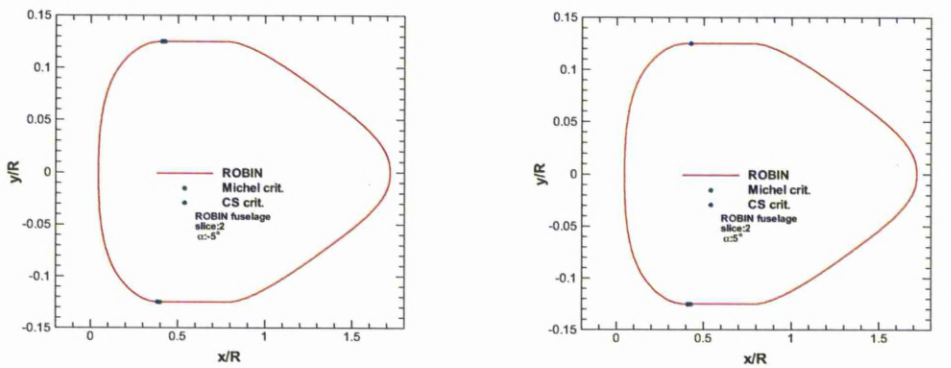

(a) $2^{nd} Slice, angle: -5$ degrees (b) $2^{nd} Slice, angle: 5$ degrees

Figure 4.19: Transition location for the second slice of the ROBIN fuselage. Calculations are for Michel criterion and Cebeci and Smith method. (z = 0.002182)

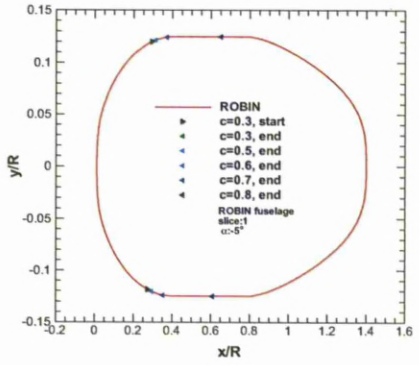

(a) $1^{st} Slice, angle$: -5 degrees

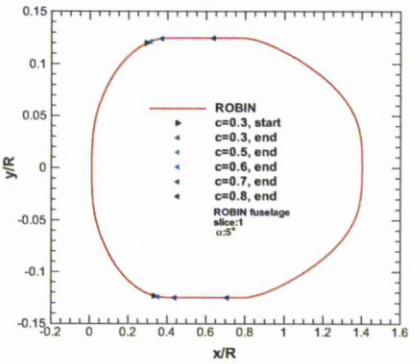

(b) $1^{st} Slice, angle$: 5 degrees

Figure 4.20: Transition location for the first slice of the ROBIN fuselage. Calculations based on the Abu-Ghannam and Shaw criterion. (z = -0.004426)

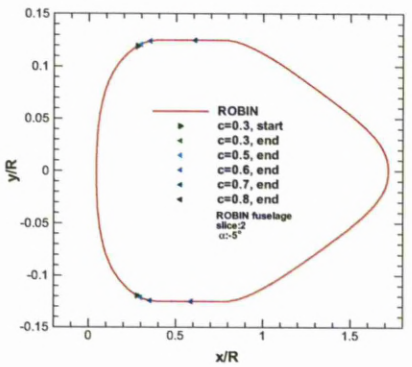

(a) $2^{nd} Slice, angle$: -5 degrees

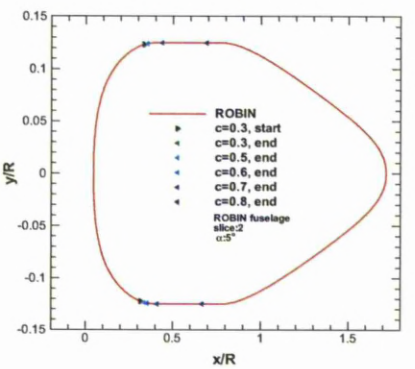

(b) $2^{nd} Slice, angle$: 5 degrees

Figure 4.21: Transition location for the second slice of the ROBIN fuselage. Calculations based on the Abu-Ghannam and Shaw criterion. (z = 0.002182)

The transition location at -5 degrees is predicted at about half way along the fuselage. The Cebeci and Smith model, estimates the onset of transition earlier than the Michel criterion due to the lower values of momentum thickness Reynolds number that produced. On the other hand, for these pitch angles, the calculations based on the Abu-Ghannam and Shaw method show a slight earlier onset of transition from the other two empirical criteria (Michel and Cebeci Smith criteria). The transitional flow based on Abu-Ghannam and Shaw method occupies 25% of the doghouse length.

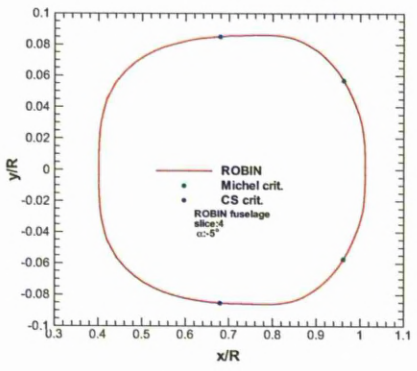

(a) $4^{th}Slice, angle$: -5 degrees

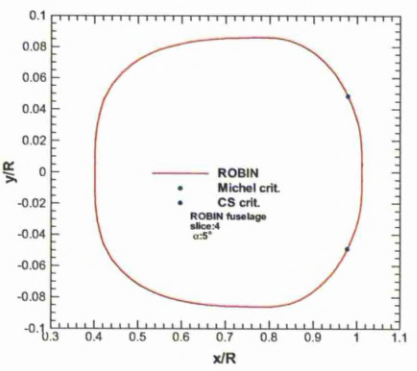

(b) $4^{th}Slice, angle$: 5 degrees

Figure 4.22: Transition location for the fourth slice of the ROBIN fuselage. Calculations are for Michel criterion and Cebeci and Smith method. (z = 0.1415)

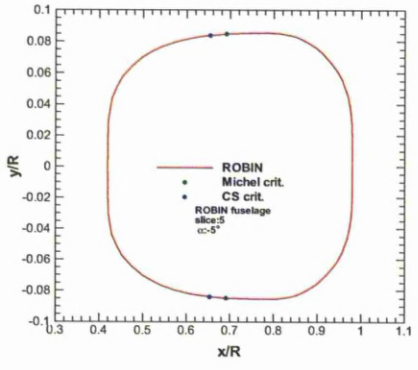

(a) $5^{th}Slice, angle$: -5 degrees

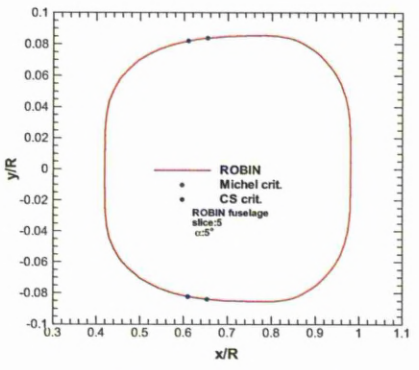

(b) $5^{th}Slice, angle$: 5 degrees

Figure 4.23: Transition location for the fifth slice of the ROBIN fuselage. Calculations are for Michel criterion and Cebeci and Smith method. (z = 0.1724)

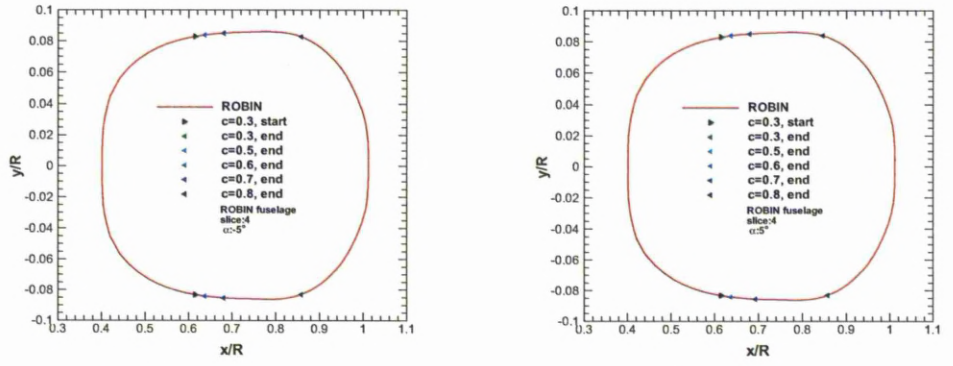

(a) $4^{th}Slice, angle: -5$ degrees

(b) $4^{th}Slice, angle: 5$ degrees

Figure 4.24: Transition location for the fourth slice of the ROBIN fuselage. Calculations based on the Abu-Ghannam and Shaw criterion. (z = 0.1415)

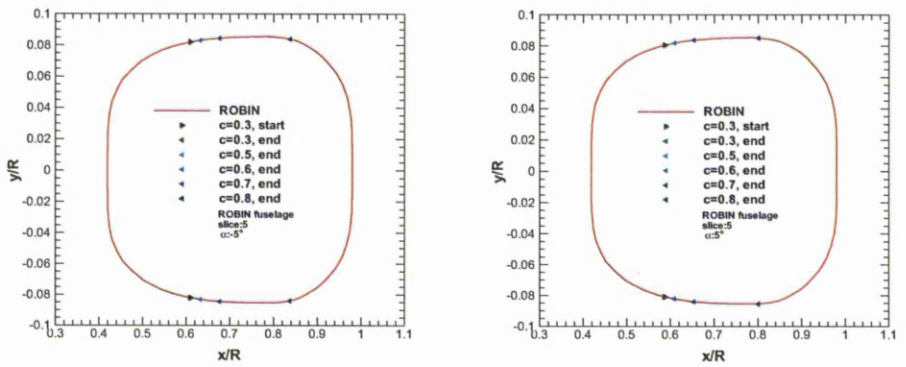

(a) $5^{th}Slice, angle: -5$ degrees

(b) $5^{th}Slice, angle: 5$ degrees

Figure 4.25: Transition location for the fifth slice of the ROBIN fuselage. Calculations based on the Abu-Ghannam and Shaw criterion. (z = 0.1724)

The previous results can be explained if the Reynolds number produced from Michel's (Re_{Mich}) and Cebeci and Smith ($Re_{Cebeci-Smith}$) criteria alongside the body of the fuselage are compared to the momentum thickness Reynolds number (Re_θ). Based on the conditions on each slide, the Reynolds number increases and the location where the curves from each model cross for the first time, shows the onset of transition. in all cases, the Cebeci and Smith criterion estimates the onset of transition earlier than when the Michel criterion is used. The comparison of the momentum thickness Reynolds number from the different transition models can be seen in the following figures.

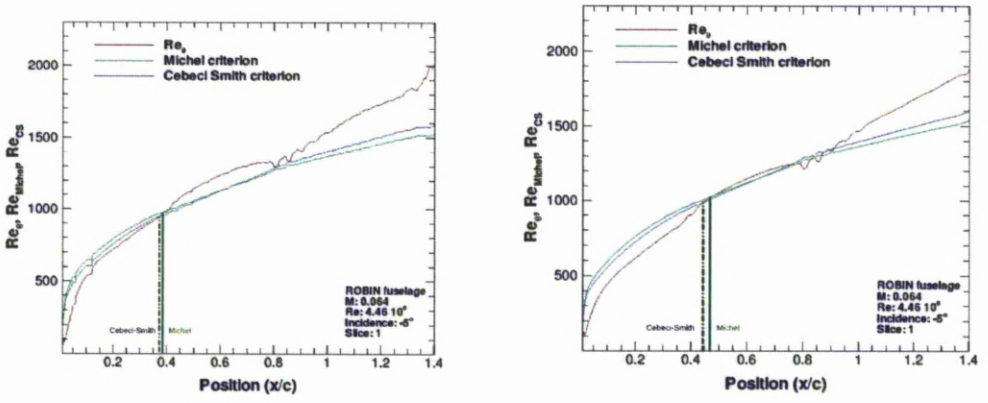

(a) Left side (b) Right side

Figure 4.26: Presentation of $Re_\theta - Re_{Michel} - Re_{Cebeci-Smith}$ for the left and the right side on the ROBIN fuselage ($1^{st} Slice, angle$: -5 degrees).

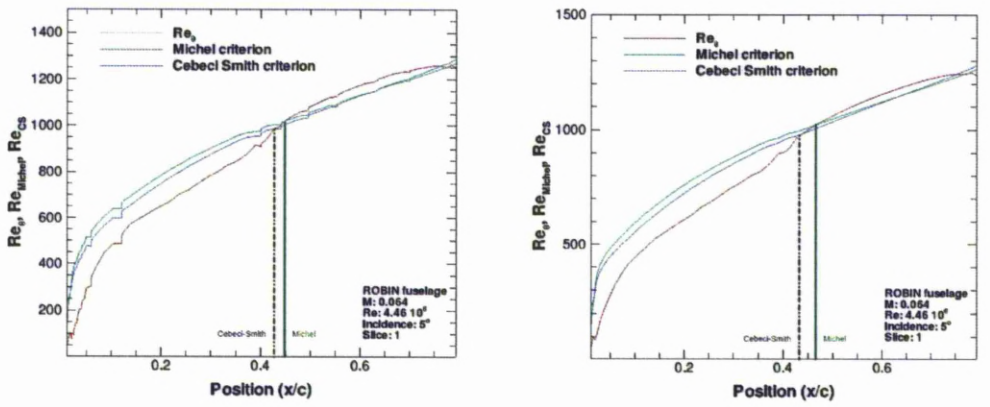

(a) Left side (b) Right side

Figure 4.27: Presentation of $Re_\theta - Re_{Michel} - Re_{Cebeci-Smith}$ for the left and the right side on the ROBIN fuselage ($1^{st} Slice, angle$: 5 degrees).

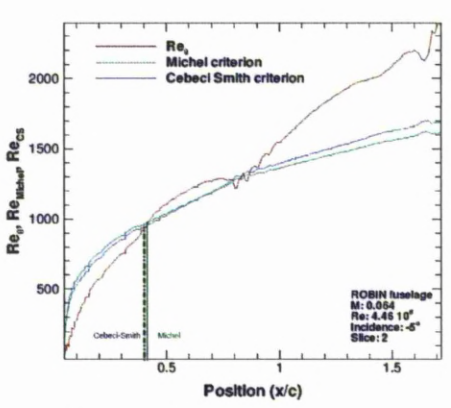

(a) Left side

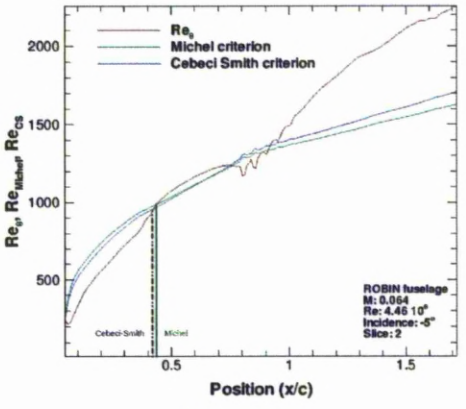

(b) Right side

Figure 4.28: Presentation of $Re_\theta - Re_{Michel} - Re_{Cebeci-Smith}$ for the left and the right side on the ROBIN fuselage ($2^{st} Slice, angle$: -5 degrees).

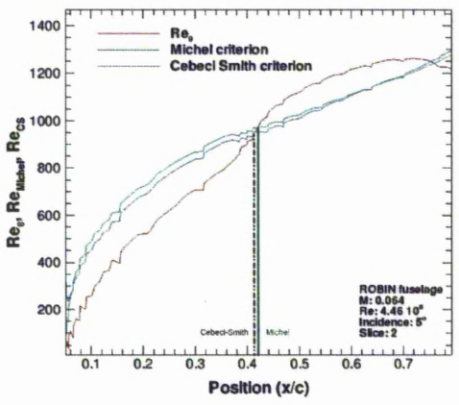

(a) Left side

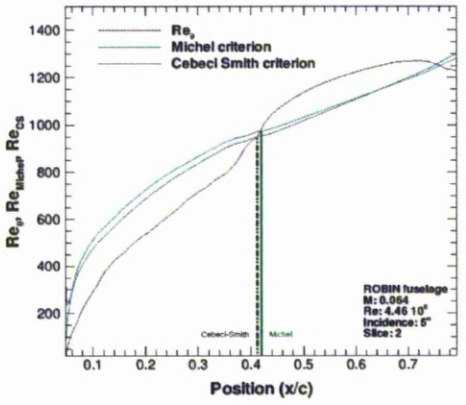

(b) Right side

Figure 4.29: Presentation of $Re_\theta - Re_{Michel} - Re_{Cebeci-Smith}$ for the left and the right side on the ROBIN fuselage ($2^{st} Slice, angle$: 5 degrees).

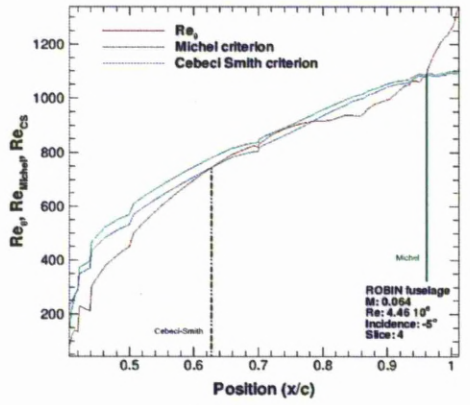

(a) Left side

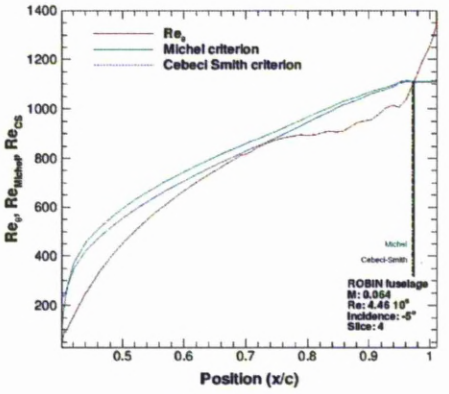

(b) Right side

Figure 4.30: Presentation of $Re_\theta - Re_{Michel} - Re_{Cebeci-Smith}$ for the left and the right side on the ROBIN fuselage ($4^{th} Slice, angle$: -5 degrees).

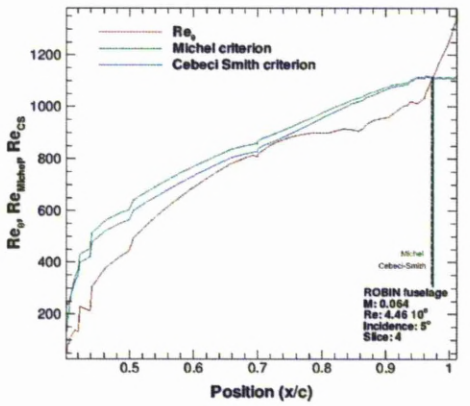

(a) Left side

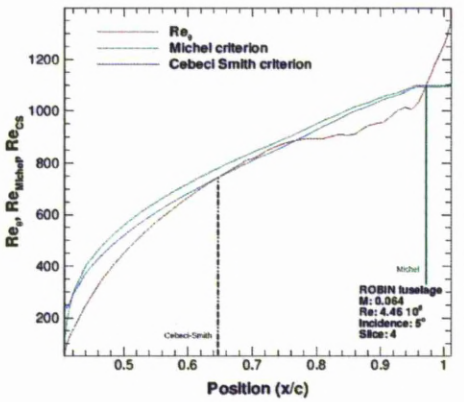

(b) Right side

Figure 4.31: Presentation of $Re_\theta - Re_{Michel} - Re_{Cebeci-Smith}$ for the left and the right side on the ROBIN fuselage ($4^{th} Slice, angle$: 5 degrees).

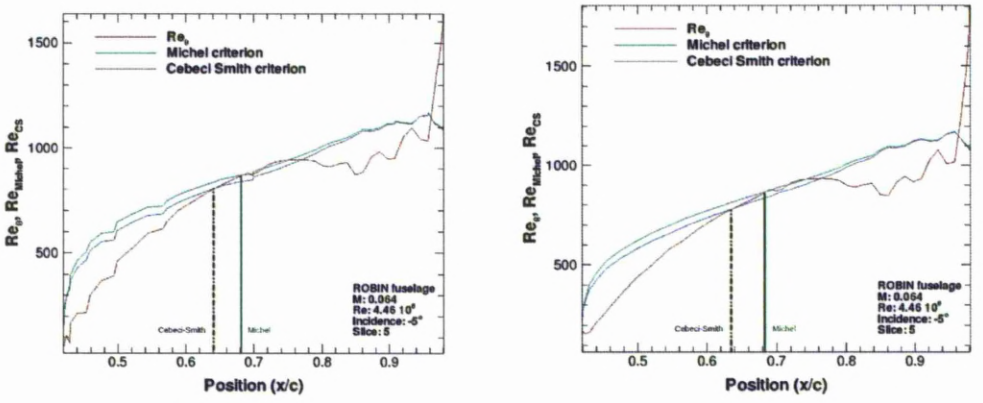

(a) Left side (b) Right side

Figure 4.32: Presentation of $Re_\theta - Re_{Michel} - Re_{Cebeci-Smith}$ for the left and the right side on the ROBIN fuselage ($5^{th} Slice, angle$: -5 degrees).

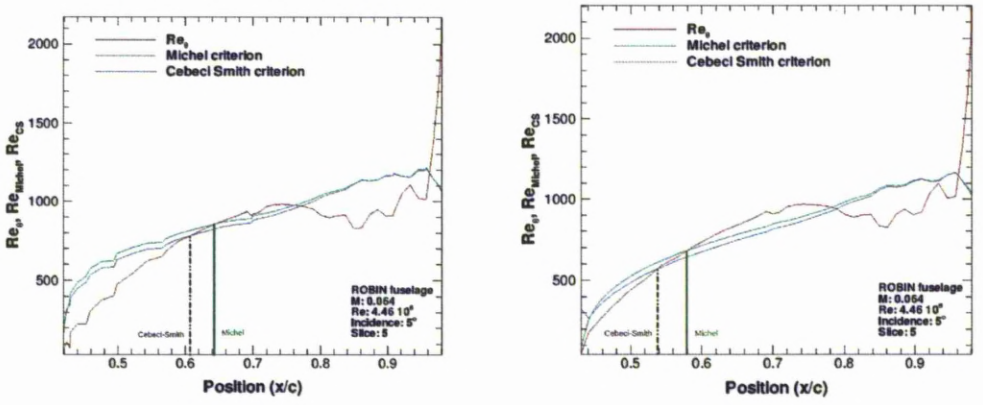

(a) Left side (b) Right side

Figure 4.33: Presentation of $Re_\theta - Re_{Michel} - Re_{Cebeci-Smith}$ for the left and the right side on the ROBIN fuselage ($5^{th} Slice, angle$: 5 degrees).

Empirical Transition Models over ROBIN fuselage using streamline

In order to calculate the onset of transition, another way was used with surface streamline to considered. Following the streamline, the empirical criteria of Michel and Cebeci and Smith were activated and the onset of transition was calculated at the location where the momentum thickness Reynolds number exceeded the criteria. A number of streamlines was selected, starting from the middle of y/R axis and increased anti-clockwise till it reached again the initial point.

Figures (4.34(a)) ,(4.34(b)), (4.35(a)) and (4.35(b)) present the onset of the transitional flow using the empirical correlation of Michel and Cebeci and Smith for -5 degrees. The results agree well with the outcome from the technique with the slices, as transition occurs at the middle of the fuselage body. Moreover, for the range of the current Reynolds number, the Cebeci and Smith correlation predicts the transition onset earlier than Michel's criterion. This was also seen at the technique with the slices. As seen for figure (4.34(b)), the distance between the points where the two empirical criteria estimate the transition onset, for the case of -5 degrees nose down angle, can reach 10% of the fuselage body.

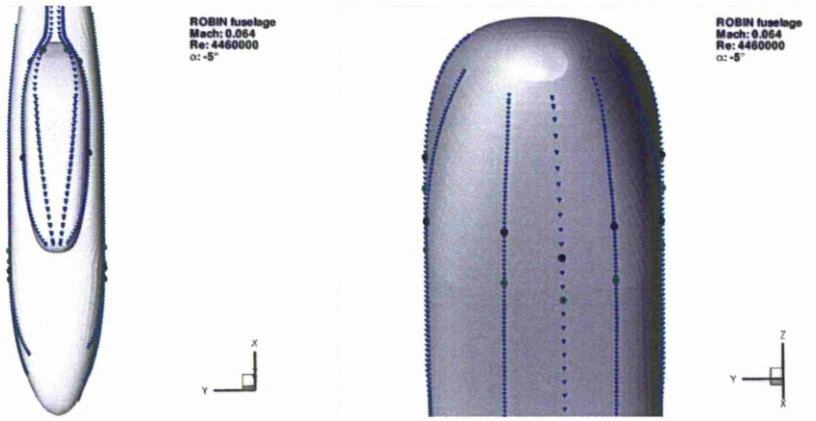

(a) Top side (b) Bottom side

Figure 4.34: Transition points for the -5 degrees nose down angle of the ROBIN fuselage body using streamlines. Results correspond to Michel's criterion (green dots) and Cebeci-Smith method (black dots).

Figures (4.36(a)) - (4.36(c)) present the results from the empirical correlations which provided the transition points. The momentum thickness Reynolds number increases and at around the 20% along the body, it crosses the momentum thickness Reynolds number based on Michel's and Cebeci and Smith models.

The ROBIN fuselage was also tested for the case of 3 degrees nose down. As can be seen in figures (4.1.3) and (4.38(a)) - (4.38(b)), the transition location occurs at the first half of the fuselage and based on the information

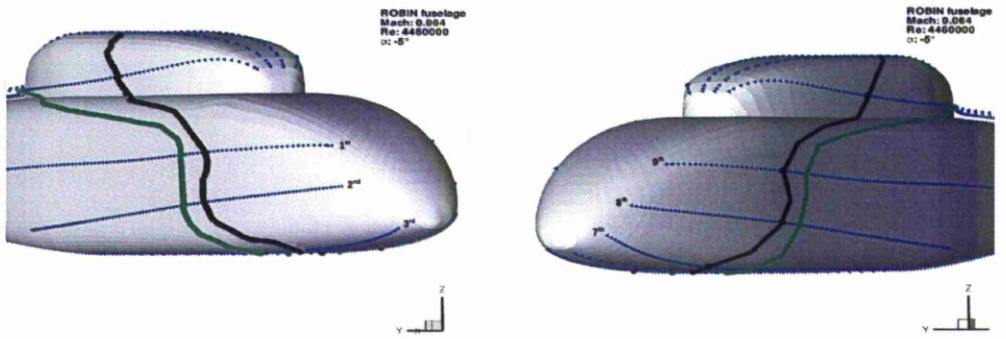

(a) Left side (b) Right side

Figure 4.35: Transition points for the -5 degrees nose down angle of the ROBIN fuselage body using streamlines. Results correspond to Michel's criterion (green dots) and the Cebeci-Smith method (black dots) for the left and right surface of the fuselage.

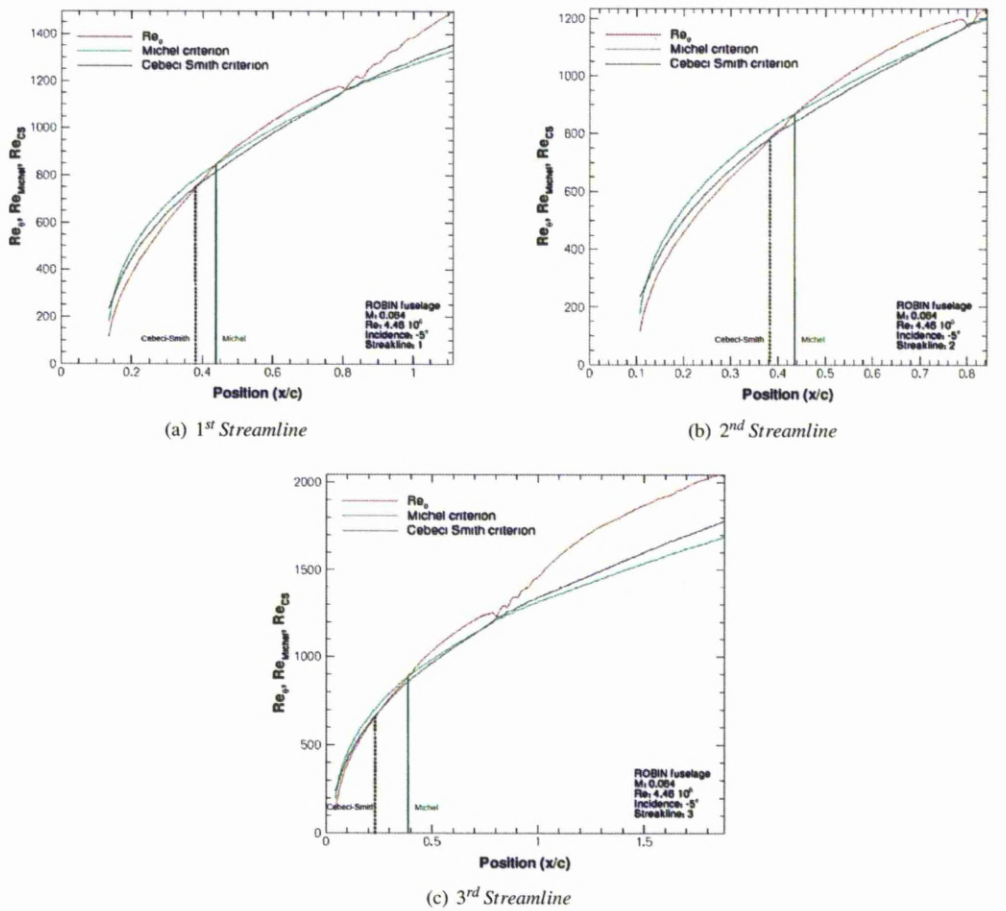

(a) 1^{st} *Streamline*

(b) 2^{nd} *Streamline*

(c) 3^{rd} *Streamline*

Figure 4.36: Presentation of $Re_\theta - Re_{Michel} - Re_{Cebeci-Smith}$ for different streamlines on the ROBIN fuselage (-5 degrees case).

derived from figures (4.39(a)) - (4.39(b)), the onset of transition can be estimated at the 20% of the body length. For the bottom surface of the body, the transition was initiated at 20% of the length of the fuselage. As streamlines closer to the doghouse of the helicopter are selected, the onset of transition moved at about 40% of the body length. On the doghouse of the fuselage the transition initiates almost mid-way along its length. This is due to a second stagnation point that is observed at the front of the doghouse and the increased pressure distribution of the area.

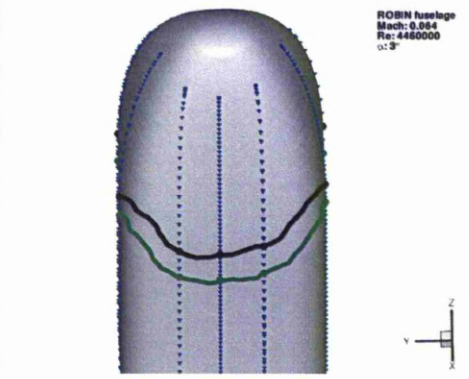

Figure 4.37: Transition points for the 3 degrees nose down angle of the ROBIN fuselage body using streamlines. Results correspond to Michel's criterion (green dots) and Cebeci-Smith method (black dots) for the lower surface of the fuselage.

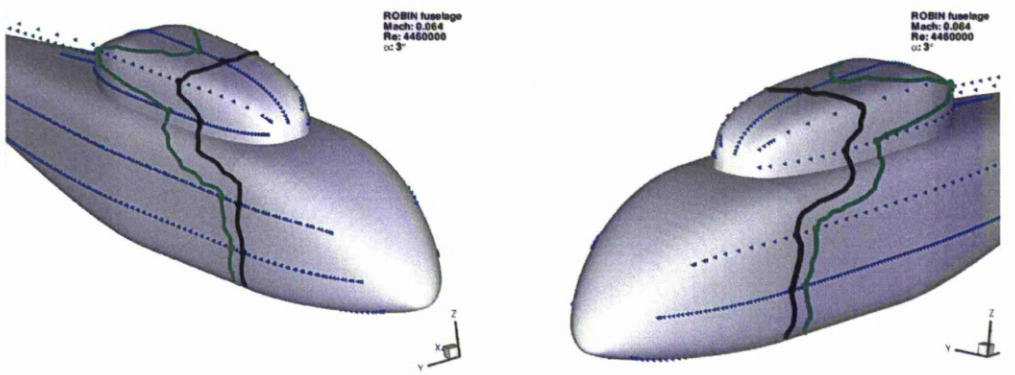

(a) Left side (b) Right side

Figure 4.38: Transition point for the 3 degrees nose down angle of the ROBIN fuselage body using the streamlines. The results are correspond to the Michel criterion (green dots) and Cebeci-Smith method (black dots) for the left and right surface of the fuselage.

$\kappa-\omega-\gamma-Re_{\theta t}$ Model over ROBIN fuselage using streamline

The ROBIN fuselage was also used as a three-dimensional case to validate the $\kappa-\omega-\gamma-Re_{\theta t}$ model. The calculations were performed for an incidence angle of 0 degrees. The convergence history of the calculations can be seen

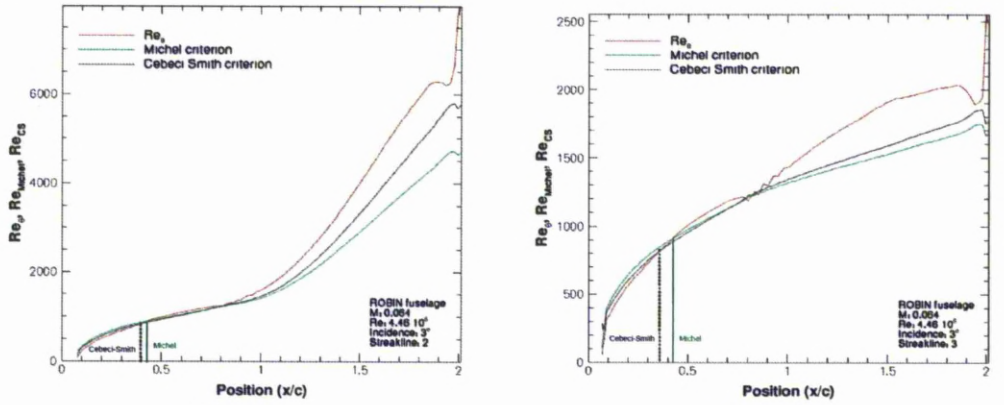

(a) 2^{nd} *Streamline* (b) 3^{rd} *Streamline*

Figure 4.39: Presentation of $Re_\theta - Re_{Michel} - Re_{Cebeci-Smith}$ for different streamlines on the ROBIN fuselage (3 degrees case).

in figures (4.40(a)) and (4.40(b)) for fully turbulent and transition calculations, respectively. Each figure presents the residuals as a function of iterations are presented with Residual-1 to be the one for the RANS equations, Residual-2 for the turbulent model, while Residual-3 to be the residual for the transition model. As residuals, the square root of the inner product (l^2-norm) of each of the variables of the equations is considered. Cpu-time, the fully turbulent calculations required almost half time in comparison to the $\kappa - \omega - \gamma - Re_{\theta t}$ model to reached a 10^{-5} residual, with 25min and 10.5sec for fully turbulent to 43min and 57.5sec for the transitional calculations.

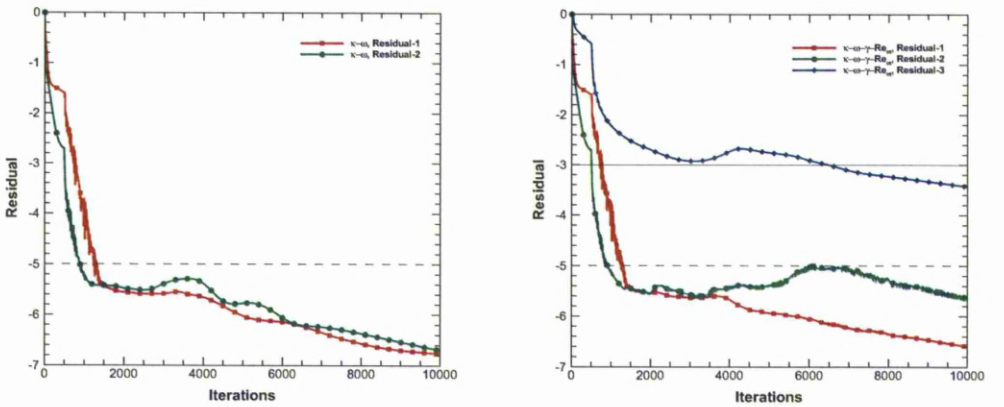

(a) Fully Turbulent $\kappa - \omega$ (b) $\kappa - \omega - \gamma - Re_{\theta t}$

Figure 4.40: Residuals as a function of iterations for the flow around a ROBIN fuselage. Comparison between the results from fully turbulent $\kappa - \omega$ and from a $\kappa - \omega - \gamma - Re_{\theta t}$ solution. Residual-1 is the residual for the RANS equations while Residual-2 is for the turbulent model. The residual for the transition model is given by the name Residual-3.

The transitional flow on the fuselage resulted in a 5.15% lift production compared to the fully turbulent solution.

A slight reduction of friction drag for 4.13% was occurred with the use of the $\kappa-\omega-\gamma-Re_{\theta t}$ model. Average values of lift and drag can be seen on table (4.4) while plots of the lift and friction drag coefficients for the ROBIN is shown in figures (4.41(a)) and (4.41(b)).

	Fully Turbulent	$\kappa-\omega-\gamma-Re_{\theta t}$
C_L	$7.796\ 10^{-4}$	$7.395\ 10^{-4}$
C_{Df}	$1.264\ 10^{-4}$	$1.212\ 10^{-4}$

Table 4.4: Lift and friction drag values for the ROBIN fuselage based on total surface of body.

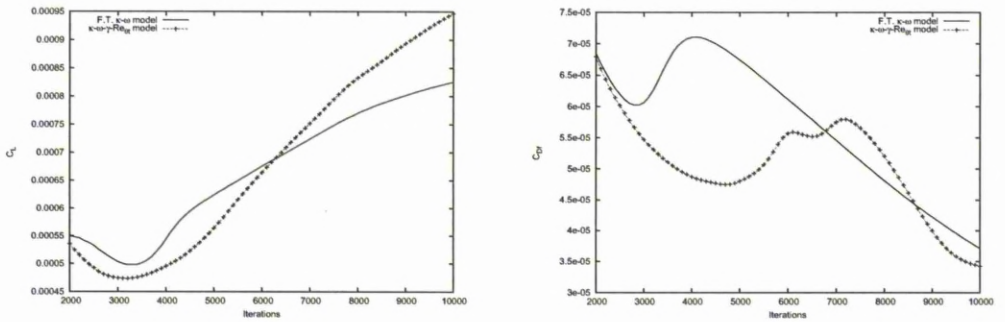

(a) Lift Coefficient

(b) Friction Drag Coefficient

Figure 4.41: Lift and friction drag distributions around whole ROBIN fuselage. Comparison between the fully turbulent $\kappa-\omega$ and the $\kappa-\omega-\gamma-Re_{\theta t}$ model ($M=0.064, Re=4.46\times10^6$).

The calculated surface pressure distribution around the ROBIN fuselage can be seen in figure (4.1.3). Both figures show the existence of two stagnation points on the fuselage, one at the very front of the body and one at the hubshroud.

The predicted turbulence Reynolds number for a fully turbulent and transitional solution is shown in figures (4.1.3). The main differences in the transitional solution are the front part of the fuselage and hubshroud are more laminar. The onset of transition is estimated at 26% of the main part of fuselage body while for the hubshroud, 48% of the body remains laminar.

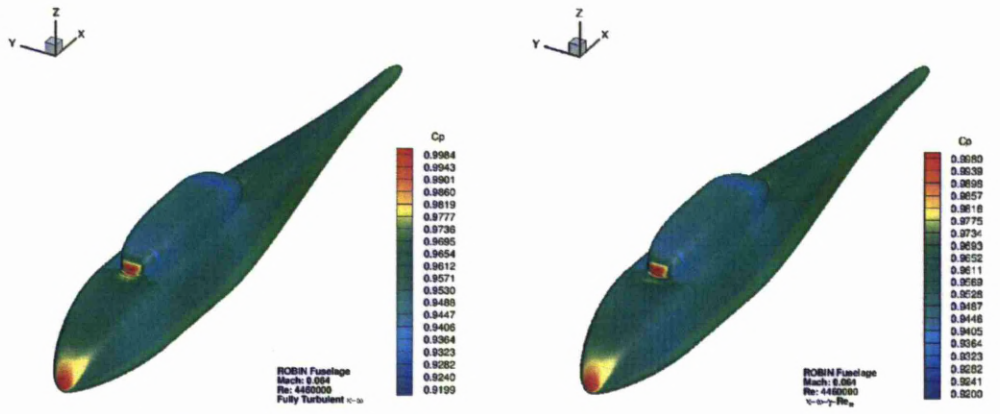

(a) Fully Turbulent $\kappa-\omega$ (b) $\kappa-\omega-\gamma-Re_{\theta t}$

Figure 4.42: Surface pressure distribution around whole ROBIN fuselage. Comparison between the fully turbulent $\kappa-\omega$ and the $\kappa-\omega-\gamma-Re_{\theta t}$ model ($M=0.064, Re=4.46\times10^6$).

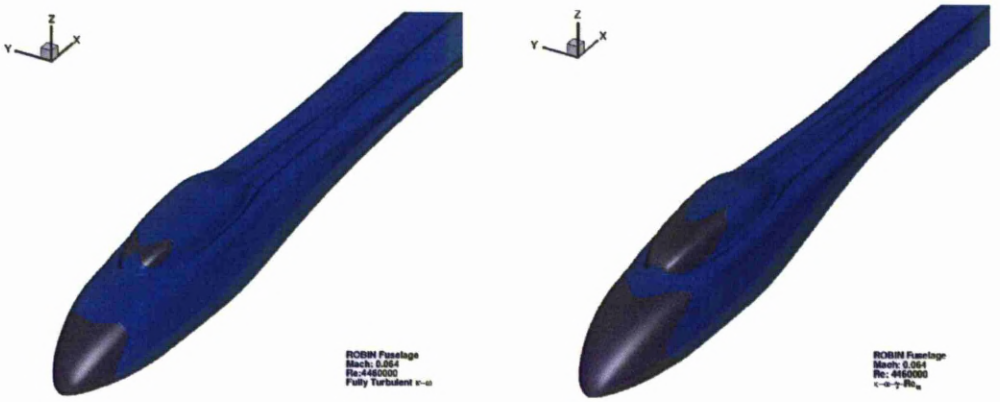

(a) Fully Turbulent $\kappa-\omega$ (b) $\kappa-\omega-\gamma-Re_{\theta t}$

Figure 4.43: Isosurfaces of turbulence Reynolds number around ROBIN fuselage. Comparison between the fully turbulent $\kappa-\omega$ and the $\kappa-\omega-\gamma-Re_{\theta t}$ model ($M=0.064, Re=4.46\times10^6$).

4.2 UH-60A Rotor

As a first configuration for the rotor test cases, a four bladed rotor system of the Blackhawk helicopter was selected. The UH-60A rotor is one of the more tested rotors[89]. Two aerofoil profiles, SC-1095 and SC-1095R8, are used to construct the surface definition of each blade. The features of the blade can be seen in figure (4.44(a)). The blade has a linear twist over the first 80% R[90]. The flow of the UH-60A rotor is interesting due to the swept-tip and the non-linear twist at the tip of the blade. Figure (4.44(b)) presents the twist distribution used in this work.

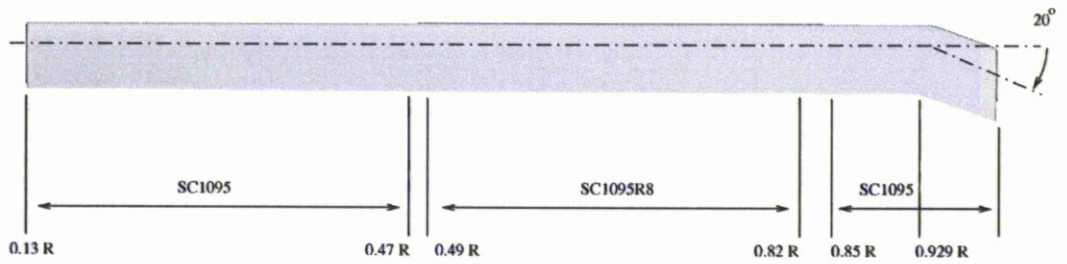

(a) UH-60A rotor blade.

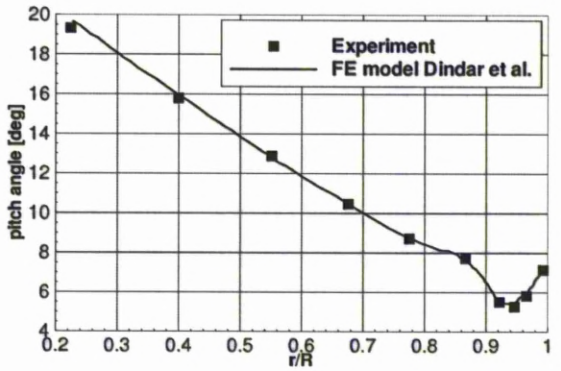

(b) Twist distribution.

Figure 4.44: Geometry of UH-60A rotor blade; nonlinear twist according to Dindar et al. [90].

4.2.1 Grid development - UH-60A Rotor

Mesh generation and mesh quality are of fundamental importance in all aerodynamics simulations and even more in rotorcraft. The construction of a mesh around a rotor case has to follow a specific procedure. In order to save computational effort, the symmetry of the rotor system is used. If the rotor at hand is a four bladed rotor, ninety degrees of azimuth is meshed with the rotor blade placed at the centre of the mesh. The rotor is considered to be at the centre of a tube. The outer surface of mesh is defined as the far-field of the computational domain. The two cut through sections are denoted as symmetry surfaces. The mesh points on these surfaces have to be identical. The top surface where the flow enters the tube is known as the inflow and the lower surface is denoted as outflow. The hub of the rotor is placed where the two symmetry planes intersect. Moreover, slices are placed between the two symmetry surfaces at every station where a blade section is defined. The domain geometry and the grid topology for the forward flight UH-60A rotor is shown in figures (4.45(a)) and (4.45(b)) respectively.

The rotor blade is modelled in space so that the point of azimuthal rotation lay upon the origin of the system. The blade was positioned so that the blade pitch axis is aligned with the quarter chord line which was positioned along the x-axis. The z-axis runs vertically in the plane between the inflow and the outflow surfaces and the y-axis runs parallel to the inflow and outflow surfaces. The chord of the blade was unit of length and everything was scaled relative to this. A C-grid is used around the aerofoil and steps similar to the creation of a 2-dimensional topologies.

The blade for the UH-60A rotor consists of two different aerofoil sections, the SC-1095 and the SC-1095R8. The inboard section runs from 0.1925R to 0.4658R and uses the SC-1095 section. Between 0.4658R and 0.4969R, a linear transition into the section SC-1095R8 is used which continues to 0.823R. Another linear transition occurs from 0.823R to 0.854R where the blade section is again the SC-1095 aerofoil. The blade finishes into a swept tip. This is achieved by rotating the section about the trailing edge at 0.9286R for 20 degrees. The total number of grid points for the UH-60A rotor is 7,980,000 points. Experience has shown that 10^{-5} chords in the normal direction gives enough resolution in the boundary layer. An exponential law perpendicular to the wall is used. The mesh around the blade can be seen in figure (4.46).

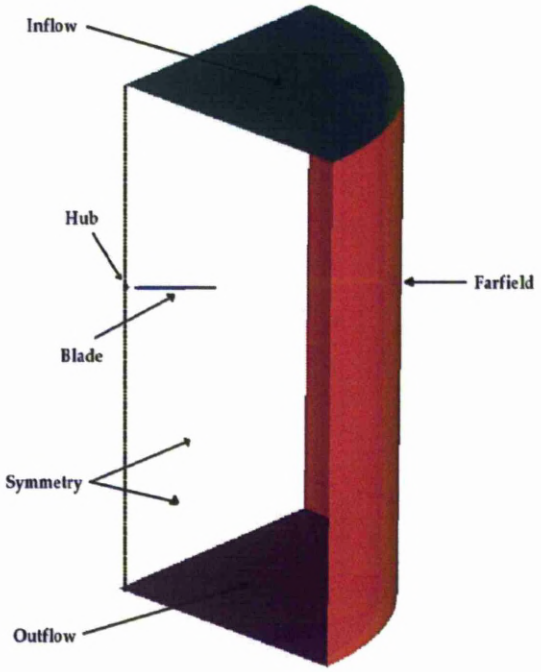

(a) Computational Domain

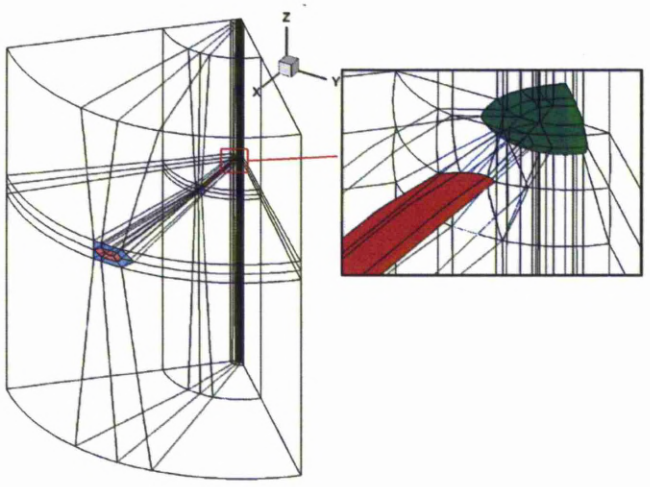

(b) Multi-block Topology

Figure 4.45: CFD domain and multi-block topology for the UH-60A rotor at forward flight conditions.

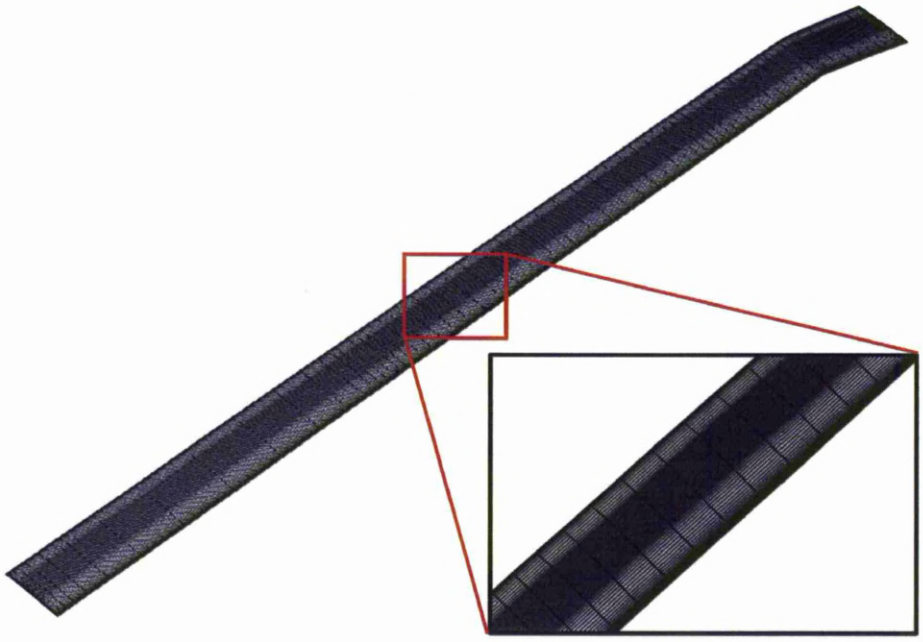

Figure 4.46: Surface grid of the UH-60A rotor blade.

4.2.2 Transitional Flow around a UH-60A Helicopter Rotor

The UH-60A main rotor was tested in forward-flight conditions considering an advance ratio of $\mu = 0.368$ and tip Mach number at $M_{tip} = 0.67$. The detailed list of parameters is presented in table (4.5).

In every radial position r/R of the UH-60A blade, the velocity of the section is the sum of the blade rotation and the free-stream velocity component. The velocity components combine a mean velocity equal to r/R times the tip velocity and a sinusoidally component due to the free-stream velocity. The conditions for different stations across the blade are presented at table (4.6).

Case	μ	M_{tip}	θ_{shaft}	θ_0	θ_{1s}	θ_{1c}	β_{1c}	β_0	β_{1c}
UH-60A	0.368	0.67	7.3	14.6	8.63	-2.39	3.43	-1.04	-0.7

Table 4.5: Parameters of forward-flight case of the UH-60A rotor.

Figures (4.47(a)) and (4.47(b)) compare the predicted sectional normal force and the pitching moments with the experimental data for the 0.675 R station . The comparison shows that the sectional normal forces and pitching

Station,%	Section	$M_{tip}(r/R)$	$M_{\psi=90}$	$M_{\psi=270}$
45	SC1095	0.3015	0.54806	0.05494
55	SC1095R8	0.3685	0.61506	0.12194
65	SC1095R8	0.4355	0.68206	0.18894
75	SC1095R8	0.5025	0.74906	0.25594
85	SC1095	0.5695	0.81606	0.32294
95	SC1095	0.6365	0.88306	0.38994

Table 4.6: Conditions at several radial stations of the UH-60A rotor blade ($M_{tip} = 0.67$ and $\mu = 0.368$).

moments are well predicted from the CFD code. A small underprediction is observed for the normal forces. Furthermore, for the pitching moment a change of the condition is observed at 180 degrees where the HMB solver starts from overpredicting the experimental data in the advance side and change to underpredict them for the retreating side of the rotor. Similar results are observed at figures (4.48(a)) and (4.48(b)) where the comparisons are for the 0.865 R station. The solver continues to underpredict the experimental data for the normal forces and for the pitching moment.

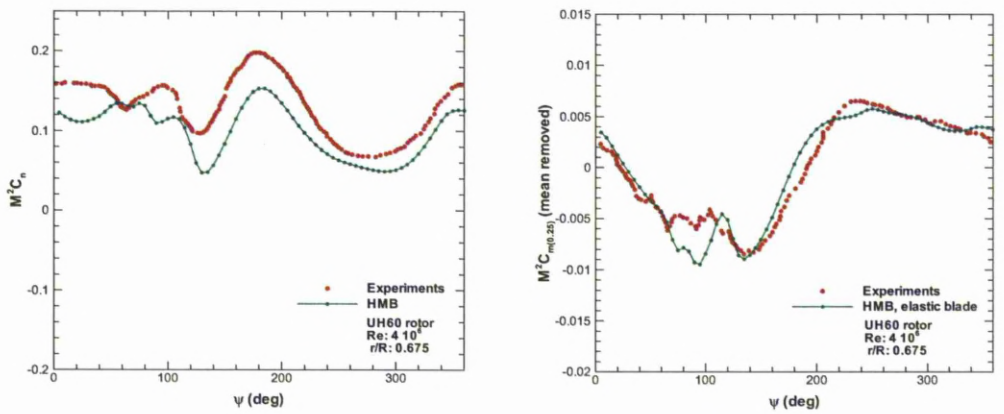

(a) C_n (b) $C_{m(0.25)}$

Figure 4.47: Azimuth variation of the sectional normal force and pitching moments for the UH-60A rotor at high forward flight, r/R=0.675.

Empirical Transition Models around UH-60A Rotor

The objective of the figures (4.49(a)) and (4.49(b)) is to present the location of the onset of transition region along different sections of the blade. The results shown are for $\psi = 60$ degrees and 315 degrees of azimuth and are predicted using the empirical criteria of Michel and Cebeci-Smith. As can be seen from figure (4.49(a)) the location of the transition region depends on the pitch angle of the blade. For stations closer to the root of the blade the transition onset occurs closer to the leading edge on the upper surface, although for the lower surface the transition points are located further downstream close to the trailing edge. On the other hand, the situation changes, as the stations closer to the tip

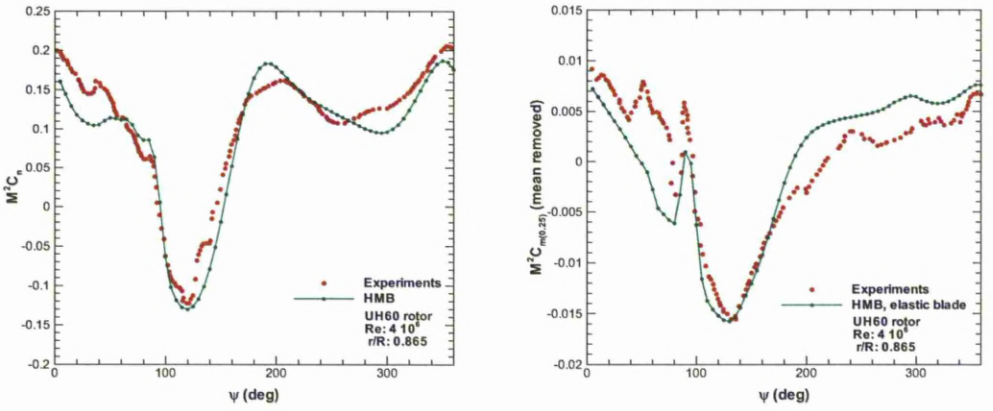

(a) C_n (b) $C_{m(0.25)}$

Figure 4.48: Azimuth variation of the sectional normal force and pitching moments for the UH-60A rotor at high forward flight, r/R=0.865.

of the blade are examined. Now, the incidence angle of the section is reduced and the transition point for the upper surface was moved downstream while at the lower surface, the transition point came closer to the leading edge. For all stations, it is obvious that the Cebeci and Smith criterion predicts earlier the transition in comparison to the Michel's criterion. For the case of $\psi = 315$ degrees azimuth angle, at the retreating side, the flow remains mainly laminar for the lower surface. For the upper surface, the onset of the transition region is closer to the leading edge mainly due to the relatively higher incidence angles experienced by the blade section.

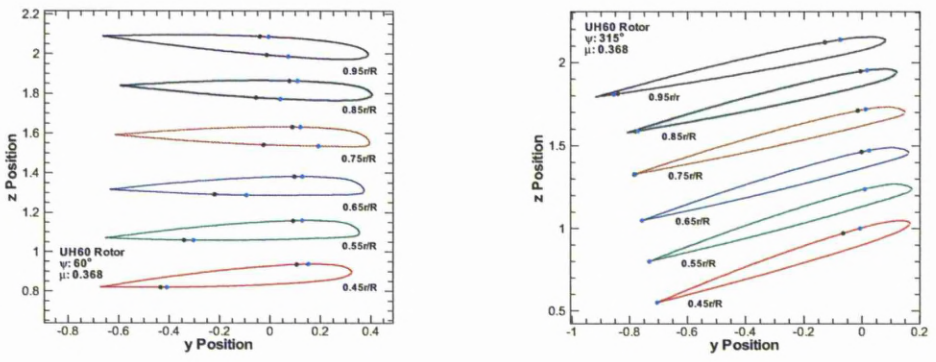

(a) $\psi = 60^o$ (b) $\psi = 315^o$

Figure 4.49: Transition location for different rotor sections and two different incidence angles. The Michel and Cebeci Smith criteria are presented.

Figures (4.50(a)) and (4.50(b)) show the transition point for the same r/R station and for different azimuth angles. The two outer stations were selected at 85% and 95% R. On the retreating side of the disk, transition for the

upper surface occurs close to the leading edge while the lower surface remains laminar. On the advancing side, based on the blade loading, transition occurs at the same location for the both sides of the blade. It is interesting how rapidly the transition point moves rapidly from leading edge to midchord as the blade rotates and moves from the advancing to the retreating side.

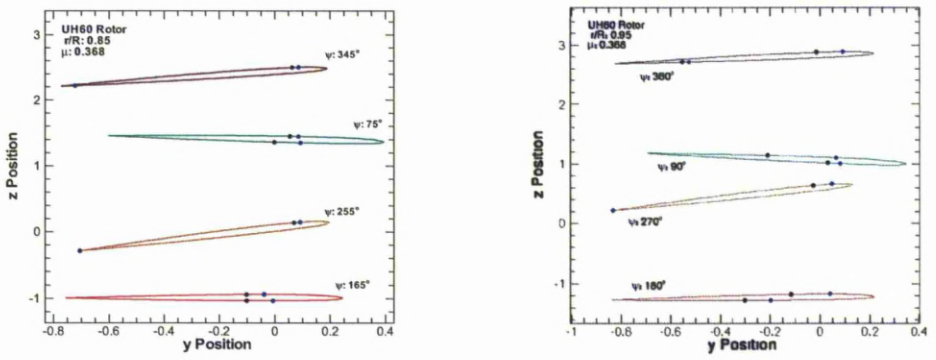

(a) $r/R = 0.85$ (b) $r/R = 0.95$

Figure 4.50: Transition location for a range of incidence angles and different rotor sections. The Michel and Cebeci Smith criteria are presented.

The onset and end of the transition region based on the Abu-Ghannam and Shaw model are presented in figures (4.51(a)) and (4.51(b)). The results are for two sections of the rotor blade at 0.75 R and 0.95 R respectively. The model showed similar trends like the previous empirical criteria. Also, similar trends observed on two dimensional aerofoils with the end of transition moving faster downstream towards the trailing edge as the pitch angle increases. On the other hand, the predictions suggest later transition.

4.3 Caradonna-Tung Rotor

Another rotor used to validate the transition models is the two-bladed rotor from Caradonna and Tung[91]. This rotor was used on wind tunnel tests for rotor performance and wake measurements. It was a two-bladed rotor, constructed using a NACA0012 profile along the blade span with untwisted and untapered geometry. The blade was of low aspect ratio (AR = 6) similar to a tail rotor configuration. The experiment was conducted in the Army Aeromechanics Laboratorys hover test facility which includes a large chamber with special ducting designed to eliminate room recirculation. The rotor was placed at the centre of the chamber and was mounted at a tall column containing a drive shaft. In their

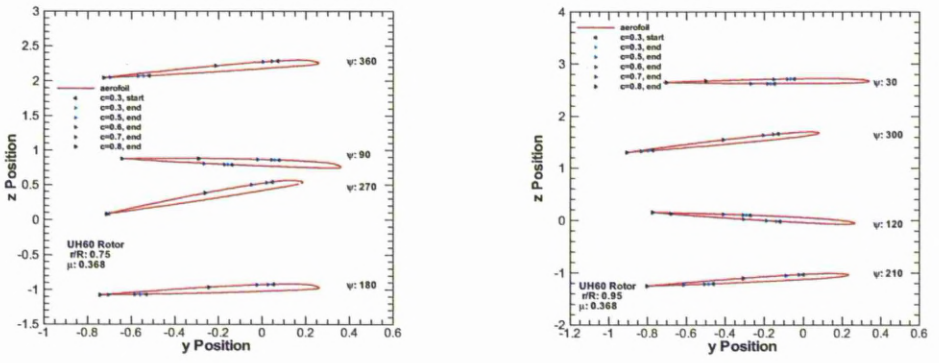

(a) r/R = 0.75

(b) r/R = 0.95

Figure 4.51: Transition onset and end based on the Abu-Ghannam and Shaw criterion. Sections at 0.75% R and 0.95% R for a range of azimuth angles.

work, the rotor in hover was simulated at a variety of collective pitch angles (from 5 degrees to 12 degrees) and tip Mach number (from 0.226 to 0.890) settings including the transonic flow regime. In the experiment, the blade surface pressure load was measured by pressure tubes connected to three valves.

4.3.1 Grid development - Caradonna-Tung Rotor

Following a similar procedure with the forward flying rotors, the symmetry of the rotor system is used. For the two bladed rotor, half the domain is meshed with the rotor blade placed at the centre of the mesh. The two cut through sections are denoted as symmetry surfaces. The mesh points on these surfaces have to be identical. The top surface where the flow enters the tube is known as the inflow and the lower surface is denoted as outflow. The hub of the rotor is placed where the two symmetry planes intersect and expands the whole z axis. The domain geometry is shown in figure (4.52).

The blade of the rotor consists of a NACA0012 profile. The total number of grid points around the rotor is 12,072,000 points. A C-topology was developed around the blade section. The C-topology is embedded in an H-block structure extended to the inflow and outflow. There are 320 points wrapped around each section while 85 points are distributed from root to the tip of the rotor blade. In the normal direction to the rotor blade, 92 points were used with initial spacing of 10^{-5} chords. A detailed view of the grid around the rotor blade can be seen in figure (4.53).

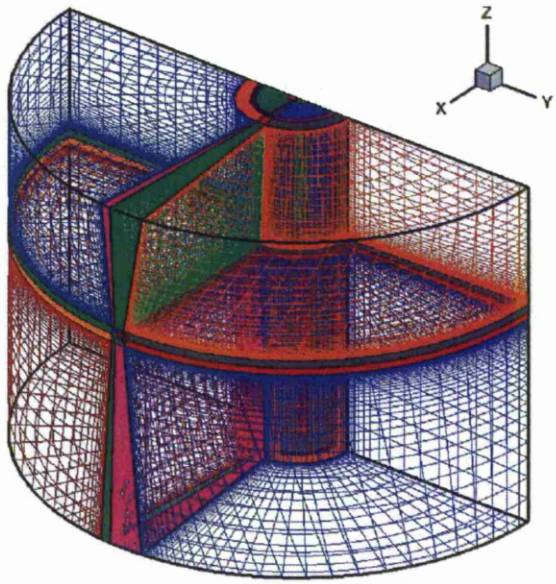

Figure 4.52: Multi-block topology around rotor in hover.

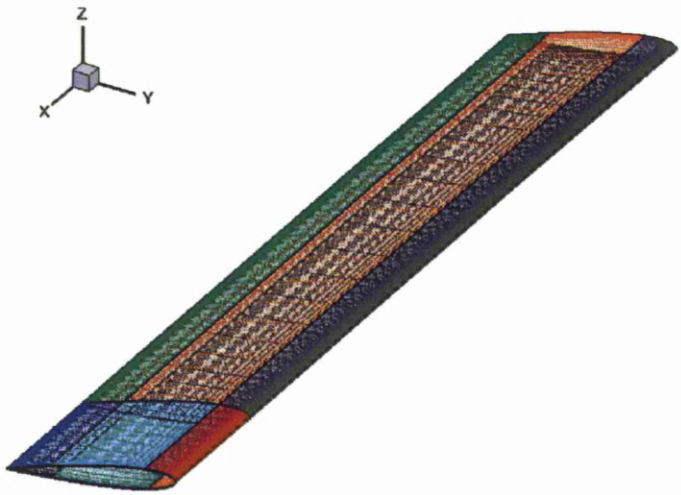

Figure 4.53: Surface grid of the rotor in hover.

4.3.2 Transitional Flow around the Caradonna-Tung Rotor

The Caradonna and Tung rotor was tested in hover conditions. For the test case, the tip Mach number of $M_{tip} = 0.468$ and the Reynolds number of 2×10^6 was used. The selected collective angle was at θ =12 degrees for this test case.

The transitional flow on the blade resulted in about 1% reduction in torque compared to the fully turbulent solution. When the lift is compared, the transitional calculations showed an 0.34% lift reduction in comparison to fully turbulent calculations. This result is apparently due to the promotion of the turbulent flow due to blade rotation and the relatively high Reynolds number.

The surface pressure coefficients at 33% and 83% of the radius for the Caradonna-Tung rotor can be seen in figures (4.54(a)) and (4.54(b)) respectively. The fully turbulent solutions show higher peak values of surface in comparison to the transitional calculations on both sections. The isosurfaces of C_P around the blade of Caradonna-Tung rotor can be seen in figures (4.55(a)) and (4.55(b)).

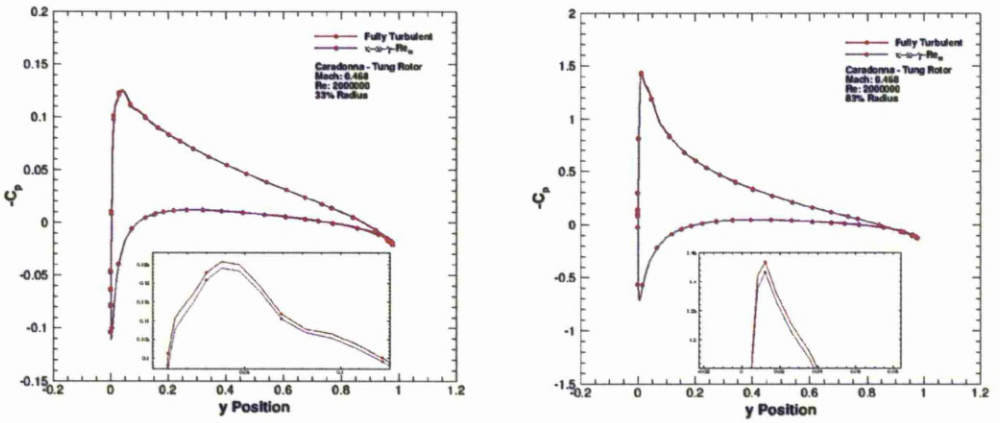

(a) 33% Radius (b) 83% Radius

Figure 4.54: Surface pressure distribution for different sections of the blade for the Caradonna-Tung rotor. ($M_{tip} = 0.468$ and $Re = 2 \times 10^6$)

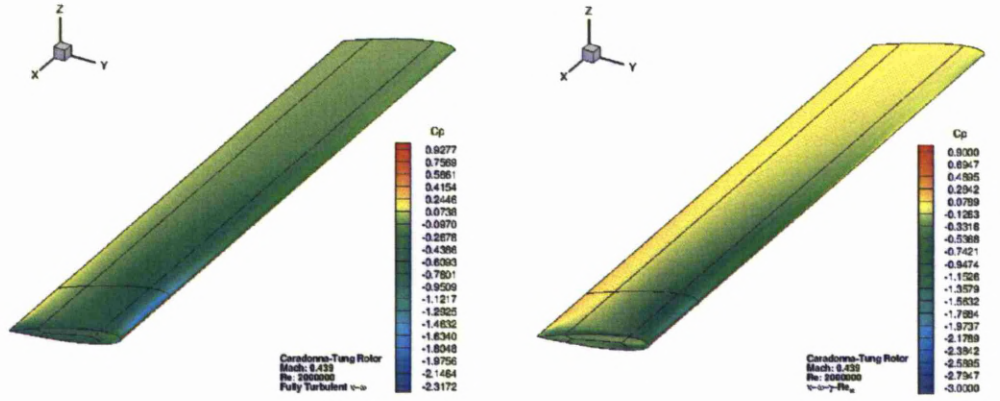

(a) Fully Turbulent $\kappa - \omega$ (b) $\kappa - \omega - \gamma - Re_{\theta t}$

Figure 4.55: Isosurfaces of surface pressure distribution around Caradonna-Tung rotor. ($M_{tip} = 0.468$ and $Re = 2 \times 10^6$)

The isosurfaces of turbulence Reynolds number can be seen in figures (4.56(a)) and (4.56(b)) for the fully turbulent and transition model respectively. The $\kappa-\omega-\gamma-Re_{\theta t}$ model seems to calculate higher values of turbulent Reynolds number from the fully turbulent calculations which indicates that the model has to be calibrated for the hover conditions.

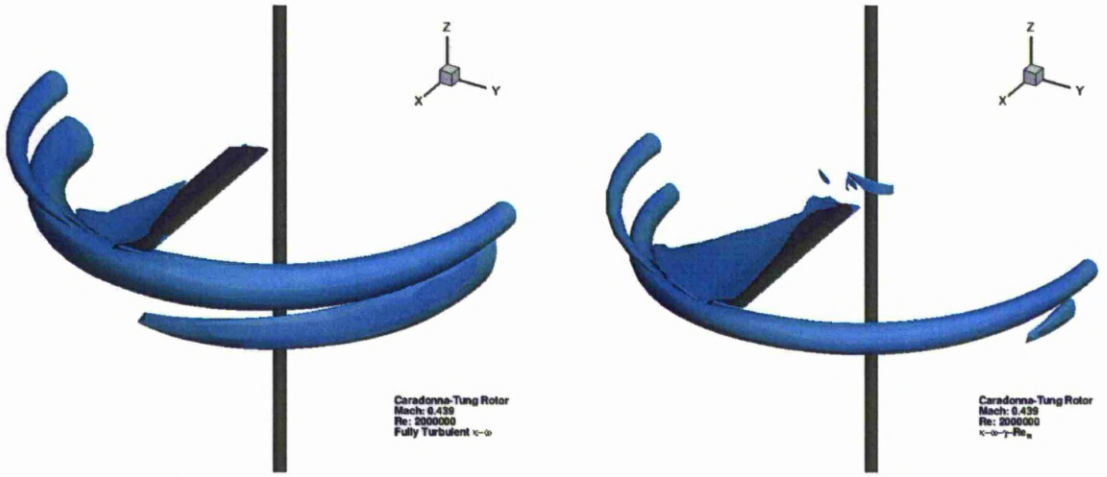

(a) Fully Turbulent $\kappa-\omega$ (b) $\kappa-\omega-\gamma-Re_{\theta t}$

Figure 4.56: Isosurfaces of turbulent Reynolds number around Caradonna-Tung rotor. ($M_{tip}=0.468$ and $Re=2\times10^6$)

4.4 Model Tail Rotor in Hover

The next case qualitatively investigates the behaviour of the transition models for a model tail rotor. There is no experimental data available for this use. The main purpose is to show that the transition models functions correctly in in hover and gives qualitatively reasonable results.

The blade consists of a NACA 0012 section. The tip Mach and Reynolds numbers for this case were considered at 0.6 and 1.1668×10^6, respectively. Two different collective angles were selected for this test case, one at 10 degrees and one at 20 degrees.

4.4.1 Grid development - Tail Rotor in Hover

For the development of the mesh, the same procedure seen in the forward flying and hover rotor was used. The block topology was developed based on a C-topology around the blade section. The C-topology is embedded in an H-block

structure extended to the inflow and outflow. Based on the general characteristic for the construction of grids for rotor cases, the normal distance for the first cells of the block adjacent to the blade surface was 10^{-5} c. An exponential law was used for the cells normal to the wall. The block topology around the tail rotor can be seen in figure (4.57) while a detailed view of the mesh around the blade is seen in figure (4.58).

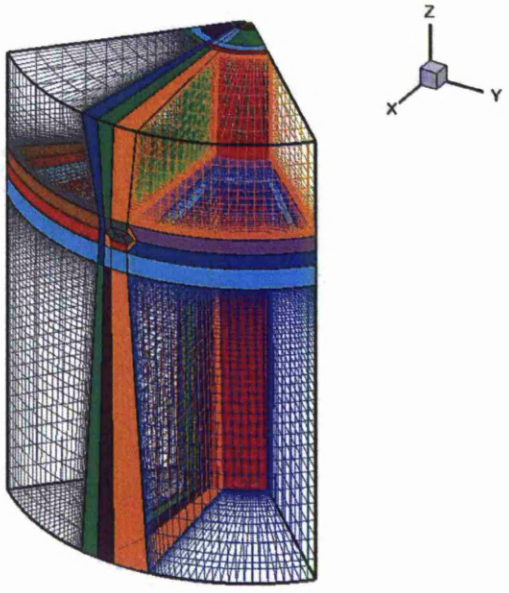

Figure 4.57: Multi-block topology around tail rotor.

Figure 4.58: Surface grid of the model tail rotor blade.

4.4.2 Transition Location for the Flow around a Tail Rotor

To estimate the transition point two methods were selected and were compared besides the different empirical criteria of Michel and Cebeci and Smith that were used. Initially, 10 slices alongside the x-direction were taken from the blade. Then using the criterion of Michel and the Cebeci and Smith method the onset of the transitional flow was found. The results from the slices were compared with the outcome from the estimation of the transition onset using surface streamlines at the same r/R of the blade. Before the method of streamlines is used, a transformation of the velocity field should be taken into account. This is due to the calculation of hovering rotor in a relative frame of reference[28].

As can be seen in figures (4.59(a))-(4.59(b)), for the θ_0 =10 degrees case, and in figures (4.60(a))-(4.60(b)), for the θ_0 =20 degrees case, the results are similar to the one observed on simple aerofoil cases. On the upper surface, the transition occurs closer to the leading edge as we approach the tip for both cases. As for the pressure side, as the θ increases the whole area laminarises sending the onset of transition at the trailing edge.

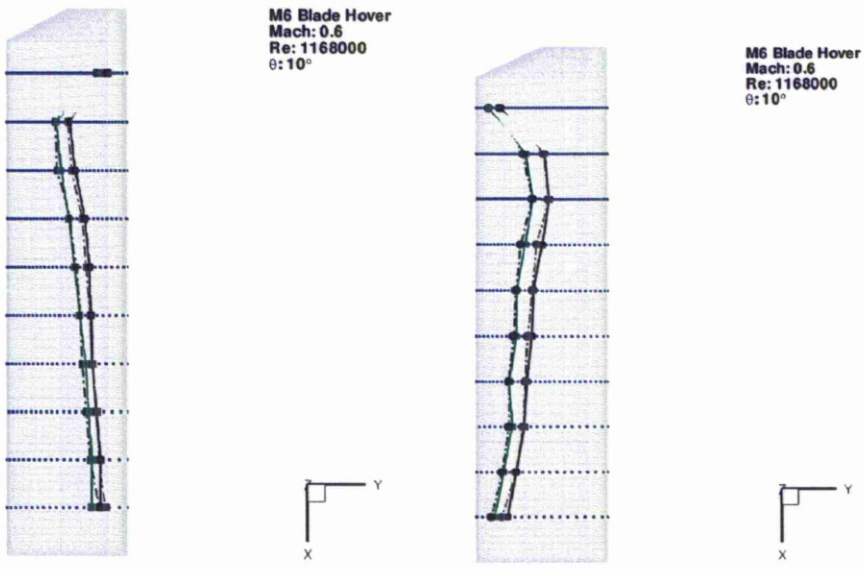

(a) Upper surface (b) Lower surface

Figure 4.59: Transition point for a range of different rotor sections. Michel and Cebeci-Smith criteria are used. Upper and Lower surface are presented. (θ_0 =10 degrees, $M_{tip} = 0.6$ and $Re = 1.1668 \times 10^6$)

The flows around rotors serve here to illustrate the empirical correlation transition methods. The correlations used here cannot capture the cross-flow effect of transition and therefore results cannot be seen as indicative of an overall effect rather than accurate predictions.

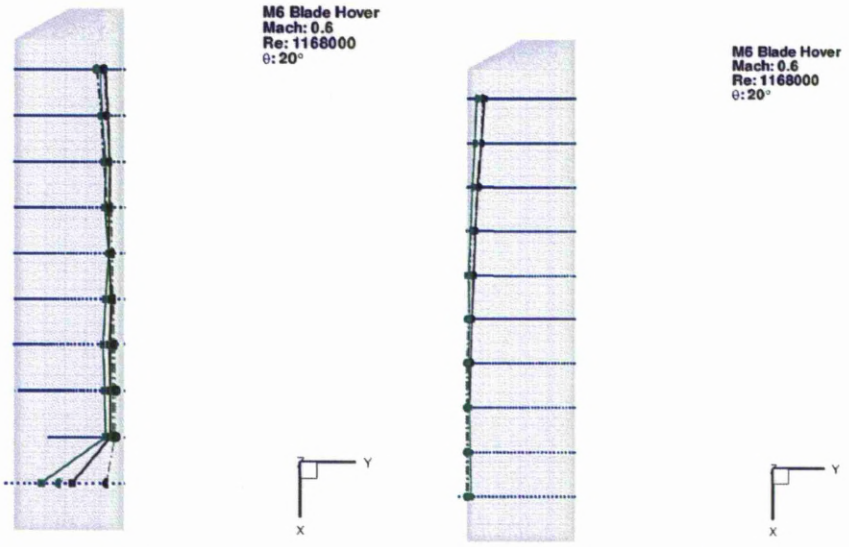

(a) Upper surface (b) Lower surface

Figure 4.60: Transition point for a range of different rotor sections. Michel and Cebeci-Smith criteria are used. Upper and Lower surface are presented. (θ_0 =20 degrees, $M_{tip} = 0.6$ and $Re = 1.1668 \times 10^6$)

4.5 Summary

In this chapter, three dimensional flow test cases were used to validate the empirical correlation model and the $\kappa - \omega - \gamma - Re_{\theta t}$ model. In general, all models showed promising results. Unfortunately, the lack of experimental data made the comparison difficult.

The empirical correlation transition models had the difficulty that the three dimensional flow had initially to be transformed into two-dimensional before they would be applied. In general, the models showed the same behaviour observed during the two-dimensional flows. The two models, Michel and Cebeci and Smith, showed similar results with the latter predicting slightly earlier transition. The Abu-Ghannam and Shaw model estimated an early start of transition showing the same sensitivity observed at the two-dimensional calculations.

The $\kappa - \omega - \gamma - Re_{\theta t}$ model showed satisfactory results. By using only local information, the model was able to calculate the transition flow easily. The results from the model for the ROBIN fuselage showed a good agreement with the results from the empirical correlation models. Nevertheless, the transition model predictions for all cases appeared to be reasonable and without the need of the transformation of the problem into a two-dimensional case by taking slices or follwing the treamlines, the model showed promising results.

Chapter 5

Conclusions and Future Work

This thesis documents the importance of transition models in rotorcraft applications using Computational Fluid Dynamics (CFD). The objective was to model the physics behind the transition flow based on Tollmien-Schlichting instabilities and to implement and validate existing transition models in Liverpool's Helicopter Multi-Block (HMB) solver. This work, also, tries to implement and validate the transition models of several families and presents a framework for the implicit treatment of these models in CFD solvers.

5.1 Summary - Conclusions

To start with, simple transition models based on empirical correlations used in the existing CFD model were presented in this work. These models are developed based on observed trends in experiments and produce acceptable results for flows similar to the cases they were derived for. The correlation based models relate transition Reynolds number to the momentum thickness Reynolds number and require the knowledge of non-local information in order to predict the transition onset. The correlation based models were implemented in the HMB code and used in conjuction with the $k-\omega$ two equation turbulence model for flows around aerofoils, fuselages and rotors. Their results were compared with experiments and if no experimental data were available, XFOIL was used instead. For steady and unsteady 2-dimensional flows, the Michel and Cebeci and Smith criteria gave similar results and the agreement with the test data was fair. The models managed to capture the transition and showed the same trend like the experiments. The Abu-Ghannam and Shaw model showed a sensitivity on the flow conditions and overpredicted the onset of transition

in the majority of the test cases.

Moreover, a recent transition model was also presented. This model is based on local information but it is not free of empirical correlation. It requires the solution of extra two transport equations similar to the existing two of the SST $k-\omega$ model with which it is coupled. The results for this category of transition models were satisfactory for two-dimensional cases. They showed good agreement with the existing experimental data and hold the promise for efficient computations of three-dimensional flows.

The CPU cost of the correlation based models was minimal although some extra CPU time was needed in comparison with the fully turbulent cases. The cost was mainly associated with the iteration process needed to establish the transition point and adjust it until convergence. On the other hand, the $\kappa-\omega-\gamma-Re_{\theta t}$ model was implemented in the HMB code adding extra terms on the implicit calculations. The code has to solve two extra transport equations added in the calculation of the SST $k-\omega$ model which almost double the CPU time needed. On the other hand, no special care is needed for solving complex 3D flows.

The validation of the models against a number of diverse and challenging test cases were presented in this work. Starting from steady flows around 2D aerofoils, then unsteady 2D flow and finally on the more complex test cases such as a 3D helicopter fuselage body, a forward flying and a hovering rotor. In general the transition models improved the predictions. They resulted in acceptable agreement with the available experimental data. For the 2D aerofoils and for certain conditions the transition models appear to be comparable with the e^N model as it is implemented in the well-known XFOIL code. The models showed a dependency on incidence angle with the transition onset moving with the angle of attack for both steady and unsteady aerofoil cases. Moreover, when skin friction was calculated, lower values of friction were estimated and a low drag bucket was predicted. The skin friction was in general overpredicted for fully turbulent calculations but all transition models gave realistic C_f curves with laminar and turbulent parts. For the complex three-dimensional flows around a helicopter fuselage or rotor, this work is the first were such cases were computed with the use of transition models. For the simple correlation based models, the three dimensional flow had to be transformed into two-dimensional sections by cutting the body in slices or following the streamlines along the surfaces. These slices showed the difficulty of the correlation-based flow to calculate three-dimensional flows. The $\kappa-\omega-\gamma-Re_{\theta t}$ model, on the other hand, by using only local information was able to calculate the transition flow easily.

It has to be mentioned that this work covers transition mechanisms due to Tollmien-Schlichting instabilities

and laminar separation. During the calculation of the transition point for three-dimensional flow no consideration was given to cross-flow dependency. This was left as an area of future investigation.

5.2 Suggestions for Future Work

The transition models presented in this thesis provided encouraging results for improvement of simulations of flows relates to rotorcraft applications. However, a number of extensions to the work presented in this thesis have been identified that would enhance further the understanding of transitional flow.

The investigation of the unsteady flow of the NACA 0012 aerofoil identified the limitation of the empirical correlation models to predict satisfactory the onset of transition leading to a very interesting idea for future development that would extend the $\kappa-\omega-\gamma-Re_{\theta t}$ model for predicting transition on unsteady calculations. This has so far never been attempted. The key difficulty is the lack of experiments for validation.

Moreover, as both the flow around the helicopter fuselage and the rotor were investigated, it will be beneficial to investigate the interaction of the rotor with the fuselage or the main rotor with the rear rotor. This has so far never been attempted. The complexity of the flows combined with the lack of experimental data for validation would be the main difficulties.

This work was basically concentrated on transition occurring due to Tollmien-Schlichting instabilities and laminar separation. However, the flow around a forward flying rotor or a rotor in hover is considered as very complex and many other transition mechanisms occurred. It would be beneficial to investigate the transition based on crossflow instabilities and bypass mechanism and extend the $\kappa-\omega-\gamma-Re_{\theta t}$ model to boundary layer flows with strong three-dimensionality. There exists a large amount of work on crossflow transition and the selection of empirical correlation for transition onset in order to account for the crossflow instability mechanism would not be difficult. The promising criteria would be based only on local flow variables in order to trigger the production of eddy viscosity inside the boundary layer.

While the importance of transition flow is recognised by many researchers, the need for experimental data that will used to validate the existing transition models and improve their accuracy is more than obvious. As the $\kappa-\omega-\gamma-Re_{\theta t}$ is a fairly new transition model and it is not free of empirical correlations like the one for the length of transition or the critical momentum thickness Reynolds number, there is always a need to continue validating the model on

additional test cases. An experiment would help develop empirical correlations for the $\kappa-\omega-\gamma-Re_{\theta t}$ model that will be more appropriate for use in rotorcraft applications. Moreover, it could provide the opportunity to validate the models on additional test cases. Such test cases could be on simple rotors with measurement techniques including surface-mounted hot-films and possibly surface flow visualisation combined with pressure taps. Alternatively pressure- or strain-sensitive paint could be used.

Bibliography

[1] J. Johansen and J.N. Sorensen, Prediction of Laminar/Turbulent Transition in Airfoil Flows, In 36^{th} *Aerospace Sciences Meeting and Exhibit*, pages 679–688, Reno, Nevada, January 1998. AIAA, AIAA 98-0702.

[2] R.R. Brodeur and C.P. Van Dam, Transition Prediction for the Two-Dimensional Navier-Stokes Solver Applied to High-Turbine Airfoils, *Wind Energy*, 4:61–75, October 2001.

[3] W. Geissler and L.P. Ruiz-Calavera, Transition and Turbulence Modelling for Dynamic Stall and Buffet, In *4th International Symposium on Engineerng, Turbulence Modelling and Measurements*, pages 679–688, May 1999.

[4] J.L. Hill, S.T. Shaw, and N. Qin, Development and Application of Engineering Transition Model for Rotorcraft Aerodynamics, In *International Congress of Aeronautical Science*, January 2004.

[5] R. Michel, Etude de la transition sur les profils d'aile, etablissement d'um critère de determination du point de transition et calcul de la trainee de profil incomprssible, Technical Report 1/1578A, ONERA, 1951.

[6] A. Benyahia, E. Berton, D. Favier, C. Maresca, K.L. Badcock, and G.N. Barakos, Detailed Evaluation of CFD Predictions Against LDA Measurements for Flow on an Airfoil, In *Integrated CFD and Experiments*, Glasgow, 8-9 September 2003.

[7] E. Berton, Characterization of the laminar separation bubble on a naca0012 oscillating airfoil, 2008.

[8] A.M. Savill, Some Recent Progress in the Turbulence Modelling of By-Pass Transition, *Near-wall turbulent flows*, pages 829–848, March 1993.

[9] H.W. Stock, Airfoil Validation Using Coupled Navier-Stokes and e^N Transition Prediction Methods, *Journal of Aircraft*, 39(1):51–58, February 2002.

[10] F. Moens, J. Perraud, A. Sraudie, and R. Houdeville, Transition Measurement and Prediction on a Generic High-Lift Swept Wing, *Proceedings of the IMechE Part G: Journal of Aerospace Engineering*, 220(6):589–603, January 2006.

[11] D. Arnal, G. Casalis, and R. Houdeville, Practical Transition Prediction Methods: Subsonic and Transonic Flows, Technical Report RTO-EN-AVT-151, NATO, January 2009.

[12] D. Arnal, R. Houdeville, A. Seraudie, and O. Vermeersch, Overview of laminar-turbulent transition investigations at ONERA Toulouse, In 45^{th} *AIAA Fluid Dynamics Conference and Exhibit*, Honolulu, Hawaii, June 2011.

[13] C.C. Heister, Semi/empirical transition Prediction an Application to an Isolated Rotor in Hover, In *46th Symposium of Applied Aerodynamics*, March 2011.

[14] C. Freeman and R. Mineck, Fuselage Pressure Measurements of a Helicopter Wind tunnel with a 3.15meter Diameter Single Rotor., Technical Report 80051, NASA, 1979.

[15] R.E. Mineck and S.A. Gorton, Steady and Periodic Pressure Measurements on a Generic Helicopter Fuselage Model in the Presence of a Rotor, Technical Report NASA TM-2000-210286, NASA, June 2000.

[16] C. Freeman, Development and Validation of a Combined Rotor Fuselage Included Flow-field Computational Model, Technical Report TR 80-B-3, NASA, 1980.

[17] M. Chaffin and J. Berry, Helicopter Fuselage Aerodynamics Under a Rotor by Navier-Stokes Simulation, *Journal of the American Helicopter Society*, pages 235–243, 1997.

[18] R.E. Mineck, Application of an Unstructured Grid Navier-Stokes Solver to a Generic Helicopter Body-Comparison of Unstructured Grid Results with StructuredGrid Results and Experimental Results, Technical Report NASA TM-1999-209510, NASA, August 1999.

[19] M.S. Chaffin and J.D. Berry, Navier-Stokes and Potential Theory Solutions for a Helicopter Fuselage and Comparison with Experiment, Technical Report NASA TM-4566, NASA, June 1994.

[20] J. Berry, V. Letnikov, I. Bavykina, and M. Chaffin, A Comparison of Interactional Aerodynamics Methods for a Helicopter in Low Speed Flight, Technical Report NASATM-1998-208420, NASA, 1998.

[21] S. Schweitzer, Computational Simulation of Flow Around Helicopter Fuselage, Master's thesis, The Pennsylvania State University, May 1999.

[22] D. Boyd, R. Barnwell, and S. Gorton, A Computational Model for Rotor-Fuselage Interactional Aerodynamics, In AIAA, editor, 38^{th} *AIAA Aerospace Sciences Meeting and Exhibit*. AIAA, January 2000, AIAA Paper 2000-0256.

[23] J. Sides, K. Pahle, and M. Costes, Numerical Simulation of Helicopters at DLR and Onera, *Journal of Aerospace Science and Technology*, 5:35-53, 2001.

[24] M. Costes, H.Frhr von Geyr, R. Collercandy, N. Kroll, P. Renzoni, M. Amato, A. Kokkalis, A. Rochetto, C. Serr, E. Larrey, A. Filippone, and D. Wehr, Computation of Helicopter Fuselage Aerodynamics Using Navier-Stokes CFD Methods, *Journal of American Helicopter Society*, pages 147–156, 2000.

[25] J. Berry and N. Bettschart, Rotor-Fuselage Interaction: Analysis and Validation with Experiments, In *American Helicopter Society* 53^{th} *Annual Forum*, May 1997.

[26] W. Splettstoesser, B. Junker, K. Schultz, W. Wagner, W. Weitemeyer, A. Protopsaltis, and D. Fertis, The HELINOISE Aeroacoustic Rotor Test in the DNW - Test Documentation and Representative Results, Technical Report 93-09, 1993.

[27] W. Khier, F. Le Chuiton, and T. Schwarz, Navier Stokes Analysis of the Helicopter Rotor-Fuselage Interference in Forward Flight., Technical report, Institute of Aerodynamics and Flow Technology, DLR, 2001.

[28] R. Steijl, G. Barakos, and K. Badcock, A Framework for CFD Analysis of Helicopter Rotors in Hover and Forward Flight, *International Journal for Numerical Methods in Fluids*, 51:819–847, January 2006.

[29] A. Jameson, Time Dependent Calculations Using Multigrid, with Applications to Unsteady Flows Past Airfoils and Wings, In *10th Computational Fluid Dynamics Conference, Honolulu, HI*, 1991, AIAA-91-1596.

[30] S. Osher and S. Chakravarthy, Upwind Schemes and Boundary Conditions with Applications to Euler Equations in General Geometries, *Journal of Computational Physics*, 50:447–481, January–February 1983.

[31] P.L. Roe, Approximate Riemann Solvers, Parameter Vectors, and Difference Schemes, *Journal of Computational Physics*, 43(2):357–372, October 1981.

[32] B. van Leer, Flux-vector splitting for the euler equations, In *Eighth International Conference on Numerical Methods in Fluid Dynamics*, volume 170 of *Lecture Notes in Physics*, pages 507–512. Springer Berlin / Heidelberg, 1982.

[33] O. Axelsson, *Iterative Solution Methods*. Cambridge University Press, Cambridge, MA, edition, 1994.

[34] M. Woodgate, K. Badcock, B. Richards, and R. Gatiganti, A Parallel 3D Fully Implicit Unsteady Multiblock CFD Code Implemented on a Beowulf Cluster, In *Parallel CFD 1999, Williamsburg, VA, USA*, 1999.

[35] P.R. Spalart and S.R. Allmaras, A One-Equation Turbulence Model for Aerodynamic Flows, In 30^{th} *AIAA Aerospace Sciences Meeting and Exhibit*, Reno, NV, January 1992. AIAA, AIAA 92-0439.

[36] D.C. Wilcox, Multiscale Model for Turbulent Flows, In 24^{th} *AIAA Aerospace Sciences Meeting and Exhibit*, Reno, Nevada, January 1986.

[37] F.R. Menter, Two-Equation Eddy-Viscosity Turbulence Models for Engineering Applications, *AIAA Journal*, 32(8):1598–1605, 1994.

[38] T. Cebeci and A.M.O. Smith, *Analysis of Turbulent Boundary Layers*. Academic Press, New York, 1974. ISBN 0-12-164650-5.

[39] B.S. Baldwin and H. Lomax, Thin Layer Approximation and Algebraic Model for Separated Turbulent Flows, In 16^{th} *AIAA Aerospace Sciences Meeting and Exhibit*, Huntsville, Alabama, January 16-18 1978. AIAA.

[40] B.S. Baldwin and T.J. Barth, A One-Equation Turbulence Transport Model for High-Reynolds Number Wall-Bounded Flows, Technical Memorandum 102847, NASA, August 1990, Also as AIAA Paper 91-0610.

[41] D.C. Wilcox, Reassessment of the Scale-Determining Equation for Advanced Turbulence Models, *AIAA Journal*, 26:1299–1310, 1988.

[42] W.P. Jones and B.E. Launder, The prediction of laminarization with a two-equation model of turbulence, *Int. J. Heat Mass Transfer*, 15:301–314, 1972.

[43] F.R. Menter, Zonal Two Equation $k-\omega$ Turbulence Models For Aerodynamic Flows, In *24th AIAA Fluid Dynamics Conference*, Orlando, Florida, 6–9 July 1993. AIAA.

[44] K. Hanjalic and B.E. Launder, A Reynolds Stress Model of Turbulence and its Application to Thin Shear Flows, *J. Fluid Mech.*, 52:609–644, 1972.

[45] P.A. Durbin, Near-Wall Turbulence Closure Modelling Without Damping Functions, *Theor. Comput. Fluid Dyn.*, 3:1–13, 1991.

[46] Craft. T.J., B.E. Launder, and K. Suga, Development and application of a cubic eddy-viscosity model of turbulence, *International Journal of Heat and Fluid Flow*, 17(2):108–115, April 1996.

[47] T.P. Sommer, R.M.C. So, and H.S. Zhang, A near-wall four-equation turbulence model for compressible boundary layers, Contractor Report 4436, NASA, April 1992.

[48] P. Malecki and R. Houdeville, Etude de Modèles de Turbulence Pour Les Couches Limites Tridimensionnelles, In *29ième Colloque d'Aérodynamiquee Appliquée*, Biscarosse, September 21–23 1992. Association Aéronautique et Astronautique de France.

[49] P. Malecki, *Etude de Modèles de Turbulence Pour Les Couches Limites Tridimensionnelles*, PhD thesis, L'Ecole National Supérieure de l'Aéronautique et de l'Espace (Supaéro), Toulouse, France, November 1994.

[50] K. Hanjalic, B.E. Launder, and R. Schiestel, Multiple-Time-Scale Concepts in Turbulent Shear Flows, In L.J.S. Bradbury, F. Durst, B.E. Launder, F.W. Schmidt, and J.H. Whitelaw, editors, *Turbulent Shear Flows*, volume 2, pages 36–49, New York, 1980. Springer-Verlag.

[51] S.W. Kim, Numerical Investigation of Separated Transonic Turbulent Flows with a Multiple-Time-Scale Turbulence Model, Technical Memorandum 102499, NASA, January 90.

[52] C.P. Chen, A Non-Isotropic Multiple-Scale Turbulence Model, Contractor Report 184217, NASA, 1990.

[53] S. Gao, Z. Yang, and P.R. Voke, Balance Equations in Finite-Volume Large-eddy Simulations, Technical Report ME-FD/94.27, University of Surrey, Dept. Mech. Eng., September 1994.

[54] W.S. Saric, D. Arnal, S.J. Cowley, X. Wu, T. Herbert, L. Kleiser, H. Reed, and B.A. Singer, Special course on progress in transition modellling, Technical report, Advisory Group for Aerospace Research and Development, April 1994.

[55] D.C. Wilcox, *Turbulence Modelling*. DCW Industries, Inc., 1993. ISBN 0-9636051-0-0.

[56] D.C. Wilcox, Simulation of Transition with a Two-Equation Turbulence Model, *AIAA Journal*, 32(2):247–255, 1994.

[57] G.B. Schubauer and H.K. Skramstad, Laminar-Boundary-Layer Oscillations and Transition on a Flat Plate, Technical Report 909, National Bureau of Standards, 1948.

[58] R.E. Mayle, The Role of Laminar-Turbulent Transition in Gas Turbine Engines, *Journal of Turbomachinery*, 113:509–537, 1991.

[59] F.M. White, *Viscous Fluid Flow 2nd edition*. McGraw-Hill Inc., 1991.

[60] A.V. Popov, R.M. Botez, and M. Labib, Transition point detection from the surface pressure distribution for controller design, *Journal of Aircraft*, 45(1):23–28, January 2008.

[61] A. Hellsten and S. Laine, Extension of the $\kappa - \omega - SST$ Turbulence Model for Flows Over Rough Surfaces, In *AIAA AFM Conference*, August 1997.

[62] T. Knopp, B. Eisfeld, and J.B. Calvo, A New Extension for $\kappa - \omega$ Turbulence Model to Account for Wall Roughness, *International Journal of Heat and Fluid Flow*, 30:54–64, 2009.

[63] B.J. Abu-Ghannam and R. Shaw, Natural Transition of Boundary Layers - The Effect of Turbulence, Pressure Gradient and Flow History, *Journal of Mechanical Engineering Science*, 22(5):213–228, 1980.

[64] B. Aupoix and P.R. Spalart, Extensions of the spalart-allmaras turbulence model to account for wall roughness, *International Journal of Heat and Fluid Flow*, 24:454–462, 2003.

[65] B. Thwaites, Approximate Calculation of the Laminar Boundary Layer, *Aeronautical Quarterly*, 1:245–280, 1949.

[66] G. Xum and L.N. Sankar, Effects of Transition and Freestream Unsteadyness on the Performance of Horizontal Axis Wind Turbines, In ASME, editor, *2000 ASME Wind Energy Symposium*, Reno, Nevada, January 2000. AIAA.

[67] H.L. Reed, T.S. Haynes, and W.S. Saric, Computational Fluid Dynamics Validation Issues in Transition Modelling, *AIAA Journal*, 36(5):742–751, May 1998.

[68] T. Cebeci and J. Cousteix, *Modeling and Computation of Boundary Layer Flows*. Horizons Publishing - Springer, New York, 2005.

[69] A.M.O. Smith and N Gamberoni, Transition, pressure gradient, amd stability theory, *Proc. Ninht Internat. Cong. Appl. Mech.*, 4:234–244, 1956.

[70] J.L. Van Ingen, A suggested semi-empirical method for the calculation of the boundary layer transition region, Technical Report VTH-74, Delft, 1956.

[71] D.P. Pasquale, A. Rona, and S.J. Garret, A selective review of CFD transition models, In 45^{th} *AIAA Fluid Dynamics Conference and Exhibit*, San Antonio, Texas, June 2009.

[72] S. Dhawan and R. Narasimha, Some Properties of Boundary Layer Flow During the Transition from Laminar to Turbulence Motion, *Journal of Fluid Mechanics*, 3(4):418–436, 1958.

[73] J. Steelant and E. Dick, Modelling of Bypass Transition with Conditioned Navier-Stokes Equations Coupled to an Intermittency Transport Equation, *International Journal for Numerical Methods in Fluids*, 23(3):193–220, 1996.

[74] J. Ryong Cho and M. Chung, K., A k-e-g Equation Turbulence Model, *Journal of Fluid Mechanics*, 237:301–322, 1992.

[75] Y.B. Suzen and P.G. Huang, Modelling of Flow Transition Using an Intermittency Transport Equation, Technical Report NASA/CR-1999-209313, September 1999.

[76] F.R. Menter, R.B. Langtry, S.R. Likki, Y.B. Suzen, P.G. Huang, and S. Völker, A Correlation-Based Transition Model Using Local Variables - Part I: Model Formulation, *Journal of Turbomachinery*, 128(3):423–433, July 2006.

[77] R.B. Langtry, J. Gola, and F.R. Menter, Predicting 2D Airfoil and 3D Wing Turbine Rotor Performance using a Transition Model for General CFD Codes, In 44^{th} *AIAA Aerospace Sciences Meeting*, volume 15, pages 4643–4653, Reno, NV, January 2006. AIAA, AIAA 2006-395.

[78] R.B. Langtry and F.R. Menter, Correlation-Based Transition Modeling for Unstructured Parallelized Computational Fluid Dynamics Codes, *AIAA Journal*, 47(12):2895–2906, December 2009.

[79] F.R. Menter and R.B. Langtry, Transition Modeling for General CFD Applications in Aeronautics, In AIAA, editor, 43rd *AIAA Aerospace Sciences Meeting and Exhibit*, pages pp 15513–15526. AIAA, January 2005, AIAA Paper 2005-522.

[80] K. Suluksna and E. Juntasaro, Assessment of Intermittency Transport Equations for Modeling Transition in Boundary Layers subjected to Freestream Turbulence, *International Journal of Heat and Fluid Flow*, 28:48–61, 2008.

[81] W. Haase, E. Chaput, E. Elsholz, M.A. Leschziner, and U.R. Muller, ECARP: European Computational Aerodynamics Research Project: Validation of Turbulence Models, In *Notes on Numerical Fluid Mechanics*, 1997, Volume 58.

[82] G. Depommier, D. Alfano, D. Leusink, and G. Leymar, Computation of Transition to Turbulence on Rotor Blades, In *37th European Rotorcraft Forum*, September 2011, paper ID 214.

[83] H. Schlichting, *Boundary Layer Theory*. McGraw-Hill Book Company, New York, 1960. 59-15472.

[84] D.M. Somers, Design and Experimental Results for a Natural-Laminar-Flow Airfoil for General Aviation Applications, Technical Report NASA TP-1861, NASA, June 1981.

[85] D.M. Somers, Design and Experimental Results for the S809 Airfoil, Technical Report NREL/SR-440-6918, NREL, January 1997.

[86] X.-D. Zhang and Z.-H. Gao, Numerical discussions on complete empirical correlation in Langtrys transition model, *Applied Mathematics and Mechanics*, 31(5):575–584, 2010. http://dx.doi.org/10.1007/s10483-010-0505-6.

[87] J.L. Hill, *The Development of a Boundary Layer Transition Model for Helicopter Rotor CFD*, PhD thesis, Cranfield University, March 2005.

[88] Drela, M. and Youngren, H., *XFOIL 6.9 User Guide*, 11 January 2001.

[89] P.M. Shinoda, H. Yeo, and T.R. Norman, Rotor Performance of a UH-60 Rotor System in the NASA Ames 80-by 120-Foot Wind Tunnel, In 58th *Annual Forum of the American Helicopter Society*, Montreal, Canada, June 2002.

[90] M. Dindar, M.S. Shephard, J.E. Flaherty, and K. Jansen, Adaptive CFD Analysis for Rotorcraft Aerodynamics, *Comput. Methods Appli. Mech. Engrg.*, 189:1055–1076, 2000.

[91] F.X Caradona and C. Tung, Experimental and Analytical Studies of a Model Helicopter Rotor in Hover, Technical Memorandum NASA TM-81232, NASA, August 1990.

[92] J.-C. Huang, *Boundary Layer Receptivity of Flow Over Compliant Surfaces*, PhD thesis, University of Liverpool, June 2006.

[93] A.H. Ercan, *Experimental Analysis And Modelling of Boundary Layer Transition*, PhD thesis, University of Liverpool, March 1997.

[94] P.E. Roach, The generation of nearly isotropic turbulence by means of grids, *International Journal of Heat and Fluid Flow*, 8(2):82–92, 1987.

[95] M.W. Johnson and J. Madadnia, Precise Measurement of Turbulent Intermittency In Transitional Boundary Layers, Technical report, Dept. of Mech. Engineering, University of Liverpool, 1989.

[96] van Albada. G.D., B. van Leer, and W.W. Roberts, A Comparative Study of Computational Methods in Cosmic Gas Dynamics, *Astronomy and Astrophysics*, 108(1):76–84, April 1982.

Appendix A

Implementation of the source functions for the $\kappa - \omega - \gamma - Re_{\theta t}$ Transition Model

A.1 Non-dimensionalisation of the basic functions and parameters

For the implementation of the models in the HMB solver, their parameters and functions have to be appropriately non-dimensionalised. Anything related to length would be non-dimensionalised with the characteristic length (L), the velocities with the freestream velocity (U_∞) while density and viscosity with their freestream values (ρ_∞) and (μ_∞) respectively. During this procedure, the Reynolds number which is given as $Re = \frac{\rho U_\infty c}{\mu} = \frac{U_\infty c}{\nu}$ is also used.

$$\begin{gathered} x^* = \frac{x}{c}, \quad y^* = \frac{y}{c}, \quad z^* = \frac{z}{c} \\ u^* = \frac{u}{U_\infty}, \quad v^* = \frac{v}{V_\infty} \quad w^* = \frac{w}{W_\infty} \\ \mu^* = \frac{\mu}{\mu_\infty}, \quad \rho^* = \frac{\rho}{\rho_\infty}, \quad p^* = \frac{p}{p_\infty}, \quad t^* = \frac{t}{c/U_\infty} \end{gathered} \tag{A.1}$$

Previously the aerofoil chord (c) is used as characteristic length.
Following this idea, the next quantities are transformed into dimensionless as follows:

- The turbulence kinetic energy (k):

$$k^* = \frac{k}{U_\infty^2} \tag{A.2}$$

- The specific dissipation rate of turbulence (ω):

$$\omega^* = \frac{\omega}{U_\infty/c} \tag{A.3}$$

- The turbulence viscosity (μ_T):

$$\begin{aligned} \mu_T &= \frac{\rho k}{\omega} = \frac{\rho^* k^*}{\omega^*} \frac{\rho_\infty U_\infty^2}{U_\infty/c} = \frac{\rho^* k^*}{\omega^*} \cdot \rho_\infty U_\infty c \\ \Leftrightarrow \mu_T^* &= \frac{\mu_T}{\mu_\infty} = \frac{\frac{\rho^* k^*}{\omega^*} \cdot \rho_\infty U_\infty c}{\rho_\infty U_\infty c} = \frac{\rho^* k^*}{\omega^*} \end{aligned} \tag{A.4}$$

- The pressure gradient parameter (λ_θ):

$$\begin{aligned} \lambda_{\theta t} &= \frac{\theta^2}{\nu} \frac{dU}{ds} = \frac{\theta^{*2}}{\nu^*} \frac{dU^*}{ds^*} \frac{c^2 U_\infty}{\nu_\infty c} \\ &= \frac{\theta^{*2}}{\nu^*} \frac{dU^*}{ds^*} \frac{U_\infty c}{\nu_\infty} = \frac{\theta^{*2}}{\nu^*} \frac{dU^*}{ds^*} Re \\ \Leftrightarrow \lambda_{\theta t}^* &= \frac{\theta^{*2}}{\nu^*} \frac{dU^*}{ds^*} = \frac{\lambda_{\theta t}}{Re} \end{aligned} \tag{A.5}$$

The pressure gradient parameter (λ_θ) can also be estimated with the use of momentum thickness Reynolds number (Re_θ) by solving for it

$$Re_\theta = \frac{\rho U \theta}{\mu} \Leftrightarrow \theta = \frac{Re_\theta \mu}{\rho U}$$

then the pressure gradient parameter (λ_θ) can be given as:

$$\begin{aligned}
\lambda_{\theta t} &= \frac{\theta^2}{\nu}\frac{dU}{ds} = \frac{Re_\theta^2 \mu^2}{\rho^2 U^2 \nu}\frac{dU}{ds} \\
&= \frac{Re_\theta^{*2}\mu^{*2}}{\rho^{*2}U^{*2}\nu^*}\frac{dU^*}{ds^*}\frac{Re^2\mu_\infty^2}{\rho_\infty^2 U_\infty^2 \nu_\infty}\frac{U_\infty}{c} \\
&= \frac{Re_\theta^{*2}\mu^{*2}}{\rho^{*2}U^{*2}\nu^*}\frac{dU^*}{ds^*}\frac{Re^2\mu_\infty}{\rho_\infty U_\infty c} \\
&= \frac{Re_\theta^{*2}\mu^{*2}}{\rho^{*2}U^{*2}\nu^*}\frac{dU^*}{ds^*}\frac{Re^2}{Re} \\
&= \frac{Re_\theta^{*2}\mu^{*2}}{\rho^{*2}U^{*2}\nu^*}\frac{dU^*}{ds^*}Re \\
\Leftrightarrow \lambda_{\theta t}^* &= \frac{Re_\theta^{*2}\mu^{*2}}{\rho^{*2}U^{*2}\nu^*}\frac{dU^*}{ds^*} = \frac{\lambda_{\theta t}}{Re}
\end{aligned} \tag{A.6}$$

- Flow acceleration parameter (K):

$$\begin{aligned}
K &= \left(\frac{\nu}{U^2}\right)\frac{dU}{ds} = \left(\frac{\nu^*}{U^{*2}}\right)\frac{dU^*}{ds^*}\frac{\nu_\infty U_\infty}{U_\infty^2 c} \\
&= \left(\frac{\nu_\infty^*}{U^{*2}}\right)\frac{dU^*}{ds^*}\frac{1}{\frac{U_\infty c}{\nu}} = \left(\frac{\nu^*}{U^{*2}}\right)\frac{dU^*}{ds^*}\frac{1}{Re} \\
\Leftrightarrow K^* &= \left(\frac{\nu^*}{U^{*2}}\right)\frac{dU^*}{ds^*} = \frac{K}{1/Re}
\end{aligned} \tag{A.7}$$

- The viscous stress (τ):

$$\begin{aligned}
\tau_{ij} &= \frac{1}{2}\mu_T\left(\frac{\partial u_i}{\partial x_j} + \frac{\partial u_j}{\partial x_i}\right) \\
&= \frac{1}{2}\mu_T^*\left(\frac{\partial u_i^*}{\partial x_j^*} + \frac{\partial u_j^*}{\partial x_i^*}\right)\rho_\infty U_\infty c\frac{U_\infty}{c} \\
&= \frac{1}{2}\mu_T^*\left(\frac{\partial u_i^*}{\partial x_j^*} + \frac{\partial u_j^*}{\partial x_i^*}\right)\rho_\infty U_\infty^2 \\
\Leftrightarrow \tau_{ij}^* &= \frac{1}{2}\mu_T^*\left(\frac{\partial u_i^*}{\partial x_j^*} + \frac{\partial u_j^*}{\partial x_i^*}\right) = \frac{\tau_{ij}}{\rho_\infty U_\infty^2}
\end{aligned} \tag{A.8}$$

- The strain rate tensor (S_{ij}):

$$\begin{aligned}
S_{ij} &= \frac{1}{2}\left(\frac{\partial u_i}{\partial x_j} + \frac{\partial u_j}{\partial x_i}\right) \\
&= \frac{1}{2}\left(\frac{\partial u_i^*}{\partial x_j^*} + \frac{\partial u_j^*}{\partial x_i^*}\right)\frac{U_\infty}{c} \\
\Leftrightarrow S_{ij}^* &= \frac{1}{2}\left(\frac{\partial u_i^*}{\partial x_j^*} + \frac{\partial u_j^*}{\partial x_i^*}\right) = \frac{S_{ij}}{U_\infty/c}
\end{aligned} \tag{A.9}$$

- The absolute value of strain rate (S):

$$\begin{aligned}
S &= (2S_{ij}^* S_{ij}^*)^{1/2}\frac{U_\infty}{c} \\
\Leftrightarrow S^* &= (2S_{ij}^* S_{ij}^*)^{1/2} = \frac{S}{U_\infty/c}
\end{aligned} \tag{A.10}$$

- The vorticity tensor (Ω_{ij}):

$$\begin{aligned}\Omega_{ij} &= \frac{1}{2}\left(\frac{\partial u_i}{\partial x_j} - \frac{\partial u_j}{\partial x_i}\right) \\ &= \frac{1}{2}\left(\frac{\partial u_i^*}{\partial x_j^*} - \frac{\partial u_j^*}{\partial x_i^*}\right)\frac{U_\infty}{c} \\ \Leftrightarrow \Omega_{ij}^* &= \frac{1}{2}\left(\frac{\partial u_i^*}{\partial x_j^*} - \frac{\partial u_j^*}{\partial x_i^*}\right) = \frac{\Omega_{ij}}{U_\infty/c}\end{aligned} \tag{A.11}$$

- The absolute value of vorticity (Ω):

$$\begin{aligned}\Omega &= (2\Omega_{ij}^*\Omega_{ij}^*)^{1/2}\frac{U_\infty}{c} \\ \Leftrightarrow \Omega^* &= (2\Omega_{ij}^*\Omega_{ij}^*)^{1/2} = \frac{\Omega}{U_\infty/c}\end{aligned} \tag{A.12}$$

- The viscosity ratio (R_T):

$$\begin{aligned}R_T &= \frac{\rho k}{\mu\omega} = \frac{\rho^* k^*}{\mu^*\omega^*}\frac{\rho_\infty U_\infty^2}{\mu_\infty \frac{U_\infty}{c}} \\ &= \frac{\rho^* k^*}{\mu^*\omega^*}\frac{\rho_\infty U_\infty c}{\mu_\infty} = \frac{\rho^* k^*}{\mu^*\omega^*}Re \\ \Leftrightarrow R_T^* &= \frac{\rho^* k^*}{\mu^*\omega^*} = \frac{R_T}{Re}\end{aligned} \tag{A.13}$$

- The momentum thickness (θ):

$$\begin{aligned}\theta &= \frac{Re_\theta \mu}{\rho U} = \frac{Re_\theta^*\mu^*}{\rho^* U^*}\frac{Re\,\mu_\infty}{\rho_\infty U_\infty} \\ \Leftrightarrow \theta^* &= \frac{\theta}{c} = \frac{Re_\theta^*\mu^*}{\rho^* U^*}\frac{\mu_\infty}{\rho_\infty U_\infty c}Re \\ \Leftrightarrow \theta^* &= \frac{Re_\theta^*\mu^*}{\rho^* U^*} = \frac{\theta}{c}\end{aligned} \tag{A.14}$$

- The displacement thickness (δ)

$$\begin{aligned}\delta &= \frac{50\Omega y}{U}\delta_{BL} = \frac{50\Omega y}{U}\frac{15}{2}\theta \\ &= \frac{50\Omega^* y^*}{U^*}\frac{15}{2}\theta^*\frac{\frac{U_\infty}{c}c}{U_\infty} = \frac{50\Omega^* y^*}{U^*}\frac{15}{2}\theta^* c \\ \Leftrightarrow \delta^* &= \frac{\delta}{c} = \frac{50\Omega^* y^*}{U^*}\frac{15}{2}\theta^*\end{aligned} \tag{A.15}$$

- The momentum thickness Reynolds number ($Re_{\theta t}$):

$$\begin{aligned}Re_{\theta t} &= \frac{\rho U\theta}{\mu} = \frac{\rho^* U^*\theta^*}{\mu^*}\frac{\rho_\infty U_\infty c}{\mu_\infty} \\ &= \frac{\rho^* U^*\theta^*}{\mu^*}Re \\ \Leftrightarrow Re_{\theta t}^* &= \frac{\rho^* U^*\theta^*}{\mu^*} = \frac{Re_{\theta t}}{Re}\end{aligned} \tag{A.16}$$

- The vorticity Reynolds number (Re_v) based on strain rate:

$$\begin{aligned} Re_v &= \frac{\rho y^2 S}{\mu} = \frac{\rho^* y^{*2} S^*}{\mu^*} \frac{\rho_\infty c^2 (\frac{U_\infty}{c})}{\mu_\infty} \\ &= \frac{\rho^* y^{*2} S^*}{\mu^*} \frac{\rho_\infty U_\infty c}{\mu_\infty} = \frac{\rho^* y^{*2} S^*}{\mu^*} Re \\ \Leftrightarrow Re_v^* &= \frac{\rho^* y^{*2} S^*}{\mu^*} = \frac{Re_v}{Re} \end{aligned} \tag{A.17}$$

- The Reynolds number based on specific dissipation rate of turbulence (Re_ω):

$$\begin{aligned} Re_\omega &= \frac{\rho y^2 \omega}{\mu} = \frac{\rho^* y^{*2} \omega^*}{\mu^*} \frac{\rho_\infty c^2 (\frac{U_\infty}{c})}{\mu_\infty} \\ &= \frac{\rho^* y^{*2} \omega^*}{\mu^*} \frac{\rho_\infty U_\infty c}{\mu_\infty} = \frac{\rho^* y^{*2} \omega^*}{\mu^*} Re \\ \Leftrightarrow Re_\omega^* &= \frac{\rho^* y^{*2} \omega^*}{\mu^*} = \frac{Re_\omega}{Re} \end{aligned} \tag{A.18}$$

- The wall distance based turbulent Reynolds number (Re_y):

$$\begin{aligned} Re_y &= \frac{\rho y \sqrt{k}}{\mu} = \frac{\rho^* y^* \sqrt{k^*}}{\mu^*} \frac{\rho_\infty c \sqrt{U_\infty^2}}{\mu_\infty} \\ &= \frac{\rho^* y^* \sqrt{k^*}}{\mu^*} \frac{\rho_\infty U_\infty c}{\mu_\infty} = \frac{\rho^* y^* \sqrt{k^*}}{\mu^*} Re \\ \Leftrightarrow Re_y^* &= \frac{\rho^* y^* \sqrt{k^*}}{\mu^*} = \frac{Re_y}{Re} \end{aligned} \tag{A.19}$$

A.2 Transport equation for the turbulent kinetic energy (k)

The equation for the the turbulent kinetic energy (k) of the $\kappa-\gamma-\omega-Re_{\theta t}$ model can be written as follows:

$$\frac{\partial}{\partial t}(\rho k) + \frac{\partial}{\partial x_j}(\rho k u_j) = \gamma_{eff} P - min[max(\gamma_{eff}, 0.1), 1.0] \cdot \hat{\beta} \rho \omega k + \frac{\partial}{\partial x_j}\left[(\mu + \sigma_k \mu_T)\frac{\partial k}{\partial x_j}\right] \tag{A.20}$$

In order to no-dimensionalise the equation, the following terms have to be considered:

$$\frac{\partial}{\partial t}(\rho k) = \left[\rho_\infty \frac{U_\infty^3}{c}\right] \cdot \frac{\partial}{\partial t^*}(\rho^* k^*) \tag{A.21}$$

$$\frac{\partial}{\partial x_j}(\rho k u_i) = \left[\rho_\infty \frac{U_\infty^3}{c}\right] \cdot \frac{\partial}{\partial x_j^*}(\rho^* k^* u_i^*) \tag{A.22}$$

Based on eqn. (A.4), the dissipation term of eqn. (A.20) can be written as

$$\begin{aligned} \frac{\partial}{\partial x_j}\left[(\mu + \sigma_k \mu_T)\frac{\partial k}{\partial x_j}\right] &= \frac{1}{c}\frac{\partial}{\partial x_j^*}\left[(\mu^* \mu_\infty + \sigma_k \mu_T^* \mu_\infty)\frac{U_\infty^2}{c}\frac{\partial k^*}{\partial x_j^*}\right] \\ &= \left[\mu_\infty \frac{U_\infty^2}{c^2}\right] \cdot \frac{\partial}{\partial x_j}\left[(\mu^* + \sigma_k \mu_T^*)\frac{\partial k^*}{\partial x_j^*}\right] \end{aligned} \tag{A.23}$$

The production term from the $k-\omega$ model based on eqn. (A.8) is written as

$$\begin{aligned} P &= \tau_{ij}\frac{\partial u_i}{\partial x_j} = \left[\rho_\infty U_\infty \frac{U_\infty}{c}\right] \cdot \tau_{ij}^* \frac{\partial u_i^*}{\partial x_j^*} \\ &= \left[\rho_\infty \frac{U_\infty^3}{c}\right] \cdot \tau_{ij}^* \frac{\partial u_i^*}{\partial x_j^*} = \left[\rho_\infty \frac{U_\infty^3}{c}\right] \cdot P^* \end{aligned} \tag{A.24}$$

The destruction term is given as

$$\beta^*\rho\omega k = \left[\rho_\infty \frac{U_\infty^3}{c}\right]\cdot\hat{\beta}\rho^*\omega^*k^* \tag{A.25}$$

After the appropriate simplifications and considering that

$$\frac{\frac{\mu_\infty U_\infty^2}{c^2}}{\frac{\rho_\infty U_\infty^3}{c}} = \frac{\frac{\mu_\infty}{c}}{\rho_\infty U_\infty} = \frac{1}{\frac{\rho_\infty U_\infty c}{\mu_\infty}} = \frac{1}{Re} \tag{A.26}$$

the dimensionless equation for k is given by

$$\frac{\partial}{\partial t^*}(\rho^*k^*) + \frac{\partial}{\partial x_j^*}(\rho^*k^*u_j^*) = \gamma_{eff}P^* - min(max(\gamma_{eff},0.1),1.0)\rho^*\hat{\beta}\omega^*k^* + \frac{1}{Re}\frac{\partial}{\partial x_j^*}\left[(\mu^*+\sigma_k\mu_T^*)\frac{\partial k^*}{\partial x_j^*}\right] \tag{A.27}$$

A.3 Transport equation for the specific turbulence dissipation rate (ω)

The equation for the specific turbulence dissipation rate is given by the following equation:

$$\frac{\partial}{\partial t}(\rho\omega) + \frac{\partial}{\partial x_j}(\rho\omega u_j) = \rho\frac{\alpha}{\mu_T}P - \beta\rho\omega^2 + \frac{\partial}{\partial x_j}\left[(\mu+\sigma_\omega\mu_t)\frac{\partial\omega}{\partial x_j}\right] + \rho S_l \tag{A.28}$$

Similar to the manipulations for the k-equation

$$\frac{\partial}{\partial t}(\rho\omega) = \left[\rho_\infty\frac{U_\infty^2}{c^2}\right]\cdot\frac{\partial}{\partial t^*}(\rho^*\omega^*) \tag{A.29}$$

$$\frac{\partial}{\partial x_j}(\rho\omega u_i) = \left[\rho_\infty\frac{U_\infty^2}{c^2}\right]\cdot\frac{\partial}{\partial x_j^*}(\rho^*\omega^*u_i^*) \tag{A.30}$$

and

$$\begin{aligned}\frac{\partial}{\partial x_j}\left[(\mu+\sigma_\omega\mu_t)\frac{\partial k}{\partial x_j}\right] &= \frac{1}{c}\frac{\partial}{\partial x_j^*}\left[(\mu^*\mu_\infty+\sigma_\omega\mu_T^*\mu_\infty)\frac{U_\infty}{c^2}\frac{\partial\omega^*}{\partial x_j^*}\right]\\ &= \left[\mu_\infty\frac{U_\infty}{c^3}\right]\cdot\frac{\partial}{\partial x_j}\left[(\mu^*+\sigma_\omega\mu_T^*)\frac{\partial\omega^*}{\partial x_j^*}\right]\end{aligned} \tag{A.31}$$

The production and dissipation terms are written as

$$\begin{aligned}\rho\frac{\alpha}{\mu_t}P &= \rho^*\rho_\infty\frac{\alpha}{\mu_T^*\rho_\infty U_\infty c}P^*\rho_\infty U_\infty c\frac{U_\infty^2}{c^2}\\ &= \left[\rho_\infty\frac{U_\infty^2}{c^2}\right]\cdot\rho^*\frac{\alpha}{\mu_T^*}P^*\end{aligned} \tag{A.32}$$

$$\beta\rho\omega^2 = \left[\rho_\infty\frac{U_\infty^2}{c^2}\right]\cdot\beta\rho^*\omega^{*2} \tag{A.33}$$

Considering that

$$\frac{\mu_\infty\frac{U_\infty}{c^3}}{\rho_\infty\frac{U_\infty^2}{c^2}} = \frac{1}{Re} \tag{A.34}$$

the resulting dimensionless equation for the ω is given by

$$\frac{\partial}{\partial t^*}(\rho^*\omega^*) + \frac{\partial}{\partial x_j^*}(\rho^*\omega^*u_j^*) = \rho^*\frac{\alpha}{\mu_T^*}P^* - \beta\rho\omega^{*2} + \rho^*\frac{c^2}{U_\infty^2}S_l^{*\prime} + \frac{1}{Re}\frac{\partial}{\partial x_j^*}\left[(\mu^*+\sigma_\omega\mu_T^*)\frac{\partial\omega^*}{\partial x_j^*}\right] \tag{A.35}$$

A.4 Transport equation for the intermittency (γ)

The equation for the intermittency (γ) is given by

$$\frac{\partial}{\partial t}(\rho\gamma)+\frac{\partial}{\partial x_j}(\rho\gamma u_j)=P_{\gamma 1}-E_{\gamma 1}+P_{\gamma 2}-E_{\gamma 2}+\frac{\partial}{\partial x_j}\Big[(\mu+\sigma_\gamma\mu_T)\frac{\partial\gamma}{\partial x_j}\Big] \tag{A.36}$$

where the term of the left side of the equation and the dissipation term are given as

$$\frac{\partial}{\partial t}(\rho\gamma)=\Big[\rho_\infty\frac{U_\infty}{c}\Big]\cdot\frac{\partial}{\partial t^*}(\rho^*\gamma), \tag{A.37}$$

$$\frac{\partial}{\partial x_j}(\rho\gamma u_i)=\Big[\rho_\infty\frac{U_\infty}{c}\Big]\cdot\frac{\partial}{\partial x_j^*}(\rho^* u_i^*\gamma) \tag{A.38}$$

and

$$\begin{aligned}\frac{\partial}{\partial x_j}\Big[(\mu+\frac{\mu_T}{\sigma_\gamma})\frac{\partial\gamma}{\partial x_j}\Big] &= \frac{1}{c}\frac{\partial}{\partial x_j}\Big[(\mu^*\mu_\infty+\frac{\mu_T^*}{\sigma_\gamma}\mu_\infty)\frac{1}{c}\frac{\partial\gamma}{\partial x_j^*}\Big] \\ &= \Big[\frac{\mu_\infty}{c^2}\Big]\cdot\frac{\partial}{\partial x_j}\Big[(\mu^*+\frac{\mu_T^*}{\sigma_\gamma})\frac{\partial\gamma}{\partial x_j^*}\Big]\end{aligned} \tag{A.39}$$

For the the production and dissipations terms of the intermittency (γ) equation some extra functions have to be estimated. The functions F_{length}, F_{onset} and F_{turb} are dimensionless.

Hence the production terms would be estimated

$$\begin{aligned}P_{\gamma 1} &= c_{a1}F_{length}\rho S[\gamma F_{onset}]^{1/2} \\ &= \Big[\rho_\infty\frac{U_\infty}{c}\Big]\cdot c_{a1}\rho^* S^* F_{length}[\gamma F_{onset}]^{1/2}\end{aligned} \tag{A.40}$$

$$\begin{aligned}P_{\gamma 2} &= c_{a2}\rho\Omega\gamma F_{turb} \\ &= \Big[\rho_\infty\frac{U_\infty}{c}\Big]\cdot c_{a2}\rho^*\Omega^*\gamma F_{turb}\end{aligned} \tag{A.41}$$

and

$$E_{\gamma 1} = \Big[\rho_\infty\frac{U_\infty}{c}\Big]\cdot e_1 P_{\gamma 1}^*\gamma \tag{A.42}$$

$$E_{\gamma 2} = \Big[\rho_\infty\frac{U_\infty}{c}\Big]\cdot e_2 P_{\gamma 2}^*\gamma \tag{A.43}$$

The following equation has to be taken under consideration

$$\frac{\frac{\mu_\infty}{c^2}}{\frac{\rho_\infty U_\infty}{c}}=\frac{\mu_\infty c}{\rho_\infty U_\infty c^2}=\frac{1}{\frac{\rho_\infty U_\infty c}{\mu_\infty}}=\frac{1}{Re} \tag{A.44}$$

Finally, the dimensionless equation for the intermittency (γ) can be written as

$$\frac{\partial}{\partial t^*}(\rho^*\gamma)+\frac{\partial}{\partial x_j^*}(\rho^*\gamma u_j^*)=P_{\gamma 1}-E_{\gamma 1}+P_{\gamma 2}-E_{\gamma 2}+\frac{1}{Re}\frac{\partial}{\partial x_j^*}\Big[(\mu^*+\frac{\mu_T^*}{\sigma_\gamma})\frac{\partial\gamma}{\partial x_j^*}\Big] \tag{A.45}$$

A.5 Transport equation for the local momentum thickness Reylonlds number ($\tilde{Re}_{\theta t}$)

The second transport equation of the $\kappa-\omega-\gamma-Re_{\theta t}$ model is the transport equation for the transition momentum thickness Reynolds number $\tilde{Re}_{\theta t}$ which is given as

$$\frac{\partial}{\partial t}(\rho\tilde{Re}_{\theta t})+\frac{\partial}{\partial x_j}(\rho\tilde{Re}_{\theta t}u_j)=P_{\theta t}+\frac{\partial}{\partial x_j}\Big[\sigma_{\theta t}(\mu+\mu_T)\frac{\partial}{\partial x_j}(\tilde{Re}_{\theta t})\Big] \tag{A.46}$$

The left hand side of the equation is becoming dimensionless as follows

$$\frac{\partial}{\partial t}(\rho\tilde{Re}_{\theta t}) = [\rho_\infty\frac{U_\infty}{c}]\cdot\frac{\partial}{\partial t^*}(\rho^*\tilde{Re}_{\theta t}) \tag{A.47}$$

$$\frac{\partial}{\partial x_j}(\rho u_i\tilde{Re}_{\theta t}) = [\rho_\infty\frac{U_\infty}{c}]\cdot\frac{\partial}{\partial x_j^*}(\rho^* u_i^*\tilde{Re}_{\theta t}) \tag{A.48}$$

The dissipation term is written as

$$\begin{aligned}\frac{\partial}{\partial x_j}[(\mu+\sigma_k\mu_T)\frac{\partial\tilde{Re}_{\theta t}}{\partial x_j}] &= \frac{1}{c}\frac{\partial}{\partial x_j^*}[(\mu^*\mu_\infty+\sigma_k\mu_T^*\mu_\infty)\frac{1}{c}\frac{\partial\tilde{Re}_{\theta t}}{\partial x_j^*}] \\ &= [\frac{\mu_\infty}{c^2}]\cdot\frac{\partial}{\partial x_j}[(\mu^*+\sigma_k\mu_T^*)\frac{\partial\tilde{Re}_{\theta t}}{\partial x_j^*}]\end{aligned} \tag{A.49}$$

For the non-dimensionalisation of the production term the following has to be considered

$$t_{scale} = \frac{500\mu}{\rho U^2} = \frac{500\mu^*}{\rho^* U^{*2}}\frac{\mu_\infty}{\rho_\infty U_\infty^2} \tag{A.50}$$

which has dimensions of time. In order to make it dimensionless, t_{scale} has to be divided with time ($\frac{c}{U_\infty}$), hence

$$\begin{aligned}t_{scale}^* &= \frac{t_{scale}}{\frac{c}{U_\infty}} = \frac{\frac{500\mu^*}{\rho^* U^{*2}}\frac{\mu_\infty}{\rho_\infty U_\infty^2}}{\frac{c}{U_\infty}} \\ &= frac500\mu^*\rho^* U^{*2}\frac{\mu_\infty U_\infty}{\rho_\infty U_\infty^2 c} = \frac{500\mu^*}{\rho^* U^{*2}}\frac{1}{Re}\end{aligned} \tag{A.51}$$

Hence the production terms can be written as

$$\begin{aligned}P_{\theta t} &= c_{\theta t}\frac{\rho}{t}(Re_{\theta t}-\tilde{Re}_{\theta t})(1-F_{\theta t}) \\ &= c_{\theta t}\frac{\rho^*\rho_\infty}{t_{scale}^*\frac{c}{U_\infty}}(Re_{\theta t}-\tilde{Re}_{\theta t})(1-F_{\theta t}) \\ &= [\rho_\infty\frac{U_\infty}{c}]\cdot c_{\theta t}\frac{\rho^*}{t_{scale}^*}(Re_{\theta t}-\tilde{Re}_{\theta t})(1-F_{\theta t})\end{aligned} \tag{A.52}$$

Finally after the appropriate simplifications, $\frac{\frac{\mu_\infty}{c^2}}{\rho_\infty\frac{U_\infty}{c}} = \frac{1}{Re}$ the equation for the $\tilde{Re}_{\theta t}$

$$\frac{\partial}{\partial t^*}(\rho^*\tilde{Re}_{\theta t}) + \frac{\partial}{\partial x_j^*}(\rho^*\tilde{Re}_{\theta t}u_j^*) = P_{\theta t} + \frac{1}{Re}\frac{\partial}{\partial x_j^*}\left[(\mu^*+\sigma_k\mu_T^*)\frac{\partial\tilde{Re}_{\theta t}}{\partial x_j^*}\right] \tag{A.53}$$

Appendix B

Positive Fourier series used for flapping and pitch

B.1 Equations for the calculation of the velocity field for forward and hover conditions

In forward flight, the rotor blades experience a number of other movements besides the rotation. In most modern helicopters, the rotor blades are attached to the rotor head by a set of hinges, a flap hinge which allows the blade to flap up and down, the lead-lag hinge which allows the blade to do an forward or backward motion and the feathering hinge which is used to change the blade pitch. Hence, when the velocity field has to be taken into account, the extra motion of the blade has to be taken into consideration.

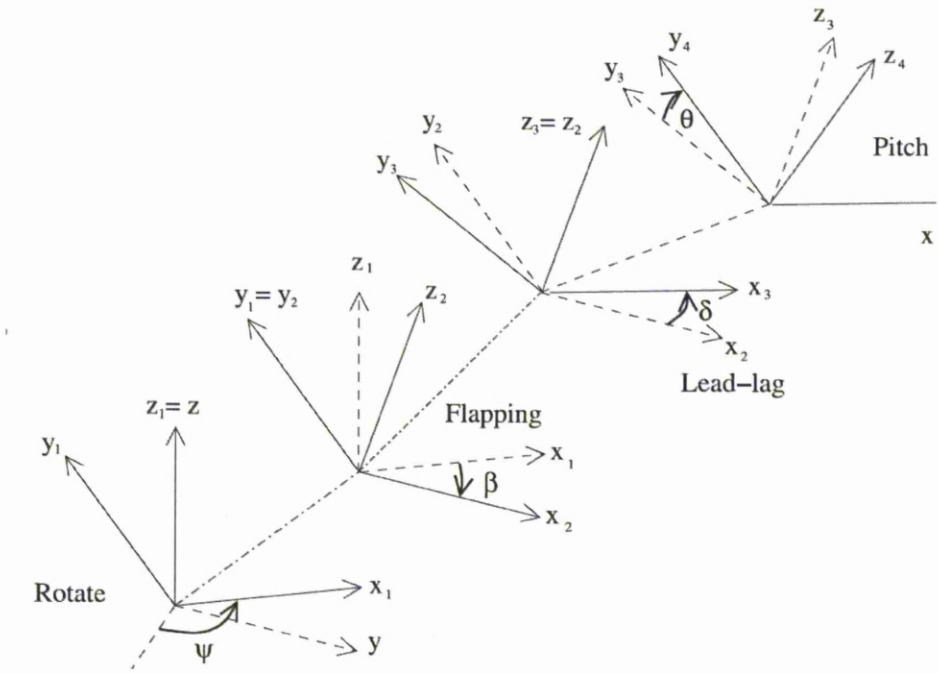

Figure B.1: Schematic of the rotor transformation.

Initially, the blades rotate and in each azimuth angle the velocity of the speed will be the sum of the free stream velocity and the velocity due to the rotation. ω_z is the rotational speed and is given by:

$$\vec{U_{new}} = \vec{U_{old}} + \vec{\omega_\psi} \times \vec{r} = \vec{U_{old}} + \begin{vmatrix} \vec{i} & \vec{j} & \vec{k} \\ 0 & 0 & -\omega_z \\ x & y & z \end{vmatrix} \tag{B.1}$$

where the rotational speed is given by

$$\begin{aligned} U_{tip} = \omega_z R \quad &\Rightarrow \quad \frac{U_{tip}}{U_\infty} = \frac{\omega_z R}{U_\infty} \\ \frac{1}{\mu} = \frac{\omega_z R}{U_\infty} \quad &\Rightarrow \quad \omega_z = \frac{U_\infty}{\mu R} \end{aligned} \tag{B.2}$$

The cross product from eqn. (B.1) is calculated as

$$\vec{\omega_\psi} \times \vec{r} = \begin{vmatrix} \vec{i} & \vec{j} & \vec{k} \\ 0 & 0 & -\omega_z \\ x & y & z \end{vmatrix} = y\omega_z\vec{i} - x\omega_z\vec{j}$$

Hence the new non-dimensional u component of the velocity would be

$$u'_{new} = u'_{old} + \frac{\omega_z}{U_\infty} y = u'_{old} + \frac{1}{\mu R} y \tag{B.3}$$

$$v'_{new} = v'_{old} - \frac{\omega_z}{U_\infty} x = u'_{old} - \frac{1}{\mu R} x \tag{B.4}$$

where the z component of the velocity remains the same.

Considering that the flapping angle is defined by a positive Fourier series :

$$\beta(\psi) = \beta_0 + \beta_{1s} sin(\psi) + \beta_{1c} cos(\psi) + \ldots \tag{B.5}$$

where β_0 is the collective pitch and only the first positive harmonic terms are considered.

The new velocity vector will be given by

$$\vec{U_{new}} + \vec{\omega_\beta} \times \vec{r} \tag{B.6}$$

where the cross product is calculated as

$$\vec{\omega_\beta} \times \vec{r} = \begin{vmatrix} \vec{i} & \vec{j} & \vec{k} \\ 0 & \omega_y & 0 \\ x & y & z \end{vmatrix} = -z\omega_y\vec{i} + x\omega_y\vec{k}$$

The rate of rotation about the y axis (ω_y) is given as

$$\begin{aligned} \omega_y &= \frac{d\beta}{dt} = \frac{d\beta}{d\psi}\frac{d\psi}{dt} = \omega_z \frac{d\beta}{d\psi} \\ &= \omega_y \Big(\beta_{1s} cos(\psi) - \beta_{1c} sin(\psi) \Big) \\ &= \frac{U_\infty}{\mu R} \Big(\beta_{1s} cos(\psi) - \beta_{1c} sin(\psi) \Big) \end{aligned} \tag{B.7}$$

The new velocity components will be given as

$$u'_{new} = u'_{old} - \frac{\omega_y}{U_\infty} z = u'_{old} + \frac{1}{\mu R} \Big(\beta_{1s} cos(\psi) - \beta_{1c} sin(\psi) \Big) z \tag{B.8}$$

and

$$w'_{new} = w'_{old} + \frac{\omega_y}{U_\infty} x = w'_{old} - \frac{1}{\mu R} \Big(\beta_{1s} cos(\psi) - \beta_{1c} sin(\psi) \Big) x \tag{B.9}$$

For the pitch, the same idea is followed. The pitch angle is given by the equation

$$\theta(\psi) = \theta_0 + \theta_{1s}sin(\psi) + \theta_{1c}cos(\psi) + \dots \tag{B.10}$$

where the positive series are considered rather than the negatives.

The rate of rotation about the x axis will be

$$\begin{aligned} \omega_x &= \frac{d\theta}{dt} = \frac{d\theta}{d\psi}\frac{d\psi}{dt} = \omega_z\frac{d\theta}{d\psi} \\ &= \frac{U_\infty}{\mu R}\Big(\theta_{1s}cos(\psi) - \theta_{1c}sin(\psi)\Big) \end{aligned} \tag{B.11}$$

Finally, the new velocity components will be

$$\begin{aligned} \vec{U_{new}} &= \vec{U_{old}} + \vec{\omega}_x \times \vec{r} == \begin{pmatrix} u'_{old} \\ v'_{old} - \frac{\omega_x}{U_\infty}z \\ w'_{old} + \frac{\omega_x}{U_\infty}y \end{pmatrix} = \end{aligned} \tag{B.12}$$

$$= \begin{pmatrix} u'_{old} \\ v'_{old} - \frac{1}{\mu R}(\theta_{1s}cos(\psi) - \theta_{1c}sin(\psi))z \\ w'_{old} + \frac{1}{\mu R}(\theta_{1s}cos(\psi) - \theta_{1c}sin(\psi))y \end{pmatrix} \tag{B.13}$$

B.2 Equations for the calculation of the velocity field during hover

In hover, the blade encounters a constant blade normal velocity and as a results no pitch is needed. Moreover, if constant collective is considered, them the velocity field is estimated by the equation:

$$\vec{U_{new}} = \vec{U_{old}} + \vec{\omega}_\psi \times \vec{r} = \vec{U_{old}} + \begin{vmatrix} \vec{i} & \vec{j} & \vec{k} \\ 0 & 0 & -\omega_z \\ x & y & z \end{vmatrix}$$

The rotational speed in the z axis during the hover is calculated by the following equation

$$U_{tip} = \omega_z R \Rightarrow \omega_z = \frac{U_{tip}}{R} \tag{B.14}$$

Hence the new non-dimensional u component of the velocity would be

$$u'_{new} = u'_{old} + \frac{\omega_z}{U_{tip}}y = u'_{old} + \frac{y}{R} \tag{B.15}$$

$$v'_{new} = v'_{old} - \frac{\omega_z}{U_{tip}}x = u'_{old} - \frac{x}{R} \tag{B.16}$$

where the z component of the velocity remains the same.

Appendix C

Wind Tunnel Experiment

C.1 Wind tunnel

All experiments were conducted in a low-speed, open circuit, wind tunnel located in the Aerodynamics Laboratory of the University of Liverpool. This wind tunnel was previously used by many researchers, e.g. Abu-Ghannam [63] circa 1980 and Huang [92] in 2006 for the investigation of transitional boundary layer. An overview of the wind tunnel can be seen in figure (C.1). At the end of the tunnel a four-bladed propeller draws air through the working section. The electric motor can run for long hours at almost constant speed. The settling chamber of the tunnel is attached to the laboratory wall and the air intake to the tunnel is guided by two rows of vanes, one at the bottom and one at the top of the tunnel. Each row has 17 vanes. To make the flow as uniform and steady as possible there are three more screens of 0.8mm wire diameter, and 2.3mm mesh size just after the blades and a honeycomb of 10mm of diameter holes and 76mm of depth to remove any large scale turbulence and swirl in the flow[93] .

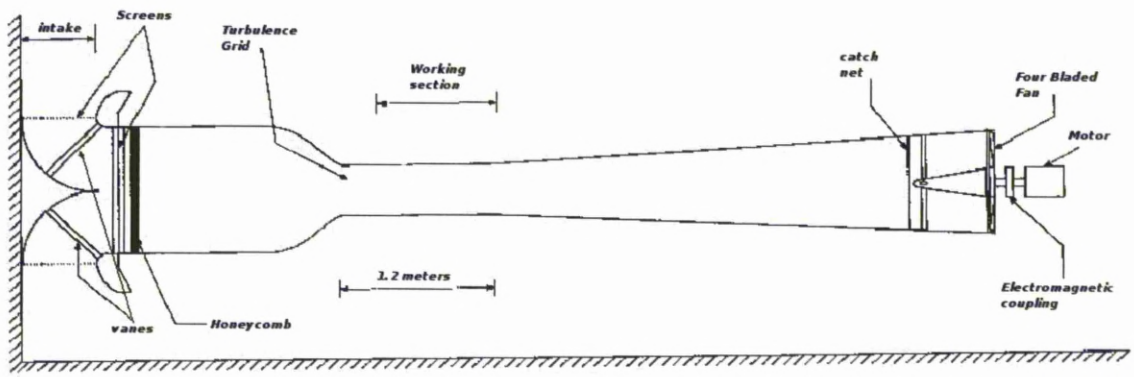

Figure C.1: Schematic of the wind tunnel. The different sections are also presented.

The working section of the tunnel is shown in figure (C.1). The size of the working section is limited to a rectangular cross-sectional area of 510mm x 715mm and 1530mm length. At both sides of the working section glass windows allow for easy access. The tunnel has an adjustable flexible ceiling that it is consisted of three different sections. This setup provides the ability to change the pressure gradients of the working section.

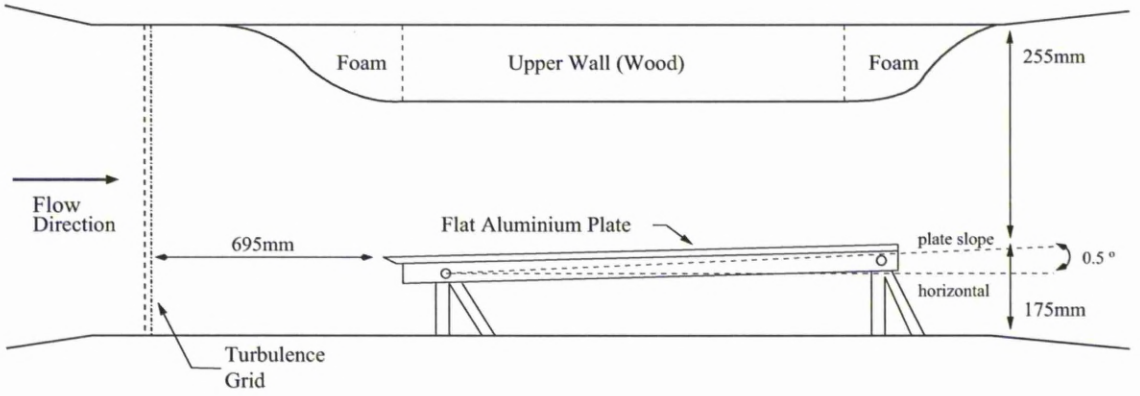

Figure C.2: Schematic of the wind tunnel test section.

C.2 Flat Plate

For the experiment a polished aluminum plate was used. It has 6.35mm of thickness, 1219.2mm length and 711.2mm width. At the middle of the plate and at distances 50.8, 279.4, 508, 736.6, 965.2 and 1168.4mm from the leading edge six static pressure holes of 0.8mm were drilled. These holes were used to measure static pressure and determine the pressure gradient over the plate. The exact location of these taps can be seen in figure (C.2).

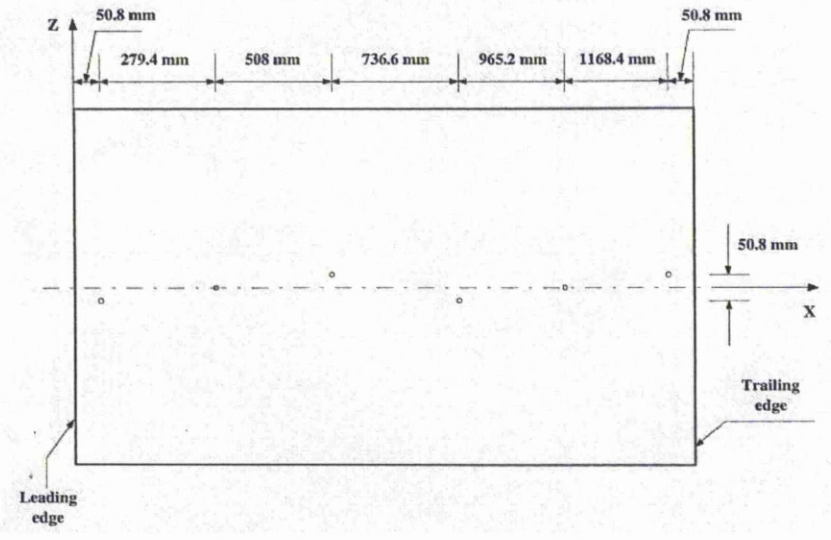

Figure C.3: Schematic of the flat plate and locations of the pressure taps.

The leading edge of the flat plate is designed to ensure that separation does not occur. It has a major chord of 50mm and a minor of 6.35mm with the elliptic 0.8mm nose radius. The shape of the leading edge can be seen in figure (C.2). The flat plate is resting on adjustable legs, and the plate was inclined by 0.5 degrees slope to avoid flow separation.

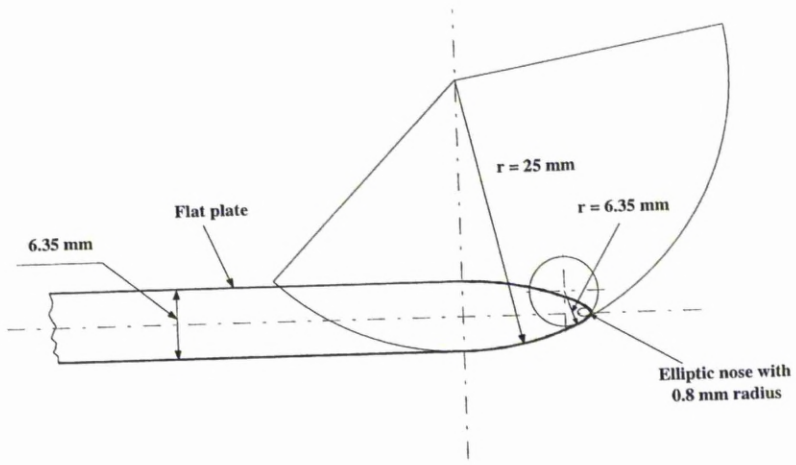

Figure C.4: Schematic of the leading edge of the flat plate.

C.3 Turbulence Grids

The wind tunnel can be equipped with different types of turbulence-generating grids. These grids were placed at 695mm upstream of the flat plate leading edge. The grids can create estimated turbulence levels in the range of 0.93% to 5.19%. The characteristics of the grids can be seen in tables (C.1) and (C.2).

Grids	Material	Bar Width (mm)	Bar Type	Mesh Size	Mesh Type
G1	Galvanised Steel	1	Circle	12.5	Square
G2	Bright Steel	3	Circle	19	Square
G3	Wood	4	Square	9	Vertical Bars
G4	Wood	9.5	Square	9	Vertical Bars
G5	Wood	5	Square	25	Square
G6	Wood	13	Square	50.5	Square

Table C.1: Materials and characteristics of the grids.

To obtain an accurate prediction of the produced turbulence level, Roach's equation[94] was used.

$$Tu = C\left(\frac{x}{d}\right)^{-\frac{5}{7}} \tag{C.1}$$

where d is the diameter of the wires and bars from which the grids are created while x is the distance downstream the grid. Parameter C is based on the shape of the grids and for the two first grids of table (C.2) 0.8 is used while for the remaining 1.13 was the selected value.

Grids	Material	Constant C	Open Area Ratio (%)	Tu (%) at leading edge
G1	Galvanised Steel	0.8	84.6	0.93
G2	Bright Steel	0.8	71.1	1.23
G3	Wood	1.13	55.5	2.24
G4	Wood	1.13	55.5	4.58
G5	Wood	1.13	64	3.12
G6	Wood	1.13	55	5.19

Table C.2: Characteristics of the grids.

C.4 Traverse gear

In order to measure the boundary layer over the flat plate, a special traverse gear was built which can be seen in figure (C.4). Inside the gear, a linear stepper motor was controlled either manually or by means of a computer program. The motor has a fine linear movement of 0.00254mm per step and it was arranged to 200steps per revolution. The spreadsheet of the motor can be seen in figure (C.4).

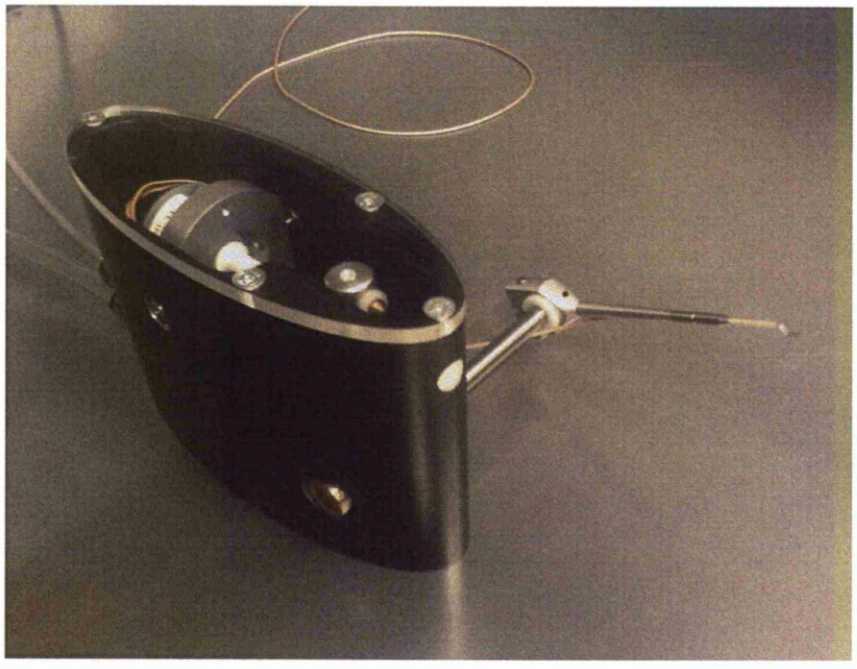

Figure C.5: The traverse gear used in the experiment.

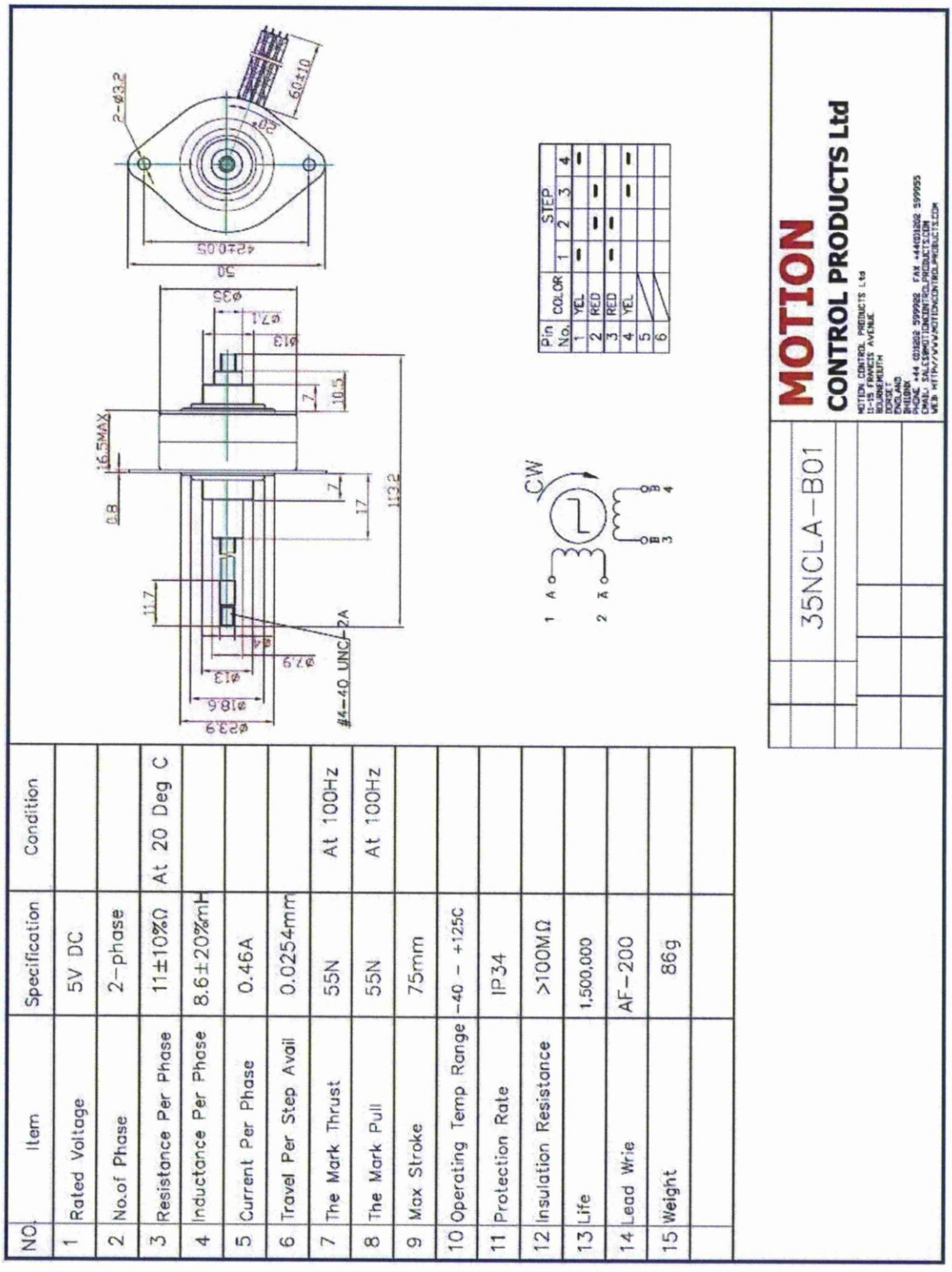

NO	Item	Specification	Condition
1	Rated Voltage	5V DC	
2	No.of Phase	2-phase	
3	Resistance Per Phase	11±10%Ω	At 20 Deg C
4	Inductance Per Phase	8.6±20%mH	
5	Current Per Phase	0.46A	
6	Travel Per Step Avail	0.0254mm	
7	The Mark Thrust	55N	At 100Hz
8	The Mark Pull	55N	At 100Hz
9	Max Stroke	75mm	
10	Operating Temp Range	-40 ~ +125C	
11	Protection Rate	IP34	
12	Insulation Resistance	>100MΩ	
13	Life	1,500,000	
14	Lead Wrie	AF-200	
15	Weight	86g	

Figure C.6: Characteristics of the step motor used in the traverse gear.

Knowing the length of the linear movement for each step of the motor and the length of the axes inside the traverse gear, the movement of the hot-wire can be calculated. The liner movement of the stepper motor is transformed in rotation at point A and that rotation is transferred into points B and C. The angle (θ) that the point turns (points B and C on figure (C.4)) can be calculated as

$$\theta = tan^{-1}(\frac{l}{(AB)}) = tan^{-1}(\frac{0.0254}{50}) \tag{C.2}$$

and then the height can be calculated as

$$h = (CD) \cdot tan(\theta) = 100 \cdot tan(\theta) = 0.0508mm \tag{C.3}$$

Schematic (C.4) shows how the height from the surface of the flat plate was calculated.

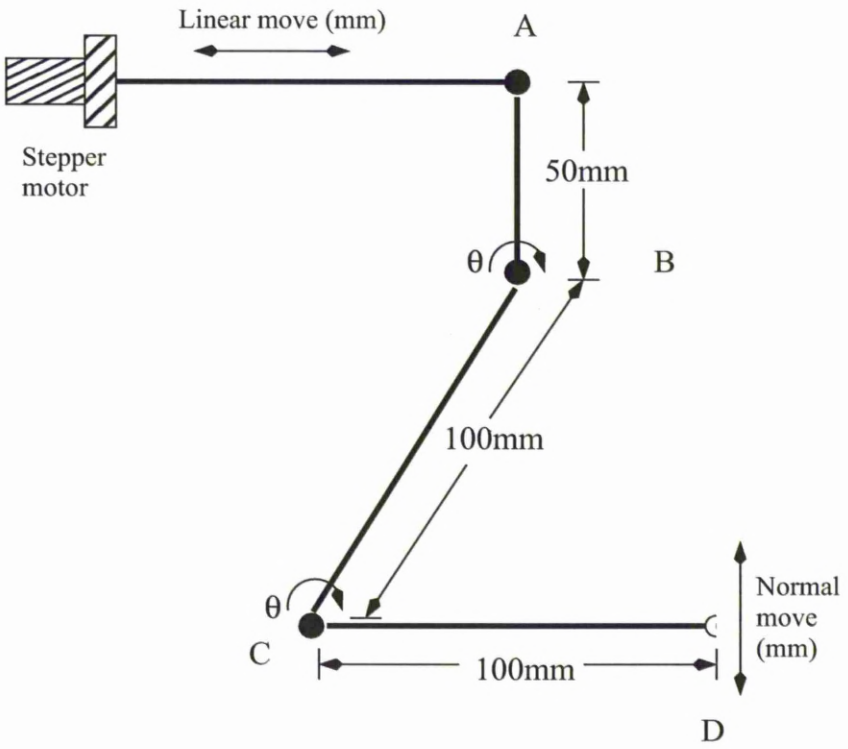

Figure C.7: Diagram for calculating the height of the hot-wire probe.

To control the traverse gear, a Labjack U12 instrument is used which can be seen in figure (C.8). This is a device specifically designed for data logging applications with 8 analog input signals and 2 outputs and a number of digital input/output.

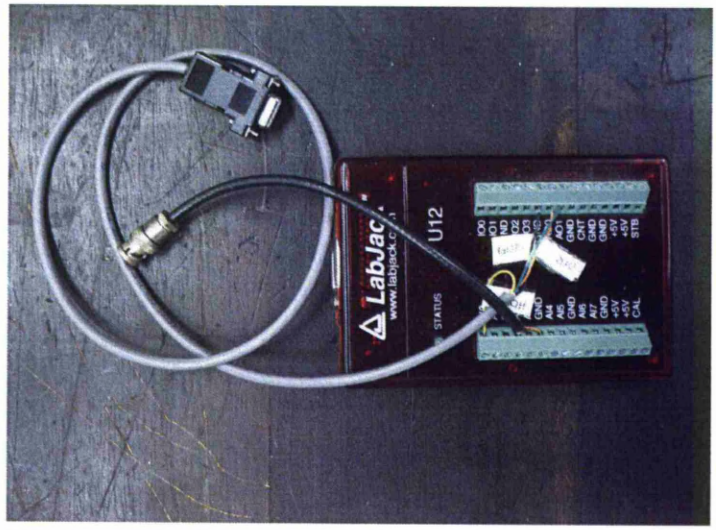

Figure C.8: Labjack U12

C.5 Manometers

A single manometer was used to measure the reference velocity of the wind tunnel and to calibrate the hot-wire probe. This manometer was set to 30° inclination with the vertical. The liquid inside the manometer is ethanol and it can be adjusted by a micrometer at the back of it.

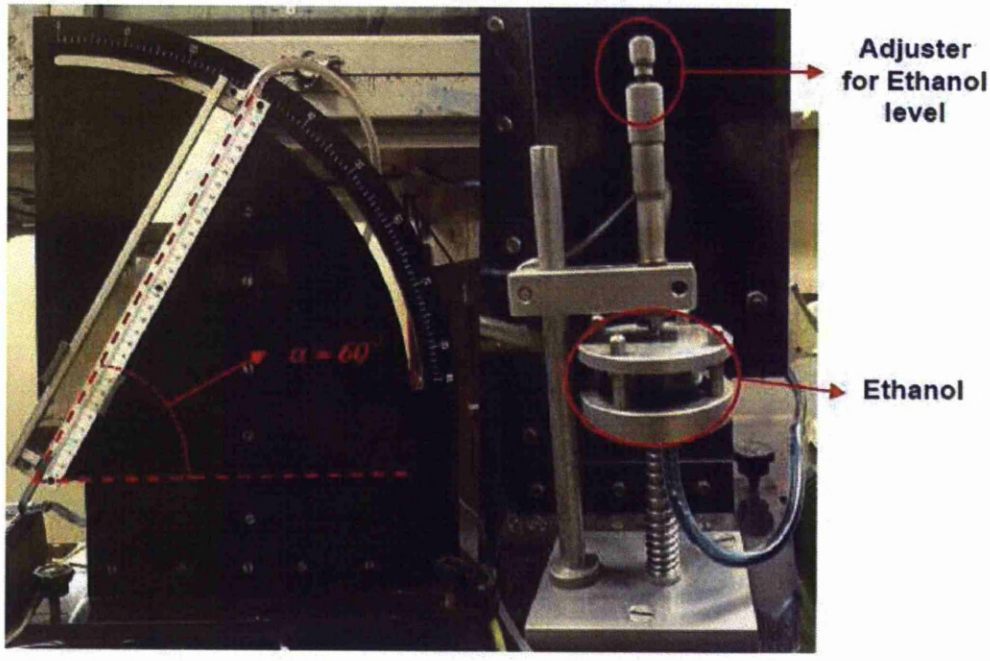

Figure C.9: Manometer connected with the pitot tube. The manometer is tilted by 60°.

Another multi-manometer was used to measure the flat plate surface static pressure during the experiment. It has a minimum of 2mm reading scale and a minimum inclination angle of 30°. On the same multi-manometer, pressure taps on the walls of the settling chamber and the diffuser of the wind tunnel, are also connected.

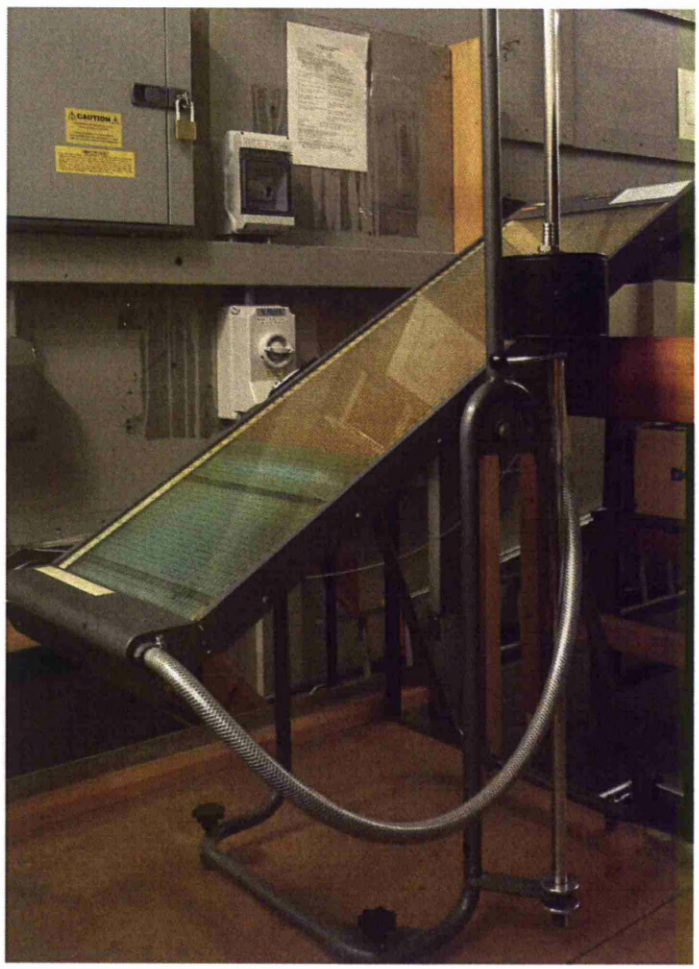

Figure C.10: Multi-manometer used for measuring the pressure at the surface of the flat plate. The Multi-manometer is tilted by 30°.

C.6 Electronic circuits

A set of devices were used during the experiment. These were a constant temperature anemometer (CTA), a digital to analog converter (DAC) and a data logger. Information relative to these is given below.

C.6.1 Constant Temperature Anemometer

During the experiment, a MiniCTA system manufactured by Dantec Dynamics was used as can be seen in figure (C.6.1). This constant temperature anemometer was selected due to its size as it is a miniature of the usual anemometers and is effective in diagnosing the characteristics of the flow. It is designed for measurements of velocity and turbulence in subsonic flows. This anemometer can accept probes with cold resistance up to 10 Ohms. The overheat setup and signal conditioning can be performed via dip switches and jumpers inside the box. The overheat can be calculated using a Microsoft Excel spreadsheet which can be downloaded from the Dantec Dynamics web site. Providing the anemometer serial number and the data from the probe container (C.3), the spreadsheet calculates the decade resistance and displays the setting for the switch. These are shown in figure (C.12).

Figure C.11: Dantec Dynamics mini constant temperature anemometer.

C.6.2 Data Logging device

For data logging, the National Instrument USB-6009 DAQ (Digital to Analog Converter) was used. It is an affordable data acquisition device with plug-and-play USB connectivity and it can be seen in figure (C.6.2). NI USB-6009 is an easy-to-use device specifically designed for data logging applications. It provides the capability to log real time data with 14-bit resolution and export them to a computer.

Mini-CTA 54T30: Selecting and adjusting overheat. **9054S4011**

Org. 980528/TSV
Rev. 081124/TSV

CTA identification prb.001 ch.1

Insert probe specific parameters etc.

Sensor resistance, R_{20}	3.24	Ω	On probe box
Sensor lead resist., RL	0.50	Ω	55P11/01 family
Support resistance, Rs	0.00	Ω	Non standard
Cable resistance, Rc	0.20	Ω	Cable 9006A1083
Sensor TCR, α_{20}	0.36%	/K	Standard tungsten
Desired wire temp., Tw	242	°C	Wire mean temperature
Temperature of flow	17	°C	Temperature during measurement

Calculating wire operating resistance etc.

Over temperature, ΔT	225	°C
Operating resist., Rw	5.83	Ω
Total resistance, R_T	6.53	Ω
Overheat ratio, a	0.80	
Bridge ratio, M	1:20	
Decade resistance, R_D	130.6	Ω

Set decade controls as follows:

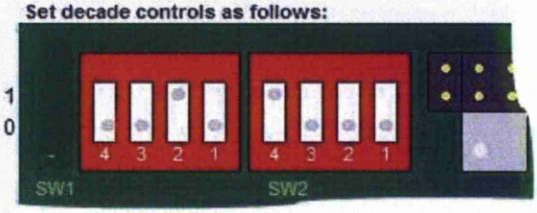

Figure C.12: Spreadsheet to define the dip switches and jumpers inside the miniCTA.

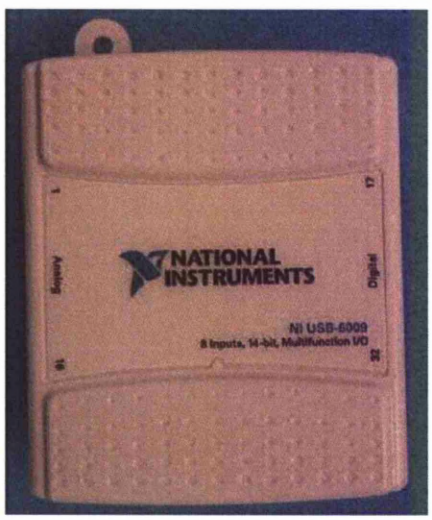

Figure C.13: National Instrument USB-6009 Digital to Analog Converter.

C.7 Hot-wire Probe

For measuring the instantaneous velocity and direction in two-dimensional flows, hot-wire probes produced by Dantec Dynamics were used. It is a single-sensor cylindrical wire probe with a gold-plated tungsten wire of 1.25mm length and $5\mu m$ diameter as shown in figure (C.14).

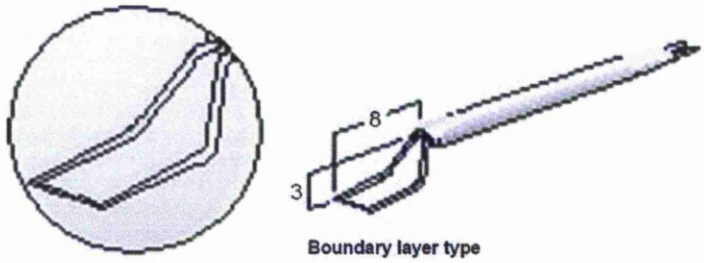

Figure C.14: Hot-wire anemometer.

The probe has to be mounted with the probe axis parallel to the direction of the main flow, so that the predominant flow vector attacks in the prong plane and is perpendicular to the fiber. An important characteristic of the probe is the operating resistance R_w. The sensor operating resistance given by:

$$R_w = R_{20} + \alpha_{20} R_{20}(T_w - 20) \tag{C.4}$$

and is calculated on the basis of the sensor operating temperature T_w, the sensor cold resistance R_{20} and its temperature coefficient of resistance TCR α_{20}. This information can be obtained from the probe manufacturer and is given below,

T_w (°C)	R_{20} (Ω)	α_{20} ($\%/K$)
250	3.24	0.36

Table C.3: Characteristics of the hot-wire probe.

C.7.1 Hot-wire Calibration

While the hot-wire probe is a very accurate flow measurement method, it has to be calibrated using manometers. This procedure is crucial because the conditions in and outside the test section change from test to test. This calibration establishes a relationship between the measurements from the hot wire and the pitot tube. It is performed by exposing the probe in a known set of velocities and then recording the voltages. This way an appropriate correlation between velocity and voltage from the hot-wire will be obtained. The voltages from the hot wire (E) and the velocity (U) estimated from the pitot tube are collected in a table and a polynomial curve fit through that points is used. During the experiment, two types of equations are used, a cubic transport and a power law equation. The latter one is known as King's Law and is given by $E^2 = A + B * U^n$ where A and B are constants and an initial value of n is n=0.45. An example of the hot-wire calibration with the use of trendline equation can be seen in figure (C.15).

C.7.2 Hot-Wire Errors

During the calibration of the hot-wire and experiment several errors may occur. These errors are basically due to changes to environmental conditions like humidity and temperature and are difficult to reduce.

Another error observed during the experiment is the wall proximity effect. This error appears as the hot-wire probe approaches the surface of the flat plate. The hot-wire probe uses a very fine wire which is heated or cooled by the air passing around it. The temperature of the plane is cooler than the hot-wire and this gives an additional heat loss. This proximity effect can be seen in figure (C.7.2).

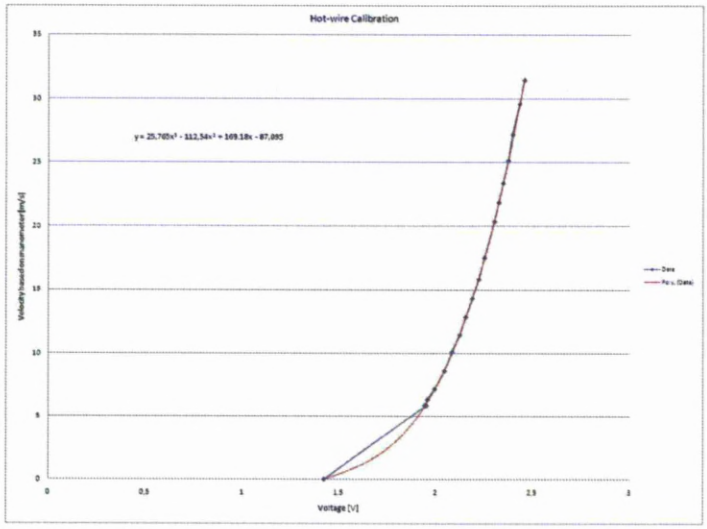

Figure C.15: Calibration line using a polynomial fit.

A change of the hot-wire voltage occurs as its distance normal to the wall is increased. The change of the voltage is significant for up to y= 4mm from the plate. From that height and above there is a small change but it is not important.

In order to eliminate this error the Will's correlation [93] has been used. This correlation corrects the readings of the hot-wire. Will's correlation is:

$$K_w = Re_m - Re_c^n \tag{C.5}$$

where K_w is a function of the height above the flat plate. Re_m and Re_c are the wire Reynolds number based on measured and corrected velocity respectively and n is equal to 0.45. The function for the K_w is given as

$$K_w = exp[1.678 - 1.229(\frac{y}{r})^{0.319}] \tag{C.6}$$

where r is the hot-wire radius.

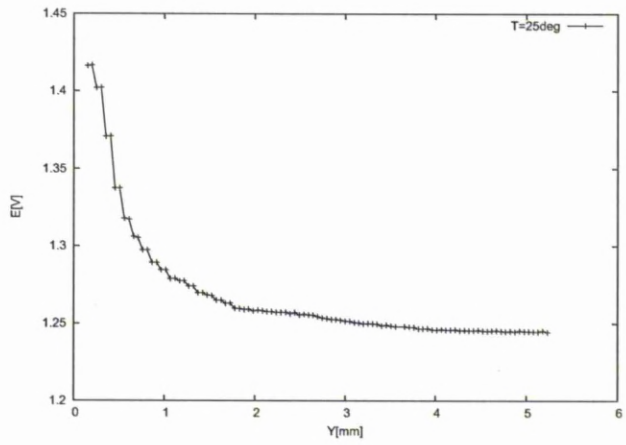

Figure C.16: Change of the hot-wire voltage as the probe moves away from the wall at external temperature of 25 degrees. Zero flow.

C.8 LabVIEW and C Programming

In order to control the traverse gear and the normal movement of the hot-wire probe, LabVIEW was used. LabVIEW provides an interface that helps to control the traverse gear and store data. Figure (C.17) shows the interface developed for this experiment. The interface can include knobs, buttons, warning indicators and paths where the data will be stored. To create this interface, LabVIEW provides a number of tools and functions for acquiring, analysing, displaying and storing data from the hot-wire and which are written in the form of code.

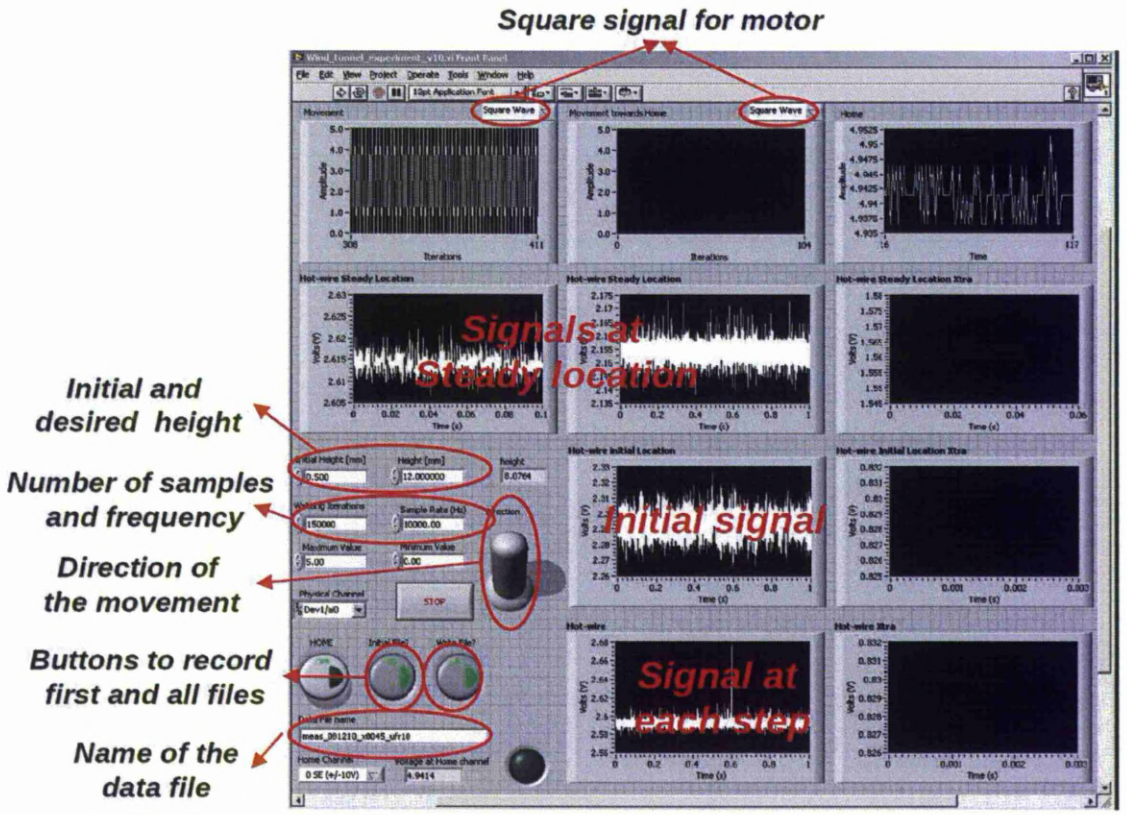

Figure C.17: Front panel of the virtual instrument.

A schematic for the correct estimation of the intermittency and other boundary layer parameters using the wind tunnel can be seen in figure (C.18).

For the connection of the hot-wire probe with the computer, a National Instrument USB-6009 DAC was used while for the control of the traverse gear a Labjack U12 equipment was connected. Both peripherals have their own internal programming functions which were included during the development of the LabVIEW code.

The user has to provide a number of inputs before the data logging begins. Initially, the user has to define the channel from where the program will log the data and then he has to move a knob which defines the direction that the traverse gear will move along. Then the initial height from where the probe will begin logging, the total height that it will move as long as the number of check points along the normal movement have to be defined. These check points define the locations where the hot-wire probe will acquire the data. Knowing the desired height, the normal height that the probe moves in each pulse and the number of check points, the program calculates the number of pulses that requires to reach each point. Based on the number of iterations, a square wave is created through the basic function generator. This function of LabVIEW requires knowledge of the amplitude and frequency of the square wave. Due to the fact that the stepper motor requires a voltage of 5V, a half amplitude of 2.5V was provided to the basic function generator. The outcome is passed in the *EAnalogOut* which sets the voltage on the output output. The latter function

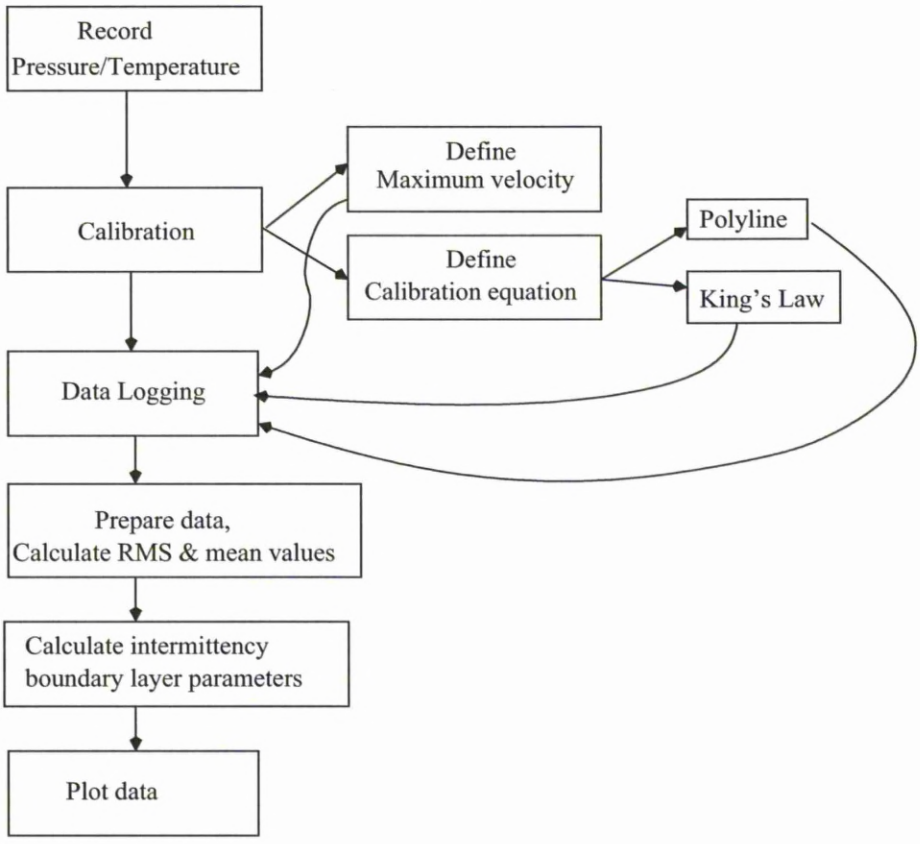

Figure C.18: A road map for the correct conduction of the wind tunnel experiment.

defines also the direction that the probe will move either by setting 0V at the output and moving it upwards or by setting it to 5V where the probe moves downwards. In order to define the home position, the *EAnalogIn* function was used to read the voltage from the first analog input. As soon as the voltage from this input falls below a specific value, in this case 4.9V, the program assumes that the traverse gear has reached its home position, it stops the movement of the traverse gear and activates a warning light.

When the iterations reached the desired position for a test point, the program stops the movement of the probe and initiates the logging of the data. The user has to define the number of samples and the sample frequency. The program opens the selected channel, reads the data and then stores these in a file of the format seen below. The function "Write to Measurement File" is used and two columns of time and voltages are written. At the first row, the initial height of the probe and the mean value of the voltages are provided. The user provides the name of the file and the name of the folder where the data will be stored. Also, by pressing the appropriate buttons, the user can move the probe without logging any data or log data from the initial probe location or even move the probe back to its home position.

The following figures ((C.19)-(C.21)) present the block diagram of the LabVIEW virtual instrument.

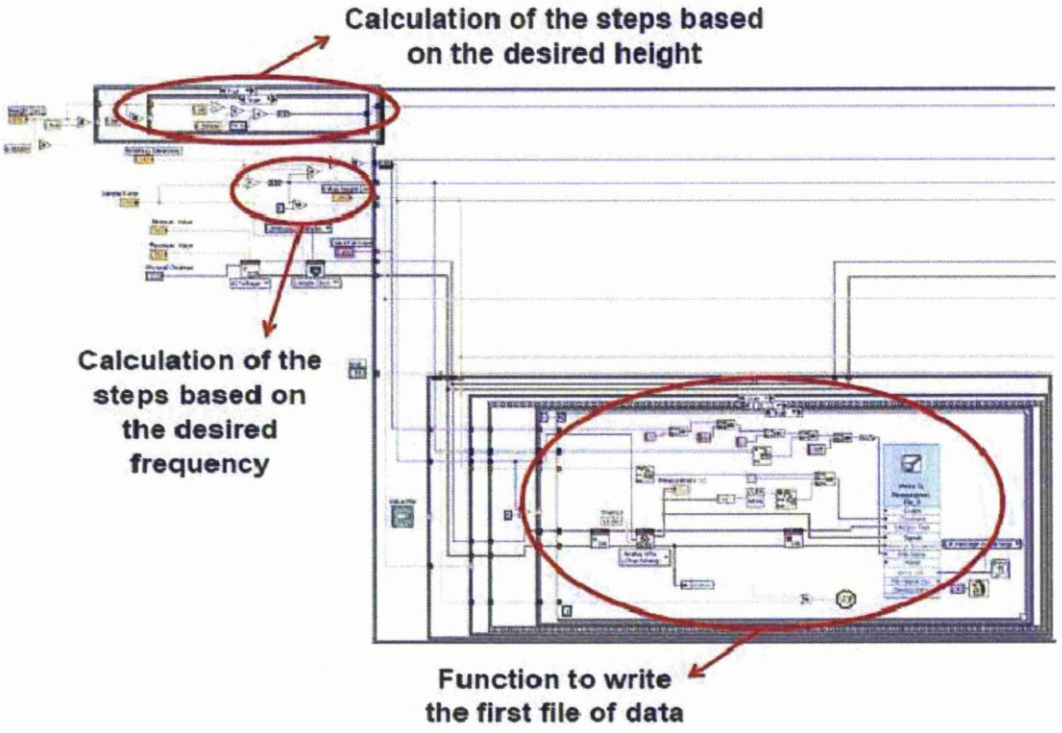

Figure C.19: Block panel of the virtual instrument, showing the functions responsible for reading the parameters.

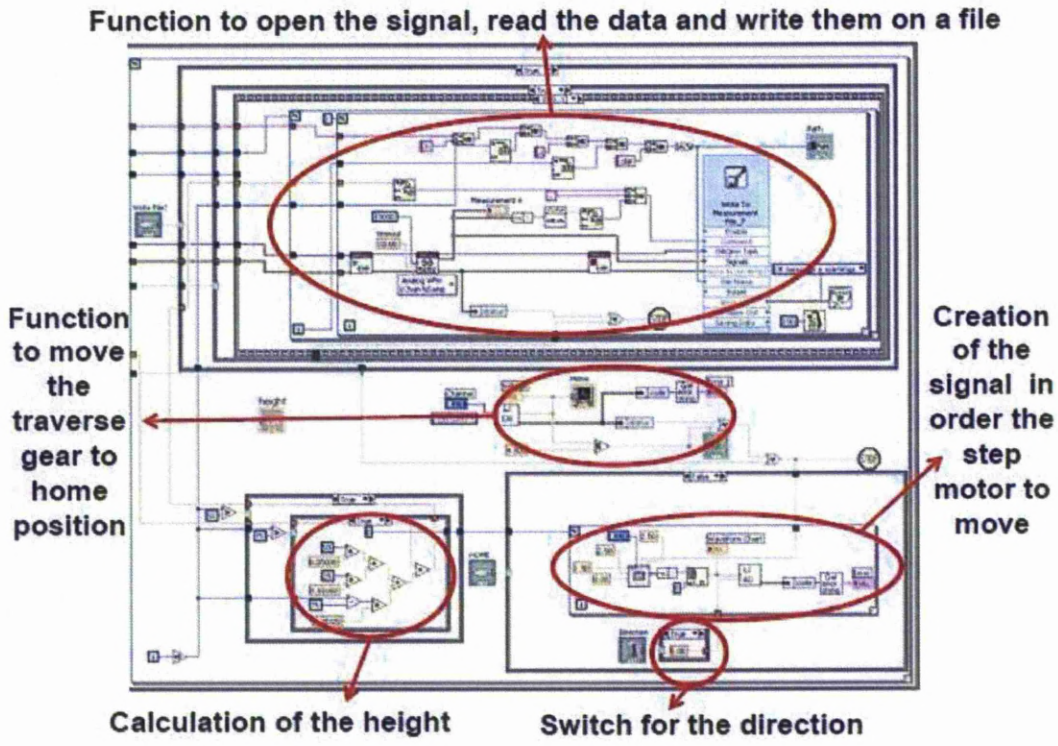

Figure C.20: Block panel of the virtual instrument, showing the functions for the signal generation and data logging.

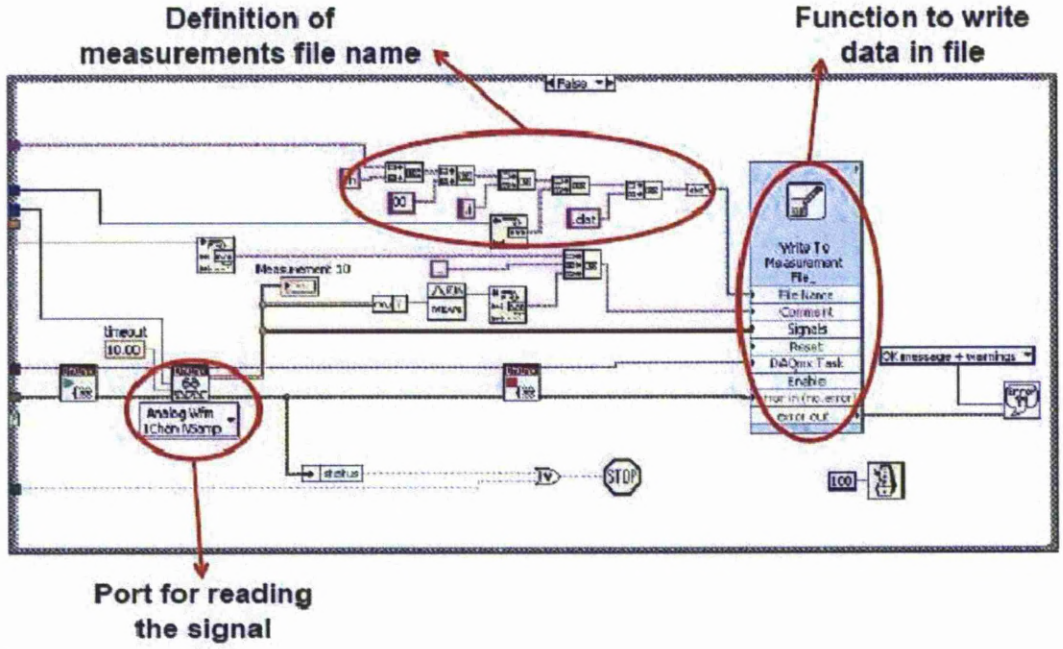

Figure C.21: Block panel of the virtual instrument, showing the functions for data logging during the moment that the hot-wire remains idle.

During the test, a number of displays are used , showing the height of the probe during the data logging phase.

```
LabVIEW Measurement
Writer_Version  0.92
Reader_Version  1
Separator       Tab
Multi_Headings  No
X_Columns       One
Time_Pref       Absolute
Operator        Giorgio Zografakis
Date    2010/03/08
Time    16:17:56.3126
***End_of_Header***

Channels        1
Samples 10000
Date    2010/03/08
Time    16:17:56.328125
Y_Unit_Label    Volts
X_Dimension     Time
X0      0.0000000000000000E+0
Delta_X 0.000100
***End_of_Header***
X_Value Dev1/ai0        Comment
0.000000        2.407497        0.500000 2.397002
0.000100        2.405587
0.000200        2.406224
0.000300        2.401769
0.000400        2.397314
0.000500        2.397314
```

Before manipulating the data, the user has to create two initial files that would provide the post-processing codes with the necessary input. Tables (C.8) and (C.8) present examples of these initials files. The number of steps/y-locations, the initial height, number of samples, frequency, pressure and temperature of the experiment are included in these files. Also, the user has to define a deviation factor and a window for the signal. Based on the method selected for the calculation of the velocity, the user has to provide the four parameters of the trendline or the E_0 (or A), b (or B) and the n parameters for the King's Law ($E^2 = A + B * U^n$).

Number of y locations	: 50
Initial station	: 45
Initial height	: 0.05
Initial voltage	: 1.422495
Number of samples	: 150000
Frequency	: 10000
Temperature	: 21.5
Pressure(mmHg)	: 746.2
Deviation factor	: 6
Window of signal	: 0.1
factor for 3rd power	: 25.76513
factor for 2nd power	: -112.538935
factor for 1st power	: 169.178568
factor for 0 power	: -87.094746

Table C.4: Example of the initial file for the polynomial method.

In order to process the data, two different programs written in C language have to be used. Each of these programs are divided based on the method that is used for the calculation of the velocity. The name of the executables and the commands that have to be given, can be see below.

Number of y locations	: 50
Initial station	: 45
Initial height	: 0.05
Number of samples	: 150000
Frequency	: 10000
Temperature	: 21.5
Pressure(mmHg)	: 746.2
Deviation factor	: 6
Window of signal	: 0.1
E0 - King's Law constant	: 1.422495
b - King's Law constant	: 0.754356659
n - King's Law constant	: 0.487202

Table C.5: Example of the initial file for the King's Law method.

For the case where the King's Law is used, the following command should be used:

```
./WTC_PRE_DATA_KING.EXE meas_140211_x0045
```

and followed by:

```
./WTC_DATA_KING.EXE velo.dat.KL meas_140211_x0045.ls
```

For the case where the polynomial method is used, the command to execute is:

```
./WTC_PRE_DATA_TRENDLINE.EXE meas_140211_x0045
```

followed by

```
./WTC_DATA_TRENDLINE.EXE velo.dat.trendline meas_140211_x0045.ls
```

The C program *WTC_PRE_DATA* is the first executable that has to be run. The program reads the data for each step and provides a file where all information will be concatenated. The new file that would be created would be named as $\{data\_name\}.ls.h\{step\}.dat$. The file will have four columns where the first one will be the time of the measurement while the second one includes the voltage that the hot-wire has measured at each step. For each vertical position, and for every time step, the velocity is calculated based on either King's Law or the polynomial method and it is included at the third column of the file. The latter values of velocity are correct for the case that the hot-wire is at the free-stream. As the hot-wire is close to the surface of the flat plate, a correction has to be taken into account in order to avoid the wall proximity effect. For this reason, the Will's correlation (see eqn.(C.5)) has been used.

The second file, this program creates, is called *velo.dat* and includes the information for all steps of the specific station. The file includes five columns where the first one indicates the height of each step/y-location starting from the first y-location that the user has initially defined. The following columns include the mean values and the RMS values for the velocity and the voltage. The mean velocity is calculated as the average of the points while the RMS is

$$u_{rms} = [\frac{\sum_{n=1}^{30000}(u(n))^2}{30000} - u_{mean}^2]^{\frac{1}{2}} \tag{C.7}$$

The second C program *WTC_DATA* is used to produce the required information for the specific station of the boundary layer. It requires the *velo.dat* and the name of the file with the concatenated data $\{data\_name\}.ls$. The velocity values from the *velo.dat* are used in order to obtain the boundary layer integral parameters. Hence, the displacement thickness, δ^* and the momentum thickness, θ, are given as

$$\delta^* = \int_{y=0}^{\delta}(1 - \frac{u}{U_{fr}})dy \tag{C.8}$$

and

$$\theta = \int_{y=0}^{\delta}\frac{u}{U_{fr}}(1 - \frac{u}{U_{fr}})dy \tag{C.9}$$

where δ is the height where the local velocity reaches 99% of the free-stream velocity (U_{fr}).

The displacement and momentum thickness easily allow for the calculation of the shape factor as the ratio of δ^* and θ

$$H = \frac{\delta^*}{\theta} \tag{C.10}$$

The skin friction coefficient C_f is calculated using

$$C_f = \frac{\mu(\frac{du}{dy})_{y=0}}{\frac{1}{2}\rho U^2} \tag{C.11}$$

where $\frac{du}{dy}|_{y=0}$ is the graduate of the velocity with wall distance. The calculation uses an average of the first five velocities.

The next step is to remove low frequency waves and filter the signal through a high-pass filter before calculating the intermittency. The intermittency factor (γ) is defined as

$$Intermittency = \frac{Turbulent\,Time\,Period}{(Turbulent + Laminar)\,Time\,Period} \tag{C.12}$$

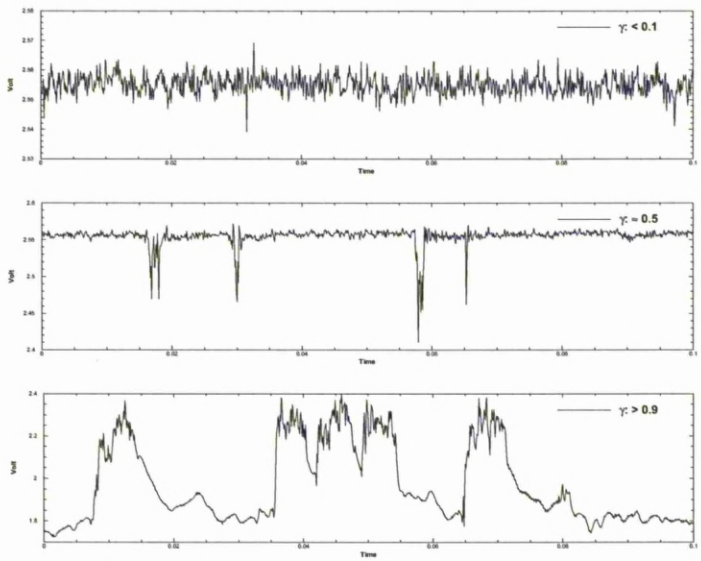

Figure C.22: *Hot wire traces at three levels of intermittency (γ)*

Figure (C.22) presents hot wire signal traces for favorable pressure gradient and for high levels of free-stream turbulence. Observing the traces, it can be seen that low amplitude instabilities are present in the laminar portions of them. In order to distinguish the laminar and the turbulent portions of the signal, the unwanted frequencies have to be removed. This is the reason a high pass filter is applied. As was mentioned in earlier studies[95] a window size of 10% of local mean velocity was used. The size and the residence time of the signal in the window dramatically effects the intermittency factor. The size of the window designate the parts of the signal that are outside the window as turbulent while those parts of the signal inside the window as laminar. If the window is too large, then transition is detected later than it appears, while if the size is considered too small, then the results have the inverse effects and transition is predicted earlier. Similarly, the residence time is the minimum permissible time between two turbulent bursts and has to be considered properly otherwise it will have effects on the calculation of transition. For this study a time period of $\frac{2\pi\delta}{U}$ sec is considered.

For the high pass filter, a frequency of $\frac{U}{2\pi\delta}$Hz was selected (U is the free stream velocity and δ denoted the boundary layer thickness). This frequency was selected as it is the frequency of the largest vortices that can be accommodated in the boundary layer.

The output of this program contains information about the skin friction, boundary layer height and momentum thickness along with the turbulence intensity and the local Reynolds number. Also, a new file under the name *gamma.dat* is created and includes for each vertical step of the station the value for the intermittency as long as the mean, RMS and fluctuations values for the velocity and the voltage respectively.

C.9 Wind Tunnel Measurements

The following table (C.6) presents the free-stream turbulence intensity created at the leading edge of the flat plate. These results are for different type of grids. G0 is the case where no grid is placed in the wind tunnel.

Grids	Tu(%) at leading edge ZPG	Tu(%) at leading edge FPG	Tu(%) at leading edge APG	Grid Blockage (%)
G0	0.744	0.968	0.56116	
G1	1.188	1.4421	1.0282	10.66
G2	2.173	2.2688	1.6748	31.42
G3	2.154	2.3928	1.2942	30.59
G4	5.485	5.2314	3.3993	26.84
G5	3.002	3.02	2.3528	31.16
G6	6.45	7.3684	5.2609	47.113

Table C.6: Free stream turbulence intensity for the different grid cases. ZPG: Zero Pressure Gradient, FPG: Favorable Pressure Gradient, APG: Adverse Pressure Gradient

The following tables present the onset of transition for the different cases. Table (C.7) show the onset of transition based on the empirical correlation model of Michel. In order to estimate the onset of transition, the experimental data from the six different free-stream turbulence intensities and three pressure gradients were used for estimating the momentum thickness and the local Reynolds number required for the Michel criterion. It is characteristic that for the zero pressure gradient and as the free-stream turbulence intensity increases, the onset of transition is moves forward closer to the leading edge. This characteristic behavior is observed for the favorable pressure gradient (FPG). In the case of the adverse pressure gradient (APG) the onset of transition is estimated near to the leading edge.

Grids	x_{start} [mm] Michel ZPG	x_{start} [mm] Michel FPG	x_{start} [mm] Michel APG
G0	745		45
G1	595	795	45
G2	395	295	45
G3	295	295	95
G4	245	195	95
G5	295	295	45
G6	95	195	95

Table C.7: Onset of transition flow based on the empirical correlation model of Michel. Comparison between the three different pressure gradients, zero (ZPG), favorable (FPG) and adverse (APG).

The onset of transition flow based on the Cebeci Smith criterion can be seen at the table (C.8). A similar behavior as for the Michel criterion is observed.

Table (C.9) presents the onset of transition based on the experimental data. As the transition location is considered to be the point where the intermittency (γ) has values higher than 0.1 . In comparison with the previous tables, it can be seen that the onset of transition is estimated slightly earlier than with the empirical correlations for the zero pressure gradient.

Grids	x_{start} [mm] Cebeci and Smith ZPG	x_{start} [mm] Cebeci and Smith FPG	x_{start} [mm] Cebeci and Smith APG
G0	695		45
G1	395	795	45
G2	345	295	45
G3	295	295	95
G4	295	195	95
G5	195	195	45
G6	95	195	95

Table C.8: Onset of transition flow based on the empirical correlation model of Cebeci Smith method. Comparison between the three different pressure gradients, zero (ZPG), favorable (FPG) and adverse (APG).

Grids	x_{start} [mm] Experimental ZPG	x_{start} [mm] Experimental FPG	x_{start} [mm] Experimental APG
G0	595	-	95
G1	595	595	45
G2	295	295	45
G3	195	195	95
G4	95	95	45
G5	145	195	45
G6	95	95	45

Table C.9: Onset of transition flow based on experimental data. Comparison between the zero (ZPG), favorable (FPG) and adverse (APG) pressure gradients.

The following figures (C.23) and (C.24) show the transition onset momentum thickness Reynolds number as a function of the pressure gradient for constant values of turbulence intensity and compare the experimental data against data by Abu-Ghannam and Shaw[63]. The plots show the limitation of the experiment with the current configuration as the experimental data don't show the sparsity of the data derived from the Abu-Ghannam and Shaw[63] experiments.

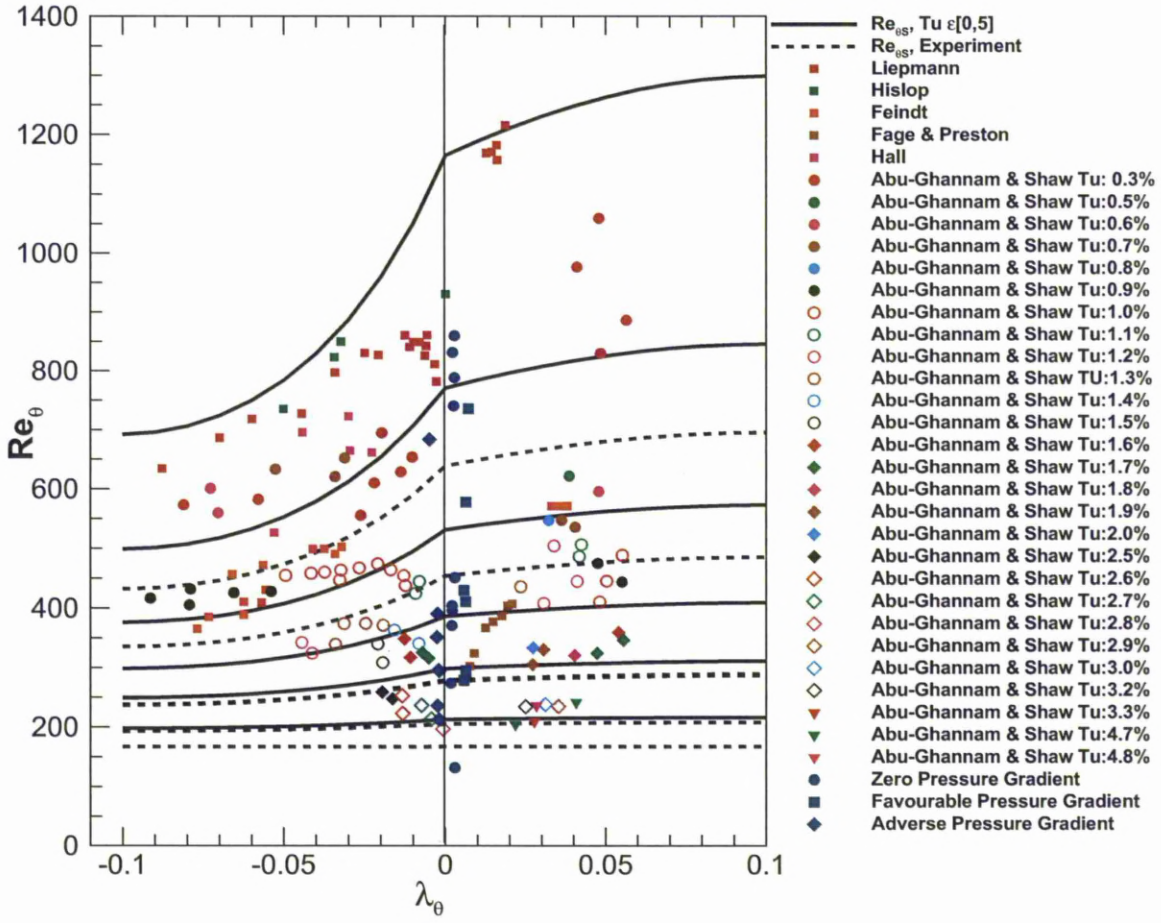

Figure C.23: Transition onset momentum thickness Reynolds number ($Re_{\theta t}$) as a function of pressure gradient (λ_θ) for constant values of turbulence intensity (Tu).

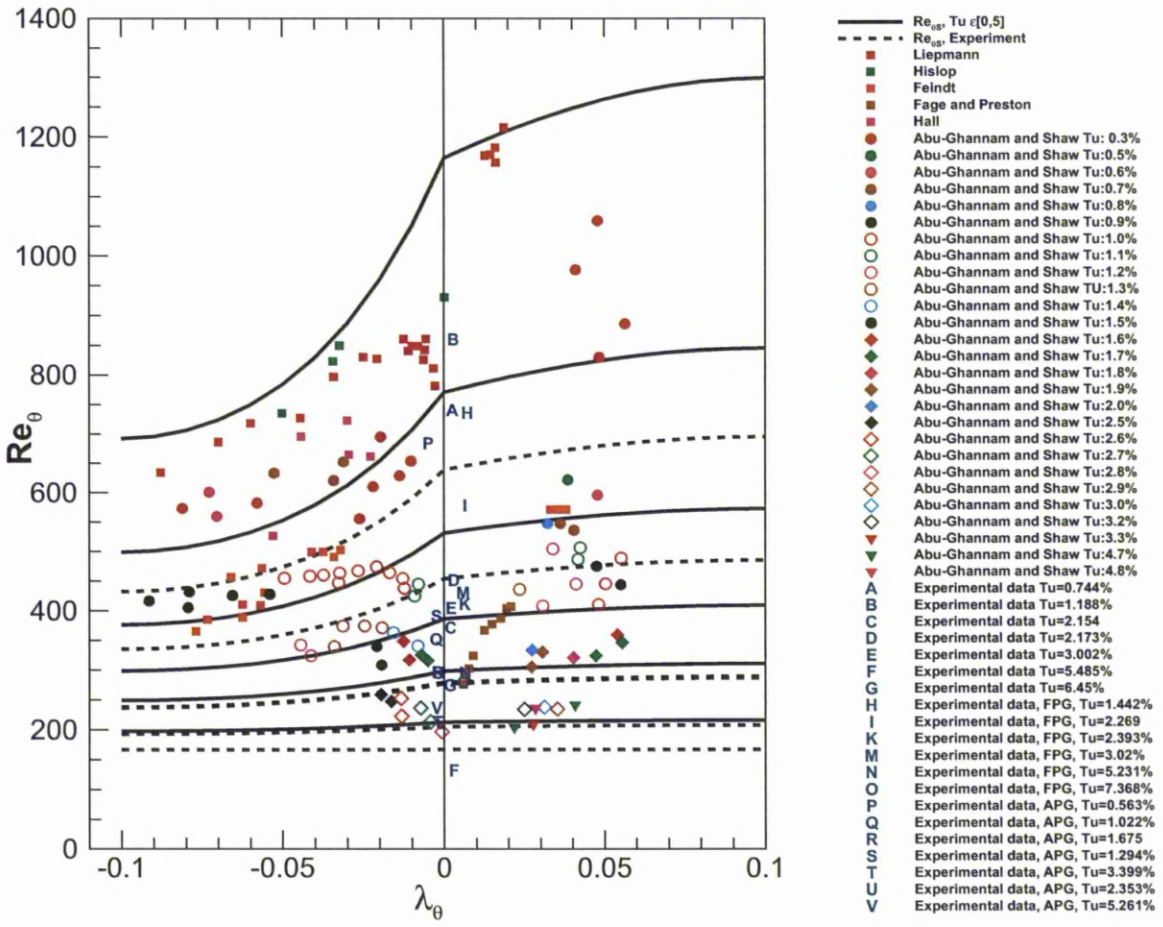

Figure C.24: Transition onset momentum thickness Reynolds number ($Re_{\theta t}$) as a function of pressure gradient (λ_θ) at constant values of turbulence intensity (Tu).

The following figures present the intermittency factor and the velocity profiles for different free-stream turbulence intensities and pressure gradients. The height is non dimensionalised with the boundary layer thickness of each station while the comparison of the data is shown for the same location on the flat plate. The location was selected as it is in the middle of the test section and at the same x location as the Pitot tube. Figures (C.25(a)) and (C.25(b)) show the results for the free-stream turbulence intensity of $Tu(\%) = 1.41$. It is obvious that in this station, the flow is considered as fully turbulent. From the comparison of the intermittency factors, it can be seen that the thickness of the boundary layer is higher for the case with the zero pressure gradient. This can be justified based on the height where the intermittency becomes zero and the highest case is for the zero pressure gradient case.

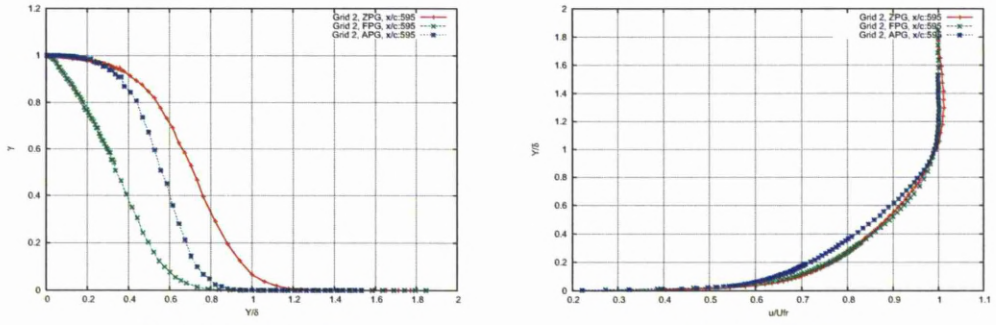

(a) Intermittency factor (b) Velocity profiles

Figure C.25: Intermittency factor and velocity profiles as a function of height for the station x:595. The G2 grid is used ($Tu(\%) = 1.41$, $Re_x = 1.15 \times 10^6$).

Increasing the free-stream turbulence intensity to $Tu(\%) = 5.19$, the flow can be considered as fully turbulent. The results can be seen in figures (C.26(a)) and (C.26(b)). Comparing the results with the previous case, it is obvious that the boundary layer thickness is smaller than the case of $Tu(\%) = 1.41$. The case with zero pressure predicts more intermittency in comparison to the adverse pressure gradient case.

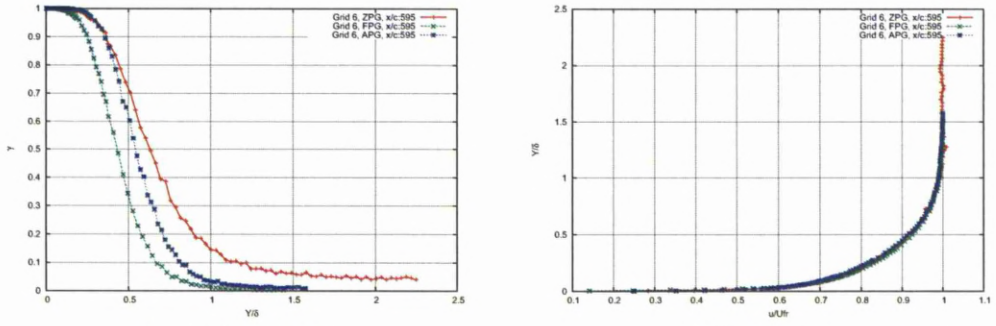

(a) Intermittency factor (b) Velocity profiles

Figure C.26: Intermittency factor and velocity profiles as a function of height for the station x:595. The G6 grid is used ($Tu(\%) = 5.19$, $Re_x = 3 \times 10^6$).

As it was seen on figures (C.23) and (C.24), the existing experimental data do not show the sparsity observed in the Abu-Ghannam and Shaw[63] experiments. Combined with the lack of time, the experiments should be repeated in order to achieve better agreement with the experimental data derived from Abu-Ghannam and Shaw.

Appendix D

Overview of the HMB flow solver

D.1 Introduction

The Helicopter Multi-Block (HMB CFD code is a sophisticated computational tool able to perform analysis for a large number of applications. The HMB solver was developed at University of Liverpool and it is a living organisation in which new characteristics and tools are added continuously.

The HMB solves the Reynolds Averaged Navier-Stokes equations on block-structured grids using a cell-centre finite volume approach combined with an implicit dual-time method. This means that the solution marches in pseudo-time for each real time-step to achieve faster convergence. The computational domain is divided into a finite number of non-overlapping control-volumes, and the governing equations are applied in integral-conservation form at each cell. For imposing boundary conditions or to allow communication between adjacent block, two layers of halo cells are used in HMB solver.

The solver has a library of turbulence closures which includes several one- and two-equation turbulence models and even non-Boussinesq version of $k-\omega$ model. Turbulence simulation is also possible using either the large-eddy or the detached-eddy approach, Lately, the effects of roughness and transition were included in the HMB. The solver was designed with parallel execution in mind, hence the MPI library along with a load-balancing algorithm is also used.

D.2 Data Structures

The HMB solver has to operate with a large amount of data produced from the models and the test cases. Hence an extra attention has to be taken during the manipulation of them. The addition of extra functionality into HMB requires that extra data have to pass through many different layers of subroutines. Hence, a specific data structure has been added. Above all is the global data structure which is constant for all blocks and contains all the data of the block. Below this data is a structure which contains all the information about all the blocks in the mesh. Each block is connected to six sides and each side has a structure related to faces. An overview of the data structure into HMB can be seen in figure (D.1).

D.3 Implicit formulation

A unique feature of HMB is the implicit time-marching technique that is used and which comes in contrast to the mainstream flow solvers that rely on explicit methods and multi-grid algorithms for convergence acceleration. As it was already mentioned, the Navier-Stokes (NS) equations are discretised using a cell-centred finite volume approach. The computational domain is divided into a finite number of non-overlapping control volumes, and the governing equations are applied to each cell in turn. The spatial discretisation of the Navier-Stokes equations leads to a set of ordinary differential equations in time,

$$\frac{d}{dt}\left(\mathbf{W}_{i,j,k}\mathscr{V}_{i,j,k}\right)+\mathbf{R}_{i,j,k}=0. \tag{D.1}$$

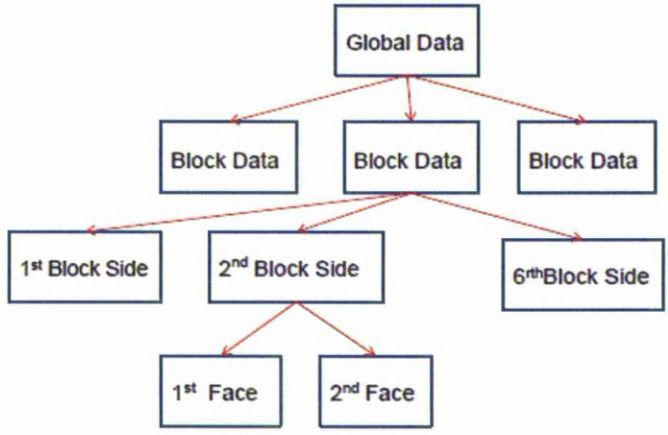

Figure D.1: An overview of the global data structure.

where $\mathcal{V}_{i,j,k}$ denotes the cell volume and $\mathbf{W}_{i,j,k}$ and $\mathbf{R}_{i,j,k}$ represent the cell variables and residuals, respectively.

The implicit dual-time method proposed by Jameson[29] is used for time-accurate calculations. The residual is redefined to obtain a steady state equation which can be solved using acceleration techniques. The following system of equations are solved in the implicit scheme during the dual-time integration process:

$$\frac{\Delta V \mathbf{W}_{i,j,k}^{m+1} - \Delta V \mathbf{W}_{i,j,k}^{m}}{\Delta V \Delta \tau} + \frac{\Delta V \mathbf{W}_{i,j,k}^{n+1} - \Delta V \mathbf{W}_{i,j,k}^{n}}{\Delta V \Delta t} = \mathbf{R}_{i,j,k}^{n+1} \tag{D.2}$$

where ΔV is the change in cell volume, $\Delta\tau$ is the pseudo time-step increment and Δt is the real time-step increment. The flux residual $\mathbf{R}_{i,j,k}^{n+1}$ is approximately defined by:

$$\mathbf{R}_{i,j,k}^{n+1} \approx \mathbf{R}_{i,j,k}^{n} + \frac{\partial \mathbf{R}_{i,j,k}^{n}}{\partial \mathbf{W}_{i,j,k}^{n}} \left(\mathbf{W}_{i,j,k}^{n+1} - \mathbf{W}_{i,j,k}^{n} \right) \tag{D.3}$$

By substituting eqn. (D.3) into eqn. (D.2), the resulting linear system can be written as:

$$\left(\frac{1}{\Delta t} + \left(\frac{\partial \mathbf{R}}{\partial \mathbf{W}} \right)^{n} \right) \Delta \mathbf{W} = -\mathbf{R}^{n} \tag{D.4}$$

where the subscripts i, j, k have been dropped for clarity and ΔW is used for $\left(\mathbf{W}_{i,j,k}^{n+1} - \mathbf{W}_{i,j,k}^{n} \right)$.

The above equation must be solved for each cell of the mesh and provides an update to the vector of variables $\Delta\mathbf{W}$ as a solution of a system of algebraic equations formulated on the residual on the right side and its Jacobian that appears on the left hand side.

D.4 Linear system solution method

The global assembly of the discrete equations over the computational domain results in a system of equations of the form Ax-b. The complexity of the direct method to compute a linear system has lead to the use of iterative methods as Conjugate Gradient (CG) methods which are capable of solving large systems of equations more efficiently in terms of time and memory. CG methods find an approximation to the solution of a linear system by minimizing a suitable residual error function in a finite dimensional space of potential solution vectors. A Generalised Conjugate Gradient (GCG)[33] method is then used in conjunction with a Block Incomplete Lower-Upper (BILU)[33] factorisation as a pre-conditioner to solve the linear system of equations, which is obtained from a linearisation in pseudo-time. The BILU factorisation is decoupled between blocks on different processors to improve parallel efficiency and this approach does not seem to have a major impact on the solution as the number of blocks increases. During the calculations, a specified number of Euler iterations are executed before switching to the implicit scheme.

D.5 Jacobian Formulation

For a block-structured mesh, equation D.4 represents a large, sparse matrix which arises from the implicit discretisation in pseudo-time. The Jacobian matrix is calculated analytically by repeated application of the chain rule. The residual for one cell is built up as a summation of the fluxes through the cell faces. The result of the above is that the Jacobian matrix which appears in the left hand side of the discretisation has a number of non-zero entries per row. By trying to reduce the number of those non-zero entries has several advantages as the low memory requirements and the reduced required CPU-time. With the use of the GCG method, the linear system is easier to solve since approximate Jacobian matrices can be used that are more diagonally dominant. All equations are solved simultaneously for the next time level which allows flexibility if the cross-terms are added to the Jacobian matrix. Advantages of this formulation is the lower memory requirements as long as the lower required CPU-time. Solving the Navier-Stokes equations augmented with the transport equations of turbulence and transition models, the resulting Jacobian matrix has a given sparsity pattern. For one and two equation turbulence models, the block structure is given by

$$\begin{bmatrix} B_{00} & B_{01} \\ B_{10} & B_{11} \end{bmatrix}$$

The B_{00} is an 5x5 matrix and is associated with the flow variables of ρ, u, v, ω and p. The B_{11} is either a scalar for a one-equation turbulence model or a 2x2 matrix for a two-equation model. The term B_{01} is related to how the fluid variables depend on the turbulent variables while block B_{10} describes how the turbulent variables depend on the fluid variables. Otherwise, one or both blocks can be considered zero and drive to more sparse system. In the case of a transition model is in use, an extra row is added. The matrix is given by

$$\begin{bmatrix} B_{00} & B_{01} & B_{02} \\ B_{10} & B_{11} & B_{12} \\ B_{20} & B_{21} & B_{22} \end{bmatrix}$$

where the first row is associated with fluid variables ρ, u, v, ω, p, the second row is related to the turbulent model, κ and ω, while the last row is related to the LCTM model (γ and $Re_{\theta t}$).

D.6 Variable extrapolation - MUSCL

The Monotone Upstream-Centred Scheme for Conservation Laws (MUSCL) was introduced by Van Leer [32]. It is a compact scheme which is used to discretise the convective part of the Navier-Stokes equations. In one dimension using a uniform spacing, the extrapolation to both sides of the face at $i+1/2$ is

$$U^L_{i+1/2} = U_i + \frac{\phi(r_i)}{4}[(1-\chi)\Delta_- U_i + (1+\chi)\Delta_+ U_i] \tag{D.5}$$

$$U^R_{i+1/2} = U_{i+1} - \frac{\phi(r_{i+1})}{4}[(1-\chi)\Delta_+ U_{i+1} + (1+\chi)\Delta_- U_{i+1}] \tag{D.6}$$

where $\Delta_+ U_i = U_{i+1} - U_i$, $\Delta_- U_i = U_i - U_{i-1}$, $\phi(r_i)$ is the limiter and $r_i = \Delta_- U_i / \Delta_+ U_i$. If $\phi(r_i) = 0$ then this is only a first order scheme but if $\phi(r_i) = 1$ then higher order schemes are activated which are at least second order for all values of χ.

The current scheme in HMB solver uses the alternative form of the van Albada limiter [96] namely

$$\phi(r) = \frac{2r}{r^2+1} \tag{D.7}$$

it should be noted that this limiter is not second order TVD since for any $r \in (1,2)$, $\phi(r) < 1$. Then value of χ is set to zero giving the final formulation

$$U^L_{i+1/2} = U_i + \frac{\Delta_- U_i \Delta_+ U_i}{2(\Delta_+ U_i^2 + \Delta_- U_i^2)}[\Delta_- U_i + \Delta_+ U_i] \tag{D.8}$$